Title
Spectroscopy of Transient Neutral Species via Negative Ion Photoelectron Spectroscopy

Author
Weaver, A.

Publication Date
1991-12-01

LBL-31877

Lawrence Berkeley Laboratory
UNIVERSITY OF CALIFORNIA

CHEMICAL SCIENCES DIVISION

Spectroscopy of Transient Neutral Species via Negative Ion Photoelectron Spectroscopy

A. Weaver
(Ph.D. Thesis)

December 1991

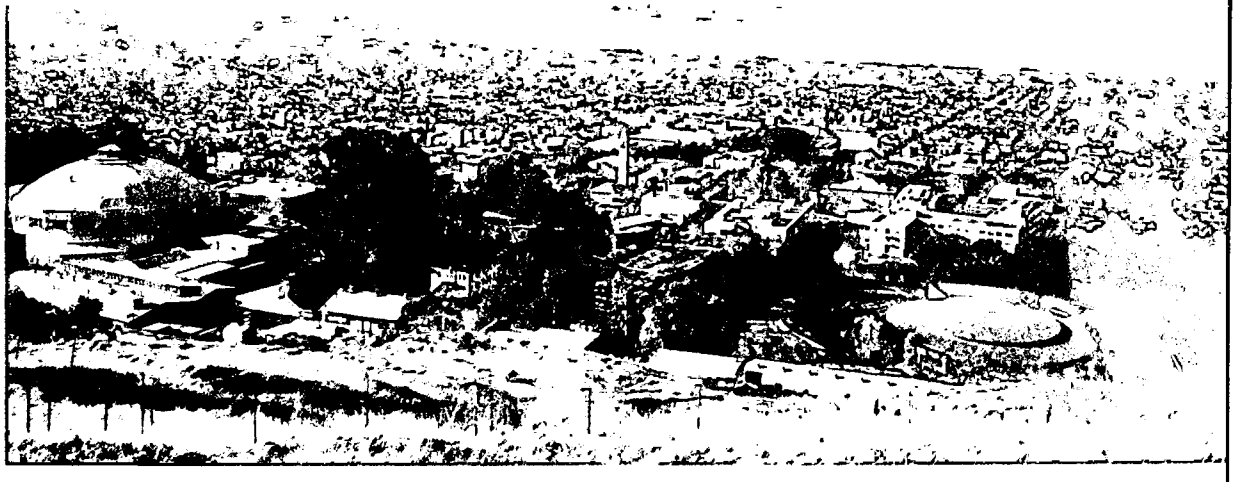

Prepared for the U.S. Department of Energy under Contract Number DE-AC03-76SF00098

DISCLAIMER

LBL-31877

Spectroscopy of Transient Neutral Species via Negative Ion Photoelectron Spectroscopy

Alexandra Weaver
Ph.D. Thesis

Department of Chemistry
University of California

and

Chemical Sciences Division
Lawrence Berkeley Laboratory
University of California
Berkeley, CA 94720

December 1991

This work was supported in part by the Air Force Office of Scientific Research under Contract No. AFOSR-91-0084, and by the Director, Office of Energy Research, Office of Basic Energy Sciences, Chemical Sciences Division, of the U.S. Department of Energy under Contract No. DE-AC03-76SF00098.

Spectroscopy of Transient Neutral Species via Negative Ion Photoelectron Spectroscopy

by

Alexandra Weaver

Spectroscopy of Transient Neutral Species via Negative Ion Photoelectron Spectroscopy

by

Alexandra Weaver

Abstract

Negative ion photoelectron spectroscopy has been used to study two types of transient neutral species: bound free radicals (NO_2 and NO_3) and unstable neutral species ([IHI] and [FH_2]). The negative ion time-of-flight photoelectron spectrometer used for these experiments is described in detail.

Photoelectron spectra of NO_2^- at 266 and 213 nm show the $\tilde{X}(^2A_1)$, $\tilde{A}(^2B_2)$ and $\tilde{C}(^2A_2)$ bands of NO_2. We obtain the energy of the $\tilde{A}(^2B_2)$ state as T_0 = 1.204 eV from Franck-Condon simulations of the vibrational structure, and the energy of the $\tilde{C}(^2A_2)$ state as T_0 = 2.02 eV. The $\tilde{C}(^2A_2)$ band includes two peaks which cannot be explained by Franck-Condon-allowed transitions, and may result from vibronic coupling between the $\tilde{B}(^2B_1)$ and $\tilde{C}(^2A_2)$ states.

Photoelectron spectra of NO_3^- at 266 nm show the $^2A_2'$ band of NO_3. Franck-Condon forbidden transition to odd quanta of a non-totally symmetric mode (ν_4) appear in the spectra and are attributed to second-order linear (pseudo-Jahn-Teller) coupling between the $^2A_2'$ and $^2E'$ states via the degenerate ν_4 mode. A vibronic coupling calculation which explicitly includes this effect reproduces the peak positions and intensities in our spectra.

Spectra at 213 nm also show the 'dark' $^2E''$ state 0.868 eV above the ground state.

The transition state region of the potential energy surface for a neutral bimolecular reaction, A + BC, can be studied by photodetachment of the corresponding stable anion, ABC^-, provided that the geometry of ABC^- is similar to that at the neutral transition state. Spectra of IHI^- and IDI^- at 266 nm show evidence of long-lived quasi-bound states of the neutral [IHI] and [IDI] complexes.

Photoelectron spectra of FH_2^-, FD_2^- and FDH^- also show evidence of quasi-bound states. These spectra are dominated by transitions to shorter-lived 'direct' scattering states, although the FH_2^- spectrum shows a sharp peak attributed to a transition to a longer-lived resonance scattering state.

Dedicated to my parents

Kalliopi Kalathaki

and

Martin Weaver

Table of Contents

List of Figures

Page

List of Tables

Page

Acknowledgements

Dan Neumark has taught me a lot about chemistry and about getting experiments to work. Working for him has been a challenge - I could never keep up with the constant supply of new ideas for experiments and for analyzing our results. Dan certainly led by example in the first couple of years of building machines, and his hard work, creativity, persistence and drive would be difficult to match. I have been very grateful for his careful design of the fixed-frequency machine, in the last five years: it is a pleasure to work on a machine which can yield data first thing in the morning, and it is even better to have more data than one has time to analyze.

My colleagues in the Neumark group are also extremely talented, and it has been a privilege to work with them. I hope that they achieve the success in later life that they all deserve. I am also very grateful for their acting as an Auxiliary Thesis Committee when no one else wanted to read any more about the Molecules of the 90's.

Theo Kitsopoulos and Ricky Metz have really been like brothers to me, although they refuse to admit it. I admire and respect both of them very much (most of the time). Theo and I had a special relationship because he was the only person in the group who ever wanted to listen to my Greek music tapes. (Personally, I found Greek music essential for adjusting Newport valves and getting difficult experiments to work. Dan never seemed to believe it.) Unfortunately, the conversational Greek I picked up from listening to him did

not go far in helping me speak to my grandmother - he uses a lot of expressions that I hope she has never heard. Ricky's zen-like character in the face of all disasters was truly amazing, as was his array of diverse talents - there are not so many windsurfing chess masters around. His 2D DVR code has made possible many of the simulations presented in this thesis.

I am grateful to Steve Bradforth for his ability to explain difficult concepts and his vast storehouse of useful knowledge. If the INS understood how much American science needs people like him, they would have waived his residency requirement. Don Arnold deserves many thanks for his help with experiments, his marvellous simulation program, unequalled mechanical ability, and his amazing good humour and enthusiasm in spite of four years on D level. American science also really needs people like Don.

Bob Continetti's phenomenally complete knowledge of experimental physical chemistry has helped me a great deal, and I am grateful for that. Doug Cyr, Caroline Chick, and Eun Ha Kim have all helped my experimental work and the writing of my thesis, and I thank them.

None of these experiments would have been possible without the skill and dedication of the machine shop staff at Berkeley. I am grateful to all of them, and especially to George Weber and Andy Anderson. Many other staff members in the department went beyond the call of duty to help us, and they deserve thanks.

I owe thanks to several professors and other senior scientists for their

help, ranging from 'fruitful discussions' to letters of recommendation: Professors Harold Johnston, Herb Strauss, Rich Saykally, Yuan Lee and David Chandler at Berkeley, John Polanyi at Toronto, Ken Kawaguchi at NRO, Randy Friedl at JPL, Celeste Rohlfing at Sandia, Michael Morse at Utah, and Anthony Merer at UBC.

I would not have come to graduate school without the help and encouragement of many people. Stan Clark, John Parry, and Maris Neimanis were high school teachers of mine who were especially influential. Tom Pratum told me I should go to Berkeley, when I was a Canadian undergraduate who thought of Berkeley as the unattainable centre of the physical chemistry universe. His encouragement, plus that of Peter Beckmann, Elliott Burnell, Terry Gough and John Hepburn, was very important.

I am very grateful to those who have given me their love and support over the last five years, especially Karen Schultz, Joel Bader, Anna Agell, Tim Zindel and Pat Choate. Lois and Bill Wilson and their friends, especially Edward, Sandy, and Virginia, have helped restore me to sanity many times, and I could not have survived without them. Many thanks to the staff at Q2 in Berkeley, particularly Sue, Ann, Karen and Vicki, for providing a wonderful environment and some balance in my life; thanks also to Dr. Linda Berry for fixing my computer-induced aches and pains. Bob Kahr told me a long time ago that I could do whatever I really wanted to do, and I have tried to

remember that. Many women scientists have provided understanding and support, and I am very grateful to Susan Solomon and Marti Crouch for their help and for their tremendous integrity.

My family deserves special thanks. Sometimes they wondered why I was in grad school, but they helped me a lot. My parents showed me how much could be accomplished through hard work, and those lessons have been very important. My grandparents, Benge and Ted Weaver and Maria Kalathaki, helped make this possible. And my sisters Helen and Mika have helped probably more than they know (unfortunately the academic world will probably lose two great scholars, because neither of them will ever want to go to grad school after watching me), by phoning and writing and being their wonderful selves.

Pete Senty has provided encouragement, support, love, help, and dinner when I needed them most this year. It is not possible to thank him enough.

This research was supported in part by the Director, Office of Energy Research, Office of Basic Energy Sciences, Chemical Sciences Division of the U.S. Department of Energy under contract No. DE-AC03-76SF00098, and in part by the Air Force Office of Scientific Research Contract No. AFOSR-91-0084.

1. Introduction

Free radical species are difficult to study experimentally because they are reactive and often unstable. Many form stable negative ions, and this work describes the study of several transient neutral species by negative ion photoelectron spectroscopy. The experiments described here include studies of the transition state regions of neutral bimolecular potential energy surfaces ($I + HI$, $F + H_2$), which we surveyed for evidence of long-lived quasi-bound states of the [IHI] and [FH_2] complexes. We also studied stable free radicals (NO_2 and NO_3), which show interesting spectroscopic phenomena as a result of vibronic coupling.

Chapter 2 gives a general introduction to negative ion photoelectron spectroscopy, including selection rules.

Chapter 3 describes the negative ion time-of-flight photoelectron spectrometer, including the pulsed free-jet expansion ion source, time-of-flight mass spectrometer, and time-of-flight electron energy analyzer.

Chapter 4 describes our experiments on NO_2^-. We analyze the vibrational structure in the $\tilde{X}(^2A_1)$, $\tilde{A}(^2B_2)$ and $\tilde{C}(^2A_2)$ bands of NO_2, using Franck-Condon factor calculations and simulated spectra to estimate the electronic state energies, vibrational frequencies and equilibrium geometries of NO_2 in the X, A and C states. We discuss the anomalous vibrational structure in the region of the $\tilde{C}(^2A_2)$ band, and the implications for vibronic coupling in the NO_2 $\tilde{B}(^2B_1)$ and $\tilde{C}(^2A_2)$ states.

Chapter 5 describes our experiments on NO_3^-. We analyze the structure of the $^2A_2'$ ground-state band, which includes Franck-Condon forbidden transitions to odd quanta of the antisymmetric bending vibration, ν_4. These are explained by vibronic coupling between the $^2A_2'$ and $^2E'$ states. We describe the method and results for a simulation of the $^2A_2'$ band including vibronic coupling effects, and show that it reproduces the experimental results.

Chapter 6 introduces a different type of neutral system: an unstable transition state complex on the potential energy surface for a bimolecular reaction. We discuss studies of I + HI/DI via photoelectron spectroscopy of IHI^- (IDI^-), as examples of the heavy + light-heavy class of triatomic reactions. Theoretical calculations predict the existence of long-lived quasi-bound states of the neutral [IHI] complex (reactive scattering resonances), and we discuss the ways in which our spectra support these predictions.

In Chapter 7 we discuss our results on F + H_2/D_2/DH, highly exoergic reactions in which evidence of resonances had already been obtained. Our spectra are compared to the predictions of quantum mechanical reactive scattering calculations and classical trajectory calculations.

2. Photoelectron Spectroscopy: General Principles

The photoelectric effect is familiar to many undergraduate students of quantum mechanics as early evidence of the limitations of classical mechanics. It is also the fundamental principle behind photoelectron spectroscopy: that an atom or molecule can absorb a photon and emit an electron

$$M + h\nu \rightarrow M^+ + e^- \tag{2.1}$$

whose kinetic energy will be the difference between the photon energy and its binding energy

$$KE = h\nu - E_b \tag{2.2}$$

By measuring the electron kinetic energy, one obtains information about the energies of the ion and neutral states involved in the transition.

Photoelectron spectroscopy was developed in the 1960's to study the electronic structure of neutral species and positive ions, using X-ray or vacuum ultraviolet photons. Applications to negative ions,

$$M^- + h\nu \rightarrow M + e^- \tag{2.3}$$

require much lower photon energies, and have only become really practical with the recent development of lasers as high-power, narrow-band light sources over the entire spectrum from infrared to ultraviolet wavelengths.

In all the experiments discussed here, we use a fixed-frequency laser to detach an electron from a negative ion, and determine the electron's binding energy by measuring the electron kinetic energy. Our photoelectron spectra

plot number of electrons (intensity) against electron kinetic energy. The electron kinetic energy is related to the neutral and anion internal energies ($E^{(0)}$ and E^-) as

$$eke = h\nu - EA(M) - E^o_{elec} - E^o_{vib} - E^o_{rot} + E^-_{elec} + E^-_{vib} + E^-_{rot} \qquad (2.4)$$

The peaks at **highest** electron kinetic energy correspond to transitions to neutral states with **lowest** internal energy.

Most of the information obtained from our spectra pertains to the neutral species, not the negative ion. Although other techniques for studying neutral species are available, some with resolution as high as thousandths of wavenumbers, many of them are limited to stable neutral species and have difficulty with short-lived or reactive species. Negative ion photoelectron spectroscopy has several advantages with these transient species, since many free radicals bind an electron to form the stable negative ion that we require. We mass-select the ion of interest, minimizing signal due to other ions. And, because the selection rules differ slightly from those of optical spectroscopy, we can observe transitions to electronic and vibrational states that cannot be observed using other techniques.

Several negative ion photoelectron spectrometers have been built. We will not discuss the threshold photodetachment machines, which use tunable light sources; the principles and details of our group's threshold photodetachment spectrometer are described by Theo Kitsopoulos in his Ph.D. thesis.[1] The instruments that use fixed-frequency lasers are of two types:

those that use hemispherical electron energy analyzers and continuous lasers and ion sources, and those like ours, that use time-of-flight electron energy analysis, pulsed lasers and pulsed ion sources. The pulsed lasers can produce higher-energy photons, so we can study a wider range of systems. We also use a pulsed free jet expansion ion source, which gives a much narrower ion vibrational state distribution than the flowing afterglow or other sources typically used in the continuous machines. This narrow distribution is particularly important in the transition state experiments discussed in Chapters 6 and 7.

2.1. Background

Several good reviews of negative ion photoelectron spectroscopy have been written,[2] but the field is advancing and branching out so rapidly that none are comprehensive. The texts on neutral photoelectron spectroscopy[3,4,5] are somewhat more complete: that by Rabalais[6] is particularly helpful. We include some relevant definitions here before discussing the analysis of our spectra.

Photodetachment is the process of removing the electron from the ion,

$$A^- + h\nu \rightarrow A + e^- \qquad (2.5)$$

We often speak of 'photodetaching an ion', although it is actually the electron that is detached from the ion.

The **adiabatic electron affinity** of the neutral A is the energy required

for the transition

$$A^-(v = 0) + h\nu \rightarrow A(v = 0) + e^- \qquad (2.6)$$

between the vibrational, rotational and electronic ground states of both species. The **vertical detachment energy** is the difference between the ion ground state energy and the neutral potential energy at the same internuclear separation.[7] This is an important distinction because many theoretical predictions are given in terms of vertical energies, which can be very different to the adiabatic electron affinities that we measure. All electron affinities discussed in later chapters are adiabatic, unless otherwise noted.[a]

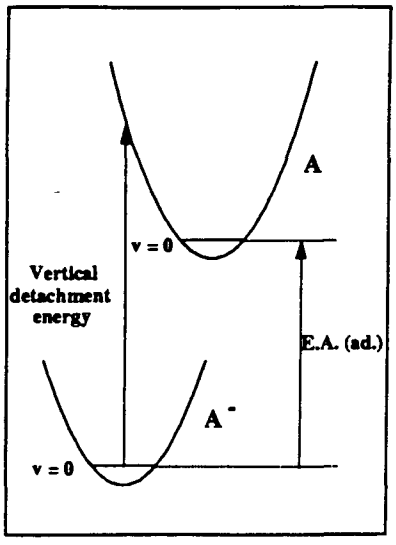

Our spectra are analyzed using the standard models for electronic and vibrational spectra, which are described in most elementary spectroscopy texts. Since some aspects of our analysis are a little different due to the ejection of the electron, we briefly develop and explain the rules for photoelectron spectroscopy here.

---

[a] The most convenient energy units are electron-volts (eV) for laser photon energy, electron affinity and electronic energy, and wavenumbers (cm^{-1}) for vibrational energies. The conversion is 8065.5 cm^{-1} = 1 eV (= 96.49 kJ/mol = 23.06 kcal/mol = 27.2116 hartree).

2.2. The basic principles

Quantum mechanically, molecular motion is described by a wavefunction Ψ that describes the electronic and nuclear motion. The total energy E of the state described by Ψ is determined by the Schrodinger equation

$$H \Psi = E \Psi \tag{2.7}$$

where the Hamiltonian includes electronic and nuclear kinetic and potential energy.

We assume that the light electrons move much faster than the heavy nuclei, and that the nuclear and electronic motions are separable: this is the Born-Oppenheimer approximation, and the separability of the Hamiltonian

$$H = H_{elec} + H_{nucl} \tag{2.8}$$

means that the wavefunction is separable into a product of nuclear and electronic wavefunctions,

$$\Psi(r;R) = \psi_{el}(r;R)\ \psi_{n}(R) \tag{2.9}$$

where the electronic coordinates r depend parametrically on the nuclear coordinates R.

The probability of a photodetachment transition between an ion state Ψ^- and a neutral + electron state Ψ is determined by the action of the dipole moment operator, which represents the interaction with the photon:[8]

$$P = |\langle \Psi(r;R)|\mu|\Psi^{-}(r;R)\rangle|^2 \tag{2.10}$$

and, substituting (2.9) into (2.10) we obtain

$$P = \left|\left\langle \psi_{el}(r;R)\psi_n(R)|\mu|\psi_{el}^{-}(r;R)\psi_n^{-}(R)\right\rangle\right|^2 \tag{2.11}$$

The dipole moment operator is also separable:

$$\mu = \mu_{el} + \mu_n \tag{2.12}$$

so the integral can be further separated

$$P = \left|\left\langle \psi_{el}(r;R)\psi_n(R)|\mu_{el}|\psi_{el}^{-}(r;R)\psi_n^{-}(R)\right\rangle + \left\langle \psi_{el}(r;R)\psi_n(R)|\mu_n|\psi_{el}^{-}(r;R)\psi_n^{-}(R)\right\rangle\right|^2 \tag{2.13}$$

The second term in Eq. (2.13) can be factored into electronic and nuclear parts,

$$\left\langle \psi_{el}(r;R)|\psi_{el}^{-}(r;R)\right\rangle \left\langle \psi_n(R)|\mu_n|\psi_n^{-}(R)\right\rangle \tag{2.14}$$

and the electronic wavefunctions ψ_{el} and ψ_{el}^{-} are orthogonal because the neutral+electron state is a continuum eigenstate of the negative ion, so the term $\langle\psi_{el}|\psi_{el}^{-}\rangle$ goes to zero.

Next, we make the rigid rotor approximation that the molecular rotations and vibrations are separable, since rotation is much faster than vibration:

$$\psi_n(R) = \psi_{vib}(R)\ \psi_{rot}(R) \tag{2.15}$$

and therefore Eq. (2.13) reduces to

$$P = \left| \left\langle \psi_{el}(r;R)\psi_v^o(R)\ \psi_r^o(R) \mid \mu_e \mid \psi_{el}^-(r;R)\psi_v^-(R)\psi_r^-(R) \right\rangle \right|^2 \qquad (2.16)$$

where the ψ^o are neutral wavefunctions. We can integrate over rotational coordinates and treat that term as a constant, since we do not resolve rotational structure, so

$$P \propto \left|\left\langle \psi_{el}(r;R) \left| \mu_{el} \right| \psi_{el}^-(r;R) \right\rangle\right|^2 \ \left|\left\langle \psi_v^o(R) \left| \psi_v^-(R) \right\rangle\right|^2 \qquad (2.17)$$

The first term of Eq. (2.17) is treated as a constant τ, the electronic transition dipole moment, which we assume independent of the nuclear coordinates. Included in this approximation is an expansion of the integral in a Taylor series about the equilibrium geometry R_o:

$$\left\langle \psi_e(r;R) \left| \mu_e \right| \psi_e^-(r;R) \right\rangle = \left\langle \psi_e(r;R_o) \left| \mu_e \right| \psi_e^-(r;R_o) \right\rangle + \left(\frac{\partial \left\langle \psi_e(r;R_o) \left| \mu \right| \psi_e^-(r;R_o) \right\rangle}{\partial R} \right)_{R_o} (R - R_o) + \ldots \qquad (2.18)$$

and truncation after the first term of the expansion. The integral will be non-zero for all neutral+electron wavefunctions that differ from the anion wavefunction by the molecular orbital occupancy of only one electron.[9] It is possible to include higher order terms which would allow two-electron transitions, through quadrupole and other interactions, but these terms are generally neglected because their probability is relatively small. The second term in Eq. (2.17) is the Franck-Condon factor; ψ_v° and ψ_v^- belong to different electronic states so they are not orthogonal.

Each of these approximations has important implications for our spectra

because it limits the neutral states that are accessible via photodetachment transitions: it imposes **selection rules.** In the next section we develop the selection rules for photoelectron spectroscopy.

2.3. Selection rules and transition probability

Electronic: The one-electron rule from Eq. (2.17) determines which electronic transitions will be observed in the photoelectron spectra.

To determine whether a transition is a one-electron transition, we look at the molecular orbital occupancies of the anion and neutral states. This requires either a theoretical calculation, experimental measurement or some approximation, usually that of Walsh,[10] to determine the relative energies of the molecular orbitals. For example, in NO_2 the ion and neutral electronic state configurations are

NO_2^- ($^1A_1$) $(1a_1)^2(1b_2)^2(2a_1)^2(2b_2)^2(1b_1)^2(3a_1)^2(1a_2)^2(3b_2)^2(4a_1)^2$

NO_2 $\tilde{X}(^2A_1)$ $...(1a_2)^2(3b_2)^2(4a_1)^1$

NO_2 $\tilde{A}(^2B_2)$ $...(1a_2)^2(3b_2)^1(4a_1)^2$

NO_2 $\tilde{B}(^2B_1)$ $...(1a_2)^2(3b_2)^2(4a_1)^0(2b_1)^1$

NO_2 $\tilde{C}(^2A_2)$ $...(1a_2)^1(3b_2)^2(4a_1)^2$

where the a_1, b_1 etc. denote molecular orbital symmetries under the operations of the C_{2v} molecular point group.[11] A transition from the ion to the B state requires that we simultaneously promote an electron from the a_1 orbital to the b_1 and remove another a_1 electron, so transitions to the B state are forbidden

by the one-electron approximation.

Note that our electronic selection rule is not the same as that imposed in optical spectroscopy. In both cases,[12] allowed electronic transitions are determined by the direct product[13]

$$\Gamma_i \otimes \Gamma_j \otimes \Gamma_\mu \subset \Gamma_A \qquad (2.19)$$

where Γ_i and Γ_j are the representations of the two electronic states involved in the transition, Γ_μ corresponds to any component of the dipole moment operator (μ_x, μ_y or μ_z), and Γ_A is the totally symmetric representation in the molecular point group. The difference between the selection rules for photoelectron and optical spectra is due to the electronic wavefunctions, because in photodetachment transitions the final wavefunction includes the electron. For example, in absorption spectra of NO_2, transitions between the $\tilde{X}(^2A_1)$ ground state and $\tilde{C}(^2A_2)$ excited state require a dipole moment component μ_i that transforms under the point group operations according to the a_2 representation, since $a_1 \times a_2 = a_2$. There is no such component of μ, so the C state is a 'dark' state and the transition from the ground state is electric dipole-forbidden. In photoelectron spectra of NO_2^-, this is simply an allowed one-electron transition. The reverse is true for the $\tilde{B}(^2B_1)$ state: the electric dipole-allowed $\tilde{X}(^2A_1) \rightarrow \tilde{B}(^2B_1)$ transition is a forbidden two-electron transition in our spectra.

Rotational: Our instrumental resolution is about 65 cm^{-1} at best, so we do not resolve rotational structure and do not need to take rotational selection rules

into account in analyzing our spectra. The rotational selection rules for photodetachment are discussed at length elsewhere.[6,14]

Vibrational: The vibrational selection rules are perhaps the most interesting, because they determine the majority of the structure in our spectra. Our discussion assumes that the initial ion state is the vibrational ground state, and that the neutral state is bound. (In chapters 4 and 5 we discuss 'hot band' transitions from excited vibrational levels of the anion.) The situation is slightly different for the I + HI and F + H_2 transition state systems discussed in chapters 6 and 7, but the fundamental principles are the same.

The foundations of our vibrational selection rules are the Franck-Condon approximation and the normal mode approximation, that all vibrational motion can be described as combinations of separable harmonic oscillator modes. An N-atom non-linear polyatomic molecule has 3N-6 normal modes: a linear molecule, 3N-5. For example, NO_2 has three normal modes: the symmetric stretch (ν_1, a_1 symmetry), bend(ν_2, a_1 symmetry), and antisymmetric stretch (ν_3, b_2 symmetry). The normal modes are numbered in order of decreasing symmetry, increasing degeneracy and decreasing frequency.[15] The exact description of these modes and their symmetry under the C_{2v} point group operations can be determined using standard techniques.[11,16]

A harmonic vibrational progression in a single mode will be a series of regularly spaced peaks at energies

$$E = \left(n + \frac{1}{2}\right) h\nu_e \tag{2.20}$$

where ν_e is the vibrational frequency

$$\nu_e = \frac{1}{2\pi}\sqrt{\frac{k}{\mu}} \tag{2.21}$$

k is the harmonic force constant and μ the reduced mass for the vibration. The dependence of ν_e on the reduced mass is particularly useful when we compare spectra of isotopically substituted molecules, as we shall discuss in Chapter 6 for IHI^- and IDI^-, since it may help to identify the active vibrational modes in the photoelectron spectrum.

In most experimental spectra the peak spacing is not exactly harmonic, due to the effects of anharmonicity or other perturbations to the potential. If we include an anharmonic term in the oscillator potential,[17]

$$V = ax^2 + bx^3 \tag{2.22}$$

the vibrational energies are

$$E = \left(n + \frac{1}{2}\right) h\nu_e + \left(n + \frac{1}{2}\right)^2 h\nu_e x_e \tag{2.23}$$

where $h\nu_e x_e$ is usually negative (we refer to this as x_{ii} in later chapters).

For the systems discussed in later chapters, identifying the active vibrational modes in the photoelectron spectrum was relatively easy. Although a molecule might have three or four normal modes, the number of vibrational

levels accessible in the photodetachment transition is severely limited. This is a result of the Franck-Condon factors that determine relative peak intensities, and the Franck-Condon approximation that the transition occurs on a time scale short with respect to that for vibrational motion (approximately 10^{-15} vs. 10^{-13} s).[18] Because the transition is so rapid, the neutral is formed with the nuclei in the same configuration as in the original ion vibrational state. As the neutral relaxes to its lowest-energy equilibrium geometry, the atoms oscillate about their equilibrium positions.

If the anion and neutral had exactly the same geometry and vibrational frequencies, no vibrational modes would be excited. The only allowed transition would be that between the ion ground state and the neutral ground state, and a single peak would appear in the photoelectron spectrum at an energy corresponding to the electron affinity. This hypothetical situation corresponds to removing an electron from a non-bonding molecular orbital, although in practice there is always some change in geometry and frequencies between ion and neutral.

If there is an appreciable geometry change between anion and neutral (due to removal of a bonding or anti-bonding electron), the active vibrational modes will be those which most closely resemble the movement of the nuclei. If the bond angles remain constant but bond lengths change, the bond stretching modes will be excited; if the angles change, the bending modes will be excited.

Vibrational modes can also be excited if there is a substantial difference between the ion and neutral frequencies (a factor of two or more), even if the change in geometry is zero.

All these rules result from the Franck-Condon factors. In addition to determining which modes will be excited, they also determine which quanta in each mode will be observed in the photoelectron spectrum. The relative intensities of vibrational peaks are determined by

$$\left| \int dR \; \psi_{\nu}^{o}(R) \; \psi_{\nu}^{-}(R) \right|^2 \tag{2.24}$$

For the totally symmetric vibrational ground state of the ion, the wave function is

$$\psi_{o}(R) \propto e^{-\alpha R^2} \tag{2.25}$$

This function has no nodes and is even with respect to displacements in R. Thus, the only neutral vibrational levels which will give a non-zero overlap integral are those with even wavefunctions: all quanta of totally symmetric vibrations,[b] but only the even quanta of non-totally symmetric vibrations.[c]

---

[b] Symmetry is defined in the point group of the anion or neutral, whichever has lower symmetry.

[c] This is not entirely true for degenerate non-totally symmetric vibrations, since all levels with v > 1 have at least one totally symmetric component. (Herzberg, Ref. 16, pp. 123-131.)

This is a very important rule, and is widely used in analyzing the spectra discussed in later chapters.

It is also possible for us to observe transitions from excited vibrational levels of the anion to levels of the neutral. The signature of these 'hot band' transitions is usually small peaks to the right (higher electron kinetic energy) of the band origin. Although hot bands can provide information about the anion vibrational frequencies, we prefer to minimize them to simplify our spectra, particularly since in the transition state spectra they tend to broaden peaks and obscure band origins rather than providing sharp peaks and information about the anion. Hot band contributions to our spectra are minimized by using a pulsed free jet expansion in our ion source, as we shall discuss in Chapter 3.

2.4. Electron angular distribution

The angular distribution of photoelectrons is determined by the following equation for the differential cross-section, $d\sigma/d\Omega$:

$$\frac{d\sigma}{d\Omega} = \frac{\sigma_{total}}{4\pi}\left(1 + \beta(E)\left(\frac{3}{2}\cos^2\theta - \frac{1}{2}\right)\right) \qquad (2.26)$$

where σ_{total} is the total photodetachment cross-section, Ω the solid angle, $\beta(E)$ is an asymmetry parameter[d] and θ measures the electron collection direction with respect to the polarization of the incident laser beam.[5]

---

[d] β is also sometimes defined to include the factor of ½.

$\beta(E)$ varies between 2 ($\cos^2\theta$ distribution) and -1 ($\sin^2\theta$ distribution). It is largely determined by the symmetry of the anion molecular orbital from which the electron is removed. Cooper and Zare[19] showed that detachment from an atomic s orbital (l=0) gives a p-wave electron (l=1) and hence a $\cos^2\theta$ distribution. Detachment from a p orbital gives s and d (l=2) wave electrons, which interfere to give a $\sin^2\theta$ distribution. The behaviour for polyatomic molecules is considerably more complicated,[1,20] and is not well understood.

We assume that all vibrational levels within one electronic band will have the same β value, since we should be far enough above threshold that β will vary only slowly with electron kinetic energy E.

2.5. Information obtained from the photoelectron spectrum

The peak positions in our photoelectron spectra provide information about the neutral electron affinity, its vibrational frequencies in the active modes, and the electronic state origins. We can also extract information about the geometry change between the anion and neutral from the relative peak intensities by calculating Franck-Condon factors, to determine the geometry change which gives peak intensities in best agreement with the experimental results. We can then refer to a known anion or neutral geometry (measured by some other technique) to obtain the geometry of the other. The simulation process is discussed at length in the chapter on NO_2.

2.6. Vibronic coupling

Our selection rules rely heavily on separation of fast and slow motions: electronic and nuclear, vibrational and rotational, and so on. If the time scales for these motions become similar, the selection rules break down. **Vibronic coupling** refers to the coupling of vibrational and electronic motion, which renders the Born-Oppenheimer approximation invalid.[21] This is one of the fundamental assumptions on which our vibrational selection rules are based, and vibronic coupling can be the most significant perturbation observed in our spectra. Although perturbations like vibration-rotation coupling, Coriolis coupling, and Fermi resonance may occur in the molecules we study, they are not sufficiently strong to have significant effects on the vibrational structure, at our resolution.

When vibrational and electronic motion are strongly coupled, harmonic oscillator and molecular orbital descriptions become inadequate. Vibronic states with different quantum numbers v and Λ (electronic orbital angular momentum) are mixed, so classifying vibronic states by v and Λ is no longer accurate, and we say that these are not 'good quantum numbers'.

The effects of vibronic coupling can be spectacular, since they represent the breakdown of all the rules presented in section 2.3. We have observed

- progressions in modes that would not normally be excited,
- odd Δv peaks in non-totally symmetric vibrations, and
- extraordinarily low vibrational frequencies

in the photoelectron spectra of NO_3^-, that we have attributed to vibronic coupling in NO_3. We confine ourselves to a brief introduction to vibronic coupling here, and reserve detailed descriptions for the chapter on NO_3.

Vibronic coupling effects can be included as perturbations to the Hamiltonian H_o, if we assume that the corrections are small enough to be approximated using perturbation theory. The Hamiltonian can be expanded in a Taylor series in the nuclear displacement Q, about the equilibrium configuration Q_0:[4,6]

$$H = H_o + \left(\frac{\partial H}{\partial Q}\right)_{Q_o} Q + \left(\frac{\partial^2 H}{\partial Q^2}\right)_{Q_o} Q^2 + \ldots \qquad (2.27)$$

with corresponding corrections to the energy

$$E = E_o + E^{(1)} + E^{(2)} + \ldots \qquad (2.28)$$

and wavefunctions.

Vibronic coupling can be classified in several ways. **Linear** coupling results from the terms in the Hamiltonian proportional to the nuclear displacement, $h \propto Q$; for **quadratic** coupling, $h \propto Q^2$. Linear coupling is further classified as first-order, or **Jahn-Teller** coupling, if the coupled electronic states are degenerate by symmetry, and second-order (**pseudo-Jahn-Teller** coupling or Herzberg-Teller intensity borrowing) otherwise. Quadratic coupling in linear molecules is called **Renner-Teller** coupling. Jahn-Teller coupling is often further classified as **dynamic**, if the degenerate

electronic state retains its symmetry at the perturbed equilibrium geometry, or **static**, if the coupling is strong enough to cause a permanent distortion of the molecule to a lower symmetry. In that case, the initial degeneracy of the electronic state is removed.

Linear coupling between electronic states ϕ_i and ϕ_j requires a vibrational mode of symmetry v,[22] where

$$\Gamma_i \otimes \Gamma_j \otimes \Gamma_v \subset \Gamma_A \tag{2.29}$$

and the symmetry is required so that the term $\langle \phi_i | \partial H/\partial Q | \phi_j \rangle$ will be different from zero. The electronic states can either be non-degenerate states, or components of a degenerate electronic state with $\Gamma_i=\Gamma_j$ the representation of the degenerate state. For example, in NO_2 the $^2A_1$ and $^2B_2$ states are coupled by the b_2 vibration (ν_3), since $a_1 \otimes b_2 = b_2$. Linear coupling between the $^2A_1$ and $^2A_2$ states would require a mode of a_2 symmetry, but none exists. Quadratic coupling can occur in all linear molecules, although it may be insignificantly small.

The effects of linear coupling include those mentioned above for NO_2 and NO_3. We observe odd Δv peaks in the coupling mode because the non-totally symmetric levels couple to symmetric levels, and borrow intensity from allowed transitions. This intensity borrowing also lends the electronic character of the coupled state to the forbidden transitions, so β can vary substantially within a single electronic band.

References

1. T. Kitsopoulos, Ph.D. Thesis (University of California, Berkeley, CA (1991)).

2. Several are included in *Gas Phase Ion Chemistry* (Academic, New York, 1984), M.T. Bowers, ed.: in Vol. 3, R.D. Mead, A.E. Stevens and W.C. Lineberger, "Photodetachment in negative ion beams", Chapter 22. In Vol. 2, B.K. Janousek and J.I. Brauman, "Electron affinities", Chapter 10. Also recommended are the review by H. Hotop and W.C. Lineberger ("Binding Energies in Atomic Negative Ions II", J. Phys. Chem. Ref. Data **14**, 731 (1985)) and an early paper on NO^- (M.W. Siegel, R.J. Celotta, J.L. Hall, J. Levine and R.A. Bennett, Phys. Rev. **A6**, 607 (1972)).

3. J.H.D. Eland, *Photoelectron spectroscopy* (Butterworth, Southampton 1982) provides a good non-mathematical discussion of many of the principles of neutral photoelectron spectroscopy, although some of the topics covered are somewhat out of date. The discussion of selection rules is particularly good.

4. R.E. Ballard, *Photoelectron Spectroscopy and Molecular Orbital Theory* (Wiley, New York, 1978) gives some brief but very nice explanations of the principles involved.

5. J. Berkowitz, *Photoabsorption, Photoionization, and Photoelectron spectroscopy* (Academic, New York, 1979).

6. J.W. Rabalais, *Principles of Ultraviolet Photoelectron Spectroscopy* (Wiley-Interscience, New York, 1977).

7. L.G. Christophorou, *Electron-Molecule Interactions and Their Applications, Vol. 1* (Academic, Orlando, 1984), p. 484.

8. Ref. 6, pp. 50-53.

9. Ref. 6, pp. 67-69.

10. A.D. Walsh, "The electronic orbitals, shapes and spectra of polyatomic molecules," Parts I-X, in J. Chem. Soc. **1953**, p. 2260 (I) etc.. A more recent treatment is discussed in R.J. Buenker and S. Peyerimhoff, Chem. Rev. **74**, 127 (1974).

11. A. Vincent, *Molecular Symmetry and Group Theory* (Wiley, Chichester, 1981) has an outstanding explanation of how to determine molecular orbital and vibrational mode symmetry. Eland (Ref. 3, Appendix I) also explains the conventions of labelling electronic states.

12. Ref. 6, p. 68.

13. A convenient reference table is included in G. Herzberg, Appendix III in *Molecular Spectra and Molecular Structure, Vol. III: Electronic Spectra and Electronic Structure of Polyatomic Molecules* (Van Nostrand, New York, 1966). The assiduous scientist could also calculate the direct product.

14. B.K. Janousek and J.I. Brauman, Phys. Rev. **A23**, 1673 (1981). R.C. Stoneman and D.J. Larson, Phys. Rev. **A35**, 2928 (1987).

15. R.S. Mulliken, J. Chem. Phys. **23**, 1997 (1955).

16. J.I. Steinfeld, Chapter 8 in *Molecules and Radiation* (Harper and Row, New York, 1974). A standard reference work for vibrational spectroscopy is

E.B. Wilson, J.C. Decius and P.C. Cross, *Molecular Vibrations* (Dover, New York, 1980), which is excellent for advanced work but is not recommended for the novice. G. Herzberg's *Infrared and Raman Spectra* (Van Nostrand, New York, 1945) is somewhat more comprehensible, and S. Califano's *Vibrational States* (Wiley, New York, 1976) is a useful and complete reference.

17. D.A. McQuarrie, *Quantum Chemistry* (University Science Books, Mill Valley, 1983), pp. 452-453.

18. Ref. 3, p. 9, and Ref. 4, p. 102.

19. J. Cooper and R.N. Zare, J. Chem. Phys. **48**, 942 (1968).

20. K.J. Reed, A.H. Zimmerman, H.C. Andersen and J.I. Brauman, J. Chem. Phys. **64**, 1368 (1976).

21. Comprehensive elementary explanations of vibronic coupling are difficult to find. Several references that may be helpful are (a) R. Englman, *The Jahn-Teller Effect in Molecules and Crystals* (Wiley-Interscience, New York, 1972) (b) G. Fischer, *Vibronic Coupling* (Academic, Orlando, 1984) and (c) I.B. Bersuker and V.Z. Polinger, *Vibronic Interactions in Molecules and Crystals* (Springer-Verlag, New York, 1989), which is more mathematically advanced.

22. Ref. 6, p. 239.

3. Experimental section: negative ion photoelectron spectrometer

Our negative ion photoelectron spectrometer includes an ion source to generate vibrationally cold negative ions, a time-of-flight mass spectrometer to monitor the ion distribution, a fixed-frequency laser to detach electrons from mass-selected negative ions, and a time-of-flight system to determine electron kinetic energy.

A schematic diagram of the instrument is shown in Figure 3.1. Our instrument is similar in design to that of Johnson and coworkers,[1] but differs in several minor respects. In this chapter, each section of the instrument is discussed in detail. One particularly important element of the design is that the interior of the source region is electrically floated at -1000 V. This is due to the design of the mass spectrometer, which requires two fields for focusing: a pulsed field (applied in the 'extraction region') and a continuous acceleration field, achieved by creating the ions at -1000 V and bringing them up to ground potential. As discussed below, floating the source affects the design of most of the interior components and their power supplies.

3.1. Negative ion source

3.1.1. Principles

We wish to generate negative ions with low internal energies. Ideally, most of the ions will be in the ground vibrational state and the lowest rotational states. We require a relatively intense ion beam and a source that

Figure 3.1: Negative ion photoelectron spectrometer (schematic diagram)

1. Pulsed valve
2. Electron beam (perpendicular to free jet)
3. Extraction region
4. Acceleration plates
5. Ion deflectors
6. Einzel lenses
7. Laser-ion beam interaction region
8. Electron baffles
9. μ-metal shielding
10. Ion detector
11. Electron detector

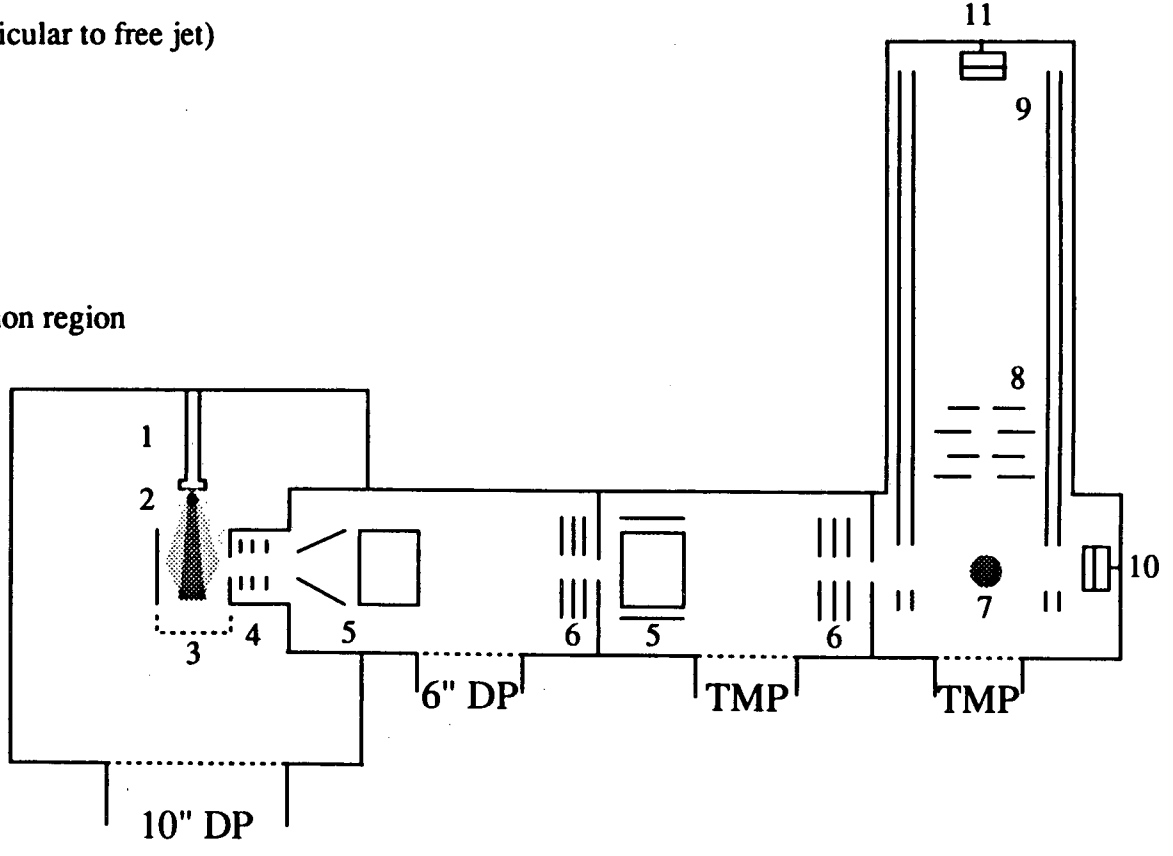

can produce a variety of ions with only minor modifications.

The crossed electron beam-free jet expansion developed by Johnson and Lineberger[2] is the ion source best suited to our experiment. A free jet expansion crossed at 90° with a 1 keV electron beam produces 'cold' negative ions in their lowest vibrational and rotational states. How can we obtain cold ions when we use an energetic electron beam? The key is the free jet expansion,[3] which is created by expanding high-pressure gas (at a few atmospheres) through a small orifice into a region under vacuum. This is an adiabatic, isentropic expansion into vacuum, and so cooling must occur.

In the high pressure stagnation region, the gas molecules' motion is random and their velocity depends on the temperature via the Maxwell distribution,[4]

$$df(v_x, v_y, v_z) = \left(\frac{m}{2\pi kT}\right)^{\frac{3}{2}} e^{-\frac{mv^2}{2kT}} dv_x dv_y dv_z \qquad (3.1)$$

During the expansion, this thermal energy is converted into kinetic energy of mass flow along the beam axis. Translational temperature determines the width of the molecular velocity distribution, and as the enthalpy of random motion is converted to enthalpy of directed flow the translational temperature drops and the velocity distribution narrows.[5]

We can use the equations developed for an expansion of an ideal monatomic gas to calculate approximate temperatures, pressures and other quantities in our free jet expansion, although this is not expected to be better

than a rough estimate because our expansion is highly perturbed by the electron beam and by clustering. In these examples, we assume an ideal monatomic gas (Ar) at stagnation pressure P_o = 2 atm and number density 4 x 10^{19}, nozzle diameter D = 0.02" and initial temperature T_o = 300 K.

In the expansion of an ideal monatomic gas, the degree of ordered vs. random molecular motion is characterized by the Mach number M,[6] [a]

$$M = A\left(\frac{x}{D}\right)^{\gamma-1} \tag{3.2}$$

where A is a constant (3.26 for an ideal monatomic gas), x is the distance from the nozzle, D the nozzle diameter and $\gamma=C_p/C_v=5/3$ the heat capacity ratio. The Mach number is related to translational temperature as $M \propto T_t^{-1/2}$. As the gas expands from the nozzle the Mach number increases and T_t drops. For this example, at 0.1" from the nozzle the local pressure would be about 4 x 10^{-4} atm, the number density about 3 x $10^{17}/cm^3$, and the translational temperature about 100 K.[7]

Eventually the frequency of collisions decreases to the point that no further cooling occurs: in an ideal expansion, this is the 'freeze-in surface'. In our example, this point occurs about 0.15" downstream from the nozzle. The collision frequency in the stagnation region is about 10^9/s; at the freeze-in

---

[a] The Mach number is conventionally defined in terms of the local speed of sound: these are 'supersonic' expansions because the Mach number is greater than unity.

surface this has decreased to about 5000/s.

Negative ions are produced in the electron beam-free jet interaction region close to the expansion orifice. Several competing mechanisms can occur:[2]

$$RA + e^- \rightarrow (RA^-)^* \rightarrow R + A^- \qquad \textit{dissociative attachment} \qquad (3.3)$$

$$\rightarrow RA + e^- \qquad \textit{autodetachment} \qquad (3.4)$$

$$\overset{M}{\rightarrow} RA^- \qquad \textit{collisional deactivation} \qquad (3.5)$$

In our source, the most important process is probably dissociative attachment, since predissociation of $(RA^-)^*$ is often fast with respect to a long-lived autodetachment resonance in a cluster or a second collision in this low-collision environment.[2] Efficient dissociative attachment requires electrons with low energies (a few eV),[8] which are produced by high-energy electrons in the 1 kV electron beam scattering off molecules in the free jet:

$$M + e^-(\sim 1\ keV) \rightarrow M^+ + e^-(<1\ keV) + e^-(>0\ eV) \qquad (3.6)$$

The subsequent thermalization of the low-energy electrons must be rapid for efficient ion formation, and is facilitated in polyatomic expansion gases by the higher frequency of inelastic collisions.[8] We can produce a variety of negative ions in our source, including simple ions like O^-, NO_3^- and cluster ions like $NO_3^-(HNO_3)_n$. Many more cations than anions will be produced because of fragmentation on electron bombardment, but this is not a problem because we

extract only the negative ions from the expansion.

Although the neutral-neutral collision rate is negligible after a certain point in the expansion, the ion-neutral collision rate is enhanced by favourable ion-induced dipole interactions and the ions in the expansion are further cooled.[2] The ion vibrational temperature can be calculated from peak intensities in the photoelectron spectrum, if 'hot band' transitions (transitions from excited vibrational levels of the anion) are resolved and are sufficiently intense. For CH_2CN^-, we calculated a vibrational temperature of 150 K from hot band intensities. Since we have an energetic electron beam perturbing the expansion, the ion vibrational temperature is not as low as the tens of Kelvin measured in the best neutral free jet expansions. Ion rotational temperatures in our source are difficult to measure, because our instrumental resolution is insufficient to resolve individual rotational transitions in photoelectron spectra; since rotations are cooled more efficiently than the higher-energy vibrations, one would expect the rotational temperature to be substantially lower.

3.1.2. Pulsed valves

Our initial experiments used a double solenoid-type pulsed valve (BV-100V, Newport Corp. Fountain Valley, CA). A Viton tip seals the orifice when the valve is closed: the tip is held in a metal bellows connected to a metal disk, which moves back and forth between the solenoids to open and close the valve. In our experience, these valves work well if exposed only to

inert gases; corrosive gas exposure and prolonged use render them unreliable and prone to failure. Viton tips were inadequate for corrosive gases, so we manufactured Teflon tips which lasted longer but required much more time to make and adjust. Repeated problems with cracked ferrite cores surrounding the solenoid coils, broken solenoid wires, leaking bellows, and the difficult and lengthy adjustment process in replacing these parts forced us to seek a durable, inexpensive, and easily adjusted replacement.

The General Valve Corporation (Fairfield, NJ) produces solenoid valves that fit these requirements. Although not originally designed for molecular beam use, these valves are widely used by research groups in north America, with various modifications and power supply circuits. We use the model 9-347-900, which is relatively simple. A spring holds the valve closed, pushing a plastic tip in to seal the orifice. A voltage pulse applied across a solenoid coil opens the valve against this spring.[9]

This valve is easy and inexpensive to repair and adjust. It is particularly suitable for corrosive gases because of its simplicity and the materials' resistance to corrosion. All parts are easily replaced, including the poppet tips. We generally use a Kel-F poppet and a 0.020" faceplate orifice: other materials and orifice sizes are easily interchangeable. The poppets usually last a few days to a week or more. Disadvantages of the General valve include its relatively slow opening time, and the bounce after

closing due to the front and back springs.

A schematic diagram of the power supply circuit for this valve is shown in Fig. 3.2; an improved version is used in our group's threshold photodetachment spectrometer.[9] We incorporated several features to protect the circuit against voltage spikes, and to isolate the pulsed valve power supply (which is floated at -1 kV) from the pulse generator which supplies the external trigger pulse (at ground).

Our primary criterion for the effectiveness of the supersonic expansion is the ion vibrational temperature, but this is difficult to measure quickly. An *in situ* measurement which is highly correlated with the ion vibrational temperature is the quality of the gas pulse, as characterized by its rise and fall times. The local pressure can be measured directly using a fast ion gauge[10] in the source chamber. With the General valve, the gas pulse quality depends on the extent of actuator motion, which is controlled by the tightness of the faceplate screwed down against the valve body. Generally, one can determine the optimal setting for a particular valve by feeling the gas pulse against a fingertip and listening to it; a loud pulse that feels sharp and powerful is best. Measurements with the fast ion gauge showed that the settings that gave a sharp, loud pulse also gave the shortest rise time and cleanest pulse.

Under typical conditions (O_2 at 40 psi, 20 Hz repetition rate), the gas pulse has a 160 μs rise time and 180 μs full-width, half-maximum (fwhm),

Figure 3.2: Pulsed valve power supply circuit diagram

Floating ground: all voltages referenced to float voltage (-1 kV).

All resistors 0.5 W. All capacitors 1 kV.

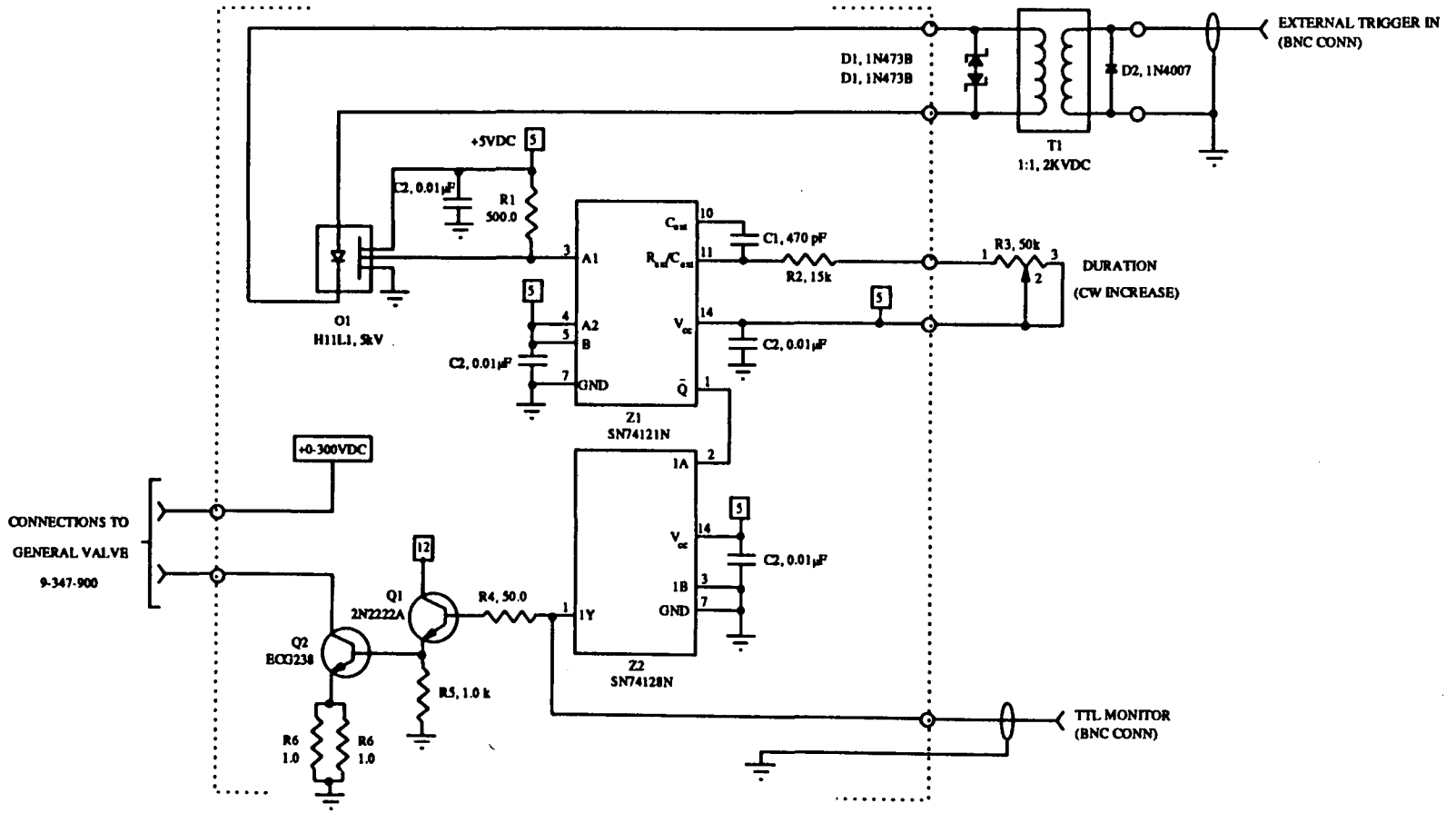

giving a source chamber pressure of 8 x 10^{-5} torr. Experiments in our group suggest that a more stable piezoelectric pulsed valve[11] gives a better expansion and lower ion vibrational temperature in this type of source. Although the Newport valve was the best choice when we started and the General valve has been extremely inexpensive and reliable, the advantages of using the piezoelectric valve appear to justify its increased expense and complexity.

3.1.3. Electron beam

The continuous electron beam is produced using a Tektronix electron gun of the type used in oscilloscopes. A diagram of the electron gun with typical operating voltages is shown in Fig. 3.3. Electrons with energies of a few tenths of an electron volt are produced by heating a thorium oxide-coated iridium filament (0.027" wide, 0.02" thick: Electron Technology, Kearny, NJ). These electrons are accelerated to 800-1000 V, and the beam is focused and directed towards the free jet expansion. (These energies are limited to 1000 V or lower to prevent electrical arcing in the source chamber.) Electron beam current is measured directly with a copper Faraday cup on the opposite side of the source chamber, and averages 400-600 μA with a new filament. The power supplies for the electron gun are APH1000M (Kepco, Flushing, NY) for the electron energy and focus element, ATE15-15M (Kepco) for the filament, and home-built supplies

Figure 3.3. Electron gun and typical operating voltages

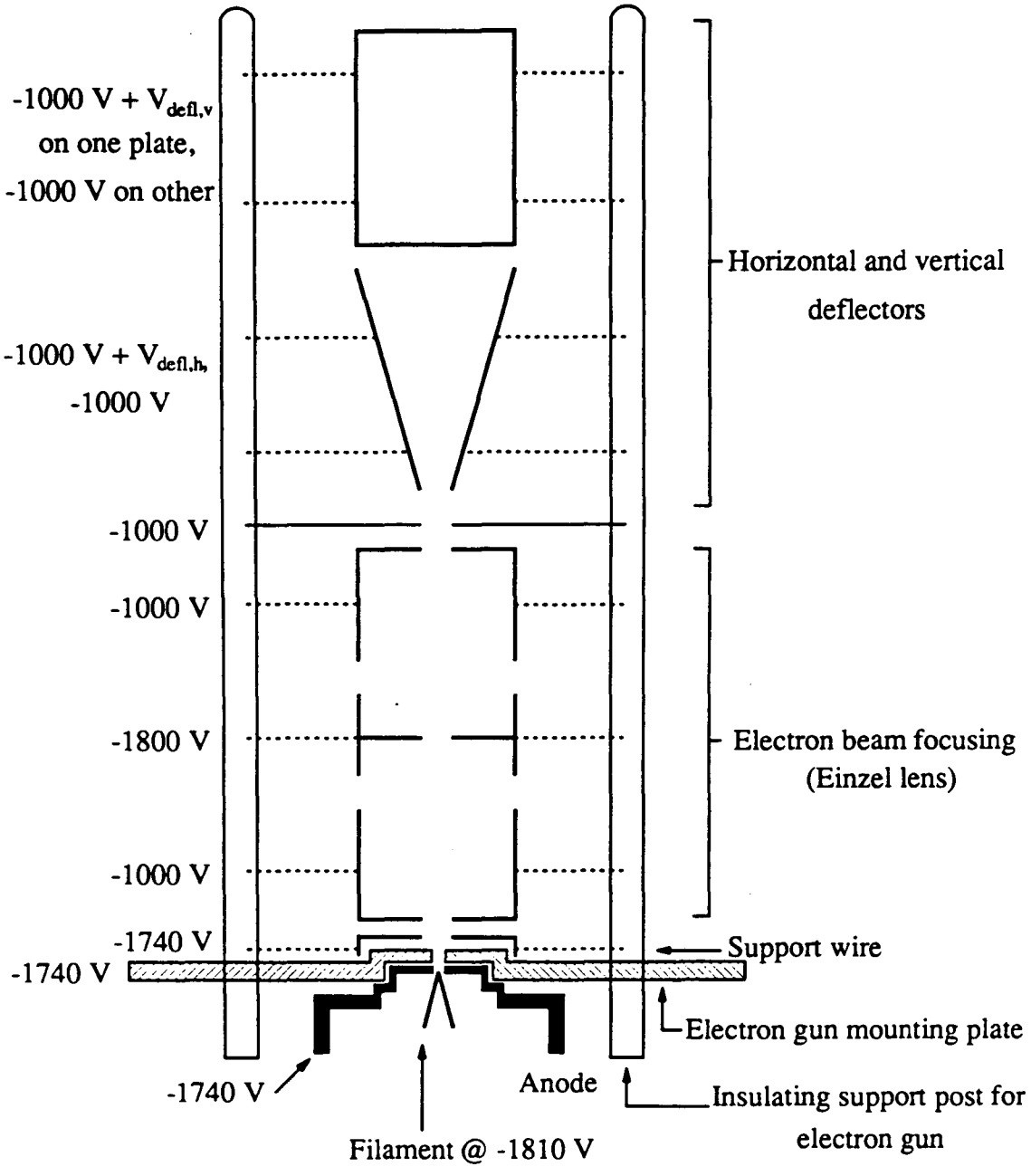

based on A0150NT05 (Acopian, Easton, PA) 150 VDC supplies for the anode and deflectors.

3.1.4. Floating source

Floating the source region requires that we float not only the internal components (molecular beam valve, electron gun, Faraday cup, etc.) but also their power supplies. The valve driver and electron gun power supplies are isolated inside a plexiglass rack and connected to their components by insulated high-voltage wire and Ceramaseal high-voltage connectors. The power to the components inside the floating rack is supplied by a high-voltage supply (Fluke) via a transformer inside the rack.

The beam valve mounting flange floats, and is isolated from the exterior of the source chamber by a Delrin insulating flange. Inside the source chamber, a homogeneous field is maintained by an interior box of thin aluminum plates. Holes cut into the box for the electron gun, diffusion pump butterfly valve and a side viewing port are covered with wire mesh as much as is practical. The box itself is isolated from the exterior source chamber by ceramic standoffs.

3.1.5. Vacuum pumps and protection circuits

The source region is pumped by a 10" oil diffusion pump (Edwards Diffstak 250/2000, air pumping speed 2000 l/s) backed by a rotary pump

(Edwards E2M40, 14 l/s). The first differential region is pumped by a 6" oil diffusion pump (Diffstak 160/700, 700 l/s) and rotary pump (E2M18, 7 l/s). The second differential and detector regions are isolated from the first two chambers by a pneumatic gate valve. The second differential and detector regions are pumped by turbomolecular pumps (Leybold-Heraeus TMP-150, 140 l/s) backed by rotary pumps (E2M8, 3 l/s and E2M12, 5 l/s respectively).

Pressures in all four chambers are measured by ionization gauges. Foreline pressures on the rotary backing pumps are measured by thermocouple gauges. Normal operating pressures are 10^{-5}-10^{-4} torr in the source, 10^{-7} torr in the first differential region, 10^{-8} torr in the second differential region, and 1×10^{-8} torr in the detector. When corrosive gases are used in the free jet, a liquid nitrogen-cooled trap in the source foreline protects the backing pump from damage.

An interlock system (Figures 3.4(a) and (b)) protects the vacuum pumps and electronics in case of equipment failure or high pressure in critical regions. In normal operation, all switches shown in Fig. 3.4(a) are closed except the BYPASS switch. The BYPASS setting is used if we need to use the detectors while the source is vented (most often to collect background noise scans, which will be described later). In normal operation, all switches shown in Fig. 3.4(b) are closed except the ROUGH switch. Loss of power via an open switch within either interlock box activates a relay and the gate valve closes, the alarm bell rings and high-

Figure 3.4(a). Diffusion pump interlock system

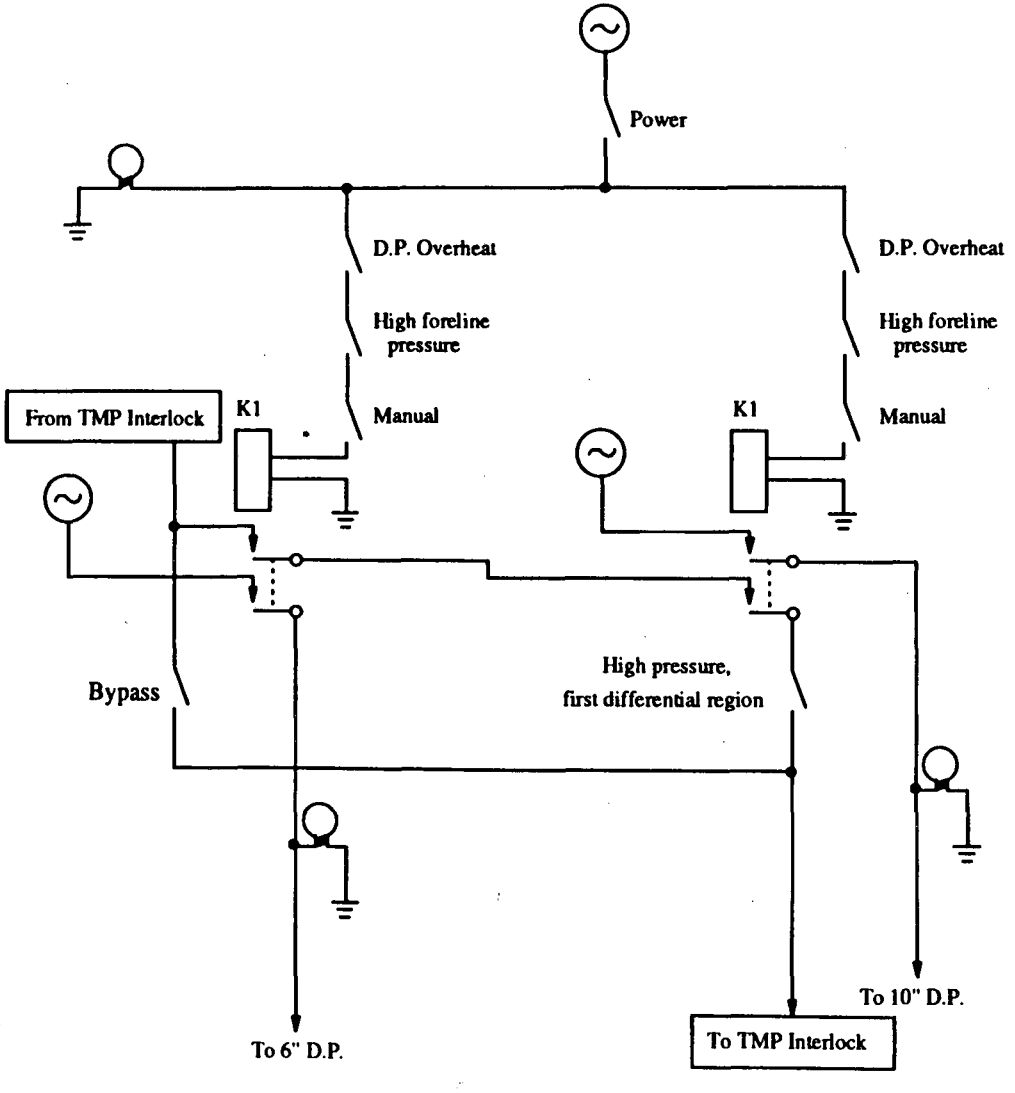

K1: Potter and Brumfeld KRP11AG Relay

Figure 3.4(b). Turbomolecular pump interlock system

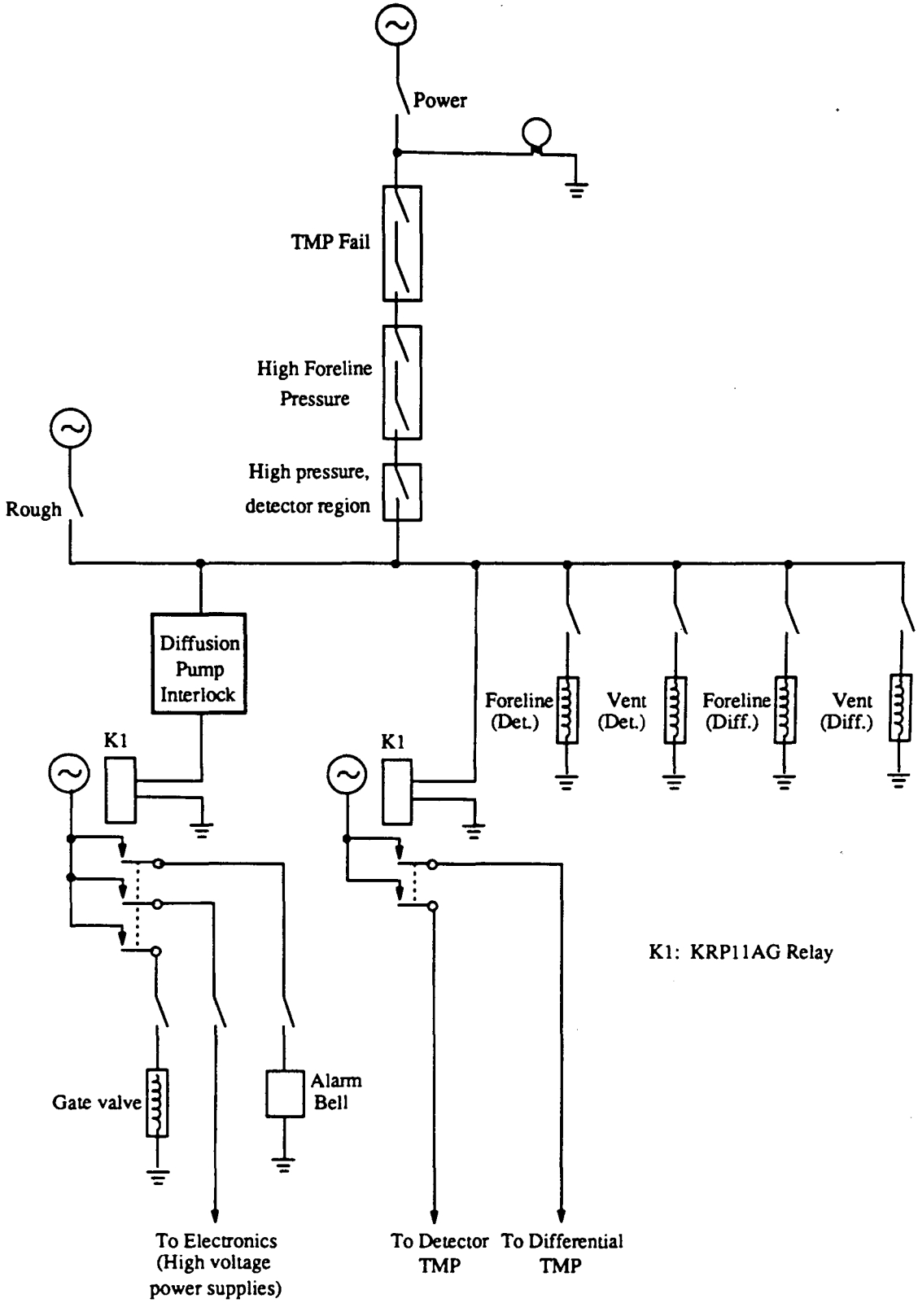

voltage power supplies shut off to protect the detectors. Problems within the second differential or detector regions cause solenoid valves to shut off those chambers from their roughing pumps, and both chambers are flooded with nitrogen to minimize possible adsorption of water or other contaminants in case of leaks. The maximum pressures are set individually for each gauge, on the ionization and thermocouple gauge controllers (Granville-Phillips model #270 and 260).

3.2. Time-of-flight mass spectrometer

3.2.1. Operating principles

We use a time-of-flight (TOF) mass spectrometer to characterize the negative ion distribution and determine the laser pulse timing for our selective photodetachment experiments. In a TOF mass spectrometer, all ions are accelerated to the same initial kinetic energy. Their subsequent velocities depend on mass, since

$$v = \sqrt{\frac{2E}{m}} \tag{3.7}$$

The lightest ions travel fastest and arrive first at the ion detector, and heavier ions arrive later in order of their mass. This technique allows us to view the entire mass spectrum simultaneously and to assess immediately the effects of changing source or other conditions.

The time-of-flight mass spectrometer is based on the Wiley-McLaren

design.[12] Negative ions are extracted from the source region by a negative voltage pulse, uniformly accelerated to a given energy in a continuous field region, and then enter a field-free drift tube. Ions separate out by mass in the field-free region and are detected at the end of the 1.5 m drift tube. This double-field design allows the ion beam to be focused at a particular point in the drift tube,

$$D = 2\, s_o k_o^{\frac{3}{2}} \left\{ 1 - \frac{1}{k_o + \sqrt{k_o}} \cdot \frac{d}{s_o} \right\} \qquad (3.8)$$

where s_o is the initial ion position with respect to the extraction plate closest to the ion drift tube, d is the length of the acceleration region (1 cm), and

$$k_o = \frac{s_o E_s + d E_d}{s_o E_s} \qquad (3.9)$$

where E_s is the pulsed extraction field and E_d the continuous acceleration field. Assuming E_s=50 V/cm, E_d=1000 V/cm, s_o=2.5 cm and d=1 cm, D=130 cm. The ion beam focus point is (theoretically) independent of ion mass, and is determined mainly by the ratio of the extraction and acceleration fields, E_d/E_s. In our instrument, D is closer to 150 cm, the extraction pulse is usually 400-800 V, and must be adjusted for optimal focusing of each ion.

3.2.2. Ion extraction

The free jet expansion passes through the middle of an extraction

region defined by two rectangular stainless steel plates (12 cm wide, 7 cm long). A pulsed field perpendicular to the free jet expansion (E_s) is applied to these plates to extract the negative ions through a 3 mm diameter aperture into the acceleration field in the first differential region.

Most of the experiments discussed here were carried out using the original extraction configuration (Figure 3.5(a)), with a plate separation of 2.5 cm and a 200-400 V extraction pulse. We later became concerned that the free jet expansion might be perturbed by the nearby extraction plates, resulting in vibrational heating of the ions, and increased the plate separation to 5 cm. To maintain the same field E_s the extraction voltage had to be approximately doubled, which was beyond the 400 V capacity of the IRF710 MOSFET in the original pulsing circuit.

We constructed a new pulsing circuit (Fig. 3.5(b)) incorporating a high voltage pulser (HV1000, Directed Energy, Inc., Fort Collins, CO), which can rapidly switch up to 950 V. The HV1000 is easily damaged by input voltage spikes, so we chose a high voltage power supply with a continuously variable output via dial controls (205B-05R, Bertan, Hicksville, NY), rather than switches which might generate voltage spikes on switching. The rapid switching generates a substantial spike at the end of the HV1000 pulse, which is apparent only if one measures L dI/dt inside the HV1000 itself. The extraction pulse voltage is limited to 800 V, since the associated 150 V spike at the end of the pulse would otherwise exceed the HV1000 capacity of

Figure 3.5: Ion extraction

(a) Pulsing circuit diagram - original version

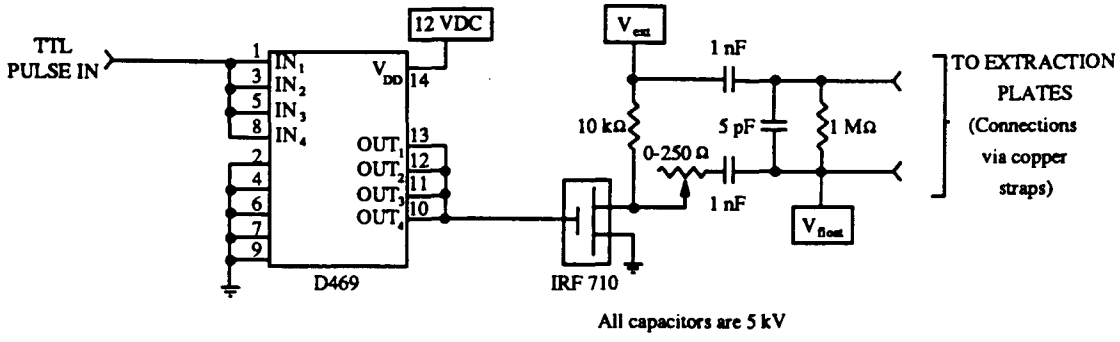

(b) Pulsing circuit diagram - revised version

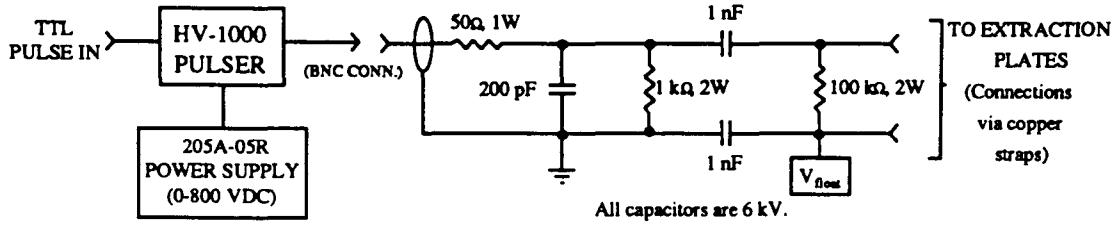

(c) Pulse sequence

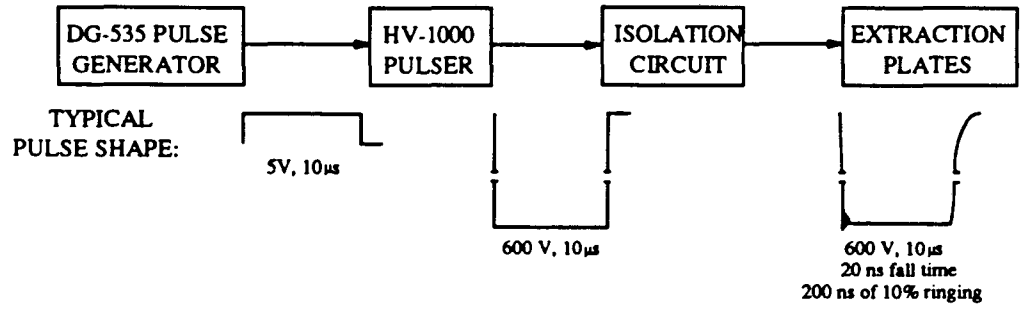

950 V.[b]

A typical pulse sequence is shown in Fig. 3.5(c). The triggering pulse for the HV1000 is generated by the digital delay/pulse generator (DG-535, Stanford Research Systems, Sunnyvale, CA) which controls the timing of the rest of the experiment. The delay between the molecular beam valve gas pulse and the ion extraction pulse is adjusted to give optimal ion levels at the ion detector.

Ringing on the falling edge of the negative extraction pulse is due to impedance mismatching between the HV1000 output and the pulsing circuit and extraction plates. This high-frequency ringing can be decreased by modifying the circuit, but the fall time then increases substantially. For example, replacing the 200 pF capacitor by 470 pF decreased the amplitude of the high-frequency ringing from 10% to substantially less, but increased the fall time from 20 to 200 ns. Adding a 250 Ω potentiometer in series with the 50 Ω resistor gave similar results, increasing the fall time to 50 ns. The connections to the extraction plates are via copper Ceramaseal feedthroughs and copper straps rather than BNC connectors and coaxial cable, which introduced low-frequency ringing and increased the fall time. This circuit represents a compromise between minimal fall time (20 ns) and

---

[b] The L dI/dt measurement is actually recommended and described by DEI. It is possible to destroy the HV1000 by neglecting this step and exceeding 950 V.

minimal ringing (200 ns at 10% of a 600 V pulse). The ions spend about 2 μs in the extraction region,[c] so this short period of ringing should not significantly affect ion energy, and the extraction pulse is long enough (10 μs) that all ions will have left the extraction region well before its end.

3.2.3. Ion acceleration, focusing and deflection

The continuous acceleration field (E_d) is created by a set of three stainless steel plates (5 cm diameter with 9 mm apertures, each spaced 5 mm apart). The entire source region is held at -1000 V and the third acceleration plate is at ground, so the ions are accelerated by 1 kV as they pass through the three plates. The plate voltages are determined by 2 MΩ resistors between sequential plates, and between the first plate and the floating source, so the ions are accelerated as soon as they leave the extraction region.

The extraction and acceleration plates are centred on the same axis as the ion detector, but the ions extracted from the free jet still have substantial non-zero vertical velocity and may have a small transverse velocity component, parallel to the extraction plates. Two sets of ion deflectors, each a vertical/horizontal pair, adjust for these effects: their

---

[c] The time spent in the extraction region is[12]

$$T_s = 1.02 \frac{\sqrt{2m}}{E_s} \left\{\sqrt{sE_s}\right\}$$

voltages are varied to give optimal ion levels at the ion detector. The deflector power supply is a home-built supply based on an Acopian A0150NT05 (150VDC).

We also installed two ion lenses to focus the ion beam. These are Einzel lenses,[13] sets of three planar 9.4 cm diameter stainless steel electrodes. They are operated in accelerating mode, with $|V_2|>|V_1|=|V_3|$;[13] because this is a negative ion beam, V_1 is set at ground, and V_2 is negative. Only the first of these Einzel lenses is used, at about -600 V. Early experiments showed that the second Einzel lens produced excessive background signal at the electron detector even in the absence of the photodetachment laser beam, perhaps due to the effect of having that high a field so close to the mass spectrometer focus.

3.2.4. Ion detection

Ions are detected at a microchannel plate detector about 1.4 m from the extraction region. The ion detector circuit diagram is shown in Fig. 3.6. Microchannel plates are essentially large-area electron multipliers with high gain and high time resolution. They are circular ceramic plates coated with metal on both sides, with thousands of pores (channels) at a uniform angle between the surfaces. The impact of a charged particle on the semiconducting channel wall releases several electrons and starts a cascading effect that results in a net gain of about 10^3-10^4 per plate.

Figure 3.6: Ion detector circuit diagram

(NOT TO SCALE)

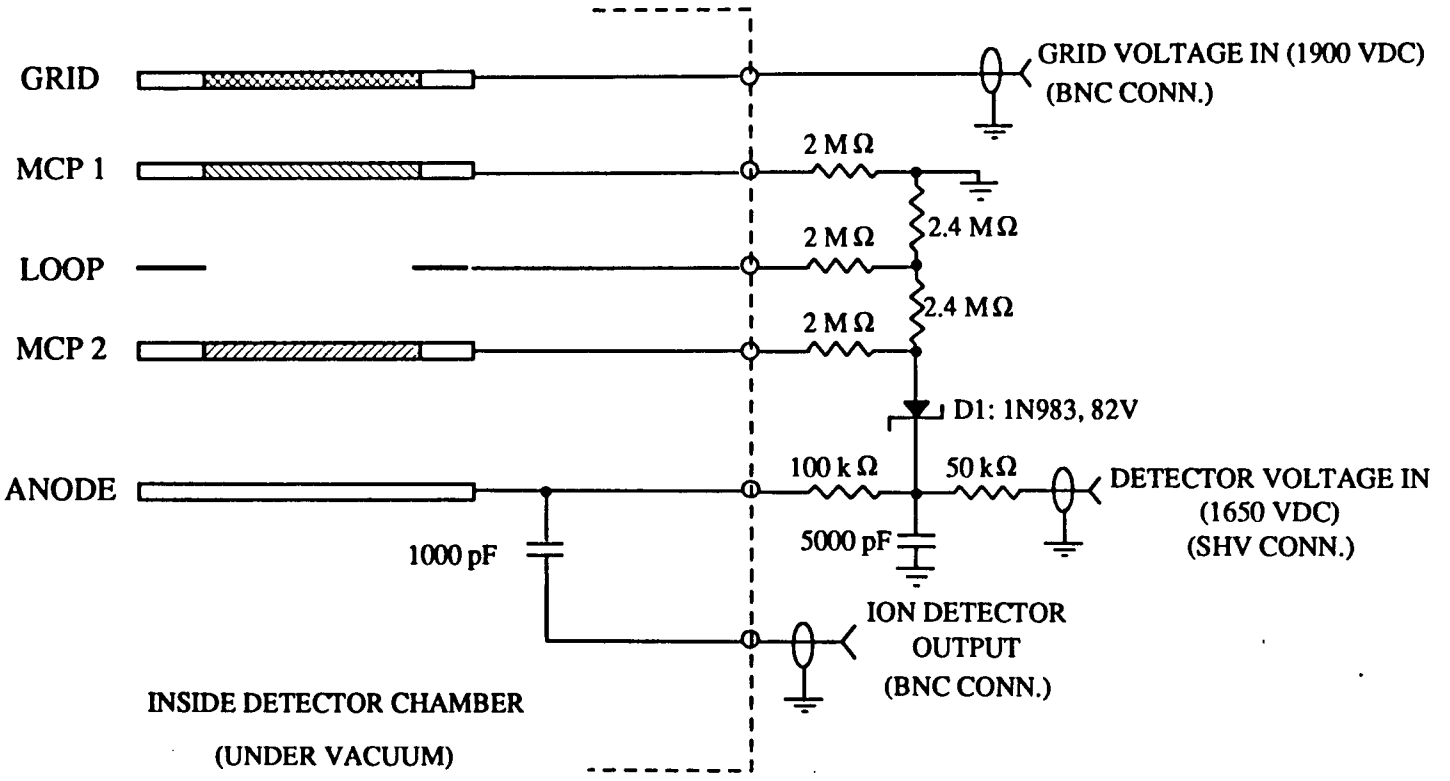

Electrons are accelerated through the circuit and charge is replenished by maintaining the front and back plate surfaces at bias voltages.

We use two 25 mm microchannel plates (Galileo Electro-Optics Corp., Sturbridge, MA), for an ion detector gain of about 10^6. The plates are 'chevron-mounted' with their channels oppositely oriented, to reduce feedback due to ionization of residual gas and ions travelling back through the channels. The output signal is collected at an anode behind the second channel plate.

The ion detector output can either be sent to an oscilloscope for monitoring the ion distribution, or collected and stored by computer so that the mass spectrum can be determined from the time-of-flight data.

3.2.5. Time-of-flight → mass conversion

The ions all have the same initial kinetic energy E, so the flight time Δt for an ion of mass m is

$$\Delta t = \sqrt{\frac{m}{2E}} \cdot \Delta x \qquad (3.10)$$

where Δx is the drift tube length. The mass scale is calibrated by identifying two peaks in the mass spectrum; the effective length Δx is then calculated for a given energy, and the conversion factor between Δt and $\sqrt{m}$ is obtained. This is an accurate calibration: an error of even one mass unit in identifying one peak can give a calculated Δx substantially different to

the approximate value of 1.44 m, indicating an incorrect assignment.

A typical mass spectrum from the NO_2^- experiments discussed in later chapters is shown in Figure 3.7. Typical ion levels for a particular mass are 500-2500 ions arriving in a pulse of fwhm 100 ns; the ion density is about 10^4-10^5/cm^3.

The mass spectrometer resolution is limited by the initial spatial spread of ions in the extraction region (space focusing). The magnitude of this effect can be estimated from the equation given by Wiley and McLaren[12] for the limit on maximum resolvable mass:

$$M_s = 16k_o\left(\frac{s_o}{\Delta s}\right)^2 \qquad (3.11)$$

where Δs is the initial spatial spread. Using typical parameters from our experiment (section 3.2.1), we obtain $M_s = 225$ if we assume $\Delta s = 2$ cm; any change in Δs will have a significant effect on this theoretical estimate. In practice our mass resolution, $m/\Delta m$, is about 200.

3.3. Photodetachment: equipment, electron detection and analysis

Once the ions are generated and characterized with the mass spectrometer, the next step is to irradiate the ions with a fixed-frequency laser beam. Electrons with binding energies less than the laser photon energy are detached, detected at the end of the electron flight tube, and their energies are determined from time of flight. The neutral molecules

Figure 3.7. Mass spectrum

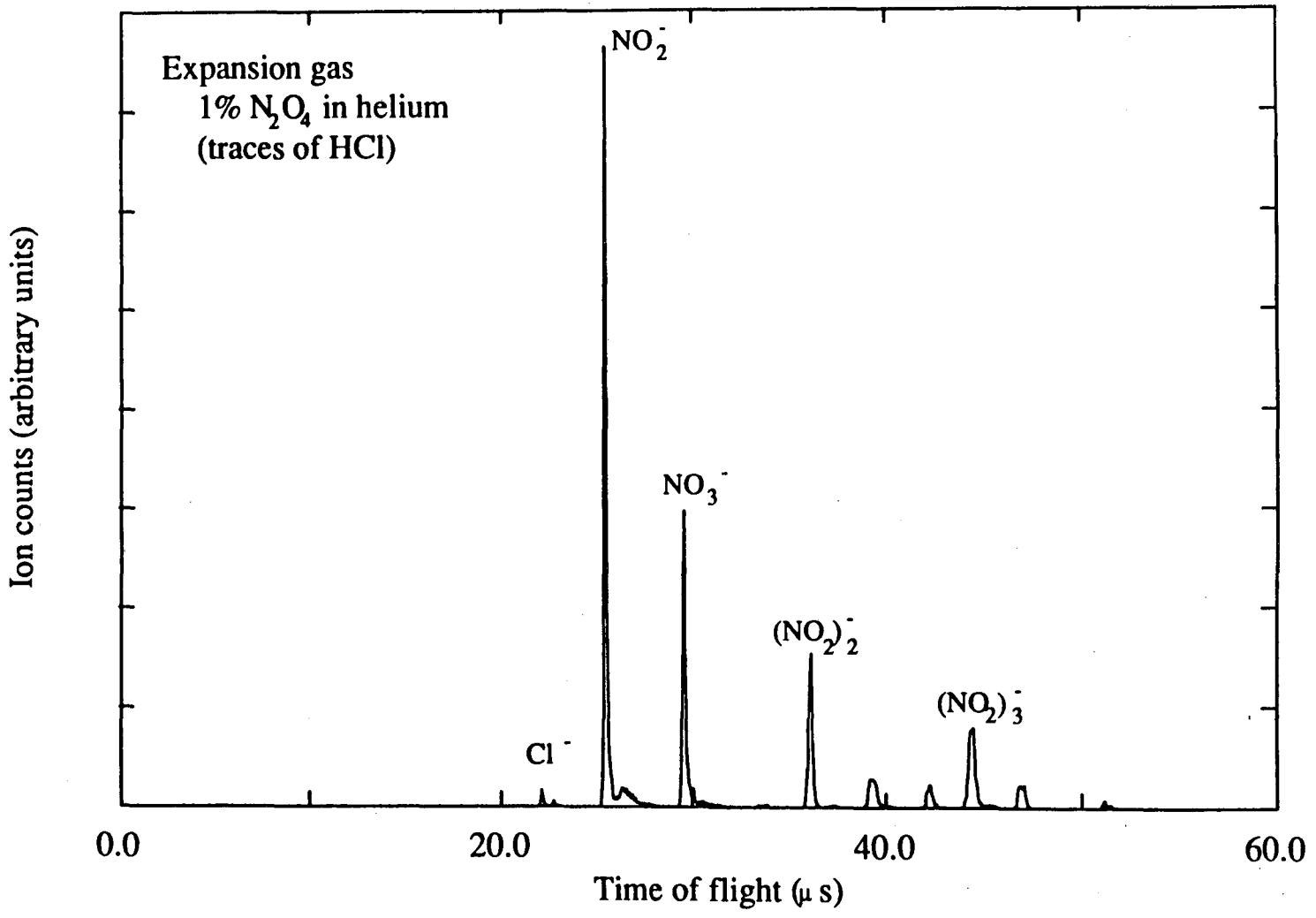

still have their original kinetic energy of about 1 keV, so they continue on to the ion detector. This section describes the lasers, optics, electron detector and instrumentation for data collection.

3.3.1. Photodetachment lasers and optics

The laser and ion beams cross at 90° about 10 cm before the ion detector. Ions of only one mass are irradiated by the pulsed laser beam. The ion packet for a particular mass is about 0.5 cm long, 3 mm wide and 3 mm high in this region (estimated from the 3 mm diameter defining aperture after the extraction region, and the length of the ion packet for mass 50 at 1300 eV), and the laser beam is focused to about 2 mm diameter in the interaction region.

The timing for the entire system is controlled by the Stanford DG-535 digital delay/pulse generator. The first pulse triggers the molecular beam valve, the second the ion extraction pulse and the third the photodetachment laser. Extraction pulse length and laser power are also controlled this way. The optimal laser pulse delay is determined by maximizing the neutral signal at the ion detector. We can selectively monitor the neutral signal by applying a negative voltage (about -1900 V) to a grid in front of the ion detector, so that ions are repelled. The measured neutral level ranges from 50% to less than 10% of the ion level, although we note that the detection efficiency for neutrals is slightly lower than that for

ions.

Early experiments on our machine used an excimer laser[14] (Lumonics HyperEx 400), operating on the XeF, KrF or ArF lines at 348 nm, 248 nm and 193 nm respectively (3.57 eV, 5.00 eV, and 6.43 eV). The ArF bandwidth limited our instrumental resolution, as we shall discuss later. Mechanical and electrical problems, the short life of ArF gas fills, and the expense of using neon in those short-lived mixtures also contributed to the overall unsuitability of this laser to our experiment.

The experiments discussed here all used a Nd:YAG photodetachment laser[14] (Quanta-Ray DCR-3G-20), which has a shorter pulse length (measured at about 7 ns), is much less expensive to operate, much more reliable, and requires little maintenance. The laser beam is plane-polarized, and laser power can be varied easily and smoothly, unlike the excimer.

The Nd:YAG fundamental lasing wavelength of 1064 nm can be converted to second and higher harmonics at 532, 355, 266 and 213 nm (2.33, 3.48, 4.66 and 5.83 eV) using KDP crystals for lower harmonics and β-barium borate (BBO) (CSK, Los Angeles, CA) for fifth harmonic generation. Most of our experiments require ultraviolet laser wavelengths and moderately high power (10-15 mJ/pulse at 213 nm). Optical components suitable for visible wavelengths are inadequate here because they quickly develop colour centres, tracks or other flaws which degrade beam quality, decrease laser power and result in more background signal in photoelectron

spectra.

Crystalline quartz is an ideal material for use at 213 and 266 nm, but it is extremely expensive. Our only crystalline quartz optic is the Pellin-Broca prism (IOS, Santa Clara, CA) which separates out the various laser harmonics (see optics diagram, Figure 3.8). It is exposed to high laser power at several wavelengths simultaneously, and we found that Suprasil[d] prisms developed tracks too quickly. We do use Suprasil for turning prisms (Melles-Griot, Irvine, CA), the 2 m lens (Acton, Acton, MA) and the detector chamber back window (Janos, Townshend, VT). At 213 nm we use wavelength-specific coated mirrors (CVI, Albuquerque, NM) instead of turning prisms, to avoid power loss and tracking. For the detector chamber front window we use either MgF_2 (Janos) or Suprasil, making a compromise between the slight birefringence of MgF_2 (undesirable with our linearly polarized laser beam) and the tendency of Suprasil to develop colour centres at 213 nm very quickly.

3.3.2. Electron flight tube

The one-meter electron flight tube is orthogonal to the laser and ion beams. Photoelectrons are ejected in all directions, but we observe only

---

[d] A grade of fused silica; at ultraviolet wavelengths, the order of preference is crystalline quartz>Suprasil I>Suprasil II> BK-7 (a type of glass frequently used for lenses and other optics).

Figure 3.8: Laser optics and detector region

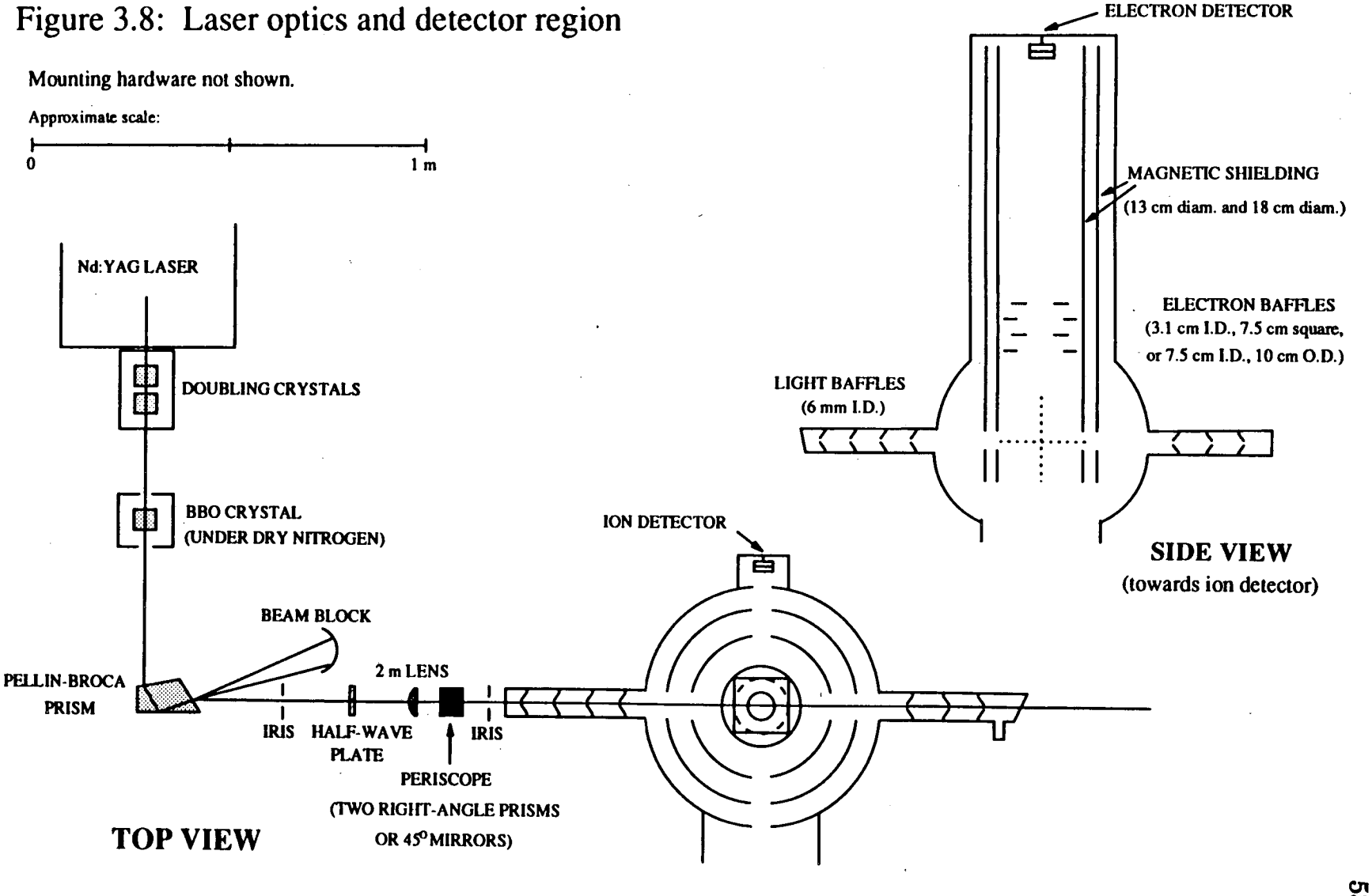

those contained in the solid angle subtended by the 40 mm-diameter electron detector, about 0.01%.[e] This low collection efficiency makes the electron detector very sensitive to the effects of scattered light.

The 266 and 213 nm ultraviolet light that we use is sufficiently energetic to exceed the work function of the metals used in the detector chamber, and so light scattering off those metal surfaces results in electron emission. Our earliest experiments showed that these could blind the ion detector to ion signal and overwhelm the photodetachment electron signal. Scattered light was reduced by installing black anodized light baffles (Fig. 3.8) in the laser beam path and trapping the laser beam reflection from the back window. Background electron signal was further reduced by four electron baffles in the flight tube (Fig. 3.8). These do not interfere with electrons travelling towards the detector in straight lines, but they do block much of the stray electron signal.

The photoelectrons of interest have low kinetic energies (less than 3 eV) and are strongly affected by stray electric and magnetic fields, which must be minimized within the flight tube. All materials used in this region must therefore have very low residual magnetization, and we used brass for the electron baffles. Concentric cylinders of Hypernom (μ-metal) inside the

---

[e] The electron detector was modified during the writing of this thesis to incorporate 75 mm channel plates, resulting in a substantial increase in the signal-to noise ratio with a small decrease in resolution.

flight tube shield the region from magnetic fields, and the inner cylinder and electron baffles are coated with colloidal graphite (Aerodag, Acheson Colloid Co.) to minimize patch potentials. Residual magnetization inside the flight tube can be decreased significantly by degaussing. We use a 30 cm, 7.5 cm diameter cylinder wrapped with 16 AWG copper wire, moved up and down the flight tube while coil current is decreased from 10 A to 1 A. This decreased the residual magnetic field from 30 mG to less than 3 mG the first time we used it, and substantially improved transmission of low-energy electrons. However, the electron signal intensity below about 0.3 eV decreases sharply in all photoelectron spectra since the transmission of these lowest-energy electrons is poor.

3.3.3. Electron detection

The electron detector (Figure 3.9) is very similar in design and operation to the ion detector, but is based on a pair of 40 mm microchannel plates. The other principal difference is that we deal with much lower energy particles - electrons at a few eV, rather than ions at 1 keV. To improve electron detection efficiency, the grid in front of the electron detector is biased so that electrons are accelerated into the first channel plate. We found the optimal bias voltage to be about 100 V; although the detection efficiency increased above that, resolution decreased. The electron detector has a surrounding shield of metal mesh coated in Aerodag, which

Figure 3.9: Electron detector circuit diagram

(NOT TO SCALE)

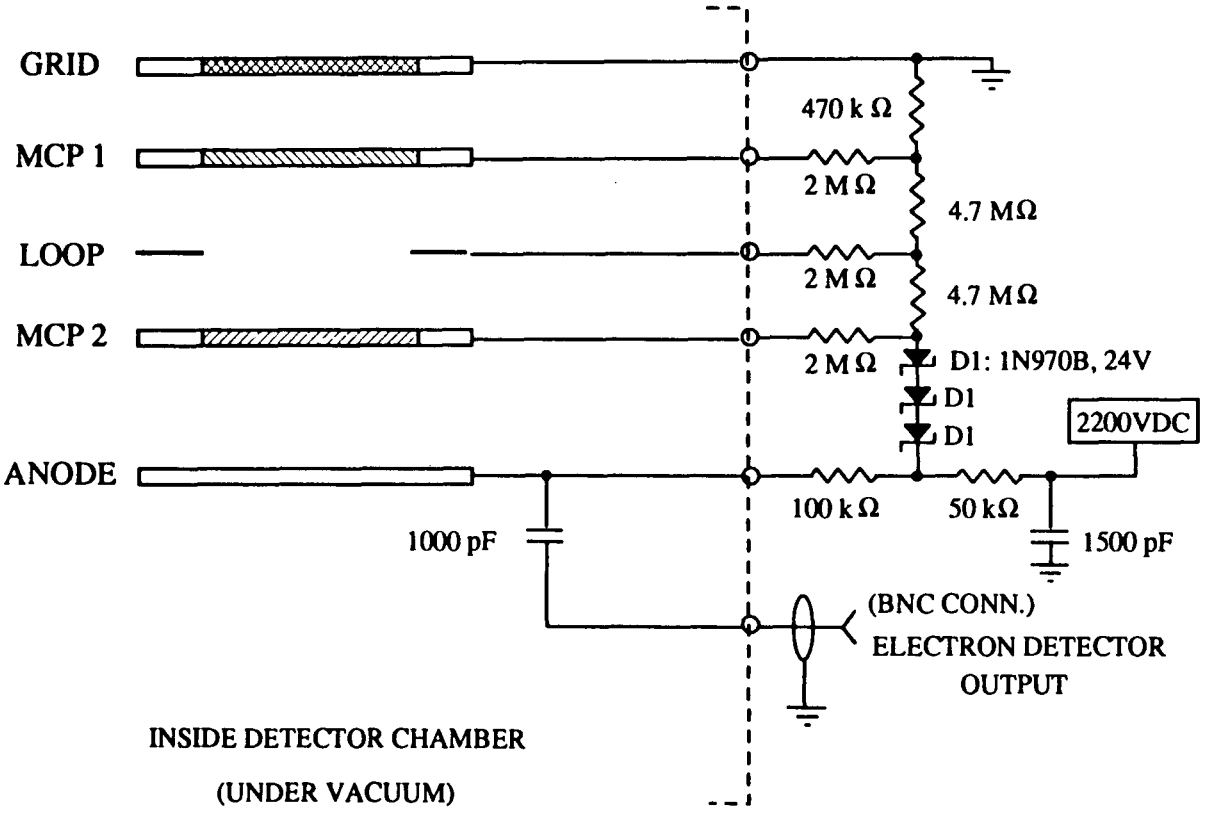

ALL CAPACITORS 6 KV. . ALL RESISTORS 0.5 W.

minimizes field leakage and improves instrumental resolution.

3.3.4. Data collection and processing

The electron detector output is preamplified (9301, EG&G Ortec, Oak Ridge, TN) sent through a discriminator (LeCroy 821, Pleasanton, CA) to remove low-level electrical noise, and converted into digital data by a 200 MHz transient recorder (LeCroy TR8828C with MM8104 memory module). Data acquisition is initiated by each laser light pulse, via a fast photodiode (Hamamatsu S1722-02) which triggers the transient recorder via a pulse generator (Systron-Donner 100C, Concord, CA). Data from each laser pulse are stored (LeCroy 6010 magic controller) and read into an IBM PC-AT computer every 200 pulses. Accumulated data are displayed on the computer monitor, and ion signal and electron signal are monitored simultaneously on an oscilloscope so that conditions can be continually optimized. The entire experiment is computer-controlled.[15] The data collection rate is largely determined by the laser repetition rate of 20 Hz: 40,000 scans require about 40 minutes. The NO_3^- data shown later required 750,000 scans for good signal to noise levels at 266 nm, since signal levels were very low; the IHI^- data required only about 100,000 scans at 266 nm.

Recording the ion detector output for mass spectra does not require preamplification or discrimination, but otherwise uses the same

instrumentation and software for data acquisition. For mass spectra, the initiating pulse is the same as that used to trigger the ion extraction pulse.

Conversion of electron time-of-flight data to electron kinetic energy is slightly more complex than the time-of-flight to mass conversion discussed earlier. An electron that arrives at the detector at time t has energy

$$E = \frac{1}{2} m_e v^2 \tag{3.12}$$

where

$$v = \frac{l}{t - t_o} \tag{3.13}$$

with l the effective flight tube length, t the flight time and t_o the timing offset (to be determined). Thus

$$E = \frac{1}{2} m_e \frac{l^2}{(t - t_o)^2} \tag{3.14}$$

In addition, we correct for the effect of the non-zero centre-of-mass velocity of the ion beam:

$$v^2_{e^-,com} = v^2_{com} + v^2_{e^-,lab} \tag{3.15}$$

$$E_{e^-,com} = \frac{1}{2} m_e v^2_{com} + \frac{1}{2} m_e \frac{l^2}{(t - t_o)^2} \tag{3.16}$$

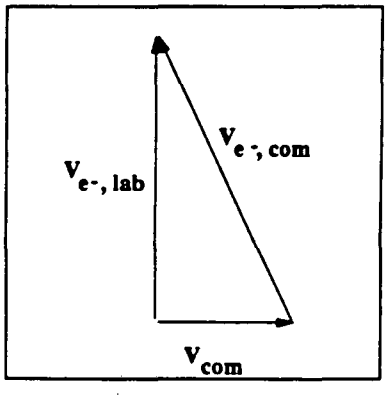

$$E_{e^-,com} - \Delta E = \frac{1}{2} m_e \frac{l^2}{(t - t_o)^2} \tag{3.17}$$

and we can determine the correction term

$$\Delta E = \frac{m_e v_{com}^2}{2} \tag{3.18}$$

by using

$$v_{com}^{e^-} = v_{com}^{ion} \tag{3.19}$$

The ion beam energy is

$$\frac{1}{2} m_{ion} v_{com}^2 = V_{float} + \frac{1}{2} V_{extrxn} \tag{3.20}$$

so

$$v_{com} = \sqrt{\frac{2\left(V_f + \frac{1}{2} V_{ex}\right)}{m_{ion}}} \tag{3.21}$$

giving

$$\Delta E = \frac{m_{e^-}}{m_i}\left(V_f + \frac{V_{ex}}{2}\right) \tag{3.22}$$

and we can plot t vs. $(E - \Delta E)^{-1/2}$:

$$t = \sqrt{\frac{ml^2}{2}} \cdot \frac{1}{\sqrt{E - \Delta E}} + \sqrt{\frac{ml^2}{2}}\, t_o \tag{3.23}$$

to obtain a straight line whose slope and intercept will give us the calibration parameters t_o and l.

Small daily variations in timing and local fields necessitate frequent calibration of t_o and l. These are determined by least-squares linear regression using the spectra of ions like F^-, Cl^-, Br^-, and I^-, (at 266 nm) for which the neutral electron affinities and spin-orbit splittings are well known. At 213 nm, the fluorine peaks are too fast for the spin-orbit splitting to be resolved. At 355 nm we use the vibrational structure in the spectrum of O_2^-, which has a lower electron affinity. A sample set of spectra and calibration parameters at 266 nm are shown in Fig. 3.10.

The instrumental electron energy resolution is affected by several factors, some of which we have already mentioned. From Eq. (3.14), we see that any uncertainty in timing, Δt, or length, Δl, are propagated as energy uncertainty[16]

$$\frac{\Delta E}{E} = \sqrt{\left(\frac{2\Delta t}{t}\right)^2 + \left(\frac{2\Delta l}{l}\right)^2} \qquad (3.24)$$

Since we measure t and not l, any factor Δl will effectively be manifested as a further timing error $\Delta t'$, and since $t \propto E^{-1/2}$, $\Delta E \propto E^{3/2}$.[17] From these equations, if we assume $\Delta l=0$, then for a 1 eV electron with flight path 100 cm and timing uncertainty 7 ns, the resolution ΔE = 0.008 eV. For a 2 eV electron, ΔE = 0.024 eV.

In practice, our instrumental electron energy resolution function is

Figure 3.10: Time of flight/electron kinetic energy conversion

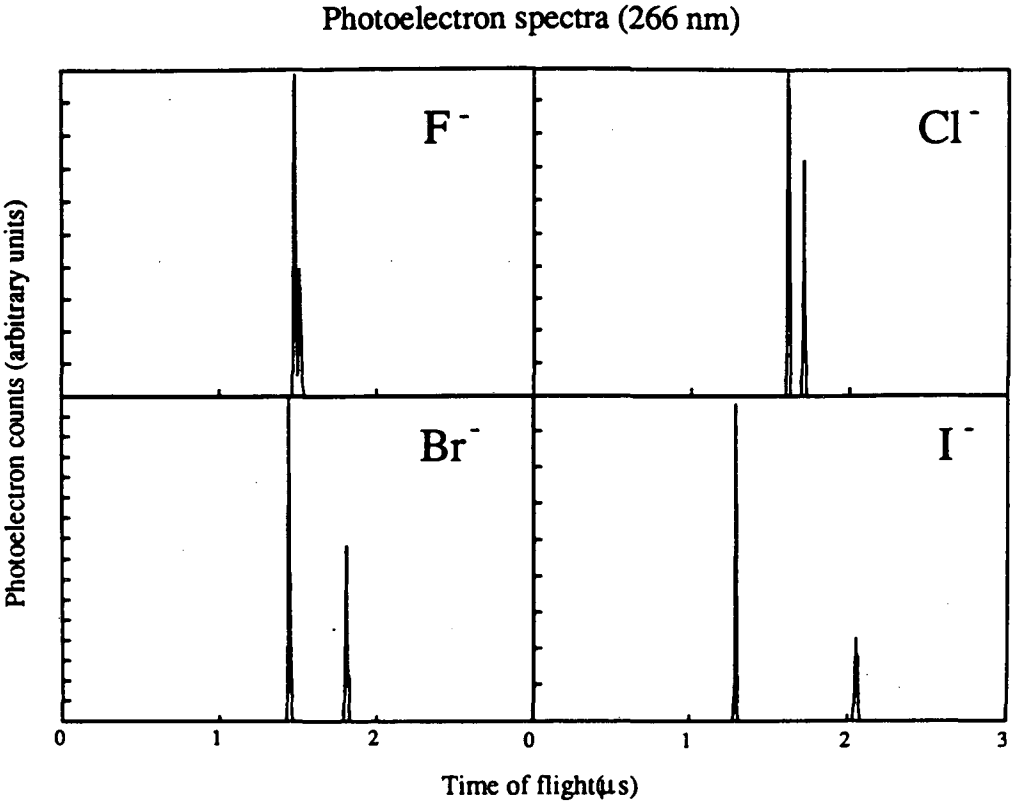

Ion	Transition	E (eV)	ΔE (eV)	t (ns)
F^-	$F(^2P_{3/2})$-F^-	1.2588	0.0347	1477.5
	$F(^2P_{1/2})$-F^-	1.2087	0.0347	1510.0
Cl^-	$Cl(^2P_{3/2})$-Cl^-	1.0473	0.0188	1617.5
	$Cl(^2P_{1/2})$-Cl^-	0.9381	0.0188	1717.5
Br^-	$Br(^2P_{3/2})$-Br^-	1.2964	0.0083	1440.0
	$Br(^2P_{1/2})$-Br^-	0.8395	0.0083	1807.5
I^-	$I(^2P_{3/2})$-I^-	1.6009	0.0052	1285.0
	$I(^2P_{1/2})$-I^-	0.6582	0.0052	2045.0

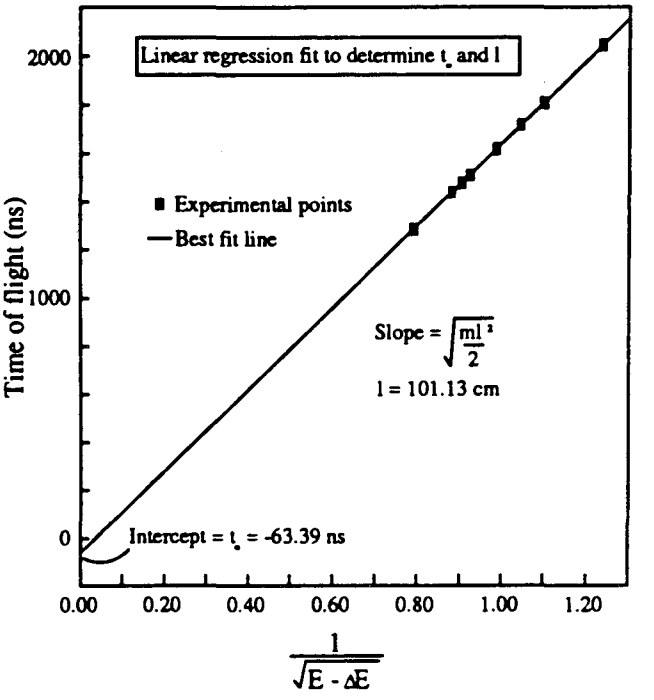

$$\Delta E = \sqrt{50 + 170E^3} \qquad (3.25)$$

where E is electron kinetic energy. This was determined from atomic negative ion photoelectron spectra at several wavelengths. The best resolution obtained is about 7 meV at 0.65 eV electron kinetic energy, and the resolution degrades as $E^{3/2}$ at higher energy. The deviation from theory is caused by several factors: the angular acceptance of the electron detector (0.0004 sr), differences in path length for curved trajectories (the electron baffles will improve our resolution by stopping many of these electrons), stray fields, time jitter in signal averaging (about 5 ns), the finite size of the laser-ion beam interaction region, and other factors. Laser pulse length is most significant: because the Nd:YAG laser pulse is about 7 ns long and the ion pulse is about 50-200 ns wide, electrons with the same energies may be generated 7 ns apart. The 100 cm^{-1} bandwidth of the ArF laser line limited our instrumental resolution with the excimer laser, but this is not a significant factor with the Nd:YAG laser.

The effects of magnetic and electric fields on resolution have already been discussed. One other very important effect is space charge, which results from Coulomb repulsion between the detached photoelectrons and the ion cloud at high ion densities.[18] Electron energy increases by the energy of repulsion and the photoelectron spectrum is shifted to higher energy and broadened, particularly for low energy electrons. This effect, which is more significant for heavy ions, can be minimized by decreasing ion

density by defocusing the ion beam (using the Einzel lens). The space charge limit is about 5-10 mV for I^-, 20 mV for lighter ions, and can be determined by measuring photoelectron spectra at gradually decreasing ion levels until the slowest peaks no longer shift to longer time.

The uncertainty in electron peak heights is the square root of the number of electron counts, since the electrons obey Poisson statistics. We usually accumulate data until this uncertainty is less than 10% for the major peaks.

3.3.5. Data smoothing and background subtraction

Our data are usually smoothed by convoluting each data point with a Gaussian peak of fwhm 6 meV, so that the structure in each spectrum will be easier to discern. In addition, the time→energy conversion tends to amplify background signal at low energies, since the peak intensities in the time-of-flight and energy spectra are related by[15]

$$I(E) \propto i(t)\, E^{-\frac{3}{2}} \tag{3.26}$$

Smoothing removes these very large noise spikes.

The background electron signal (section 3.3.2) is significant only at 213 nm, or when the photodetachment cross section is very low at 266 nm (e.g. NO_3^-). In those cases we subtract a background spectrum from the electron time-of-flight spectrum. A background spectrum is collected under

the same conditions as the photoelectron spectrum (except that no ions are present), and filtered to remove high-frequency noise.[19] This procedure requires that the electron time-of-flight spectrum (usually averaged for 120,000 laser shots) be Fourier transformed, convoluted with a narrow Lorentzian function, and back-transformed to give the smoothed background spectrum. Since the shape of the background varies very little from day to day, we do not need to collect background scans between individual photoelectron spectra.

A typical background scan is shown in Fig. 3.11(a), the smoothed background spectrum in Fig. 3.11(b), and the photoelectron spectrum with and without background subtraction in Fig. 3.11(c) and (d). We collect about one background electron per laser shot at 213 nm.

3.3.6. Electron angular distribution

The photoelectron angular distribution can provide important information about the nature of the electronic states involved in photodetachment, as mentioned in Chapter 2. The Nd:YAG laser beam is plane-polarized, and laser polarization can be rotated using a wavelength-specific half-wave plate (Melles-Griot for 213 nm, CVI for all others). Since cross section depends on laser polarization angle through

Figure 3.11: Background subtraction

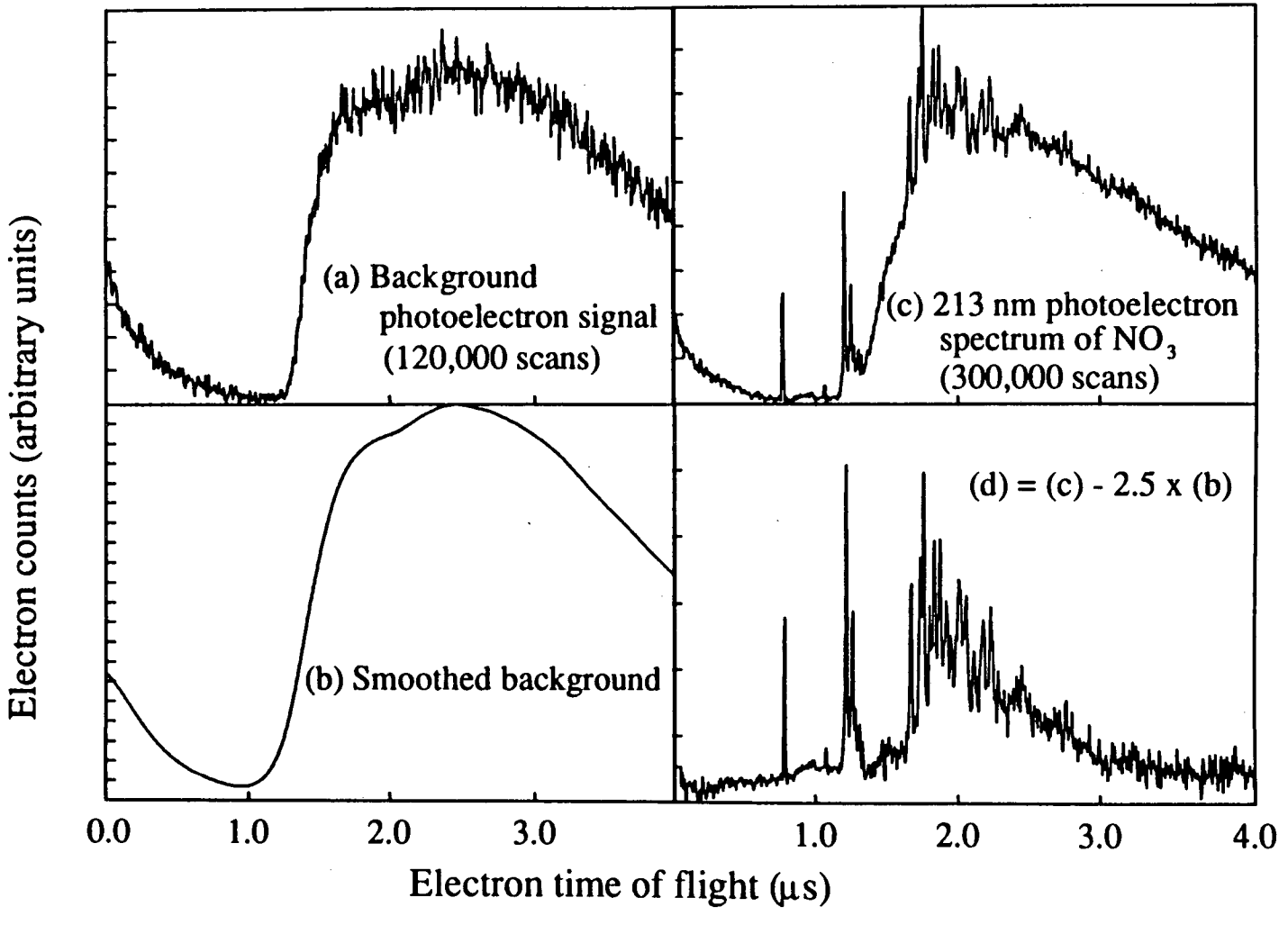

$$\frac{d\sigma}{d\Omega} = \frac{\sigma_{total}}{4\pi}\left(1 + \beta(E)\left(\frac{3}{2}\cos^2\theta - \frac{1}{2}\right)\right) \qquad (3.27)$$

this rotation may change the photoelectron angular distribution, depending on the form of β. Any such changes will be manifested as variations in peak intensities, since we collect electrons emitted in only one direction.

For example, the I^- photoelectron spectrum at 266 nm shows peaks due to detachment to the two spin-orbit states of iodine atom ($^2P_{1/2}$ and $^2P_{3/2}$). The relative intensity of these peaks changes as the polarization varies; the $^2P_{3/2}$ peak height is approximately constant, but the $^2P_{1/2}$ peak is much more intense at θ= 90°. Thus, intensity changes with polarization may indicate that different peaks correspond to different electronic states of the neutral. As we shall see later, this may be extremely helpful in assigning peaks in spectra of polyatomic molecules.

References:

1. L.A. Posey, M.J. DeLuca and M.A. Johnson, Chem. Phys. Lett. **131**, 170 (1986).

2. M.A. Johnson and W.C. Lineberger, in *Techniques of Chemistry* **20**, 591 (1988), J.M. Farrar and W.H. Saunders, ed. (Wiley, New York, 1988).

3. For an elementary discussion of supersonic expansions, see D.H. Levy, Scientific American **250**, 96 (1984). More comprehensive explanations are found in D.R. Miller (Chapter 2) and W.R. Gentry (Chapter 3) in *Atomic and Molecular Beam Methods, Vol. I*, G. Scoles, ed. (Oxford University Press, New York, 1988).

4. P.W. Atkins, *Physical Chemistry* (W.H. Freeman, San Francisco, 1982), p. 868.

5. D.H. Levy, Science **214**, 263 (1981).

6. D.H. Levy, Ann. Rev. Phys. Chem. **31**, 197 (1980).

7. Using the equations of Miller, Ref. 3.

8. L.G. Christophorou, D.L. McCorkle and A.A. Christoulides, Chapter 6 in *Electron-Molecule Interactions and Their Applications* (Academic: New York, 1984), L.G. Christophorou, ed.

9. A full description of the General valve and the valve driver is given by Theofanis Kitsopoulos in his Ph.D. thesis (Chemistry Dept., University of California, Berkeley (1991)).

10. Robert Continetti, Ph.D. Thesis (Chemistry Dept., University of

California, Berkeley, CA (1989)).

11. R. Proch and T. Trickl, Rev. Sci. Inst. **60**, 713 (1989). This valve is described more fully in Ref. 10.

12. W.C. Wiley and I.H. McLaren, Rev. Sci. Inst. **26**, 1150 (1955).

13. "Charged particle optics", Chapter 5 in *Building Scientific Apparatus*, J.H. Moore, C.C. Davis and M.A. Coplan (Addison-Wesley, 1989).

14. W. Demtröder, *Laser Spectroscopy* (Springer-Verlag, New York, 1988).

15. The annotated data acquisition computer program is included in the Ph.D. thesis of Ricardo Metz (Chemistry Dept., University of California, Berkeley, CA, 1991).

16. D.G. Wilden, P.J. Hicks and J. Comer, J. Phys. **B 9**, 1959 (1976).

17. J. Berkowitz, *Photoabsorption, photoionization and photoelectron spectroscopy* (Academic, New York, 1979), pp. 436-437.

18. This is discussed at length, and the equations derived, in the Ph.D. thesis of T. Kitsopoulos (Ref. 9).

19. W.H. Press, B.P. Flannery, S.A. Teukolsky and W.T. Vetterling, *Numerical Recipes*, pp. 417-420 (Cambridge University Press, New York, 1989).

4.1. Observation of the $\tilde{A}(^2B_2)$ and $\tilde{C}(^2A_2)$ states of NO_2 by negative ion photoelectron spectroscopy of NO_2^- [a]

A. Weaver,[b] R.B. Metz,[c] S.E. Bradforth[d] and D.M. Neumark[e]

Department of Chemistry, University of California, Berkeley, CA 94720

This communication describes a study of the electronically excited $\tilde{A}(^2B_2)$ and $\tilde{C}(^2A_2)$ states of NO_2 by photoelectron spectroscopy of NO_2^-. NO_2 has been extensively studied via optical spectroscopy,[1,2] but negative ion photoelectron spectroscopy offers several advantages as a probe of the excited states. For example, the calculated $\tilde{A}(^2B_2)$ state geometry (r_{NO} = 1.26 Å, θ_{ONO} = 102°)[3] differs greatly from the experimentally determined equilibrium geometry of the $\tilde{X}(^2A_1)$ ground state (1.19 Å, 133.9°).[4] Because of this large geometry change, the $\tilde{A}\leftarrow\tilde{X}$ band, which comprises much of the near infrared and visible absorption spectrum of NO_2, is dominated by transitions to highly excited (and perturbed) vibrational levels of the $\tilde{A}$ state. Transitions to the lowest vibrational levels are not observed because of poor Franck-Condon overlap.

---

[a] Published in J. Chem. Phys. **90**, 2070 (1989).

[b] NSERC (Canada) Postgraduate Scholar

[c] NSF Predoctoral Fellow

[d] University Fellow, University of California

[e] NSF Presidential Young Investigator

The experimentally determined geometry of NO_2^- (1.25 Å, 117.5°)[5] is much closer to the $\tilde{A}$ state geometry, and we observe transitions to lower, previously unobserved vibrational levels of the $\tilde{A}$ state. This allows us to estimate the $\tilde{A}$ state origin directly from our experimental data. in addition, although the $\tilde{C}(^2A_2)\leftarrow\tilde{X}(^2A_1)$ one-photon transition is electric dipole-forbidden, the $\tilde{C}$ state is accessible via a one-electron photodetachment transition from NO_2^-. Our results represent the first direct observation of the 'dark' $\tilde{C}(^2A_2)$ state.

The photoelectron spectrometer used for these experiments will be described elsewhere.[6] Important features include a pulsed, jet-cooled beam of NO_2^-, time-of-flight mass selection of the ion, and photodetachment of the selected ion using the third, fourth or fifth harmonic (355, 266 and 213 nm respectively) of a pulsed Nd:YAG laser. The electron kinetic energy distribution is determined by time of flight. The instrumental resolution is 8 meV at 0.65 eV electron kinetic energy, and degrades as $E^{3/2}$ at higher energy.

Ervin et al.[5] recently obtained the photoelectron spectrum of NO_2^- using the 351 nm (3.532 eV) line of an argon ion laser. Our spectrum at 355 nm (not shown) reproduces their results. At this energy, only the $\tilde{X}(^2A_1)$ state of NO_2 is accessible. Comparison of our results to those of Ervin et al. shows that hot band contributions to our spectrum (transitions from excited vibrational levels of NO_2^-) are negligible. At the origin of the $\tilde{X}$ state progression Ervin's resolution is better than ours (9 meV vs. 21 meV), so we have used their electron affinity of 2.273 ± 0.005 eV in our calculations of excited state term

values.

The 266 nm (4.660 eV) spectrum in Fig. 4.1A shows two full bands and the beginning of a third; the 213 nm (5.825 eV) spectrum in Fig. 4.1B shows three distinct bands. The improved resolution at lower electron energy is evident in these spectra. The three bands are assigned to the $\tilde{X}$, $\tilde{A}$ and $\tilde{C}$ states of NO_2, based on the calculated term values.[3] (The $\tilde{B}(^2B_1)$ state is not accessible by a one-electron transition from NO_2^-.)

As a first approximation, we have simulated the vibrational structure in the $\tilde{A}$ and $\tilde{C}$ bands using experimental values of the NO_2^- geometry and vibrational frequencies,[5] and *ab initio* values for the NO_2 excited state properties.[3] The peaks in the $\tilde{A}(^2B_2)$ band are approximately 750 cm^{-1} apart and are predominantly due to a progression in the bending mode, for which the calculated frequency[3] is 739 cm^{-1}. However, the symmetric stretch frequency is predicted to be almost exactly twice that of the bend,[3] and combination bands are superimposed on the more intense bending progression. Antisymmetric stretching progressions are not expected to appear in any of these bands.[5]

The first peak that clearly belongs to the $\tilde{A}$ state is at 1.183 eV electron energy in the 266 nm spectrum. The electron kinetic energy is $E = h\nu - EA - E_v - T_o$, where $h\nu$ is the laser photon energy, EA is the electron affinity of NO_2, E_v is the vibrational energy above zero point, and T_o is the term value for the electronic state, including zero-point energy. (We assume that the ions are

Figure 4.1. Photoelectron spectra of NO_2^-. A: 266 nm (4.660 eV). B: 213 nm (5.825 eV). The $\tilde{X}(^2A_1)$, $\tilde{A}(^2B_2)$, and $\tilde{C}(^2A_2)$ bands are marked. The data were convoluted with 6 meV Gaussian peak envelopes, and smoothed background signal was subtracted from the 213 nm spectrum. The laser was polarized perpendicular to the electron detection direction.

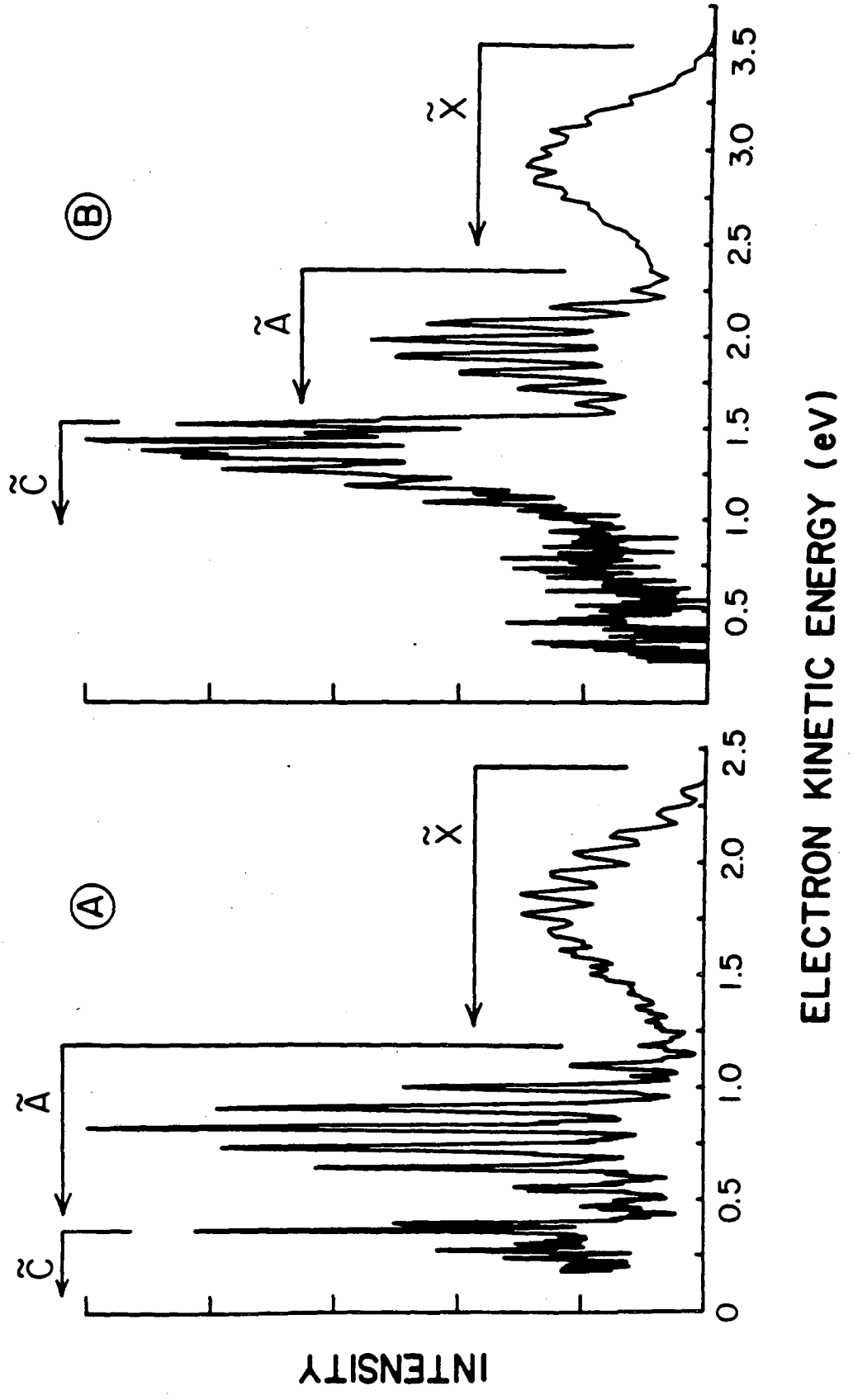
Ⓑ
Ⓐ
X̃
Ã
C̃
INTENSITY
ELECTRON KINETIC ENERGY (eV)
0
0.5
1.0
1.5
2.0
2.5
3.0
3.5

rotationally cold and that the rotational energy contribution is negligible.) Using hν = 4.66 eV, EA = 2.273, E_v = 0 and E = 1.183, we obtain 1.204 ±0.010 eV as an upper limit to T_o for the $\tilde{A}$ state. Until we analyze the spectrum completely, we cannot be sure that the origin of the $\tilde{A}(^2B_2)$ state band is not obscured by the end of the $\tilde{X}(^2A_1)$ state band, and can only assign an upper limit to T_o. Our value agrees well with the prediction of Gillispie et al.[3] and the extrapolated experimental value of Merer and Hallin.[7]

At the lowest electron energies in Fig. 4.1A, the $\tilde{A}(^2B_2)$ progression overlaps the start of the $\tilde{C}(^2A_2)$ band. The full $\tilde{C}(^2A_2)$ band appears in the 213 nm spectrum (Fig. 4.1B). Our analysis indicates that both the bend and symmetric stretch are active. The best match between simulated and experimental spectra is obtained by assigning the peak at 0.359 eV in Figure 1A to the $\tilde{C}$ state band origin. (This occurs at 1.516 eV in Figure 1B.) This yields T_o = 2.028 ±0.009 eV for the $\tilde{C}(^2A_2)$ state, which is within the estimated error of the theoretical prediction of 1.84 ± 0.3 eV.[3] The experimental $\tilde{C}$ state progression is more extended than the simulated progression, which suggests that the bond angle in this state is smaller than the *ab initio* value of 110°.[3]

In conclusion, we have observed the dark $\tilde{C}(^2A_2)$ state of NO_2 for the first time and have directly measured an upper bound to T_o for the $\tilde{A}$ state. Our preliminary analysis indicates that the *ab initio* calculations of Gillispie et al.[3] provide reasonable estimates of the geometries, vibrational frequencies, and term values of the $\tilde{A}$ and $\tilde{C}$ states. A more comprehensive analysis of our data

(in progress[8]) will provide more accurate values of these properties.

We are grateful to C.E. Miller for helpful discussions and for providing NO_2. Support from the Air Force Office of Scientific Research under Contract No. AFOSR-87-0341 is gratefully acknowledged. D.M.N. thanks the Research Corporation and the donors of the Petroleum Research Fund, administered by the American Chemical Society, for support.

References for section 4.1

1. D.K. Hsu, D.L. Monts and R.N. Zare, Spectral Atlas of NO_2, 5530 to 6480 Å (Academic, New York, 1978) and references within.

2. K. Tsukiyama, K. Shibuya, K. Obi and I. Tanaka, J. Chem. Phys. **82**, 1147 (1985). H.J. Vedder, G. Persch and H.-J. Foth, Chem. Phys. Lett. **114**, 125 (1985). P. Bolduan and H.J. Jodl, J. Mol. Struct. **118**, 213 (1984). N. Sugimoto, N. Takeuchi and S. Takezawa, Chem. Phys. Lett. **99**, 475 (1983). H.J. Vedder, M. Schwarz, H.-J. Foth and W. Demtroder, J. Mol. Spec. **97**, 92 (1983).

3. G.D. Gillispie, A.U. Khan, A.C. Wahl, R.P. Hosteny and M.M. Krauss, J. Chem. Phys. **63**, 3425 (1975).

4. Y. Morino, M. Tanimoto, S. Saito, E. Hirota, R. Awata and T. Tanaka, J. Mol. Spec. **98**, 331 (1983).

5. K.M. Ervin, J. Ho and W.C. Lineberger, J. Phys. Chem. **92**, 5405 (1988).

6. R.B. Metz, T. Kitsopoulos, A. Weaver, S.E. Bradforth and D.M. Neumark, to be published. For a description of a similar instrument, see L.A. Posey, M.J. DeLuca and M.A. Johnson, Chem. Phys. Lett. **131**, 170 (1986).

7. A.J. Merer and K.-E.J. Hallin, Can. J. Phys. **56**, 838 (1978).

8. A. Weaver, R.B. Metz, S.E. Bradforth and D.M. Neumark, to be published.

4.2. Analysis of the NO_2 $\tilde{X}(^2A_1)$, $\tilde{A}(^2B_2)$ and $\tilde{C}(^2A_2)$ bands in the photoelectron spectra of NO_2^-

When the NO_2 paper of section 4.1 was written, we had carried out many Franck-Condon simulations of the NO_2^- spectra but had not found definitive answers to many questions, including the A and C state origins and an explanation of the C state vibrational structure. These are still difficult questions to answer, but several factors are now in our favour. Our analytical techniques and our simulations are much improved, as is our understanding of vibronic coupling. High-level *ab initio* calculations[1,2,3,4] have provided new estimates of A state parameters, and new experimental information has been obtained on the A[5,6,7,8,9] and C[10,11] states.

In this section we analyze the five photoelectron spectra of NO_2^-. Our analysis is based on comparisons between these spectra and Franck-Condon simulations using various experimental and *ab initio* estimates of the electronic state energies, vibrational frequencies and equilibrium geometries. We also discuss the occurrence of vibronic coupling in NO_2 and its effects on our spectra.

4.2.1. Introduction

The photoelectron spectra of NO_2^- at 355, 266 and 213 nm are shown in Figures 4.2-4.6. The spectra at 266 and 213 nm were each taken at two laser polarization angles, 0° and 90°.

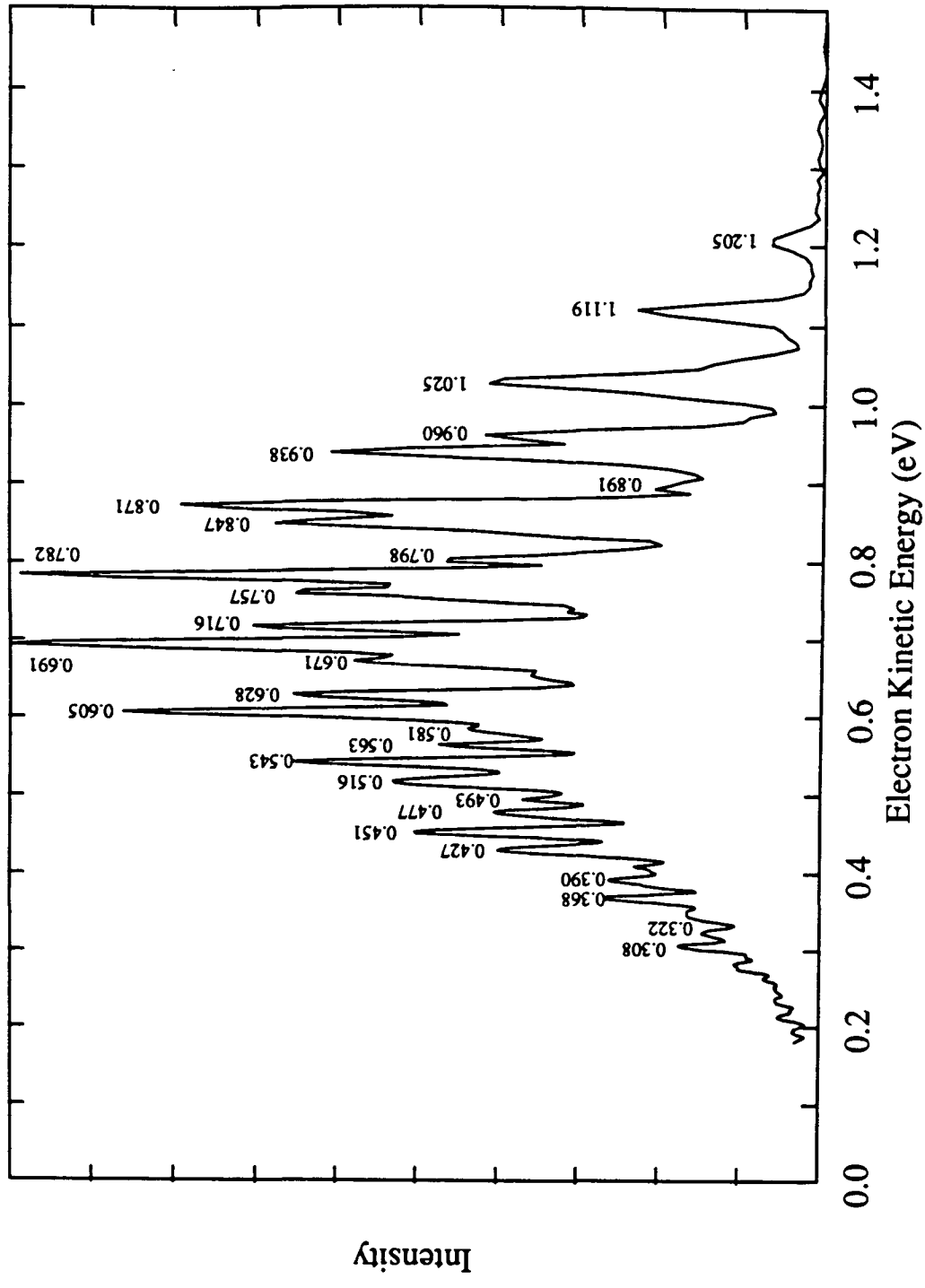

Figure 4.2. Photoelectron spectrum of NO_2^- at 355 nm, $\theta = 90^o$.

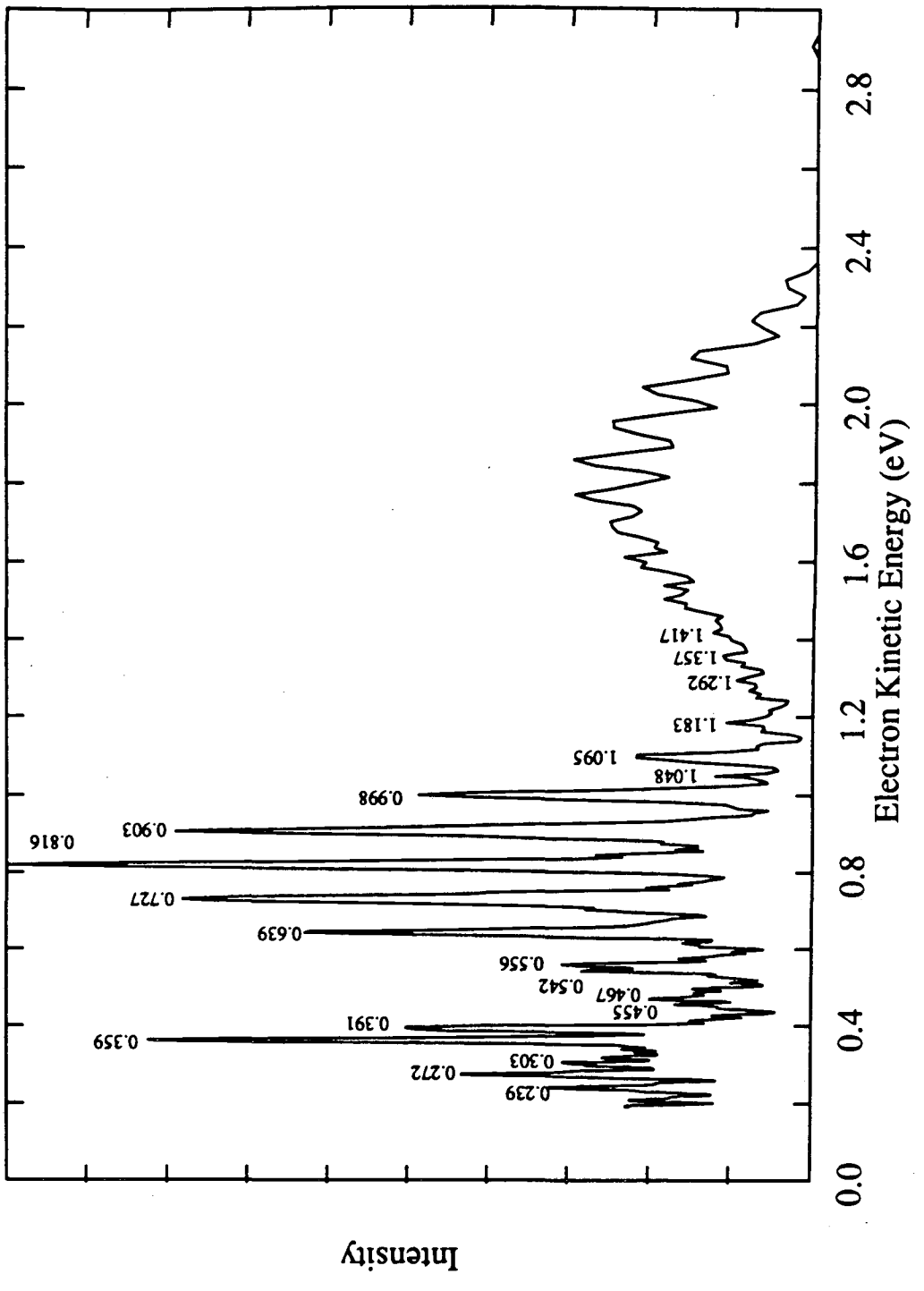

Figure 4.3. Photoelectron spectrum of NO_2^- at 266 nm, $\theta = 90^\circ$.

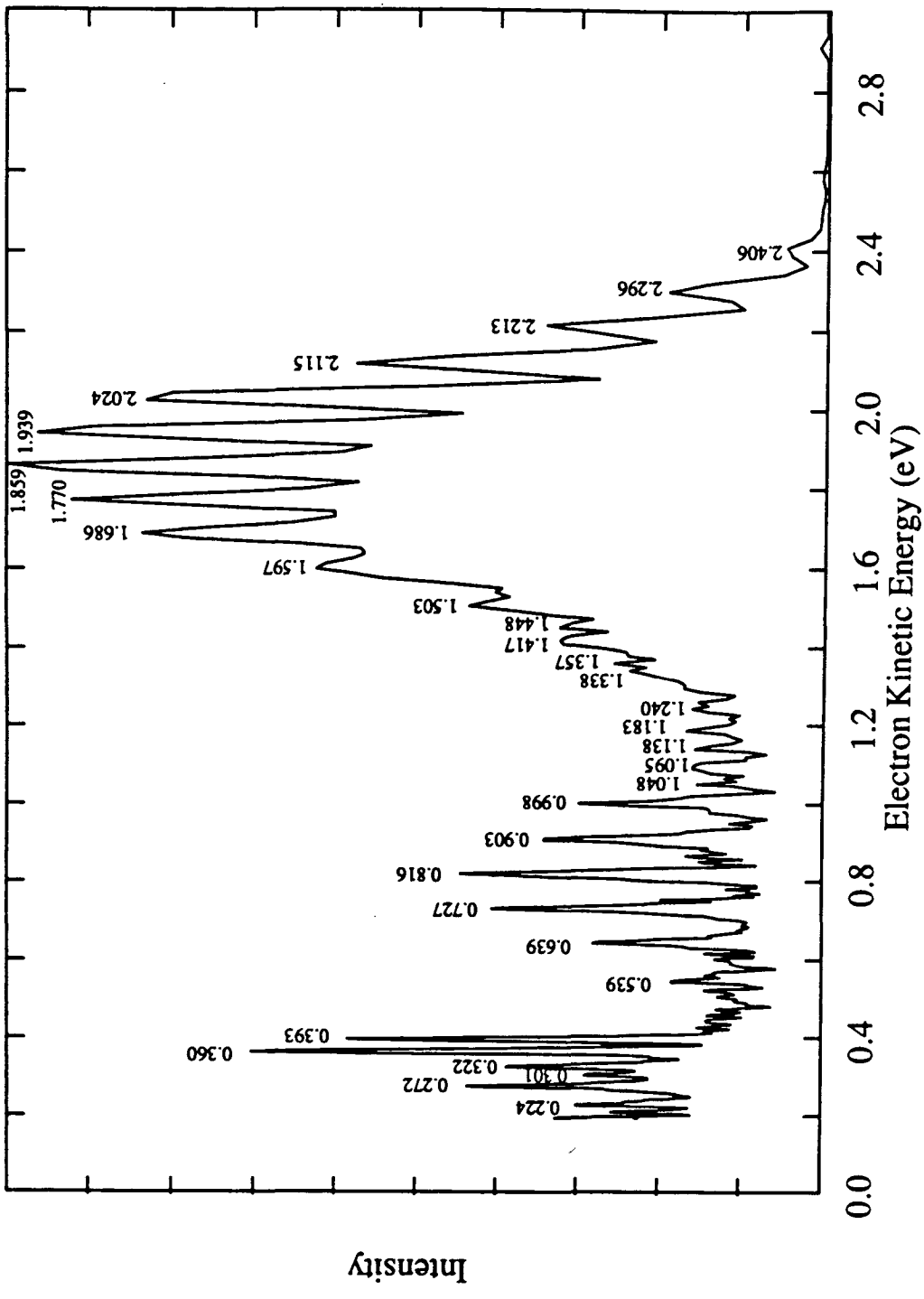

Figure 4.4. Photoelectron spectrum of NO_2^- at 266 nm, $\theta = 0^\circ$.

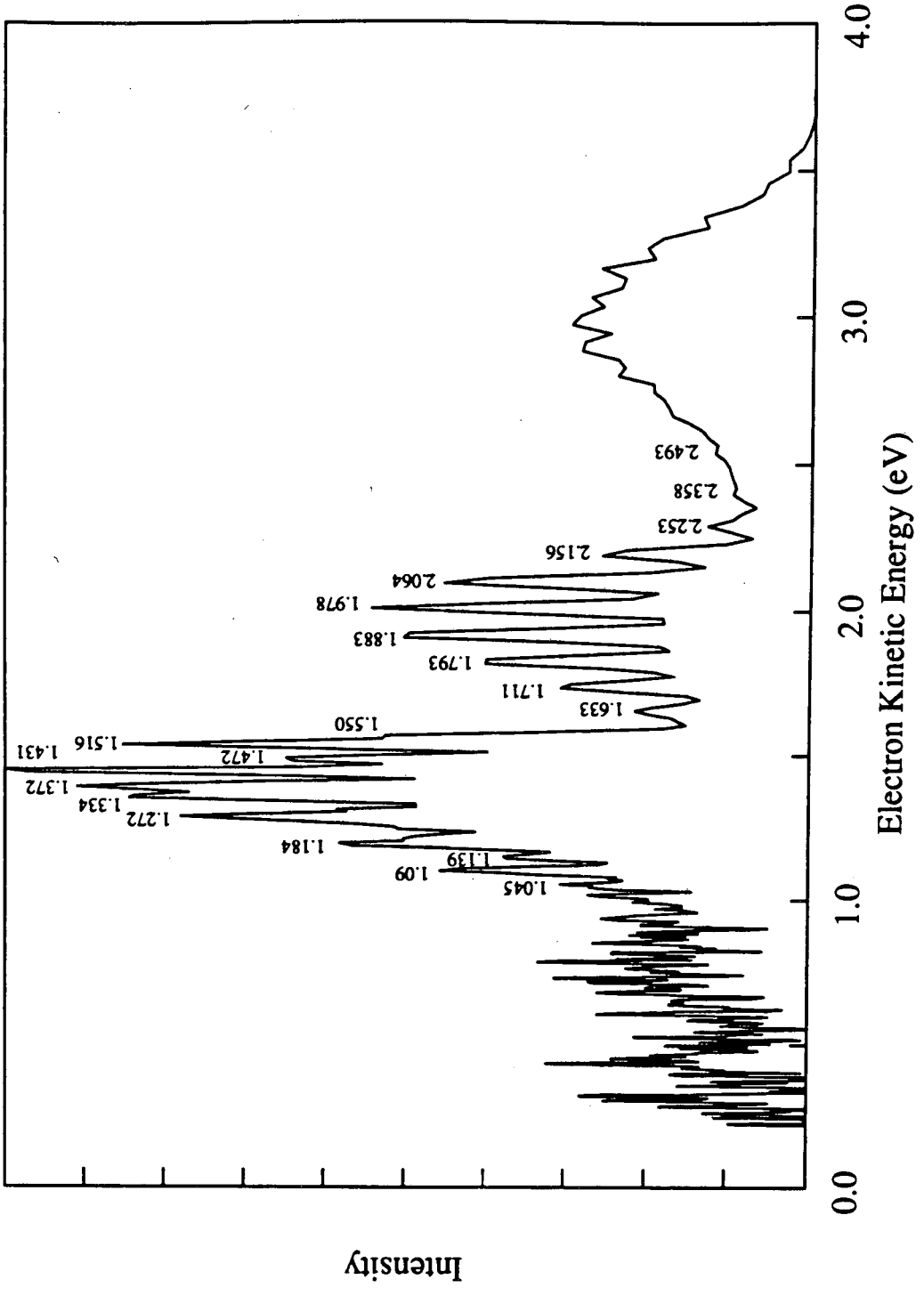

Figure 4.5. Photoelectron spectrum of NO_2^- at 213 nm, $\theta = 90^o$.

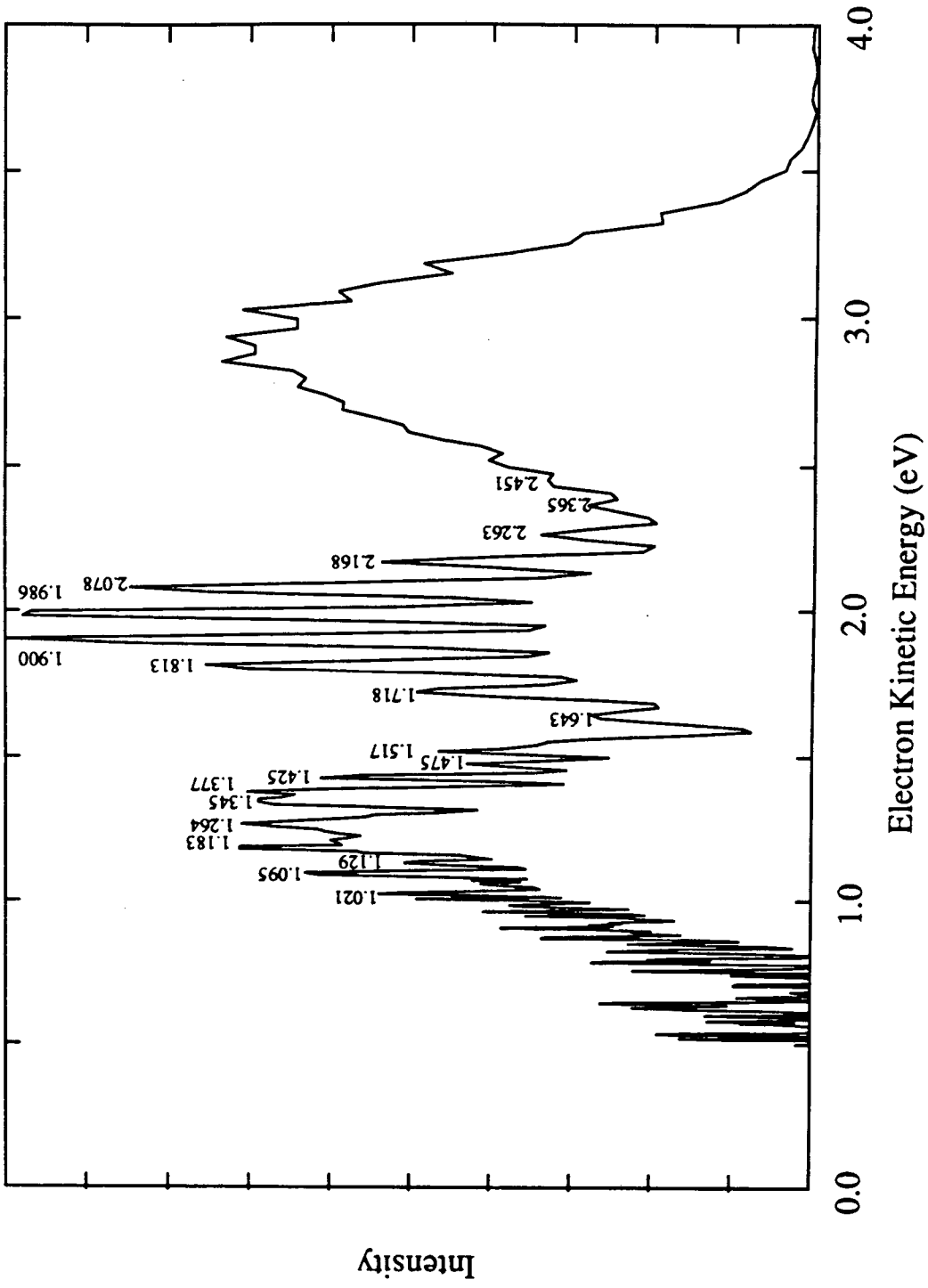

Figure 4.6. Photoelectron spectrum of NO_2^- at 213 nm, $\theta = 0^\circ$.

An elementary explanation of the structure observed in these spectra is given in section 4.1. Each spectrum shows vibrational structure in one to three distinct bands, each of which corresponds to one electronic state of the neutral NO_2. These are assigned to the $\tilde{X}(^2A_1)$, $\tilde{A}(^2B_2)$ and $\tilde{C}(^2A_2)$ electronic states of NO_2 by their energies, and also in part because of the one-electron propensity rule for photodetachment transitions.[12] The molecular orbital occupancies for NO_2^- and the lowest electronic states of NO_2 are (assuming C_{2v} symmetry)[13] [a]

NO_2^- ($^1A_1$) $(1a_1)^2(1b_2)^2(2a_1)^2(2b_2)^2(1b_1)^2(3a_1)^2(1a_2)^2(3b_2)^2(4a_1)^2$

NO_2 $\tilde{X}(^2A_1)$ $...(1a_2)^2(3b_2)^2(4a_1)^1$

NO_2 $\tilde{A}(^2B_2)$ $...(1a_2)^2(3b_2)^1(4a_1)^2$

NO_2 $\tilde{B}(^2B_1)$ $...(1a_2)^2(3b_2)^2(4a_1)^0(2b_1)^1$

NO_2 $\tilde{C}(^2A_2)$ $...(1a_2)^1(3b_2)^2(4a_1)^2$

One-electron transitions between the anion and the X, A and C configurations are possible; the $NO_2^- \rightarrow NO_2$ $\tilde{B}(^2B_1)$ transition requires simultaneous changes in the molecular orbital occupancy of two electrons, so we do not expect this band to contribute significantly to the photoelectron spectrum.

---

[a] The orientation of the x and y axes defines the b_1 and b_2 representations in the C_{2v} point group. The convention has changed since the earliest work on NO_2, so that some earlier papers reverse the labelling of the $^2B_2$ and $^2B_1$ states. (See J. Chem. Phys. **23**, 1997 (1955).)

4.2.2. Analyzing the NO_2^- photoelectron spectra

We derive two types of information from our spectra: the neutral electron affinity, electronic state energies and vibrational frequencies, which are obtained directly from the peak positions, and the geometry difference between the anion and neutral, which is obtained indirectly from the peak intensities and can be used to determine the ion or neutral geometry given a reference value for the other. We obtain the geometry difference from the peak intensities by calculating the overlap of the ion and neutral wavefunctions (Franck-Condon factors), and varying their relative displacement until the calculated intensities reproduce the experimental peak intensities.

Although we are well aware of the spectral chaos induced in higher-resolution spectra by vibronic coupling,[14,15] the vibrational structure of our spectra appears to be relatively simple and regular (at first glance), so our analysis relies on Franck-Condon calculations. In addition, any deficiencies in these simulations may provide more information about the exact nature of any anomalies observed in our spectra.

Our simulation procedure is based on the method of Hutchisson,[16] which uses analytical expressions for the energy levels and Franck-Condon factors. We assume separable one-dimensional harmonic oscillator potentials for the vibrational modes of NO_2^- and NO_2,

$$V = \sum_i \frac{1}{2} k_i x_i^2 \qquad (4.2.1)$$

with k_i the harmonic force constant for mode i. The resulting energy levels are given by

$$E = \sum_i \left(n_i + \frac{1}{2}\right) h\nu_i \qquad (4.2.2)$$

Our simulation code includes provisions for adding anharmonic terms to the potential, with corresponding corrections to the harmonic energies:

$$E = \sum_i \left(n_i + \frac{1}{2}\right) h\nu_i + \sum_i \sum_j \left(n_i + \frac{1}{2}\right)\left(n_j + \frac{1}{2}\right) x_{ij} \qquad (4.2.3)$$

where x_{ij} is negative (energy levels get closer together with increasing n_i). The Franck-Condon factors are also corrected. Because we assume separable oscillators, there is no provision for including cross-anharmonicities (x_{ij}, $i \neq j$). The form of the analytical equations also excludes calculations with $x_{ii} > 0$, where the energy level spacings increase with n_i.

The Franck-Condon factors must be convoluted with a resolution function to simulate our experimental peak widths and shapes. In our spectra of bound neutral species, peak widths are determined by instrumental resolution rather than species lifetime. The instrumental resolution function is discussed in Chapter 3; we convolute the Franck-Condon factors with Gaussian peaks of widths determined by the instrumental resolution at that energy. We do not model rotational contours, since we assume that the

rotational temperature is relatively low.

We use normal coordinate displacements[17] in our calculations of Franck-Condon factors. The normal coordinate displacements can be related to changes in bond length and bond angle if we know the force constants for vibrational motion, which determine the transformation matrix. These force constants can be determined from high resolution experimental data, but the only full set of force constants measured for NO_2 are those for the X state.[18] Its geometry is so different from that of the A and C states (the bond angle is 133.5°,[19] compared to 117.5° [20] for the anion and 102-110° [21] predicted for the other states) that we believed the normal coordinates might be very different, and that this would not be a good approximation.

The force constants can be calculated[17] from measured frequencies, but since the number of force constants to be determined is usually greater than the number of measured parameters, some of those force constants must be neglected. The valence force approximation[17(d)] applied to NO_2 assumes the symmetric stretch-bend interactions to be negligible. The calculations of Blank and Overend[17(e)] show that this is not a particularly good approximation, but we wanted a consistent set of normal coordinates for the X, A and C states so we used this method to calculate force constants. Unfortunately, using the valence force approximation for the C state gives imaginary force constants f_{11} and f_{22}, whether we assume Gillispie's *ab initio* values for the geometry and frequencies[21] or use parameters estimated from our experimental spectrum (see

below).

The other possibility is to use force constants calculated from *ab initio* potential energy surfaces, as the derivatives of the potential at the equilibrium geometry. For NO_2, calculation of accurate potential energy surfaces requires a very high level of theory,[22,23] and we were not prepared to perform such a calculation. The only published set of normal coordinates for all four electronic states of NO_2 is that of Gillispie et al..[21] Although the force constants were determined at a particular equilibrium geometry for each state, those geometries are close to the values we use in our simulations. There are also deficiencies in the *ab initio* C state calculation, but we used Gillispie's normal coordinates because of the lack of an alternative.

For each neutral electronic state, the normal coordinates are expressed in terms of the internal coordinates R_1 and R_2, where

$$R_1 = r_{NO} \sin\frac{\theta_{ONO}}{2}, \qquad R_2 = r_{NO} \cos\frac{\theta_{ONO}}{2} \tag{4.2.4}$$

The normal coordinates for the ν_1 and ν_2 modes are defined by the coefficients b_{ij} determined by Gillispie,

$$\begin{aligned} Q_1 &= b_{11}\left(R_1 - R_1^e\right) + b_{12}\left(R_2 - R_2^e\right) \\ Q_2 &= b_{21}\left(R_1 - R_1^e\right) + b_{22}\left(R_2 - R_2^e\right) \end{aligned} \tag{4.2.5}$$

where for the X state, $b_{11} = 4.184$, $b_{12} = 2.100$, $b_{21} = 3.807$ and $b_{22} = -2.308$, in units of $amu^{1/2}$: the Q_i have dimensions $amu^{1/2}$·length.

We neglect Duschinsky rotation, the rotation of the ion and neutral

normal coordinates with respect to each other.[24] Ervin et al.[20] have shown that this parallel mode approximation is reasonable for the NO_2 X state. Since the vibrational frequencies in the A and C states are similar, this is probably a good approximation for those states also. If we assume that we can also use the neutral normal coordinates for the ion in transitions to each electronic state, then

$$\begin{aligned} Q_1^- &= 4.184\left(R_1^- - R_1^{-,e}\right) + 2.100\left(R_2^- - R_2^{-,e}\right) \\ Q_2^- &= 3.807\left(R_1^- - R_1^{-,e}\right) - 2.308\left(R_2^- - R_2^{-,e}\right) \end{aligned} \qquad (4.2.6)$$

Since $R_1^- = R_1^X$ and $R_2^- = R_2^X$, the normal coordinate displacements $\Delta Q_i^X = Q_i^X - Q_i^-$ are

$$\begin{aligned} \Delta Q_1^X &= 4.184\left(R_1^{-,e} - R_1^{X,e}\right) + 2.100\left(R_2^{-,e} - R_2^{X,e}\right) \\ \Delta Q_2^X &= 3.807\left(R_1^{-,e} - R_1^{X,e}\right) - 2.308\left(R_2^{-,e} - R_2^{X,e}\right) \end{aligned} \qquad (4.2.7)$$

for the ground state, where $R_i^{-,e}$ and $R_i^{X,e}$ are the anion and neutral equilibrium values, respectively.

We do not require ΔQ_3 because we do not expect the antisymmetric stretching mode, ν_3, to be active in our spectra. The ion and neutral states are all believed to be of C_{2v} or higher symmetry, with two equal N-O bonds, so $\Delta Q_3=0$. The ν_3 mode might be excited in the A state since the ion and neutral vibrational frequencies are very different, but then transitions from the totally symmetric ion ground state are Franck-Condon allowed only to the even Δv_3 levels of the neutral.

The normal coordinate displacements for the other neutral states are

$$\begin{aligned} \Delta Q_1^A &= 2.608\left(R_1^{-,e} - R_1^{A,e}\right) + 2.769\left(R_2^{-,e} - R_2^{A,e}\right) \\ \Delta Q_2^A &= 5.020\left(R_1^{-,e} - R_1^{A,e}\right) - 1.439\left(R_2^{-,e} - R_2^{A,e}\right) \end{aligned} \tag{4.2.8}$$

$$\begin{aligned} \Delta Q_1^C &= 2.741\left(R_1^{-,e} - R_1^{C,e}\right) + 2.730\left(R_2^{-,e} - R_2^{C,e}\right) \\ \Delta Q_2^C &= 4.948\left(R_1^{-,e} - R_1^{C,e}\right) - 1.512\left(R_2^{-,e} - R_2^{C,e}\right) \end{aligned} \tag{4.2.9}$$

Many of the data used in our simulations were obtained from other experimental results or from *ab initio* calculations. The most relevant data are given in Table 4.1.

4.2.3. The 355 nm spectrum: the $\tilde{X}(^2A_1)$ state

The 355 nm (3.495 eV) photoelectron spectrum of NO_2^- (Fig. 4.2, θ=0°) shows only one electronic band, with vibrational structure which is assigned to progressions in the symmetric stretching (ν_1, a_1 symmetry) and bending (ν_2, a_1) modes. Although the overall appearance of the band is very similar to that in the spectrum at 351 nm obtained by Ervin et al.,[20] there are two minor differences between our spectra. First, our origin is at 1.205 eV, giving an electron affinity of 2.290±0.021 eV, compared to their estimate of 2.273±0.005 eV. The two values overlap; the greater estimated error in our measurement is due to our resolution at this energy being worse than Ervin's.

Second, the relative maximum in our X state progression occurs at 0.671 eV (4307 cm^{-1} from the origin) and is assigned to the $1_0^1 2_0^4$ transition, but

Table 4.1: Previous work on NO_2^-, NO_2 $\tilde{X}(^2A_1)$ and $\tilde{A}(^2B_2)$.

Expt./Theory, Ref.	r_{NO} (Å)	θ_{ONO} (°)	ν_1 (cm^{-1})	ν_2 (cm^{-1})	ν_3 (cm^{-1})	Energy (eV)
NO_2^-						
E, Ervin[20]	1.25	117.5	1284	776	-	EA 2.273
T, Kaldor 1990[38]	1.265	116.5	1364	796	1296	EA 2.15
NO_2 $\tilde{X}(^2A_1)$						
E, Lafferty[25]			1325	750	1634	
E, Morino 1983[19]	1.194	133.5				
E, Hardwick[37]	1.195	133.8				
E, Morino 1985[26]			1349	760	1671	
NO_2 $\tilde{A}(^2B_2)$						
E, Delon[8]			1320	750	1617	1.207
E, Merer[27]				720		1.21
E, Brand[28]	1.244	102.6	1350	730		1.21
T, Gillispie[21]	1.26	102	1461	739		1.18*
T, Hirsch 1985[29]	1.27	102.4				0.917*
T, Blahous[1]	1.281	101.3	1391	730	359	1.058*
T, Hirsch 1991[3]	1.277	101.9				1.08*
T, Kaldor 1991[4]	1.27	100.6	1480	758	792	1.049

* These are vertical rather than adiabatic energy differences.

Table 4.2: Previous work on NO_2 $\tilde{B}(^2B_1)$ and $\tilde{C}(^2A_2)$.

Expt./Theory, Ref.	r_{NO} (Å)	θ_{ONO}(°)	ν_1 (cm^{-1})	ν_2 (cm^{-1})	ν_3 (cm^{-1})	Energy (eV)
$\tilde{B}(^2B_1)$						
E, Bolduan[35]			1230	450	2040	1.763
T, Hirsch 1985[29]	1.21	180				1.905
T, Gillispie[21]	1.20	180	1192	960		1.66*
T, Xie[23]						1.67*
$\tilde{C}(^2A_2)$						
E, Shibuya[11]	1.4	102				
T, Gillispie[21]	1.27	110	1360	798		1.84*
T, Kaldor 1991[4]	1.286	109.4				1.934†

* These are vertical rather than adiabatic energy differences.

† This is the energy at the constrained C_{2v} geometry; the C_s minimum is at 1.933 eV.

Ervin's $1_0^1 2_0^3$ peak (3545 cm^{-1} from the origin) is the maximum.

We fit the peak positions in the X band using linear regression, and obtained best-fit vibrational frequencies and anharmonicities in agreement with the results of high resolution experiments.[25] We simulated the X band, using ν_1 = 1266.3 ± 17.0 cm^{-1}, ν_2 = 714.2 ± 2.0 cm^{-1} and x_{11} = -5.58 ± 4.3 cm^{-1}, from a linear regression fit; we excluded x_{12} and x_{22} from the fitting parameters because our simulation program does not include provisions for cross-anharmonicity (x_{ij}), and excluding x_{12} gave $x_{22}>0$, which we also cannot incorporate. The simulation also assumed Ervin et al.'s ion frequencies and geometry (ν_1 = 1284 cm^{-1}, ν_2 = 776 cm^{-1}, r_{NO} = 1.25 Å, θ = 117.5°), the X state geometry obtained from high resolution absorption spectra (r_{NO} = 1.194 Å, θ = 133.5° [19]) and our estimated electron affinity. The resulting simulated spectrum fitted our peak positions well, but the $1_0^1 2_0^3$ peak was the maximum.

We then varied the ion geometry from Ervin's values to obtain the best fit to our peak intensities. The best fit normal coordinate displacements, ΔQ_1 = 0.265 and ΔQ = -0.611 $amu^{1/2}$Å, correspond to an anion geometry of r_{NO} = 1.255 Å, θ = 115.5°. This is in agreement with Ervin et al.'s results (1.27±0.02 Å, 117.5±2°).

The difference in peak intensities between our spectrum and Ervin's may be explained by the difference in the assumed instrumental peak shapes: our peaks are approximated by Gaussian functions of variable width, but theirs are envelopes of rotational distributions. The difference affects peak shapes

and relative peak intensities, and the broad area beneath the X band structure is more intense in Ervin's spectrum. Trial simulations using a different convolution function ($\exp[-a(x-x_0)]$ instead of $\exp[-a(x-x_0)^2]$) produced spectra that resembled the Ervin spectrum more closely; the maximum shifted to the $1_0^1 2_0^3$ peak, and the broad region under the sharp structure increased in intensity.

In all simulations at 266 and 213 nm, we used the following parameters for the anion and X state: NO_2^-: ν_1 = 1284 cm^{-1}, ν_2 = 776 cm^{-1},[20] r_{NO} = 1.255 Å, θ = 115.5°; NO_2 $\tilde{X}(^2A_1)$: ν_1 = 1325 cm^{-1}, ν_2 = 750 cm^{-1}, x_{11} = -5.47 cm^{-1}, x_{22} = -0.47 cm^{-1},[25] r_{NO} = 1.194 Å, θ = 133.5°;[26] E.A. (NO_2) = 2.290 eV.

4.2.4. The 266 nm spectrum: the $\tilde{A}(^2B_2)$ state

The 266 nm (4.66 eV) photoelectron spectra of NO_2^- (Fig. 4.3, θ = 90° and Fig. 4.4, θ = 0°) show the X and A bands and the beginning of the C band. Our interest is primarily in the excited state bands; because the instrumental resolution degrades at higher electron kinetic energy, the X progression is not particularly interesting.

We examine the A state progression first, to determine the origin. The A state has been extensively studied by absorption spectroscopy and fluorescence techniques.[8,27,28] However, the origin has not been determined conclusively because the geometry difference between the X and A states results in very poor Franck-Condon overlap with the lowest vibrational levels

of the A state (X: r_{NO} = 1.194 Å, θ = 133.5°;[19] A: r_{NO} = 1.244 Å, θ = 102.6° [28]). This is also a problem in the photoelectron spectra, although the anion geometry (r_{NO} = 1.275, θ = 117.5°) is closer to that of the A state and Franck-Condon overlap with the lowest vibrational levels is somewhat better.

It is impossible to determine the A state origin unambiguously by inspecting the photoelectron spectra. Although the relative intensities of the X and A bands vary with laser polarization and the A band is much more intense at 90°, there is still no clearly defined origin. Subtraction of the scaled 0° and 90° spectra from each other (which has been used to determine band origins) yielded no further information. In section 4.1, we identified the peak at 1.183 eV in the θ=90° spectrum as the peak at highest electron kinetic energy that was clearly associated with the A state. That assignment gives an upper limit to the term value, T_0 = 1.204 eV (assuming EA = 2.273 eV), which agrees with the recent experimental estimate of Delon and Jost (1.207 eV).[8]

We simulated the 266 nm spectrum (Figure 4.7) using Delon and Jost's vibrational frequencies (ν_1 = 1320 cm^{-1}, ν_2 = 750 cm^{-1}),[8] Gillispie's geometry (1.26 Å, 102°)[21] and T_0 = 1.204 eV. The simulated A band is in excellent agreement with our experimental result, although the peaks on the high electron kinetic energy side of the band are a little too intense. However, even this good agreement does not give a conclusive value for T_0.

The uncertainty in the A state origin, and the disagreement between the experimental T_0 values and recent *ab initio* estimates (T_0 ~ 1.0 eV, see Table

Figure 4.7: Simulated and experimental photoelectron spectrum of NO_2^- at 266 nm, $\theta = 0^\circ$, including the $\tilde{X}(^2A_1)$ and $\tilde{A}(^2B_2)$ bands.

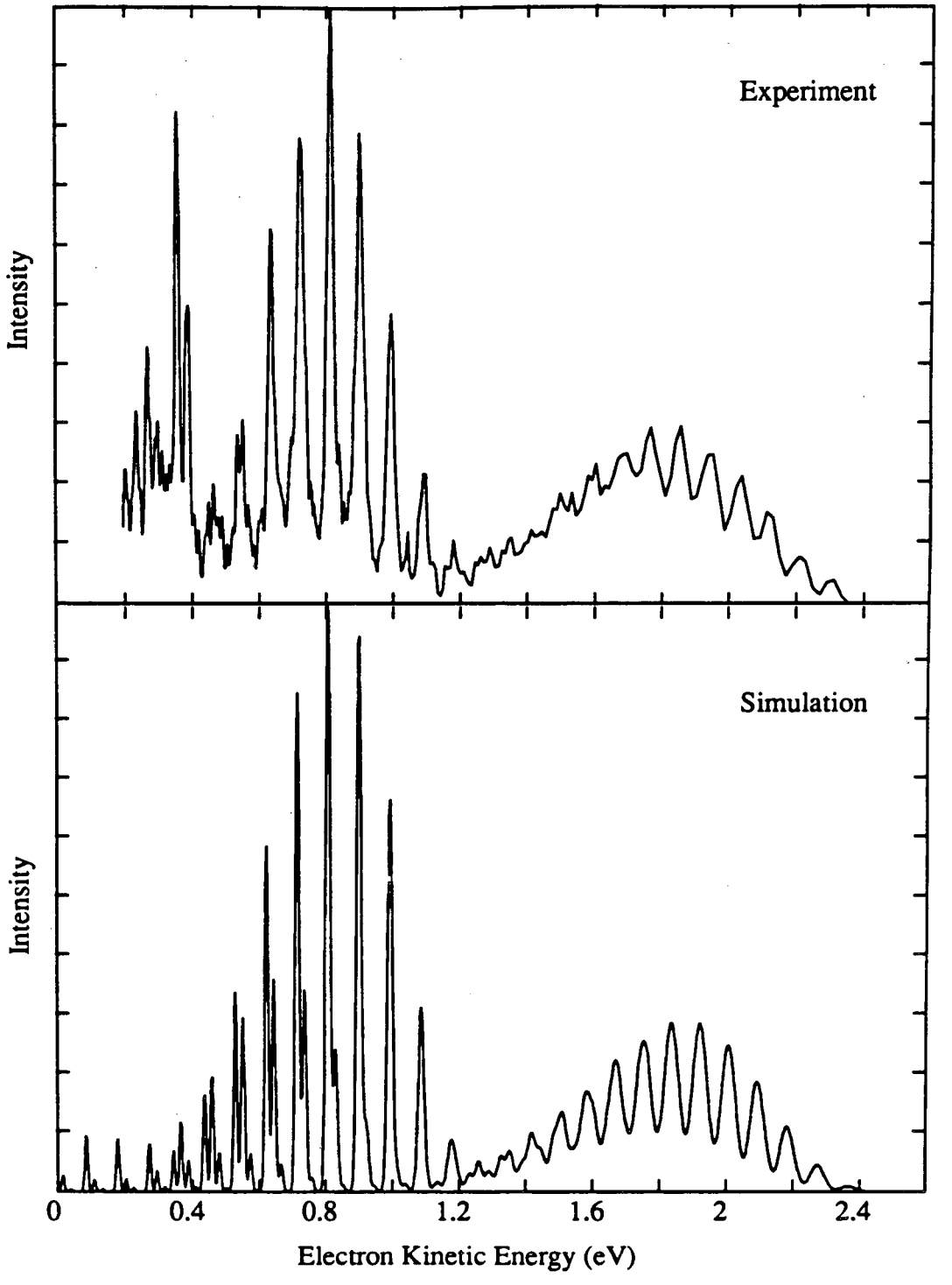

4.1), motivated us to carry out many simulations of the 266 nm spectrum. We found that we could fit the A band using values of T_0 between 1.018 and 1.204 eV (origin at 1.369 to 1.183 eV eKE), using various *ab initio* geometries[1,3,4,21,29] (Table 4.1), with displacements calculated from Gillispie's force constants. Although these simulations gave adequate agreement with the experimental peak positions and intensities, none of them was as good as the simulation shown in Fig. 4.7; instead, the progression was broader and the peaks on both sides of the maximum were all about 30-50% larger than in the experimental spectrum. It is possible that, with enough adjustment of fitting parameters, one could improve the fit for these simuulated spectra. However, the very good agreement between Delon and Jost's and our results provides support for the higher value of T_0(A).

We now look at the beginning of the third electronic band in the 266 nm spectra. Both the 0° and 90° spectra show sharp, intense peaks at about 0.391 and 0.359 eV, only 0.032 eV (258 cm^{-1}) apart. This is too small for any predicted B or C state vibrational frequency. Because these peaks occur at energies where the electron transmission decreases sharply, we will look to the 213 nm spectrum for a more complete picture.

4.2.5. The 213 nm spectra: the $\tilde{C}(^2A_2)$ state

The 213 nm (5.825 eV) photoelectron spectra of NO_2^- at θ=0°and 90° (Figures 4.5 and 4.6) show three full electronic bands. These include the X and

A bands that we have already discussed, and no further information on those states can be obtained from these spectra. The third band is assigned to the 'dark' $\tilde{C}(^2A_2)$ state; although the $\tilde{B}(^2B_1)$ state lies about 1.7 eV above the ground state, its linear geometry will result in very poor Franck-Condon overlap with the ion vibrational levels, and those would be two-electron transitions.

As discussed above, assigning the vibrational structure in this band is immediately problematic. Let us initially assign the peak at 1.516 eV in the θ=0° spectrum to the C band origin. We expect a progression in the bending mode, at about 800 cm^{-1};[21] this should be shorter than the X and A band bending progressions because the C state bond angle is predicted to be closer to that of the anion. We also expect a short progression in the symmetric stretch, at about 1300 cm^{-1}.[21] The peaks closest to these energies are those at eKE 1.431 eV (686 cm^{-1} from the origin) and 1.372 eV (1161 cm^{-1}). Other peaks below 1.372 eV can be assigned as overtones and combinations of these two frequencies; linear regression gives the best fit as ν_1=1125 cm^{-1}, ν_2=673 cm^{-1} (excluding anharmonicity). However, we still have not assigned the sharp peak at 1.472 eV, only 355 cm^{-1} from the assigned origin, or the shoulder at 1.550 eV (-274 cm^{-1}). These are intense peaks in the 266 nm spectra and cannot be neglected. They are too intense to be hot band transitions, since the X band shows no evidence of hot bands in any of the five spectra.

If the origin were earlier, could we then fit these peaks? Both *ab initio*

estimates of the $\tilde{C}(^2A_2)$ state energy (T_0 = 1.934 eV,[4] T_e = 1.84 eV[21]) are consistent with the 2.04 eV obtained if the origin is at 1.516 eV eKE. We carried out simulations at both *ab initio* geometries (see Table 4.2), varying the electronic energy and vibrational frequencies to obtain optimal agreement with the experimental spectrum. In all simulations, the $1_0^0 2_0^0$ peak was largest and the peak intensities were very different to the experimental band, suggesting that the *ab initio* neutral geometries are too similar to that of the ion. The agreement would not improve substantially if the electronic energies were adjusted.

We varied the neutral geometry to try to improve the simulation, and approximately reproduced most of the peak positions and intensities in the C band (using ν_1 = 1355 cm^{-1}, $\nu 2$ = 807 cm^{-1}, x_{11} = -8.1 cm^{-1}, r_{NO} = 1.28 Å, θ = 106°). However, the peak at 1.550 eV could not be reproduced with any reasonable combination of parameters, and the peak at 1.472 eV was also very difficult to simulate.

The intensities of these two anomalous peaks relative to the rest of the C band vary with laser polarization angle, suggesting that they might be associated with a different electronic state. Compared to the peak at 1.516 eV, they are relatively much more intense at θ=0° in the 266 and 213 nm spectra, but the A and C bands are more intense at θ=90°. Could they be associated with the $\tilde{B}^2B_1$ state, either as allowed transitions or through vibronic coupling?

Vibrational levels of the $\tilde{B}(^2B_1)$ state certainly exist at these energies,

since the origin is about 1.7 eV above the ground state (1.9 eV eKE at 213 nm). However, the geometry change between the anion and the linear B state is so large that the Franck-Condon intensity of transitions to the lowest vibrational states should be very small. The substantial intensity of these observed peaks suggests that they are not due to Franck-Condon allowed transitions to the B state. We are left with the possibility of vibronic coupling, which we consider in the next section.

4.2.6. Vibronic coupling in NO_2

NO_2 is an interesting case study in vibronic coupling because four electronic states within 2 eV of each other are coupled, some very strongly. The $\tilde{X}(^2A_1)$ and $\tilde{A}(^2B_2)$ states interact through linear coupling via the ν_3 vibration (b_2 symmetry), as do the $\tilde{B}(^2B_1)$ and $\tilde{C}(^2A_2)$ states. In addition, the $\tilde{X}(^2A_1)$ and $\tilde{B}(^2B_1)$ states are the components of a Renner-Teller coupled pair ($^2\Pi_g$) that are degenerate in the linear configuration, as are the $\tilde{A}(^2B_2)$ and $\tilde{C}(^2A_2)$ states ($^2\Phi_g$).[30]

The effects of the linear $\tilde{X}(^2A_1)$-$\tilde{A}(^2B_2)$ coupling on the visible absorption and other optical spectra are well documented.[8,31,32,33] The A state spectrum is extremely complicated, especially near and above the conical intersection of the $\tilde{X}(^2A_1)$ and $\tilde{A}(^2B_2)$ surfaces at about 1.2 eV [1,3] above the ground state. This has been interpreted as evidence for strong linear coupling, and the $\tilde{X}(^2A_1)$-$\tilde{B}(^2B_1)$ quadratic (Renner-Teller) coupling is generally neglected

because it is believed to be relatively weak with respect to the linear coupling.[30]

By contrast, we observe an apparently regular A state vibrational progression. Our peak positions are in excellent agreement with the vibronic origins estimated by Delon and Jost[8] and Brand et al..[34] The apparent contradiction between our regular progressions and the highly irregular absorption spectra may be resolved by considering our experimental resolution. Since we cannot resolve rotational lines, we do not observe the highly perturbed rotational structure present in high-resolution optical spectra, and we see a relatively regular vibrational progression. In addition, we do not observe any progression in the coupling mode, ν_3, which should show the most significant effects.

Absorption spectra of the $\tilde{B}(^2B_1)$ state[35,36] show structure much more regular than that for the $\tilde{A}(^2B_2)$ state, which was taken as evidence that the $\tilde{B}(^2B_1)$-$\tilde{C}(^2A_2)$ linear coupling is much weaker than the $\tilde{X}(^2A_1)$-$\tilde{A}(^2B_2)$ coupling. Haller's calculation of the B state absorption spectrum[31] produced a near-regular progression in ν_2 with greater perturbations at high energies near the $^2B_1$-$^2A_2$ conical intersection, where non-adiabatic effects become more important. However, the $\tilde{B}(^2B_1)$ state spectra also exhibit irregular vibrational spacings and anomalous rotational effects.[35] Attempts to explain these effects using Renner-Teller coupling alone have been unsuccessful, although this is usually the only mechanism considered. Bolduan and Jodl[35] observed odd Δv_3

transitions in the absorption spectrum, but dismissed vibronic coupling as a viable explanation. Transitions to the $\tilde{B}(^2B_1)$ state are nominally forbidden in our spectra because of the one-electron propensity rule.

The $\tilde{C}(^2A_2)$ state has been observed experimentally by only one other group since our first experiments, and the majority of theoretical attention has been devoted to the other three states. As we noted above, the $\tilde{B}(^2B_1)$-$\tilde{C}(^2A_2)$ linear coupling is generally assumed to be relatively weak, and the $\tilde{A}(^2B_2)$-$\tilde{C}(^2A_2)$ quadratic coupling even weaker. However, the anomalous spacings of the first few peaks in our $\tilde{C}(^2A_2)$ progression and their intensity variation with polarization are reminiscent of spectra of other vibronically coupled molecules (similar effects in NO_3 are discussed in the next chapter). The experimental spectrum is also very different to that simulated at the *ab initio* geometries; the progression is longer and more intense at low electron kinetic energy.

It is possible that linear coupling of the $\tilde{B}(^2B_1)$ and $\tilde{C}(^2A_2)$ states via the antisymmetric stretch, ν_3, could explain both the anomalous effects in the B state absorption spectra and the anomalous peaks in the C band in our photoelectron spectra. The interaction would couple odd v_3 vibrational states in each electronic state to even v_3 states in the other, and Franck-Condon-forbidden transitions could borrow intensity from the allowed transitions, which would explain the odd Δv_3 peaks observed in the B state absorption spectrum. Photodetachment transitions to v_3 vibrational levels of the B state might borrow intensity from the strong C band observed in our spectra and

gain some electronic character of the C state, so that the borrowed peaks would behave differently on variation of laser polarization, as we observe in the photoelectron spectrum.

The best quantitative approach to this problem is an exact vibronic coupling calculation which explicitly includes the coupling terms in the Hamiltonian. Such calculations have already been performed to simulate the visible absorption spectrum of NO_2,[31,32] and show that this is a very challenging computation. If quadratic coupling is ignored, the matrix Hamiltonian for linear coupling can be separated into the $\tilde{X}(^2A_1)$-$\tilde{A}(^2B_2)$ and $\tilde{B}(^2B_1)$-$\tilde{C}(^2A_2)$ manifolds, but the vibrational modes are not separable and all three must be included in the calculation. In solving the $\tilde{B}(^2B_1)$-$\tilde{C}(^2A_2)$ linear coupling problem, Haller et al.[31] diagonalized matrices of dimensions about 20000 x 20000. Although we have done vibronic coupling calculations for NO_3 (which are discussed in the next chapter, where we describe the procedure), the NO_2 problem is beyond our present capabilities. We hope that as theoretical interest in the $\tilde{C}(^2A_2)$ state increases, others will find this calculation worthwhile.

4.2.7. Summary

We have obtained photoelectron spectra of NO_2^- at 355, 266 and 213 nm, the latter two at laser polarization angles of both 0° and 90°. We calculated simulated spectra to compare our experimental results to those of

other experiments and *ab initio* calculations.

The 355 nm spectrum shows the $\tilde{X}(^2A_1)$ state band. Our best fit gives NO_2^- parameters in agreement with those determined by Ervin et al..[20]

The 266 nm spectra show the $\tilde{A}(^2B_2)$ and $\tilde{X}(^2A_1)$ bands. The $\tilde{A}(^2B_2)$ vibrational progression is regular and does not show evidence of significant perturbations. Simulations using the vibrational frequencies of Delon and Jost and Gillispie's *ab initio* geometry are in excellent agreement with our experimental spectra and support the value of 1.204 eV for $T_0(A)$ estimated previously. Simulations assuming other *ab initio* geometries and T_0 are adequate, but not as good.

The 213 nm spectra show the full $\tilde{C}(^2A_2)$ band as well as the $\tilde{X}(^2A_1)$ and $\tilde{A}(^2B_2)$ bands. The effects of vibronic coupling appear to be stronger in the $\tilde{C}(^2A_2)$ state, probably due to linear coupling with the $\tilde{B}(^2B_1)$ state via the ν_3 antisymmetric stretching mode. Several peaks appear which cannot be explained by Franck-Condon allowed transitions to vibrational levels of either the B or C state.

Acknowledgements

We thank Remy Jost and Uzi Kaldor for communicating their results prior to publication. We also thank Don Arnold for use of his Franck-Condon factor program, and Kent Ervin for sending us his simulation program. This research was funded by the Air Force Office of Scientific research under grant

no. AFOSR-91-0084.

References for section 4.2:

1. C.P. Blahous III, B.F. Yates, Y. Xie and H.F. Schaefer III, J. Chem. Phys. **93**, 8105 (1990).

2. G. Hirsch, R.J. Buenker and C. Petrongolo, Mol. Phys. **70**, 835 (1990).

3. G. Hirsch, R.J. Buenker and C. Petrongolo, Mol. Phys. **73**, 1085 (1991).

4. U. Kaldor, Chem. Phys. Lett. **185**, 131 (1991).

5. F. Bylicki, G. Persch, E. Mehdizadeh and W. Demtröder, Chem. Phys. **135**, 255 (1989).

6. X.Z. Zhao, T.X. Lu and Z.F. Cui, Chem. Phys. Lett. **162**, 140 (1989). X.Z. Zhao, T.X. Lu and Z.F. Cui, Spectroscopy Lett. **23**, 1159 (1990).

7. K.-m. Chen, G.-P. Wang, C.-n. Kuo and C.-c. Pei, Chem. Phys. **144**, 383 (1990).

8. A. Delon and R. Jost, J. Chem. Phys. **95**, 5686 (1991).

9. A. Delon, R. Jost and M. Lombardi, J. Chem. Phys. **95**, 5701 (1991).

10. H. Nagai, K. Aoki, T. Kusumoto, K. Shibuya and K. Obi, J. Phys. Chem. **95**, 2718 (1991).

11. K. Shibuya, T. Kusumoto, H. Nagai and K. Obi, J. Chem. Phys. **95**, 720 (1991).

12. J.W. Rabalais, *Principles of Ultraviolet Photoelectron Spectroscopy* (Wiley, New York, 1977), p. 67.

13. D.K. Hsu, R.L. Monts and R.N. Zare, *Spectral Atlas of NO_2: 5530 to 6480 Å* (Academic, New York, 1978).

14. K.K. Lehmann and S.L. Coy, Ber. Bunsenges. Phys. Chem. **92**, 306 (1988).

15. G. Persch, E. Mehdizadeh, W. Demtröder, Th. Zimmermann, H. Köppel and L.S. Cederbaum, Ber. Bunsenges. Phys. Chem. **92**, 312 (1988).

16. D.W. Arnold (Chemistry Dept., University of California, Berkeley); E. Hutchisson, Phys. Rev. **36**, 410 (1930).

17. (a) G.M. Barrow, *Introduction to Molecular Spectroscopy* (McGraw-Hill, New York 1962), Chapter 6, gives a good, simple explanation of normal coordinates. (b) G.W. King, *Spectroscopy and Molecular Structure* (Holt, Rinehart and Winston, New York, 1964), Chapter 9 explains the transformation between Cartesian, internal and normal coordinate systems very well, as well as the FG matrix method. (c) I.N. Levine, *Molecular Spectroscopy* (Wiley, New York, 1975) Chapter 6, offers a more mathematical treatment. (d) J.I. Steinfeld, *Molecules and Radiation* (Harper and Row, New York, 1974), Chapter 8, briefly describes the theory and includes the FG matrix method for a linear triatomic molecule. (e) The complete process for NO_2 is worked out in J.F. Blanke and J. Overend, 'Normal coordinates and the vibrations of polyatomic molecules', Chapter 3 in *Vibrational spectra and structure, Vol. 7*, J.R. Durig, ed. (Elsevier, New York, 1978).

18. Y. Morino and M. Tanimoto, J. Mol. Spec. **115**, 442 (1986).

19. Y. Morino, M. Tanimoto, S. Saito, E. Hirota, R. Awata and T. Tanaka, J. Mol. Spec. **98**, 331 (1983).

20. K.M. Ervin, J. Ho and W.C. Lineberger, J. Phys. Chem. **92**, 5405 (1988).

21. G.D. Gillispie, A.U. Khan, A.C. Wahl, R.P. Hosteny and M. Krauss, J. Chem. Phys. **63**, 3425 (1975).

22. The work by C.J. Marsden and B.J. Smith, J. Mol. Structure (Theochem) **187**, 337 (1989) is appropriately titled "*Ab initio* force constants: a cautionary tale concerning nitrogen oxides."

23. Y. Xie, R.D. Davy, B.F. Yates, C.P. Blahous III, Y. Yamaguchi and H.F. Schaefer III, Chem. Phys. **135**, 179 (1989).

24. D.C. Moule, Chapter 4 in *Vibrational Spectra and Structure, Vol. 6*, J.R. Durig, ed. (Elsevier, New York, 1978) provides an excellent explanation of Duschinsky rotation.

25. W.J. Lafferty and R.L. Sams, J. Mol. Spec. **66**, 478 (1977).

26. Y. Morino and M. Tanimoto, Can. J. Phys. **62**, 1315 (1984).

27. A.J. Merer and K.-E.J. Hallin, Can. J. Phys. **56**, 838 (1978).

28. J.C.D. Brand, K.J. Cross, and A.R. Hoy, Can. J. Phys. **60**, 1081 (1982).

29. G. Hirsch and R.J. Buenker, Can. J. Chem. **63**, 1542 (1985).

30. C.F. Jackels and E.R. Davidson, J. Chem. Phys. **65**, 2941 (1976).

31. E. Haller, H. Köppel and L.S. Cederbaum, J. Mol. Spec. **111**, 377 (1985).

32. H. Köppel, L.S. Cederbaum and W. Domcke, Adv. Chem. Phys. **57**, 59 (1984).

33. A.E. Douglas, J. Chem. Phys. **45**, 1007 (1966).

34. J.C.D. Brand, J.L. Hardwick, R.J. Pirkle and C.J. Seliskar, Can. J. Phys. **51**, 2184 (1973).

35. F. Bolduan and H.J. Jodl, J. Mol. Spec. **118**, 213 (1984).

36. H.D. Bist, J.C.D. Brand, A.R. Hoy, V.T. Jones and R.J. Pirkle, J. Mol. Spec. **66**, 411 (1977).

37. J.L. Hardwick and J.C.D. Brand, Can. J. Phys. **54**, 80 (1976).

38. U. Kaldor, Chem. Phys. Lett. **170**, 17 (1990).

5.1. Examination of the $^2A_2'$ and $^2E''$ states of NO_3 by ultraviolet photoelectron spectroscopy of NO_3^- *

A. Weaver[a], D. W. Arnold[b], S. E. Bradforth[c], and D. M. Neumark[d]

Department of Chemistry, University of California, Berkeley, CA 94720

Abstract

The photoelectron spectrum of the NO_3^- anion has been obtained at 266 nm and at 213 nm. The 266 nm spectrum probes the $^2A_2'$ ground state of NO_3. The 213 nm spectrum represents the first observation of the $^2E''$ lowest-lying excited state of NO_3. The $^2A_2'$ band shows vibrational progressions in the ν_1 symmetric stretch and the ν_4 degenerate in-plane bend of NO_3. Our analysis of this band indicates that the NO_3 ground state has a D_{3h} equilibrium geometry and is vibronically coupled to the $^2E'$ second excited state via the ν_4 mode. We also obtain the electron affinity of NO_3, 3.937 ± 0.018 eV, and the heat of formation of NO_3 at 298 K, 0.777 ± 0.034 eV (17.9 ± 0.8 kcal/mol). The $^2E''$ state of NO_3 lies 0.868 ± 0.046 eV above the ground state. The $^2E''$ band

---

* Published in J. Chem. Phys. **94**, 1740 (1991).

[a]NSERC (Canada) Postgraduate Scholar.

[b]NSF Predoctoral Fellow.

[c]University Fellow, University of California.

[d]NSF Presidential Young Investigator and Alfred P. Sloan Fellow.

shows complex and extensive vibrational structure. Several possible assignments of this structure are discussed.

5.1.1. Introduction

Nitrogen trioxide, NO_3, is one of the most important free radicals in atmospheric chemical reactions. As one of the NO_x species, it is implicated in reaction cycles involving ozone and in hydrocarbon and halocarbon oxidation.[1] Although NO_3 is rapidly photolyzed during the day, it is essential to the cycle of reactions which form HNO_3 at night and is thus an important contributor to acid precipitation.[2] The significance of NO_3 in atmospheric chemistry has prompted numerous spectroscopic and kinetic experiments and theoretical studies, but questions remain concerning its ground state structure, excited electronic states, and photochemistry. In this paper, we use photoelectron spectroscopy of NO_3^- to address two of these issues: the geometry of the ground electronic state and characterization of the first excited electronic state of NO_3.

Walsh[3] predicted that NO_3 would be planar with a threefold symmetry axis (D_{3h} point group) in the ground electronic state and first two excited states ($^2A_2'$, $^2E''$ and $^2E'$, respectively). The proposed threefold symmetry of the ground state has been disputed. Rotationally resolved infrared spectra[4,5,6] of the ground state support Walsh's prediction of a $^2A_2'$ ground state with D_{3h} symmetry, but vibrationally resolved dispersed fluorescence spectra have been

interpreted as evidence of either D_{3h} [7] or Y-shaped planar[8] (C_{2v}) structure by different researchers. *Ab initio* predictions of the ground state equilibrium geometry are divided between D_{3h} [9,10,11,12,13] and C_{2v} [11,14,15,16,17,18] symmetry. Discrepancies between these predictions are partly due to the inherent difficulty of treating NO_3 properly, since it is an open-shell molecule with partial double bonds and low-lying excited electronic states.

Considerably less is known about the excited electronic states of NO_3. The only electronic transition that has been observed is the $^2E' \leftarrow {}^2A_2'$ band, with its origin at 662 nm. This band has been studied using absorption[19,20,21] and fluorescence excitation[7,8,22] spectroscopy, but the diffuse vibrational structure evident in these spectra has not been fully analyzed. Johnston and coworkers[23] see no rotational structure in this band even at 0.007 cm^{-1} resolution. The $^2E''$ state is predicted to lie between the ground state and the $^2E'$ state[3,11,16,24,25,26] but has not been observed because the $^2E'' \leftarrow {}^2A_2'$ transition is electric-dipole forbidden. The exact energy of the $^2E''$ state is important because some features of the ground-state spectrum have been attributed to perturbations by a low-lying electronic state, but *ab initio* predictions of its energy vary from 0.04 eV (300 cm^{-1})[16] to 1.61 eV (13,000 cm^{-1})[11] above the ground state.

We present here ultraviolet photoelectron spectra of the nitrate anion, NO_3^-, which provide new information about the ground state of NO_3 and represent the first direct observation of the $^2E''$ state. We observe the 'dark'

$^2E''$ state because negative ion photodetachment experiments can generally study all neutral electronic states formed by removing a single valence electron from the ion. The anion is expected to have a D_{3h} equilibrium geometry,[10,12,27,28] with the molecular orbital configuration $...(e'')^4(e')^4(a_2')^2$ in the $^1A_1'$ ground state.[3] The $^2A_2'$, $^2E''$, and $^2E'$ electronic states of the NO_3 radical, which have the configurations $...(e')^4(e'')^4(a_2')$, $...(e')^4(e'')^3(a_2')^2$, and $...(e')^3(e'')^4(a_2')^2$, respectively, are all accessible via one-electron photodetachment transitions from the ground state of NO_3^-. Our spectra show distinct bands corresponding to the $^2A_2'$ and $^2E''$ states of NO_3, which yield the electron affinity of NO_3 and the energy of the previously unobserved $^2E''$ excited state. With the laser currently in use, the $^2E'$ state is beyond the range of our photoelectron spectrometer.

The photoelectron spectra show vibrational progressions within each electronic band which provide new information about the frequencies and molecular geometry in the $^2A_2'$ and $^2E''$ states. In particular, these progressions indicate that vibronic coupling is important in both electronic states. Normally, the relative intensities of vibrational transitions within a single electronic band in a photoelectron spectrum depend only on the Franck-Condon overlap of neutral and anion wavefunctions for the relevant vibrational states.[29] The longest progressions generally occur in totally symmetric vibrational modes of the neutral. For NO_3 in D_{3h} symmetry, the symmetric stretch (ν_1) is the only such mode. Progressions in non-totally symmetric

modes may occur, but normally the only allowed transitions are those involving even changes in vibrational quantum number (even Δv transitions) between the anion and neutral. If the anion or neutral electronic state is degenerate, however, vibronic coupling due to the Jahn-Teller effect[30,31] can complicate the photoelectron spectrum. For example, odd Δv transitions can occur in non-totally symmetric vibrational modes. Such effects have been observed in photoelectron spectra of CH_3O^- [32,33] and $C_5H_5^-$,[34] and in photoelectron spectra of neutral molecules such as BF_3 [35,36,37] and CH_4.[38]

The $^2E''$ and $^2E'$ states of NO_3 are both degenerate, and the ν_3 antisymmetric stretch and ν_4 in-plane deformation can be Jahn-Teller active in each state. Our photoelectron spectra do provide evidence of vibronic coupling in the $^2E''$ state. However, we also observe what appear to be $\Delta v_4 = 1$ transitions in the ground state ν_4 progression. This is somewhat surprising, since the $^2A_2'$ state is non-degenerate and should not be affected by first-order Jahn-Teller coupling. This observation is discussed at length below, and is ultimately attributed to pseudo-Jahn-Teller coupling between the $^2A_2'$ and $^2E'$ states. This mechanism has previously been invoked by Haller et al.[36,37] to explain similar phenomena in the photoelectron spectrum of the isoelectronic molecule BF_3.

5.1.2. Experimental

The time-of-flight photoelectron spectrometer used in these experiments is shown in Figure 5.1 and briefly described here. (See Ref. 39 for a more detailed description.) Negative ions are generated by crossing the free jet expansion from a pulsed molecular beam valve (1) with a 1 keV electron beam (2). For the NO_3^- spectra presented here, we used a gas mixture made by bubbling 5% NF_3 in argon through HNO_3 (red fuming, 90%). We also made NO_3^- from a 1% N_2O_4/He mixture, and obtained very similar spectra. The principles of operation of the ion source have been discussed at length by Johnson and Lineberger.[40] Electron impact ionization of the argon carrier gas generates low energy secondary electrons, which efficiently produce F^- from NF_3 by dissociative attachment. The subsequent exothermic proton transfer reaction of F^- with HNO_3 forms NO_3^-. The ions are formed in the continuum flow region of a free jet expansion, so they are expected to cool internally as the expansion progresses. We have measured vibrational temperatures of 100-150 K for CH_2CN^- produced in this source, and a rotational temperature of about 75 K for SH^- in a similar source.[41]

A 200 - 400 V negative pulse applied at (3) extracts the negative ions into a time-of-flight mass spectrometer.[42] The ions are accelerated to 1 keV, and ion deflectors and lenses (4) are adjusted to ensure optimal ion levels at the detector (5). Ions separate into bunches according to mass as they travel along the 150 cm flight tube, and the ion of interest is selectively

Figure 5.1. Schematic diagram of time-of-flight photoelectron spectrometer.

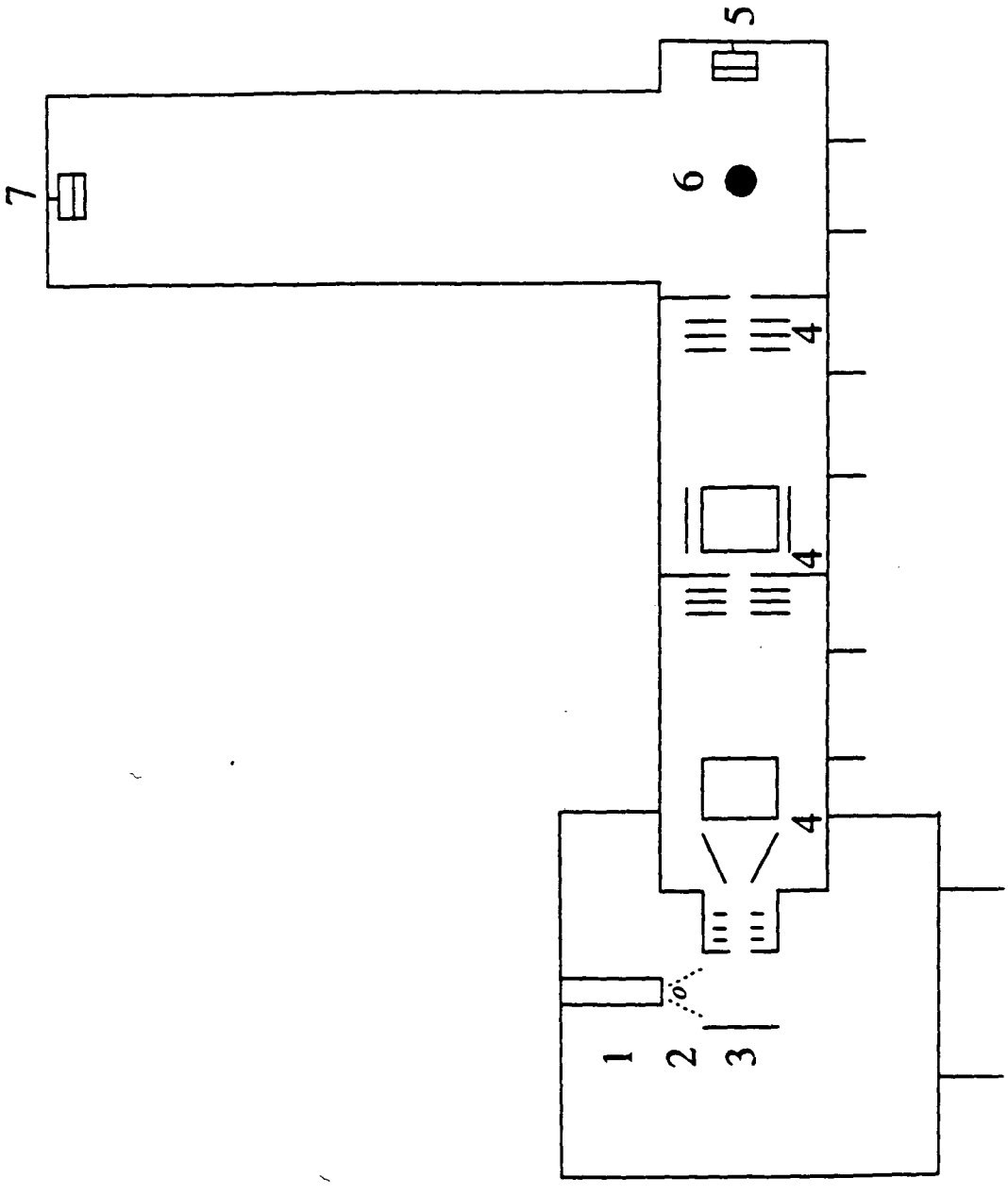
5
7
6
4
4
4
1
2
3

photodetached (6) by varying the delay between ion extraction and the firing of the photodetachment laser. The signal level of negative ions, plus fast neutrals resulting from photodetachment, is monitored with a 25 mm dual microchannel plate detector. The neutral signal alone can be measured at this detector by applying -1400 V to a grid in front of the detector.

Photoelectrons are detected at the end of a one meter flight tube by a 40 mm dual microchannel plate detector (7) and are energy-analyzed by time of flight. We detect 0.01% of the ejected photoelectrons; this fraction is determined by the solid angle subtended by the electron detector. The instrumental resolution is 0.008 eV (64 cm^{-1}) at 0.65 eV electron kinetic energy, and degrades as $E^{3/2}$ at higher energy. The resolution in the spectra presented here is somewhat worse due to space charge effects (see below), and is 0.018-0.025 eV for electron kinetic energies near 1 eV. Rotational peaks are not resolved in the NO_3^- photoelectron spectra.

Spectra of NO_3^- were taken using the fourth (266 nm, 4.66 eV) and fifth (213 nm, 5.83 eV) harmonics of a Nd:YAG laser. The laser light is plane-polarized, and the polarization at each wavelength can be rotated with a half-wave plate. Each spectrum shown here was averaged for about 500,000 laser shots, at 20 Hz repetition rate. The spectra were smoothed by convolution with Gaussian peaks of 6 meV fwhm. A background noise spectrum was subtracted from the 213 nm spectrum, to remove the photoelectron signal generated by stray laser photons which strike the metal

surfaces of the chamber.

5.1.3. Results

Photoelectron spectra of NO_3^- at 266 nm and 213 nm are shown in Figures 2 and 3, respectively. The spectra are plotted as intensity (number of photoelectrons) vs. electron kinetic energy (eKE). The electron energy is given by

$$eKE = h\nu - EA - T_0 - E_v^{(0)} + E_v^{(-)}. \qquad (5.1.1)$$

where hν is the photodetachment laser energy, EA the electron affinity of NO_3, T_o the term value for the particular NO_3 electronic state, and $E_v^{(0)}$ and $E_v^{(-)}$ the vibrational energy of the neutral and anion, respectively. (We neglect the rotational contribution to the internal energy.) Peaks at highest electron kinetic energy correspond to transitions to the lowest electronic and vibrational energy levels of NO_3.

The 266 nm spectrum shows a single band with well-resolved vibrational structure. The peak positions are listed in Table 5.1. The 213 nm spectrum shows this band at higher energy (hence poorly resolved), plus a band at lower electron energy with extensive vibrational structure. Peak positions of this second band are listed in Table 5.2. Each band represents a series of transitions to vibrational levels within one electronic state of NO_3. The band in the 266 nm spectrum is assigned to the $^2A_2'$ ground state of NO_3, and the band at lower electron energy in the 213 nm spectrum is assigned to the $^2E''$

Figure 5.2. Photoelectron spectrum of NO_3^- at 266 nm, showing the progression in the $^2A_2'$ state of NO_3. Laser polarization angle $\theta = 90°$.

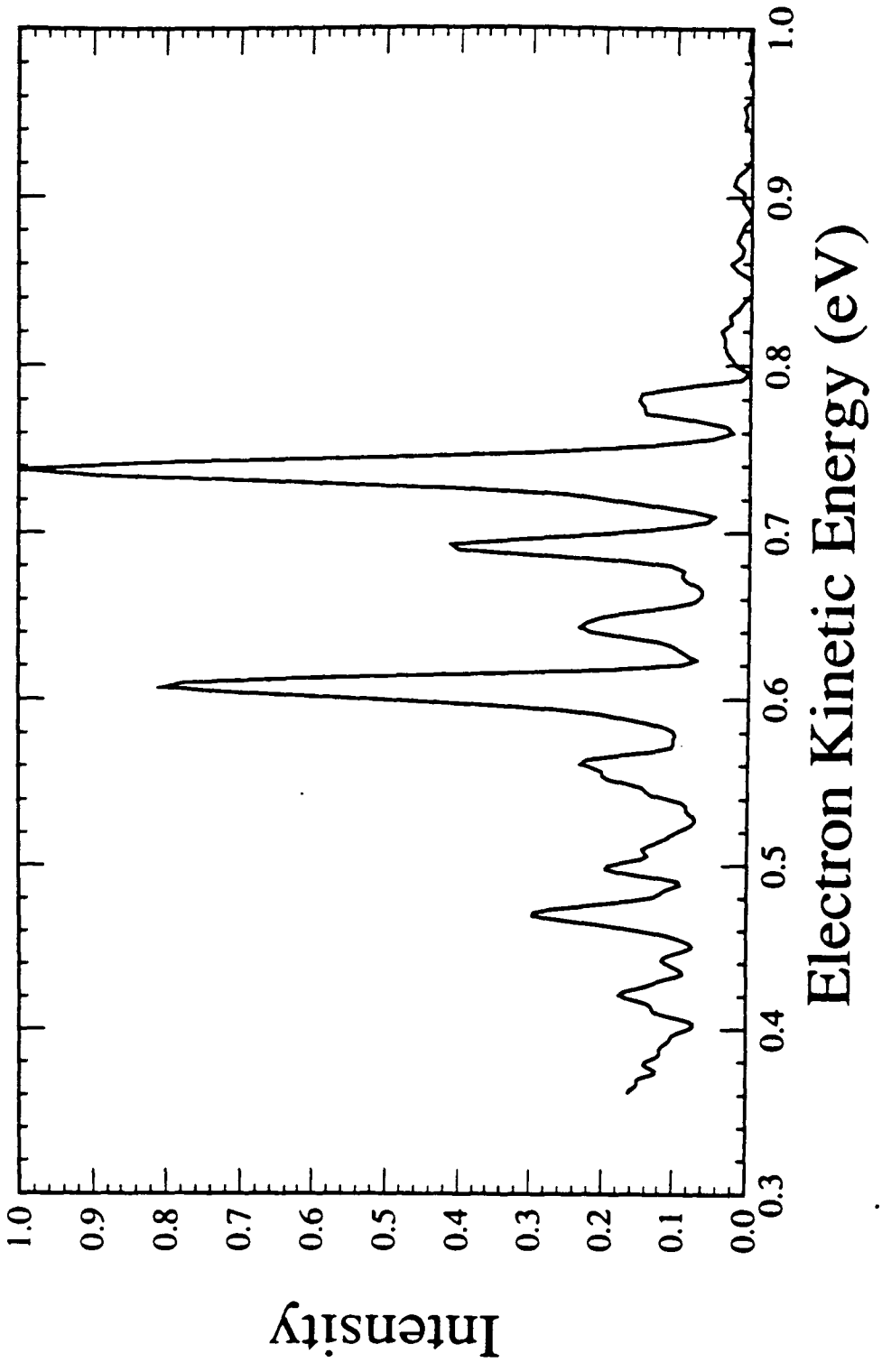
Intensity
1.0
0.9
0.8
0.7
0.6
0.5
0.4
0.3
0.2
0.1
0.0
0.3
0.4
0.5
0.6
0.7
0.8
0.9
1.0
Electron Kinetic Energy (eV)

Figure 5.3. Photoelectron spectrum of NO_3^- at 213 nm, showing progressions in the $^2A_2'$ and $^2E''$ states of NO_3. Laser polarization angle θ = 0°.

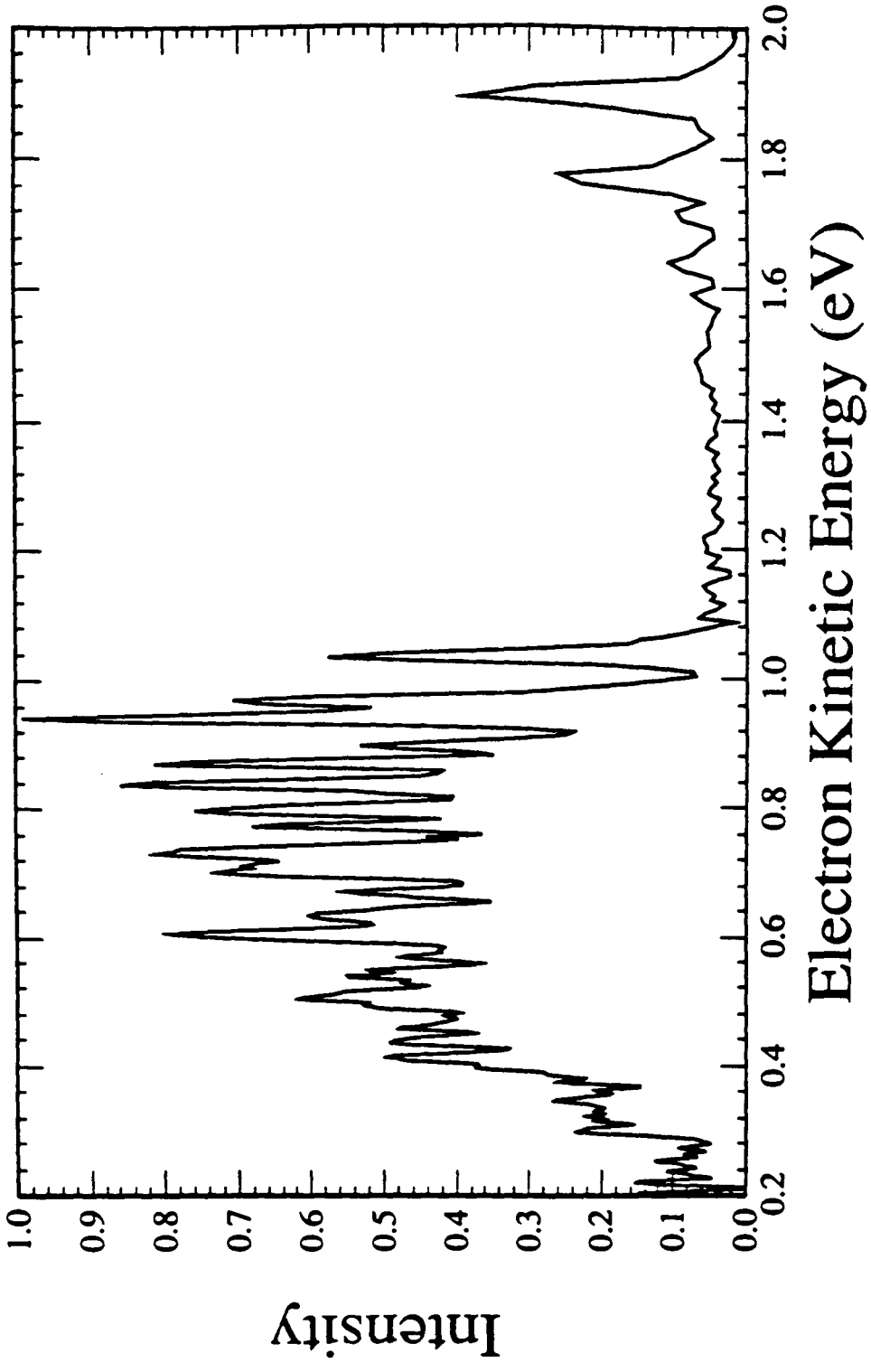
Intensity
1.0
0.9
0.8
0.7
0.6
0.5
0.4
0.3
0.2
0.1
0.0
0.2
0.4
0.6
0.8
1.0
1.2
1.4
1.6
1.8
2.0
Electron Kinetic Energy (eV)

Table 5.1: Peak positions, 266 nm spectrum

Position	
eV	cm^{-1}
0.820	-661
0.780	-339
0.738	0
0.693	363
0.644	758
0.607	1057
0.562	1420
0.511	1831
0.498	1936
0.470	2162
0.442	2387
0.421	2557

Table 5.2: Peak positions and intensities of $^2E''$ band, 213 nm spectrum

Position (experimental)		v_1 [a]	v_4	Position[a] (calc.)	Intensity[b]
eV	cm^{-1}				
1.035	0	0	0	1.035	0.57
0.970	524	0	1	0.968	0.70
0.942	750	1	0	0.935	1.00
0.900	1089	0	2	0.901	0.53
0.871	1323	1	1	0.868	0.83
0.838	1589	2	0	0.836	0.87
		0	3	0.834	
0.798	1912	1	2	0.801	0.77
0.774	2105	2	1	0.769	0.70
0.731	2452	3	0	0.736	0.82
		1	3	0.734	
0.703	2678	2	2	0.701	0.73
0.672	2928	3	1	0.669	0.55
0.635	3226	4	0	0.636	0.62
		2	3	0.634	
0.606	3460	3	2	0.602	0.80
0.569	3759	4	1	0.569	0.50

[a] These tentative assignments of v_1 and v_4 are made using the best fit frequencies of 804 and 541 cm^{-1}, respectively. The calculated positions are based on these assignments and harmonic frequencies.

[b] Since we assume uniform peak widths (0.022 eV), the intensity of each peak is proportional to the Franck-Condon factor (area under the peak).

0.540	3992	{	5	0	0.537	} 0.55
		{	3	3	0.535	}
0.505	4275		4	2	0.502	0.65
0.458	4654		5	1	0.470	0.48
0.437	4823	{	6	0	0.437	} 0.49
		{	4	3	0.435	}
0.414	5009		5	2	0.402	0.50

first excited electronic state. If we assign the peaks at 0.738 eV in the 266 nm spectrum and 1.035 eV in the 213 nm spectrum to the origins of the $^2A_2'$ and $^2E''$ progressions, respectively, we calculate T_o for the $^2E''$ state to be 0.868 ± 0.046 eV (7000 ± 370 cm^{-1}).

Our results indicate a strikingly low partial photodetachment cross section into the $^2A_2'$ state of NO_3 at both 266 and 213 nm. The integrated intensity of the $^2A_2'$ state progression in the 213 nm spectrum is ten times less than that of the $^2E''$ state progression. This effect is independent of laser polarization angle (see below). In addition, our photoelectron signal levels were exceptionally low at 266 nm, where only the $^2A_2'$ state is accessible, and we photodetached only 2% of the ions (estimated by comparing the fast neutral signal to the ion signal) with a laser fluence of 120 mJ/cm^2. At 213 nm, where detachment to the $^2E''$ state dominates, we photodetached nearly 50% of the ions at a lower laser fluence of 60 mJ/cm^2 and the same ion level. This higher detachment rate is more typical of our experience with other ions.

The low cross-section for the $^2A_2'$ state required high ion densities to ensure adequate electron signal at 266 nm, and we obtained the 213 nm spectra at the same ion density. The peaks in our spectra were slightly broadened and shifted to higher energy by the resulting space charge effects, which arise from Coulomb repulsion between photoelectrons and the negative ion cloud. To estimate the magnitude of this shift, we took spectra of Br^- at 266 nm at comparable ion levels, since its mass and electron affinity (3.365

eV[43]) are relatively close to those of NO_3^-. We estimate that the peak at 0.738 eV in the NO_3^- 266 nm spectrum shifted by +0.015 eV from its true position. This shift is approximately constant across the photoelectron spectrum, so the electron affinity is the only parameter affected. We obtain a value of 3.937 ± 0.018 eV for the electron affinity of NO_3, in good agreement with the most recent previous estimate of 3.91 ± 0.24 eV.[44]

The heat of formation of NO_3 at 298 K can be estimated from our electron affinity and the measured heat of formation of NO_3^-:

$$\Delta_f H^o(NO_3)_{298K} = \Delta_f H^o(NO_3^-)_{298K} + EA(NO_3) + \frac{5}{2} RT + \int_0^{298} \{C_p(NO_3) - C_p(NO_3^-)\} \quad (5.1.2)$$

where the 5/2 RT (=1.481 kcal/mol) term corrects for the heat capacity of the electron,[45,46] and the heat capacities of NO_3 and NO_3^- are estimated from the vibrational frequencies listed below (Section 5.1.4).[47] We have also used those NO_3^- vibrational frequencies to calculate $\Delta_f H°(NO_3^-)_{298\ K}$ from the previously reported value of $\Delta_f H°(NO_3^-)_{391\ K}$ = -3.269 ± 0.023 eV (-75.39 ± 0.54 kcal/mol).[44] We obtain $\Delta_f H°(NO_3)_{298\ K}$ = 0.777 ± 0.034 eV (17.91 ± 0.79 kcal/mol). This does not agree with the most recent measurement of $\Delta_f H°(NO_3)_{298\ K}$ = 0.667 ± 0.033 eV (15.39 ± 0.75 kcal/mol),[48] but does agree with the previous value of 0.737 ± 0.217 eV (17.0 ± 5.00 kcal/mol).[49]

Photoelectron spectra at 266 nm and 213 nm were taken at two laser polarization directions, θ = 0° and 90°, where θ is the angle between the

electric field vector of the laser light and the direction of electron collection. The angular distribution of the ejected photoelectrons is described by[50]

$$\frac{d\sigma}{d\omega} = \frac{\sigma_{tot}}{4\pi}\left\{1 + \beta(E)\left(\frac{3}{2}\cos^2\theta - \frac{1}{2}\right)\right\} \qquad (5.1.3)$$

where β(E) is the asymmetry parameter for the electronic transition in question, E is the energy above the photodetachment threshold, and θ is the polarization angle. If relative peak intensities across a progression change significantly with θ, this may indicate the presence of overlapping electronic states or vibronic coupling effects, since β may be different for each electronic transition. The 213 nm spectra of NO_3^- are essentially the same at θ = 0° and 90°, indicating that β is approximately zero for the $^2A_2'$ and $^2E''$ transitions at this wavelength. At 266 nm, the peaks at 0.693 and 0.607 eV (363 and 1057 cm^{-1} relative to the origin at 0.738 eV) change intensity relative to the peak at 0.738 eV; at θ = 90°, they are 50% and 29% more intense, respectively. The 50% change at 363 cm^{-1} is unusually large and may be due to vibronic coupling, which mixes the ground state with an excited electronic state; this is discussed in detail in Section 5.1.5.

5.1.4. Analysis and Discussion

Background

The analysis of our NO_3^- photoelectron spectra is facilitated by the results of previous experiments on the anion and neutral. Although NO_3^- has

not been studied in the gas phase, X-ray and neutron diffraction experiments on crystalline sodium nitrate indicate that the ion has D_{3h} equilibrium geometry with an average NO bond length of 1.23 Å.[28] Vibrational frequencies of NO_3^- have been measured by infrared[51,52] and Raman[52,53] spectroscopy of condensed-phase nitrates. Average values are: ν_1 = 1054 cm^{-1} (symmetric stretch, a_1'), ν_2 = 834 cm^{-1} (out-of-plane bend, a_2''), ν_3 = 1379 cm^{-1} (antisymmetric stretch, e'), and ν_4 = 723 cm^{-1} (in-plane bend, e'). The 1054 cm^{-1} mode was not observed in the infrared spectra, nor the 834 cm^{-1} mode in Raman spectra, in accordance with the selection rules for a D_{3h} molecule. Both modes could be observed, in principle, if NO_3^- had C_{2v} or C_{3v} symmetry in the ground state.

Vibrational frequencies in the ground state of gas-phase NO_3 have been obtained from two types of experiments. In 1983, Ishiwata[7] and Nelson[8] independently reported measurements of dispersed fluorescence from excitation of the 0-0 transition in the $^2E' \leftarrow {}^2A_2'$ band, but drew conflicting conclusions from their data. Nelson assumed the NO_3 ground state to have C_{2v} symmetry. Ishiwata and coworkers interpreted the vibrational structure in the dispersed fluorescence spectrum in terms of a D_{3h} ground state, and obtained values for ν_1, ν_3, and ν_4 of 1060 cm^{-1}, 1480 cm^{-1}, and 380 cm^{-1}, respectively, for the ground state. This assignment meant that they were observing odd Δv transitions in the non-totally symmetric ν_3 and ν_4 modes, which could be explained by the Jahn-Teller coupling expected in the $^2E'$ state.

Rotationally resolved infrared absorption measurements on gas-phase NO_3 [4,5,6] gave a more accurate value of ν_3 (1492.393 cm^{-1}) and measured the ν_2 out-of-plane bending frequency (762.327 cm^{-1})[5] for the first time. The high resolution spectra of the ν_2 and ν_3 bands exhibit rotational structure characteristic of a planar symmetric top with a threefold symmetry axis, consistent with a D_{3h} equilibrium geometry for the NO_3 ground state. No infrared absorption was observed in the vicinity of the totally symmetric ν_1 mode (1060 cm^{-1}), again consistent with D_{3h} symmetry. The pattern of rotational lines shows that the 762 cm^{-1} band is a parallel transition ($\Delta K = 0$) and the 1492 cm^{-1} band a perpendicular transition ($\Delta K = \pm 1$). The out-of-plane bend is the only infrared-active mode which should appear as a parallel band, so the 762 cm^{-1} band is confirmed to be the ν_2 mode. The rotational analysis yields an N-O bond length of 1.240 Å.

Although the rotationally resolved spectra strongly suggest a D_{3h} ground-state geometry, several *ab initio* calculations[11,12,14,15,16,17,18] predict a Y-shaped planar C_{2v} configuration for the ground state. In addition, some of the dispersed fluorescence[8] and electron resonance[54] experimental results have been interpreted as evidence of C_{2v} symmetry. Similar discrepancies have been reported for CO_3^-,[55] which is isoelectronic with NO_3. The high resolution spectra of NO_3 rule out a rigid C_{2v} structure, because that would result in rotational structure characteristic of an asymmetric top. However, it is possible that the NO_3 ground state structure is non-rigid. This could occur, for

example, if the potential energy surface had three equivalent shallow minima, each corresponding to a 'Y-shaped' C_{2v} equilibrium structure. Ishiwata et al.[4,6] have argued against a triple-minimum potential, since that should lead to additional bands which were not observed in their spectra. We will consider this issue below.

One complication in the analysis of the high resolution spectra is the role of the excited $^2E''$ state, which had not previously been observed because the transition from the $^2A_2'$ ground state is electric-dipole forbidden. Ishiwata et al.[4] and Friedl and Sander[5] suggested that a very low-lying excited electronic state (less than 2000 cm^{-1} above the ground state) might account for anomalous features observed in the high resolution spectra. For example, Friedl and Sander observed an additional Q branch, which they could not assign, near the Q branch of the ν_2 band. Several *ab initio* calculations[11,16,24,25] also predict the existence of a $^2E''$ state close to the ground state. Our spectra clearly show that the $^2E''$ state lies much further above the ground state (7000 cm^{-1}).

<u>NO_3 ground state: features of the spectrum</u>

Our understanding of the NO_3 ground state is derived from the vibrational structure observed in the 266 nm photoelectron spectrum. The peak positions and intensities in this spectrum provide information about vibrational frequencies and molecular geometry in the ground state. In the Franck-Condon approximation, the transition intensity between the vibrational

levels v'' in the anion and v' in the neutral is given by[29]

$$I \propto |\tau_e|^2 |\langle \psi_{v'} | \psi_{v''} \rangle|^2 . \qquad (5.1.4)$$

Here τ_e is the electronic transition dipole moment between the anion electronic wavefunction Φ_{e^-} and neutral + photoelectron wavefunction $\Phi_{e'}$,

$$\tau_e = \langle \Phi_{e'} | \mu_e | \Phi_{e''} \rangle \qquad (5.1.5)$$

which is assumed to be constant for vibrational transitions within a single electronic band. The Franck-Condon factor, $|\langle \psi_v' | \psi_v'' \rangle|^2$, depends on the spatial overlap of ion and neutral vibrational wavefunctions ψ_{v^-} and $\psi_{v'}$. This overlap will be identically zero unless the direct product $\Gamma_{v'} \otimes \Gamma_{v^-}$ contains the totally symmetric representation in the molecular point group. Transitions to all levels of totally symmetric vibrations in NO_3 are allowed from the totally symmetric ground vibrational state of NO_3^-, as are transitions to even quanta of the non-totally symmetric vibrations. The frequency of a particular non-totally symmetric mode, ν_i, must change substantially between the ion and neutral if transitions other than those with $v_i' = v_i''$ are to have significant intensity.[56]

Within the Franck-Condon approximation (Eq. 5.1.5), the appearance of the NO_3^- photoelectron spectra can be predicted from relevant changes in geometry and frequency between the anion and neutral. In the ground state,

the small change in N-O bond length upon photodetachment should result in a short progression in the ν_1 symmetric stretch of NO_3. No progression in the out-of-plane bend is expected, because the ion and neutral are planar with similar ν_2 frequencies. Similar reasoning applies to the ν_3 antisymmetric stretch. However, the ν_4 frequency decreases considerably upon photodetachment, from 723 cm^{-1} to 380 cm^{-1} (assuming the assignment by Ishiwata et al.[7] to be correct), so that transitions with even Δv_4 might be observed.

The experimental photoelectron spectrum in Figure 5.2 fulfills some of these predictions. We initially assign the intense peak at 0.738 eV to the origin of the $^2A_2'$ band. The most intense progression appears as peaks at 0.738, 0.607 and 0.470 eV, and the average spacing of 0.134 eV (1080 cm^{-1}) corresponds to the ν_1 frequency. A second progression has peaks at 0.738, 0.693, and 0.644 eV, and the peaks at 0.607, 0.562, and 0.511 eV appear to be the associated combination band with $v_1' = 1$. The peak spacings in the second progression, of 0.045 and 0.094 eV (363 and 758 cm^{-1}), suggest a progression in the ν_4 in-plane bend. The ν_4 progression is unusual, since transitions only to even v_4 levels of NO_3 should be allowed from the $v_4'' = 0$ level of NO_3^-. The observed peak spacing should then be 720 cm^{-1}, assuming ν_4=360 cm^{-1}.[57] The apparent occurrence of odd Δv_4 transitions requires explanation, and the analysis described below focuses on this phenomenon.

Finally, we assign the small peak at 0.780 eV to a 'hot band' originating

from an excited vibrational level of the ion. Its energy is correct for the $NO_3^-(\upsilon_4''=1)\rightarrow NO_3(\upsilon_4'=1)$ transition. The intensity of this hot band implies a vibrational temperature of 435 K for NO_3^-, which is somewhat higher than that expected from our experience with other ions. We do not observe intense hot bands in the ν_1 progression, because at 435 K the population of the $\upsilon_1'' = 1$ level is about six times smaller than that of the $\upsilon_4'' = 1$ level.

<u>NO_3 ground state: detailed analysis</u>

This section describes our attempts to simulate the experimental ground-state progression within the Franck-Condon approximation, neglecting the possible effects of vibronic coupling. We consider only the ν_1 and ν_4 modes, which are assumed to be separable. The ν_1 mode is modelled as a one-dimensional harmonic oscillator in the anion and neutral, and various two-dimensional potential energy functions are used for the neutral ν_4 mode.

Eigenfunctions and eigenvalues of each potential energy function are calculated numerically. We use a variational method for the one-dimensional ν_1 calculations,[58] and a discrete variable representation (DVR)[59] procedure for the two-dimensional ν_4 calculations. The transition intensity between the anion level $\upsilon_1''\upsilon_2''...$ and neutral level $\upsilon_1'\upsilon_2'...$ is proportional to the product of Franck-Condon factors:

$$I \propto |\langle \psi_{\upsilon_1'}(Q_1) | \psi_{\upsilon_1''}(Q_1)\rangle|^2 \cdot |\langle \psi_{\upsilon_2'}(Q_2) | \psi_{\upsilon_2''}(Q_2)\rangle|^2 ... \qquad (5.1.6)$$

In this calculation, we neglect mixing of the neutral normal coordinates relative to those of the anion (Duschinsky rotation), and assume the same normal coordinates for both. Ervin et al.[60] showed that this was a reasonable approximation in analyzing the photoelectron spectrum of NO_2^-.

The simulation of the ν_1 progression is relatively simple. We assume ν_1 = 1057 cm^{-1} in the neutral and 1054 cm^{-1} in the anion. The anion and neutral symmetric stretch potentials are assumed to be displaced by an amount $\Delta Q_1 = 6.9\ \Delta r_{NO}$ (ΔQ_1 in $amu^{1/2}$·Å, Δr_{NO} in Å); this ratio was determined from the reduced mass for the ν_1 mode and the appropriate symmetry coordinate.[61] The displacement ΔQ_1 is varied, and Franck-Condon factors calculated, until the intensity distribution of the simulated ν_1 progression agrees with the experimental result. The optimal displacement, $|\Delta Q_1| = 0.21 \pm 0.05$ $amu^{1/2}$·Å, corresponds to an NO_3^- bond length of 1.21 ± 0.01 Å, assuming that r_{NO} = 1.24 Å in NO_3 and that the N-O bond in the ion is shorter than that in the neutral (as determined in previous experiments, see above). This NO_3^- bond length is close to the 1.23 Å average measured for crystalline $NaNO_3$ (variation 1.21-1.24 Å).[28] The direction of displacement and the specific form of the Q_1 normal coordinate affect only the calculated N-O bond length, and not the calculated Franck-Condon factors. The same Franck-Condon factors for ν_1 are used in all our simulations.

The ν_4 progression is more difficult to reproduce in simulations. The simplest explanation for the 360 cm^{-1} peak spacing in the experimental

spectrum is that the ν_4 fundamental frequency is 180 cm^{-1}, and that we observe transitions only to even overtones of the ν_4 mode, in accordance with our selection rules. With this assignment, the ν_4 transitions observed in the dispersed fluorescence spectra[7,8] would also correspond to even v_4 levels of the NO_3 ground state, so that those results could be explained without invoking vibronic coupling in the $^2E'$ state.

We simulated the NO_3^- photoelectron spectrum with ν_4 = 180 cm^{-1} in the NO_3 ground state. The degenerate ν_4 mode is assumed to be a two-dimensional isotropic harmonic oscillator in both the anion and neutral. Since this is a non-totally symmetric mode, the normal coordinate displacement $\Delta Q_4 = 0$. Transitions other than $\Delta v_4 = 0$ would have zero intensity if not for the large frequency change between the anion and neutral (723 cm^{-1} to 180 cm^{-1}). The resulting simulated spectrum is shown in Fig. 5.4. We assume Gaussian peak envelopes of fwhm 0.022 eV, determined by space charge rather than instrumental resolution. The simulation reproduces the peak positions below 0.738 eV reasonably well, but the simulated $v_4' = 4$ peak at 0.644 eV is too small. A more serious problem is that the simulation fails to reproduce the position of the hot band at 0.780 eV. Instead, hot bands appear at 0.760 eV ($v_4' = 3 \leftarrow v_4'' = 1$) and 0.805 eV ($v_4' = 1 \leftarrow v_4'' = 1$) in the simulated spectrum. The choice of a 180 cm^{-1} isotropic oscillator for the ν_4 potential is thus unsatisfactory.

In order to gain more flexibility in simulating both the intensity

Figure 5.4. Simulated photoelectron spectrum of NO_3^- (266 nm) assuming an isotropic oscillator potential for the ν_4 coordinate of NO_3. $\nu_1 = 1057\ cm^{-1}$, $\nu_1^- = 1054\ cm^{-1}$, $\nu_4 = 180\ cm^{-1}$, $\nu_4^- = 723\ cm^{-1}$, T = 435 K.

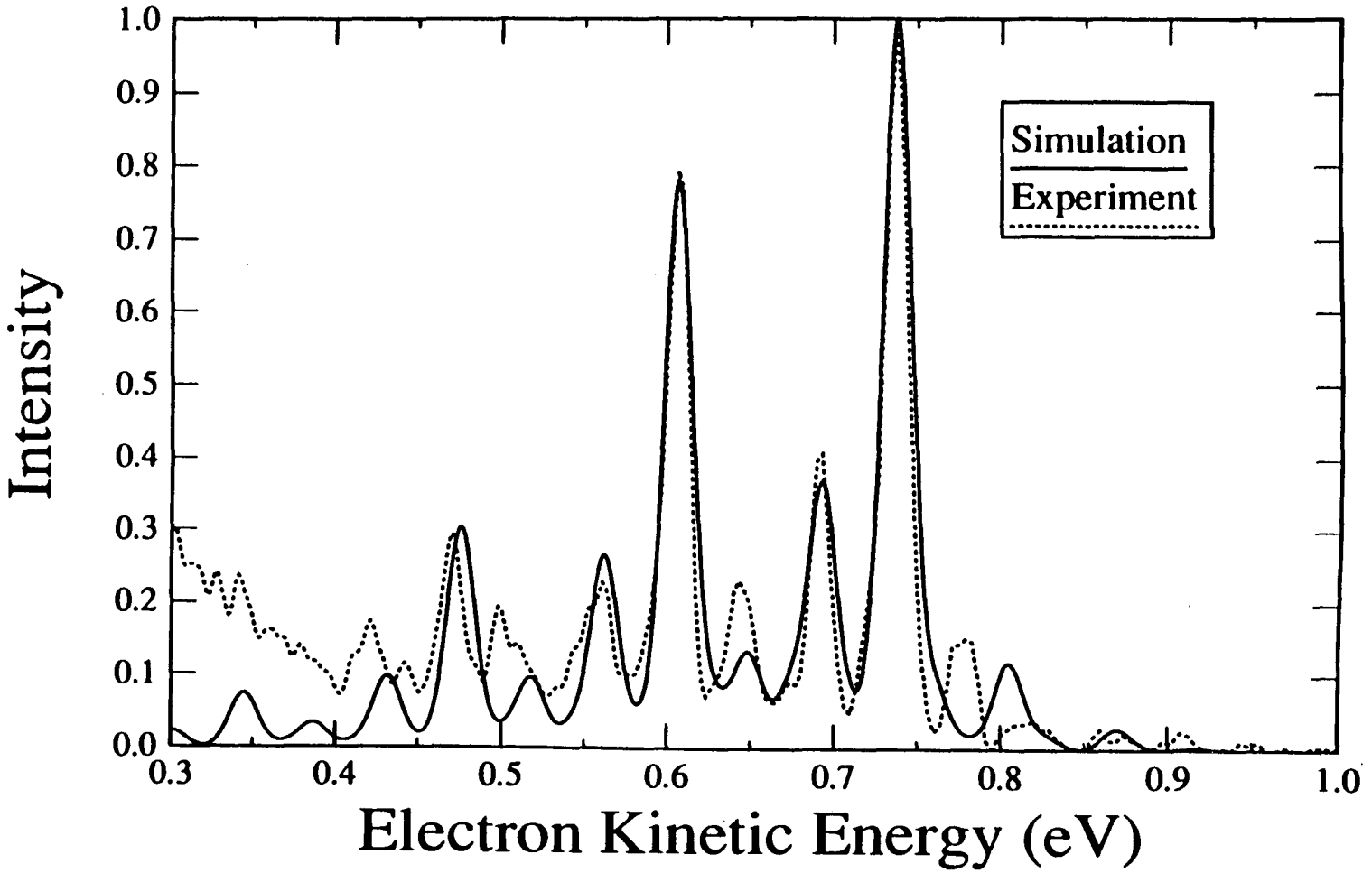
Intensity
1.0
0.9
0.8
0.7
0.6
0.5
0.4
0.3
0.2
0.1
0.0
0.3
0.4
0.5
0.6
0.7
0.8
0.9
1.0
Electron Kinetic Energy (eV)
Simulation
Experiment

distribution in this progression and the hot band position, we next consider a perturbed harmonic oscillator potential for the NO_3 ν_4 coordinate, with a barrier at the D_{3h} configuration. We use potentials of the form

$$V = \frac{1}{2}kr^2 - ar \tag{5.1.7}$$

where r is the radial polar coordinate

$$r = \sqrt{Q_{4a}^2 + Q_{4b}^2} \tag{5.1.8}$$

and Q_{4a} and Q_{4b} are the degenerate components of the normal coordinate for the ν_4 mode.[62] This surface has a circular trough surrounding a barrier of height $a^2/2k$.

The energy levels of this perturbed potential differ significantly from those of the isotropic oscillator. Fig. 5.5 shows the energy levels and associated symmetry labels for (a) a two-dimensional isotropic harmonic oscillator and (b, c) perturbed oscillators. The energy levels in (a) show the (n+1)-fold degeneracy expected for the nth level of the two-dimensional isotropic oscillator. The corresponding vibrational wavefunctions are classified as a_1', a_2'', or e' according to their properties under the symmetry operations of the D_{3h} point group. The only transitions with non-zero Franck-Condon factors are those between levels of the same symmetry: for example, from the a_1' $v_4'' = 0$

Figure 5.5. Vibrational energy levels for the degenerate ν_4 mode, assuming (a) an isotropic oscillator, ν_4 = 180 cm^{-1}, (b) a cylindrically symmetric potential (Eq. 5.1.7; a = 0.065 eV/Å, k = 0.212 eV/Å^2), (c) a triple-minimum potential (Eq. 5.1.9; a = 0.340 eV/Å, k = 0.531 eV/Å^2). The isotropic oscillator energy level with v = n is (n+1)-fold degenerate; in (b) and (c), the perturbations partially remove this degeneracy.

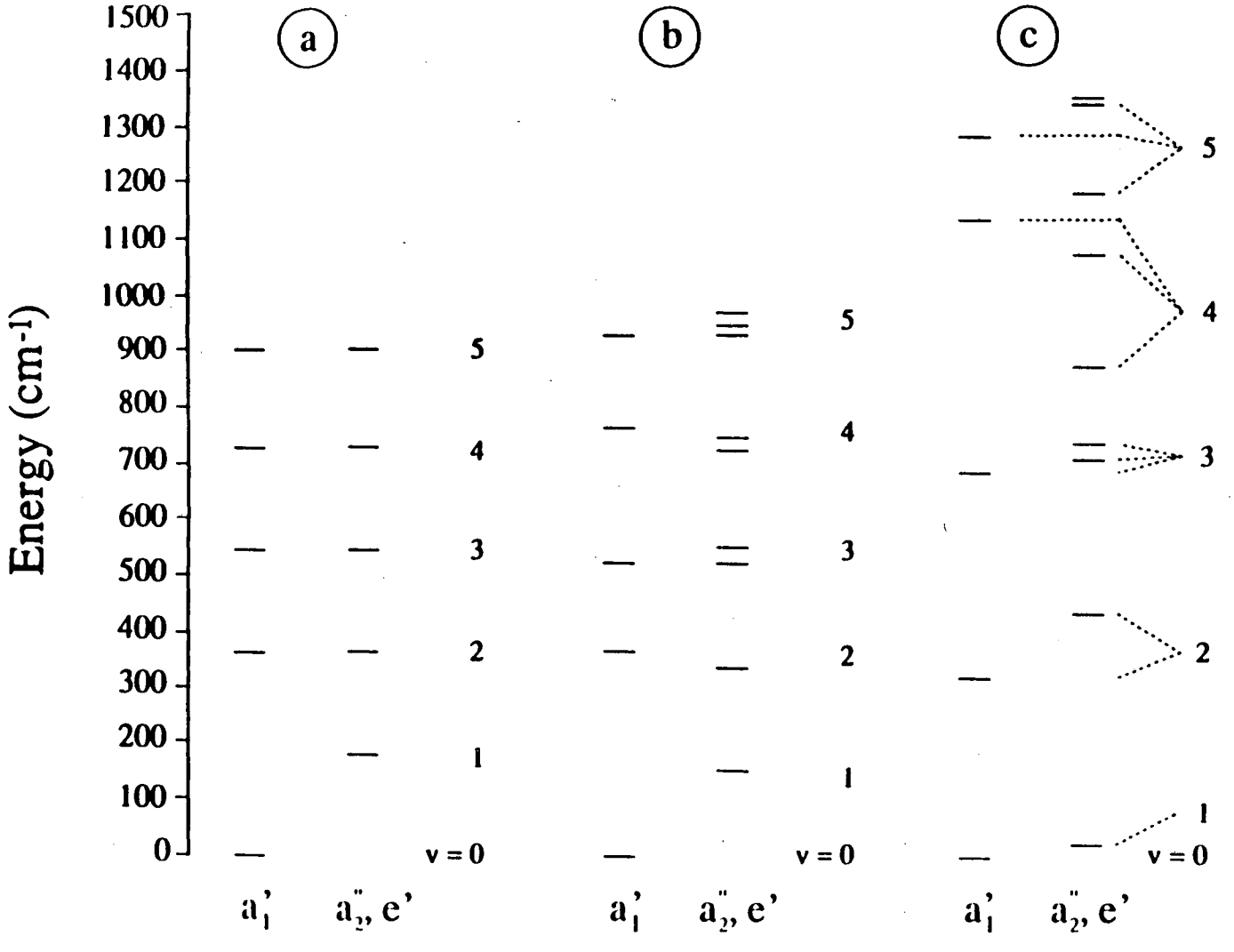
Energy (cm-1)
1500
1400
1300
1200
1100
1000
900
800
700
600
500
400
300
200
100
0
a
b
c
5
4
3
2
1
v = 0
a1'
a2'', e'

level of the ion to a_1' levels of the neutral, or from the e' $v_4'' = 1$ level of NO_3^- to e' levels of NO_3. This restriction is equivalent to the even Δv selection rule discussed above.[63] The eigenfunctions of Eq. 5.1.7 can be classified with the same symmetry labels as the two-dimensional harmonic oscillator eigenfunctions, and the same selection rules apply. However, the perturbation due to the central barrier splits the degeneracy of levels with different symmetries, and an irregular energy level pattern results.

In our simulations assuming a potential of the form of Eq. 5.1.7, we vary both k and a (related to the unperturbed oscillator frequency and central barrier height) until the simulated peak positions and intensities agree best with the experimental spectra. In these calculations, we make the assumptions about separable modes and normal coordinates discussed above, and use the same frequencies and harmonic potential energy functions as above for ν_1 and ν_4 in NO_3^- and for ν_1 in NO_3. Assuming the peak at 0.738 eV to be the origin, the best result is obtained for a barrier of 80 cm^{-1} (a = 0.065 eV/Å), with k = 0.212 eV/Å^2. The energy levels for this potential are shown in Fig. 5.5(b). The simulated spectrum is similar to that shown in Fig. 5.4 for the isotropic oscillator. The slightly uneven spacing of the experimental ν_4 progression is reproduced using this perturbed oscillator potential, but the simulated peak intensities and hot band positions are still not satisfactory.

Our third set of simulations assumes a triple-minimum potential energy surface for the NO_3 ν_4 coordinate, encouraged by theoretical predictions that

a Y-shaped C_{2v} equilibrium geometry for NO_3 should be slightly more stable than the symmetric D_{3h} geometry.[17] We use a model potential of the form[c]

$$V = \frac{1}{2}kr^2 + ar(1 + \cos 3\theta) \tag{5.1.9}$$

where r and θ are polar coordinates, r as in Eq. 5.1.8 and

$$\theta = \tan^{-1}\frac{Q_{4a}}{Q_{4b}} \tag{5.1.10}$$

This potential energy surface has three equivalent minima at Y-shaped C_{2v} configurations, and conversion between the minima proceeds along the minimum-energy path through the D_{3h} configuration. The barrier height at the D_{3h} configuration is $a^2/2k$.

The simulations using the triple-minimum surface for ν_4 follow the procedure described above for the first perturbed oscillator. With the origin at 0.738 eV, the best result is obtained for a barrier of 210 cm^{-1}, with k = 0.332 eV/Å^2 and a = 0.134 eV/Å. The simulated spectrum is shown in Figure 5.6. Although agreement with experiment is satisfactory for the peaks below 0.738 eV, the position of the hot band at 0.780 eV is incorrect.

Our problems with reproducing the intensity and position of the hot band at 0.780 eV suggest that it might instead be the origin of the $^2A_2'$ state band. This requires a higher barrier at the D_{3h} geometry, so that the 0-0 transition is no longer the most intense peak and the ν_4 progression is more

---

[c] This corrects the original paper, which read V=½kr^2 + ar cos 3θ.

Figure 5.6. Simulated photoelectron spectrum of NO_3^- (266 nm), assuming a triple-minimum potential for the ν_4 coordinate of NO_3, with a barrier of 210 cm^{-1} (a = 0.134 eV/Å, k = 0.332 eV/Å^2), origin at 0.738 eV, T = 435 K.

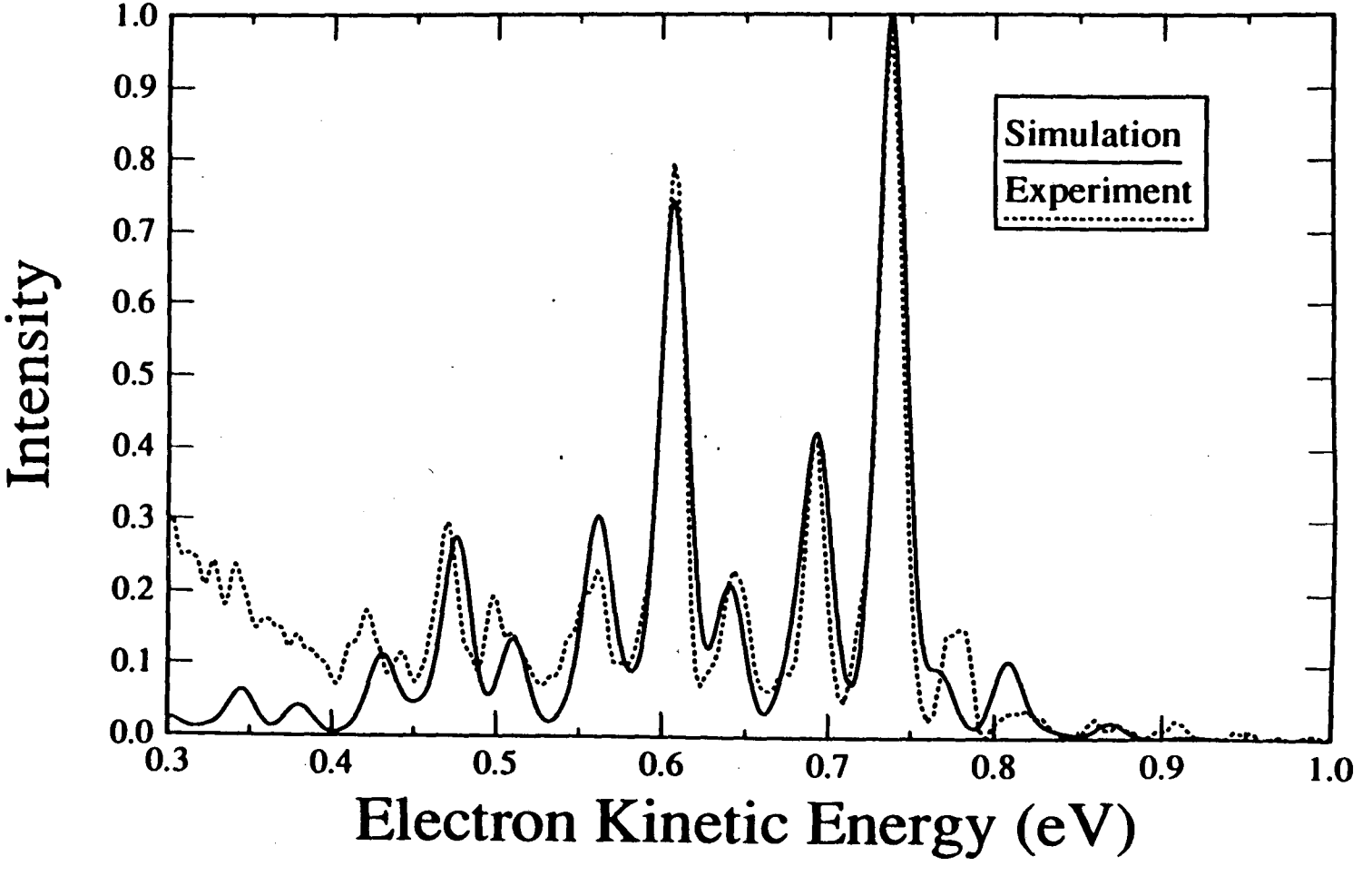
Intensity
1.0
0.9
0.8
0.7
0.6
0.5
0.4
0.3
0.2
0.1
0.0
0.3
0.4
0.5
0.6
0.7
0.8
0.9
1.0
Simulation
Experiment
Electron Kinetic Energy (eV)

extended. In this case, we assume *no* vibrational excitation in NO_3^-. The best result is obtained using a triple-minimum potential with a barrier of 870 cm^{-1} (k = 0.531 eV/Å^2 and a = 0.340 eV/Å in Eq. 5.1.9) and is shown in Figure 5.7. This simulation reproduces the positions of the major peaks in the experimental photoelectron spectrum, but the experimental intensity distribution is not reproduced as accurately as in other simulations.

Although the simulation in Figure 5.7 is the only one which reproduces the experimental peak positions including the peak at 0.780 eV, it implies a triple-minimum potential for the ν_4 coordinate, with a barrier at the D_{3h} geometry that is considerably higher than the ν_4 zero-point energy. Such a potential is inconsistent with the high resolution infrared spectra of NO_3. Figure 5.5(c) shows the first few energy levels of the triple-minimum potential used for the simulation of Figure 5.7. The v_4 = 1 e' level lies only 22 cm^{-1} above the v_4 = 0 level, and will be substantially populated at room temperature. As discussed by Ishiwata,[4] additional 'hot bands' originating from this level should thus occur in the infrared spectrum of the ν_3 band, due to vibration-rotation transitions between the (v_3" = 0, v_4" = 1) and (v_3' = 1, v_4' = 1) levels. These hot band transitions should be quite distinct from those transitions originating from the (ν_3" = ν_4" = 0) ground state. In the ground vibrational state, only K" = 3n rotational levels have nonzero statistical weight, whereas only K" = 3n ± 1 levels have nonzero statistical weight for the (v_3 = 0, v_4 = 1) vibrational level. Ishiwata et al.[4,6] observe only transitions with K" = 3n in the ν_3 band, ruling

Figure 5.7. Simulated photoelectron spectrum of NO_3^- (266 nm), assuming a triple-minimum potential for the ν_4 coordinate of NO_3, with a barrier of 870 cm^{-1} (a = 0.340 eV/Å, k = 0.531 eV/Å^2), origin at 0.780 eV, T = 1 K.

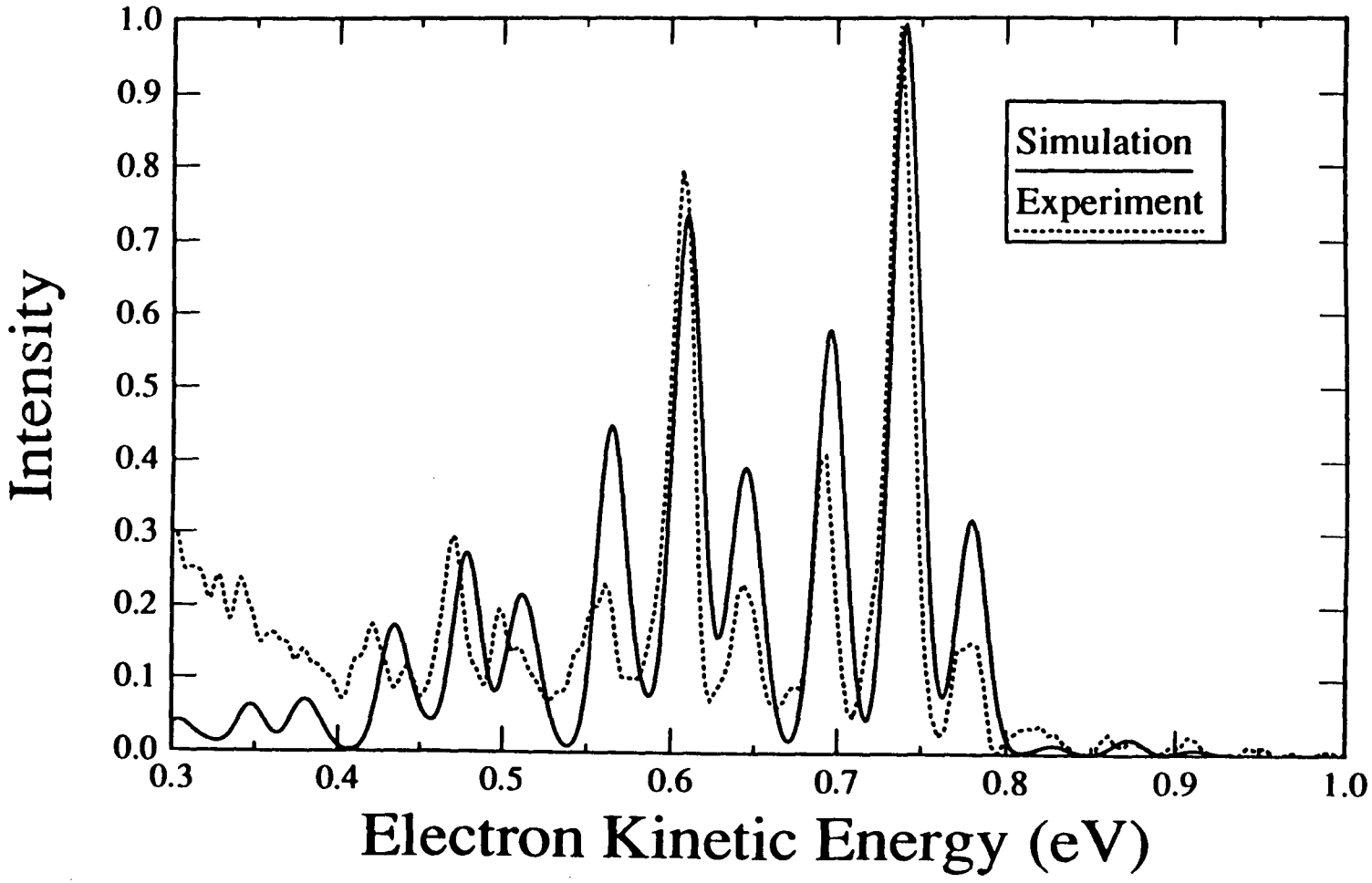
Intensity
1.0
0.9
0.8
0.7
0.6
0.5
0.4
0.3
0.2
0.1
0.0
0.3
0.4
0.5
0.6
0.7
0.8
0.9
1.0
Simulation
Experiment
Electron Kinetic Energy (eV)

out a low-lying v_4=1 level such as in Figure 5.5(c).

In summary, none of the simulations discussed in this section is satisfactory. We must therefore search for another explanation for the 360 cm^{-1} progression in our photoelectron spectrum.

5.1.5. Vibronic coupling in the NO_3 ground state

In this section, we consider vibronic coupling between the electronic states of NO_3 as an alternative explanation for the apparent odd Δv_4 transitions in the ground state band. Our selection rules were derived assuming nuclear and electronic motion to be separable (Eq. 5.1.6). Vibronic coupling makes this approximation invalid, and lends intensity to Franck-Condon forbidden transitions. The photoelectron spectrum of BF_3, which is isoelectronic with NO_3^-, shows effects similar to those that we observe. In particular, odd Δv_3 transitions are observed in the $^2A_1'$ excited state progression, due to coupling between the $^2A_1'$ and $^2E'$ states of BF_3^+. Our interpretation of our NO_3^- spectra is largely based on the comprehensive analysis of BF_3^+ by Haller et al..[37]

This vibronic interaction between dissimilar electronic states is called Herzberg-Teller,[64] or pseudo- (or second-order) Jahn-Teller coupling.[35,65,66] The necessary symmetry condition for a mode v to couple electronic states m and n is $\Gamma_v \otimes \Gamma_m \otimes \Gamma_n \supset \Gamma_A$,[67] where Γ_A is the totally symmetric representation in the molecular point group. In NO_3, the ν_3 and ν_4 modes (Γ_v = e') couple the

$^2A_2'$ ground state to the $^2E'$ state, and the ν_2 mode ($\Gamma_\nu = a_2''$) couples the $^2E'$ and $^2E''$ states. The ν_3 and ν_4 modes are also Jahn-Teller active within both the $^2E''$ and $^2E'$ states.

To examine the effects of vibronic coupling on the NO_3 ground state, we incorporate the interaction term into the molecular Hamiltonian. For simplicity, we consider only pseudo-Jahn-Teller coupling between the $^2A_2'$ and $^2E'$ electronic states (to be referred to henceforth as the A and E states) via ν_4, and neglect Jahn-Teller coupling within the $^2E'$ state. The Hamiltonian for motion in the ν_4 coordinate (using the notation of Haller et al.[37]) is

$$H_4^{PJT} = \Omega_4 \cdot \mathbf{I}_3 + \begin{bmatrix} \varepsilon_A & \lambda_4 q_{4a} & \lambda_4 q_{4b} \\ \lambda_4 q_{4a} & \varepsilon_E & 0 \\ \lambda_4 q_{4b} & 0 & \varepsilon_E \end{bmatrix} \qquad (5.1.11)$$

Here q_{4a} is one of the degenerate components of the dimensionless normal coordinate q_4,[68] where

$$q_i = \sqrt{\frac{2\pi c \nu_i}{\hbar}}\, Q_i \quad . \qquad (5.1.12)$$

Ω_4 is the harmonic oscillator Hamiltonian for nuclear motion in the ν_4 mode,

$$\Omega_4 = -\frac{1}{2}\omega_4^{(A,E)}\left(\frac{\partial^2}{\partial q_{4a}^2} + \frac{\partial^2}{\partial q_{4b}^2}\right) + \frac{1}{2}\omega_4^{(A,E)}\left(q_{4a}^2 + q_{4b}^2\right) \qquad (5.1.13)$$

where $\omega_4^{(A,E)}$ is the energy spacing between the unperturbed harmonic oscillator levels of the A or E state. $\mathbf{I}_3$ is the 3 x 3 unit matrix in the space of the A and

E electronic states, λ_4 is the pseudo-Jahn-Teller coupling constant for the ν_4 mode, and ε_i is the energy of the electronic state i. The eigenfunctions and eigenvalues of H^{PJT} can be determined using the techniques developed by Köppel et al.,[35] who use coupling constants and vibrational frequencies calculated by *ab initio* methods. Their 'exact' methods use vibronic basis functions which are products of harmonic oscillator nuclear wavefunctions and diabatic electronic wavefunctions for the A and E states. Assuming ω_4^A and ω_4^E to be equal, the nuclear basis functions coupled by the $\lambda_4 q_{4\alpha}$ terms in H_4^{PJT} differ by one quantum of v_4.

The pseudo-Jahn-Teller interaction therefore couples the v_4=n level of the $^2A_2'$ state with the v_4=n±1 levels of the $^2E'$ state. This explains the odd Δv_4 transitions observed in the ground state progression. The photodetachment transition probability from the NO_3^- ground state to odd vibronic levels of NO_3 is no longer zero, since these nominally forbidden transitions borrow intensity from allowed transitions to the even v_4 levels of the $^2E'$ state. In addition, the A state vibronic levels obtain some of the character of those E state levels, which might explain the variation in the 0.693 eV (363 cm^{-1} from the origin) peak intensity with laser polarization.

We now wish to determine the coupling strength, λ_4, necessary to explain the intensity distribution in our spectra. Since we do not have a reliable *ab initio* estimate of λ_4, we calculate an approximate value from the experimental peak intensities, using the expression derived by Haller et al.:[36]

$$\frac{I_{v_1,\, v_4=1}(A)}{I_{v_1,\, v_4=0}(A)} \propto \frac{2|\tau_{E'}|^2 \lambda^2}{|\tau_A|^2} \cdot \frac{1}{(\Delta\varepsilon + \omega_4)^2} \qquad (5.1.14)$$

Here v_i is the quantum number in the ith vibrational mode, $\Delta\varepsilon \approx \varepsilon_A - \varepsilon_{E'} = -1.87$ eV, and τ is the electronic transition dipole moment for a particular state. This is a simplified version of their expression, which is based on first-order perturbation theory approximations to the wavefunctions. The unperturbed frequency, ω_4, is assumed to be the same in the ion and in the neutral A and E states (720 cm^{-1}). To calculate λ_4, we require the ratio $2|\tau_{E'}|^2/|\tau_A|^2$. This would be given by the ratio of the integrated intensities of the $^2E'$ and $^2A_2'$ bands in the 213 nm spectrum. Since we observe the $^2E''$ state but not the $^2E'$ state, we assume $\tau_{E'} \approx \tau_{E''}$. The transition moment ratio is thus $2|\tau_{E'}|^2/|\tau_A|^2 \approx 10$, the ratio of the integrated areas under the $^2E''$ and $^2A_2'$ state progressions at 213 nm. (As discussed in Section 5.1.3, the photodetachment cross section to the $^2A_2'$ state, which is proportional to $|\tau_A|^2$, is exceptionally low.) For the $I_{v1,v4=1}/I_{v1,v4=0}$ ratio in Eq. 5.1.14 we use four peak intensity ratios measured from the NO_3 ground state progression. We use the results for v_1=0 and 1, and those at two laser polarization angles (θ = 0° and 90°).

We calculate an average value for λ_4 of 0.348 ± 0.058 eV, which is similar to the $^2A_2'$ - $^2E'$ coupling constants calculated for BF_3^+. Our value of λ_4 indicates that this vibronic coupling mechanism provides a reasonable

explanation for the odd Δv_4 transitions that we observe. However, the intensity borrowing effect of the pseudo-Jahn-Teller interaction in NO_3 is amplified, relative to BF_3^+, by the large $|\tau_{E'}|^2/|\tau_A|^2$ value.

If the vibronic coupling is sufficiently strong, the equilibrium geometry of the NO_3 ground state may be affected. The adiabatic electronic potentials for the A and E states should then show minima at configurations other than the symmetric D_{3h} position ($q_4 = 0$). These adiabatic potential energy surfaces, for motion along the q_4 coordinate, are determined by neglecting the nuclear kinetic energy in H^{PJT} (Eq. 5.1.11), setting $\omega_4^A = \omega_4^E$, and diagonalizing the resulting matrix:

$$\begin{bmatrix} \varepsilon_A + \frac{1}{2}\omega_4 q_4^2 & \lambda_4 q_{4a} & \lambda_4 q_{4b} \\ \lambda_4 q_{4a} & \varepsilon_E + \frac{1}{2}\omega_4 q_4^2 & 0 \\ \lambda_4 q_{4b} & 0 & \varepsilon_E + \frac{1}{2}\omega_4 q_4^2 \end{bmatrix} \qquad (5.1.15)$$

where $q_4^2 = q_{4a}^2 + q_{4b}^2$. For a given value of λ_4, we estimate ω_4 by comparing the first few vibrational levels on the A state surface with the experimental ν_4 progression. If we set λ_4=0.348 (the perturbation theory value), the best agreement with experimental peak positions is obtained for $\omega_4 \approx 0.125$ eV (1000 cm^{-1}). The experimental $v_4 = 1$ and 2 peaks are 363 and 758 cm^{-1} from the origin. The eigenvalues of the adiabatic surface reproduce this uneven spacing, but the calculated positions are 359 and 842 cm^{-1}. Decreasing λ_4 and adjusting ω_4 accordingly improves the fit. At $\lambda_4 = 0.290$ eV, the lower limit of

our calculated coupling strength, ω_4 = 0.1 eV (805 cm^{-1}) gives peaks at 360 and 780 cm^{-1}.

The estimate of ω_4, the unperturbed vibrational frequency, obtained from our simulations is similar to the measured ν_4 = 720 cm^{-1} in NO_3^-. Vibronic coupling may thus explain the anomalously low measured ν_4 frequency in the NO_3 $^2A_2'$ state, in addition to explaining other features of the ground state progression. Figure 5.8 shows the adiabatic curves with and without the pseudo-Jahn-Teller interaction energy, for λ_4 = 0.290 eV and ω_4^A ($=\omega_4^E$) = 0.1 eV (805 cm^{-1}). One of the components of the $^2E'$ state is not affected by the perturbation, but the other interacts repulsively with the $^2A_2'$ state.

This perturbed potential for the A state has a minimum at q_4 = 0, corresponding to a D_{3h} equilibrium geometry. Haller et al.[37] have shown that this will be true as long as $\lambda_4^2/\omega_4 \leq \frac{1}{2}(\varepsilon_E - \varepsilon_A)$. Even with λ_4 = 0.348 eV and ω_4 = 0.125 eV, the barrier in the adiabatic potential is only 0.001 eV. We believe that our lower estimate of λ (0.290 eV), which gives a better fit to the experimental peak spacings, is closer to the true PJT coupling constant. To obtain the transition moment ratio $|\tau_{E'}|^2/|\tau_A|^2$ used in Eq. 5.1.14, we assumed that $|\tau_{E'}|^2 = |\tau_{E''}|^2$. It is likely that the $^2E''$ and $^2E'$ states have somewhat different integrated intensities, so the perturbation theory estimate of λ_4 = 0.348 eV is a good first guess, at best. The coupling constant derived from fitting peak spacings is more reliable because we are then using experimental information to adjust λ_4 and ω_4. The comparison of adiabatic eigenvalues to

Figure 5.8. Potential energy of the NO_3 $^2A_2'$ and $^2E'$ states as a function of q_4, the dimensionless normal coordinate. The solid curves are the adiabatic pseudo-Jahn-Teller-perturbed potentials calculated from Eq. 5.1.15, with ω_4 = 0.1 eV (805 cm^{-1}), and λ_4 = 0.290 eV. We have neglected Jahn-Teller coupling in the $^2E'$ state. The unperturbed harmonic oscillator potentials for the $^2A_2'$ (x) and $^2E'$ (+) states are also shown.

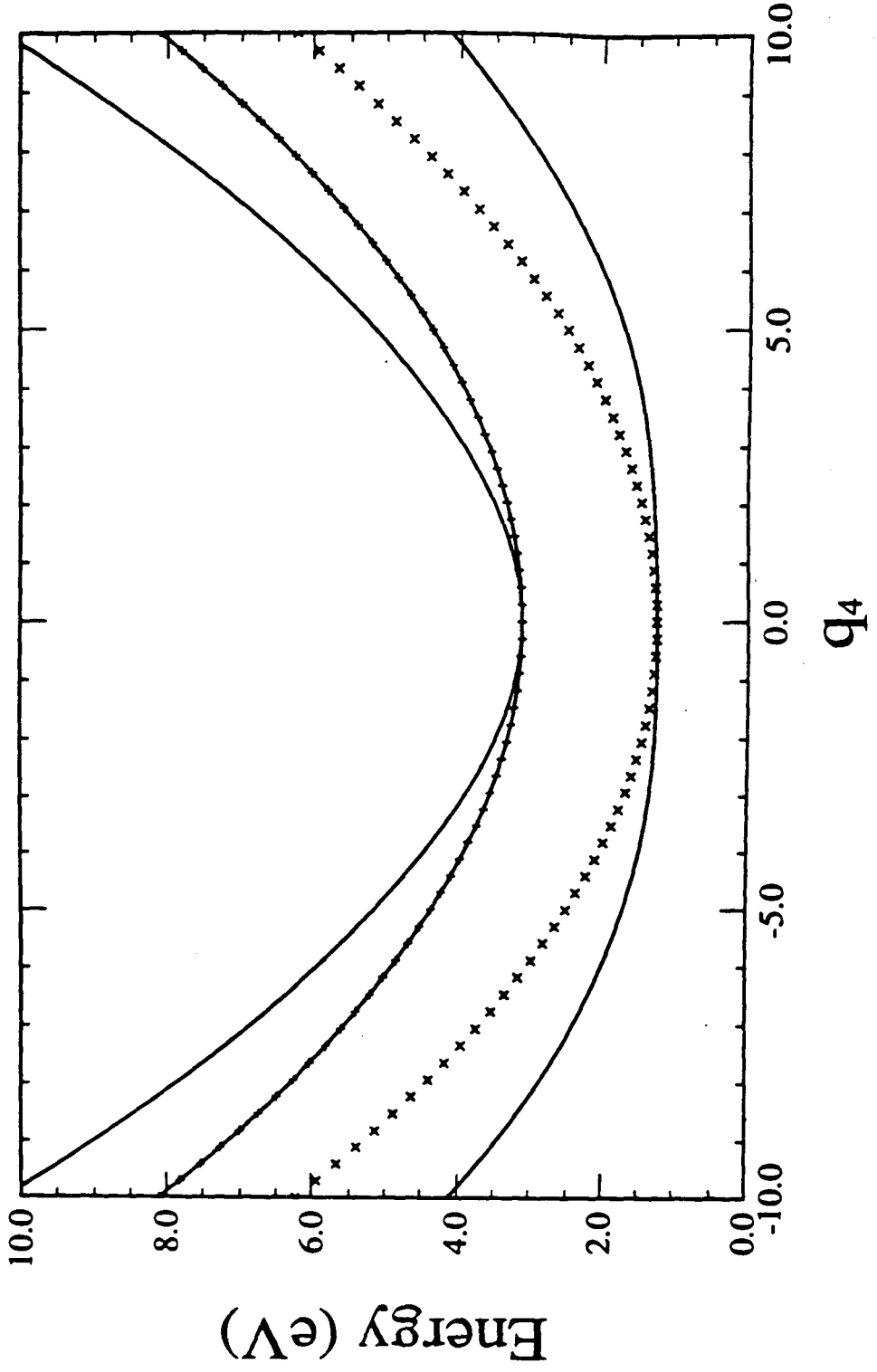
Energy (eV)
10.0
8.0
6.0
4.0
2.0
0.0
-10.0
-5.0
0.0
5.0
10.0
q4

experimental peak spacings is not strictly valid, since non-adiabatic coupling due to the nuclear kinetic energy operator will mix vibronic levels of the individual A and E surfaces.[66,69] However, the v_4 = 0, 1 and 2 levels of the A state lie well below the E state, so non-adiabatic effects on these low-lying states are probably small. Our calculated vibronic coupling strength is sufficient to induce intensity in forbidden transitions, but is weak enough that the NO_3 $^2A_2'$ state still has D_{3h} symmetry.

In summary, pseudo-Jahn-Teller coupling between the $^2A_2'$ and $^2E'$ states of NO_3 via the ν_4 mode accounts for the observed peak positions in the ground state band of the NO_3^- photoelectron spectrum. The coupling strength necessary to reproduce our results does not break the D_{3h} symmetry of the $^2A_2'$ state, and this explanation is consistent with the D_{3h} equilibrium geometry implied by the high resolution spectra of NO_3. An important test of our analysis should result from obtaining a photoelectron spectrum which includes the $^2E'$ state of NO_3. This will allow the direct measurement of $2|\tau_{E'}|^2/|\tau_A|^2$, the parameter which controls intensity borrowing via pseudo-Jahn-Teller coupling. This experiment should be possible using an ArF excimer laser (photon energy 6.42 eV).

5.1.6. NO_3 excited state

The 213 nm spectrum of NO_3^- shows an excited state progression 0.868 ± 0.046 eV (7000 ± 370 cm^{-1}) above the ground state. This is identified as the

$^2E''$ state of NO_3, since the $^2E'$ state has been observed at 1.87 eV[7,8,21,23,70] and the 'dark' $^2E''$ state is predicted to lie between the ground state and $^2E'$ state. The $^2E''$ band shows extensive vibrational structure. A satisfactory fit to the peak positions is obtained by assuming only two active harmonic vibrational modes, with frequencies of 804 ± 4 cm^{-1} and 541 ± 8 cm^{-1}; the 804 cm^{-1} progression is considerably longer.

We first try to assign these two progressions by comparing their frequencies to those observed in NO_3^- and other electronic states of NO_3. Since the $^2E''$ state is degenerate, the degenerate ν_3 and ν_4 modes can be activated in the photoelectron spectrum via first-order Jahn-Teller coupling, which allows odd Δv transitions to occur in these modes. As discussed above, a change in the N-O bond length upon photodetachment to the $^2E''$ state will also lead to a progression in the ν_1 symmetric stretch. If vibronic interactions between the $^2E''$ state and other electronic states are negligible, the ν_2 out-of-plane bending mode should not be active since the $^2E''$ state is expected to be planar.

The measured ν_4 frequencies in NO_3^- and in the $^2A_2'$ state of NO_3 are 723 cm^{-1} and 360 cm^{-1}, respectively, so either the 541 cm^{-1} or the 804 cm^{-1} frequency in the $^2E''$ band could correspond to the ν_4 mode. The ν_1 frequency is about 1060 cm^{-1} in the ion and neutral ground state, and 950 cm^{-1} in the neutral $^2E'$ state,[20,70] but the average ν_3 frequency in the ion and two neutral states is 1440 cm^{-1}. Assuming that these are the only possible active modes, the most

reasonable assignment on the basis of frequency alone is that the 804 cm^{-1} progression corresponds to the ν_1 mode and the 541 cm^{-1} progression to the ν_4 mode. Using this assignment, Table 5.2 lists the v_1 and v_4 quantum numbers for each peak in the band. With this assignment, the $v_4' = 1 \leftarrow v_4'' = 1$ transition, which is prominent in the $^2A_2'$ state progression, should occur at 1.060 eV. The 0-0 peak at 1.038 eV does have a shoulder in the right place for this 'hot band' transition.

We next consider the intensity distribution in the $^2E''$ band. Table 5.2 lists peak intensities relative to the ($v_1 = 1, v_4 = 0$) peak at 0.935 eV (calculated position). These were obtained by assuming Gaussian peaks, each of fwhm 0.022 eV, and determining the peak intensities required for the cumulative simulated spectrum to match the experimental spectrum. Peak positions were calculated from the harmonic frequencies. Figure 5.9 shows that we can reproduce the peak positions and the broad, intense base under the $^2E''$ band with overlapped Gaussians.

The intensity distribution in Table 5.2 presents two problems. If we assume that the two modes are separable, the intensity of each peak should be given by a product of Franck-Condon factors as in Eq. 5.1.6. The intensity ratio for the peaks (v_1 = n, v_4) and (v_1 = m, v_4) is then independent of v_4. However, the observed (1,0)/(0,0) ratio is 1.75, the (1,1)/(0,1) ratio is 1.19, and the (1,2)/(0,2) ratio is 1.45. Similar discrepancies occur throughout the band.

In addition, if we assume the ν_1 mode to be a one-dimensional harmonic

Figure 5.9. Experimental and 'simulated' photoelectron spectra of NO_3^- (213 nm), for detachment to the NO_3 $^2E''$ state. The simulation assumes two active modes, of frequency 804 and 541 cm^{-1}, and shows that a combination of Gaussian peaks (fwhm 0.022 eV) can reproduce the peak positions and shape of the $^2E''$ band.

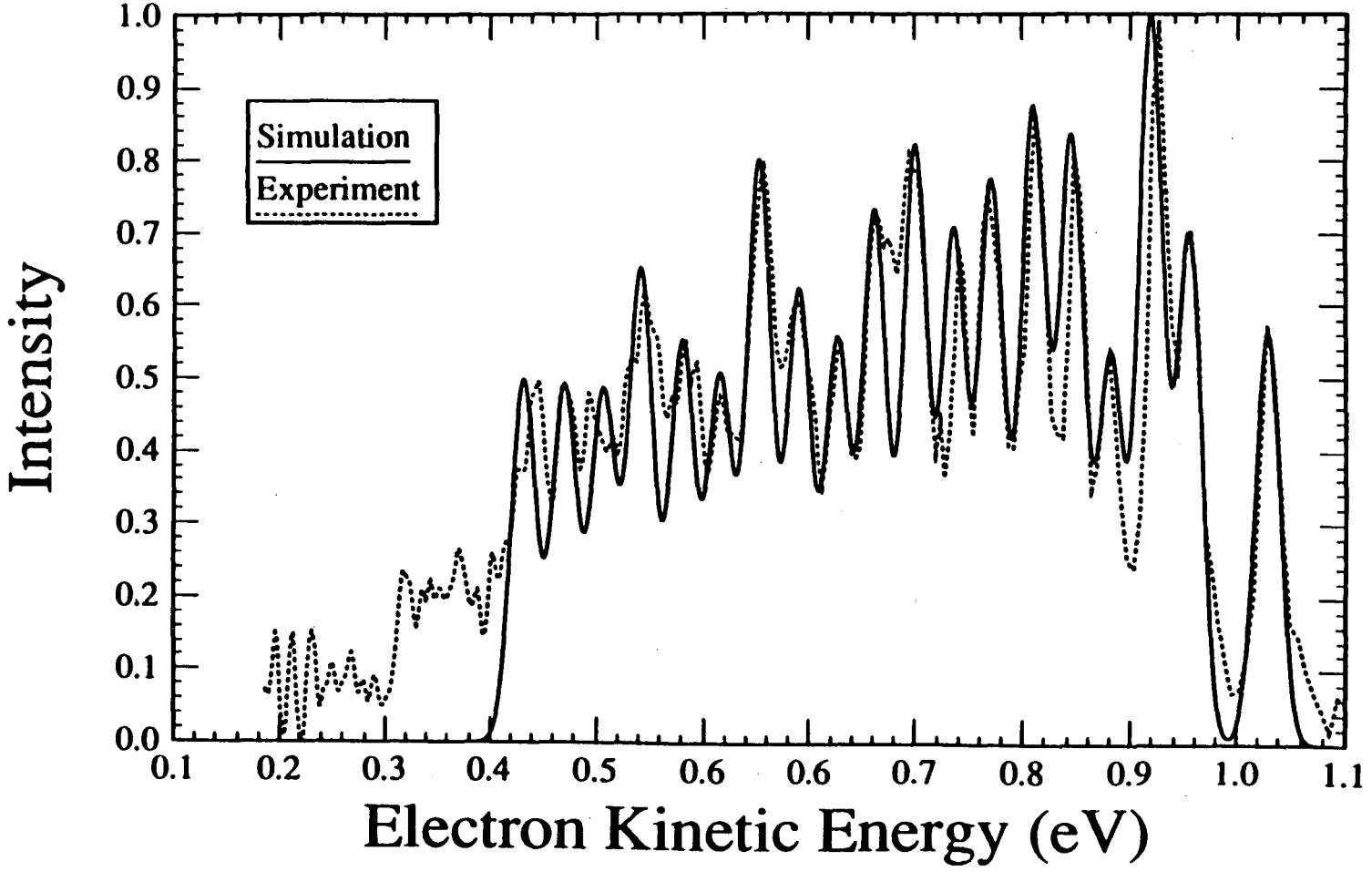
Simulation
Experiment
Intensity
Electron Kinetic Energy (eV)
1.0
0.9
0.8
0.7
0.6
0.5
0.4
0.3
0.2
0.1
0.0
0.1
0.2
0.3
0.4
0.5
0.6
0.6
0.7
0.8
0.9
1.0
1.1

oscillator displaced from the oscillator in the ion, which is appropriate for a totally symmetric mode, we are unable to model the (n,0) progression. Specifically, if we match the experimental (1,0)/(0,0) ratio the simulated peak intensities for $v_1 \geq 4$ are considerably lower than the experimental intensities. If we assume that $\Delta Q_1 = 6.9\ \Delta r_{NO}$ for the $^2E''$ state, as we did for the $^2A_2'$ state (Section 5.1.4), the displacement necessary to match the experimental (1,0)/(0,0) ratio requires that the N-O bond length change by 0.07 Å between the ion and the $^2E''$ state. This seems excessive for the removal of a nominally non-bonding e" electron[3] from the ion. (By comparison, removal of a non-bonding a_2' electron in the transition from NO_3^- to the $^2A_2'$ state results in a bond length change of only about 0.03 Å.)

The intensity distribution in the $^2E''$ band shows that separability of the two active modes in the $^2E''$ state is a poor assumption. This leads us to question our assignment of the 804 cm^{-1} progression to the symmetric stretch, since the ν_1 and ν_4 modes are of different symmetries and should not mix. An alternative explanation for this progression involves vibronic coupling with other electronic states. In Section 5.1.5, the ν_4 progression in the $^2A_2'$ band was attributed to pseudo-Jahn-Teller coupling between the $^2A_2'$ and $^2E'$ states via the ν_4 mode. This vibronic coupling mechanism also exists between the $^2E''$ and $^2E'$ states via the ν_2 out-of-plane bend (a_2'' symmetry) and can activate the ν_2 mode in the $^2E''$ band. The ν_2 frequency is 834 cm^{-1} in NO_3^- and 762 cm^{-1} in the NO_3 $^2A_2'$ state, so the 804 cm^{-1} progression in the $^2E''$ state is in the right

frequency range for the ν_2 mode. If this assignment were correct, the extended nature of the 804 cm^{-1} progression would imply substantial vibronic coupling, possibly large enough to cause distortion from a planar equilibrium geometry for the $^2E''$ state. Haller et al.[37] calculated the analogous pseudo-Jahn-Teller coupling constant for BF_3^+ to be relatively small.

More theoretical work on NO_3 is required before we can determine whether this alternative assignment is realistic. Ideally, vibronic coupling constants could be obtained by *ab initio* methods, and then used in calculations of the type developed by Cederbaum and coworkers. These simulations of the $^2E''$ band should clearly indicate the relative importance of different vibronic coupling mechanisms.

5.1.7. Summary and Conclusions

We have observed the $^2A_2'$ ground state and $^2E''$ first excited state of NO_3 via photoelectron spectroscopy of the NO_3^- anion. The electron affinity of NO_3 is 3.937 ± 0.018 eV, and we calculate $\Delta_f°H(NO_3)_{298\,K}$ = 0.777 ± 0.034 eV (17.91 ± 0.79 kcal/mol). Our analysis of the $^2A_2'$ band indicates that the NO_3 ground state has a D_{3h} equilibrium geometry, but is perturbed by vibronic coupling to the $^2E'$ second excited electronic state through the ν_4 degenerate in-plane bend. This coupling explains both the appearance of odd Δv_4 transitions in this band and the anomalously low ν_4 vibrational frequency in the $^2A_2'$ state.

Our results represent the first direct observation of the $^2E''$ state of NO_3,

which lies 0.868 ± 0.046 eV above the ground state. The $^2E''$ band shows extensive vibrational structure which has been tentatively assigned to progressions in the ν_1 symmetric stretch and the Jahn-Teller active ν_4 mode. However, this assignment is not completely satisfactory, and the analysis of the $^2E''$ band could clearly benefit from further theoretical work.

Acknowledgements

This research is supported by the Air Force Office of Scientific Research under Grant No. AFOSR-87-0341. We thank R. Boehm, H.F. Davis, R. Davy, E. Hirota, K. Kawaguchi, B. Kim, W.C. Lineberger and H.F. Schaefer for communicating their results prior to publication, and also H. Köppel for helpful discussions.

References for section 5.1:

1. *Atmospheric ozone 1985: assessment of our understanding of the processes controlling its present distribution and change*, World Meteorological Organization, Global Ozone Research and Monitoring Project - Report No. 16 (NASA, Washington D.C., 1985), pp. 32-35.

2. J.H. Seinfeld, Science **243**, 745 (1989); S.E. Schwartz, Science **243**, 753 (1989); M.B. McElroy and R.J. Salawitch, Science **243**, 763 (1989).

3. A.D. Walsh, J. Chem. Soc. 2301 (1953).

4. T. Ishiwata, I. Tanaka, K. Kawaguchi, and E. Hirota, J. Chem. Phys. **82**, 2196 (1985).

5. R.R. Friedl and S.P. Sander, J. Phys. Chem. **91**, 2721 (1987).

6. K. Kawaguchi, E. Hirota, T. Ishiwata, and I. Tanaka, J. Chem. Phys., **93**, 951 (1990).

7. T. Ishiwata, I. Fujiwara, Y. Naruge, K. Obi, and I. Tanaka, J. Phys. Chem. **87**, 1349 (1983).

8. H.H. Nelson, L. Pasternack, and J.R. McDonald, J. Phys. Chem. **87**, 1286 (1983).

9. A. Lund and K.-Å. Thuomas, Chem. Phys. Lett. **44**, 569 (1976).

10. N.C. Baird and K.F. Taylor, Chem. Phys. Lett. **80**, 83 (1981).

11. R.C. Boehm and L.L. Lohr, J. Phys. Chem. **93**, 3430 (1989).

12. R.C. Boehm and L.L. Lohr, J. Comput. Chem., submitted 1990.

13. U. Kaldor, Chem. Phys. Lett. **166**, 599 (1990).

14. J.F. Olsen and L. Burnelle, J. Am. Chem. Soc. **92**, 3659 (1970).

15. M.J.S. Dewar and H.S. Rzepa, J. Am. Chem. Soc. **100**, 784 (1978).

16. P.E.M. Siegbahn, J. Comput. Chem. **6**, 182 (1985).

17. R.D. Davy and H.F. Schaefer III, J. Chem. Phys. **91**, 4410 (1989).

18. B. Kim, B.L. Hammond, W.A. Lester, Jr., and H.S. Johnston, Chem. Phys. Lett., **168**, 131 (1990).

19. E.J. Jones and O.R. Wulf, J. Chem. Phys. **5**, 873 (1937).

20. D.A. Ramsay, Proc. Colloq. Spectrosc. Int. **10**, 583 (1962).

21. R.A. Graham and H.S. Johnston, J. Phys. Chem. **82**, 254 (1978).

22. H.H. Nelson, L. Pasternack, and J.R. McDonald, J. Chem. Phys. **79**, 4279 (1983).

23. W.J. Marinelli, D.M. Swanson, and H.S. Johnston, J. Chem. Phys. **76**, 2864 (1982).

24. T.E.H. Walker and J.A. Horsley, Mol. Phys. **21**, 939 (1971).

25. B. Kim, H.S. Johnston, D.A. Clabo, Jr., and H.F. Schaefer III, J. Chem. Phys. **88**, 3204 (1988).

26. R. Lefebvre and E. Ressayre, Theor. Chim. Acta **18**, 31 (1970).

27. M. Hotokka and P. Pyykkö, Chem. Phys. Lett. **157**, 415 (1989) and references within; H. Teramae, K. Tanaka, K. Shiotani, and T. Yamabe, Solid State Comm. **46**, 633 (1983); L. Radom, Aust. J. Chem. **29**, 1635 (1976).

28. G.L. Paul and A.W. Pryor, Acta Cryst. **B27**, 2700 (1971); P. Cherin, W.C. Hamilton, B. Post, Acta Cryst. **23**, 455 (1967), and references within.

29. J.W. Rabalais, *Principles of Ultraviolet Photoelectron Spectroscopy* (Wiley, New York, 1977), p. 53.

30. H.C. Longuet-Higgins, Adv. Spectrosc. **2**, 429 (1961).

31. H.C. Longuet-Higgins, U. Öpik, M.H.L. Pryce, and R.A. Sack, Proc. Roy. Soc. London **A244**, 1 (1958).

32. S.D. Brossard, P.G. Carrick, E.L. Chappell, S.C. Hulegaard, and P.C. Engelking, J. Chem. Phys. **84**, 2459 (1986).

33. W.C. Lineberger, unpublished results.

34. P.C. Engelking and W.C. Lineberger, J. Chem. Phys. **67**, 1412 (1977).

35. H. Köppel, W. Domcke, and L.S. Cederbaum, Adv. Chem. Phys. **57**, 59 (1984).

36. E. Haller, H. Köppel, L.S. Cederbaum, G. Bieri and W. von Niessen, Chem. Phys. Lett. **85**, 12 (1982).

37. E. Haller, H. Köppel, L.S. Cederbaum, W. von Niessen, and G. Bieri, J. Chem. Phys. **78**, 1359 (1983).

38. Ref. 29, pp. 243-251.

39. R.B. Metz, A. Weaver, S.E. Bradforth, T.N. Kitsopoulos, and D.M. Neumark, J. Phys. Chem. **94**, 1377 (1990).

40. M.A. Johnson and W.C. Lineberger, in *Techniques of Chemistry, Vol. 20: Techniques for Study of Ion-Molecule Reactions*, J.M. Farrar and W.H. Saunders, Jr., eds.. (Wiley, New York, 1988), p. 591.

41. T.N. Kitsopoulos, I.M. Waller, J.G. Loeser, and D.M. Neumark, Chem. Phys. Lett. **159**, 300 (1989).

42. W.C. Wiley and I.H. McLaren, Rev. Sci. Instrum. **26**, 1150 (1955).

43. H. Hotop and W.C. Lineberger, J. Phys. Chem. Ref. Data **14**, 731 (1985).

44. J.A. Davidson, F.C. Fehsenfeld, and C.J. Howard, Int. J. Chem. Kinetics **9**, 17 (1977).

45. S.G. Lias, J.E. Bartmess, J.F. Liebman, J.L. Holmes, R.D. Levin, and W.G. Mallard, *Gas-Phase Ion and Neutral Thermochemistry*, J. Phys. Chem. Ref. Data **17**, Supplement 1 (1988), pp. 5-30.

46. M.W. Chase, Jr., C.A. Davies, J.R. Downey, Jr., D.J. Frurip, R.A. McDonald, and A.N. Syverud, *JANAF Thermochemical Tables, Third Edition, Part I*, J. Phys. Chem. Ref. Data **14**, Supplement I (1985), pp. 10-18.

47. E.B. Wilson, Jr., Chem. Rev. **27**, 17 (1940).

48. A.H. McDaniel, J.A. Davidson, C.A. Cantrell, R.E. Shetter, and J.G. Calvert, J. Phys. Chem. **92**, 4172 (1988).

49. Ref. 46, p. 1537, and references within.

50. J. Cooper and R.N. Zare, J. Chem. Phys. **48**, 942 (1968).

51. N. Smyrl and J.P. Devlin, J. Phys. Chem. **77**, 3067 (1973); R. Kato and J. Rolfe, J. Chem. Phys. **47**, 1901 (1967); V. Narayanamurti, W.D. Seward, and R.O. Paul, Phys. Rev. **148**, 481 (1966); A.K. Ramdas, Proc. Ind. Acad. Sci. **A37**, 441 (1953).

52. J.D. Riddell, D.J. Lockwood, and D.E. Irish, Can. J. Chem. **50**, 2951 (1972); G. Pollard, N. Smyrl and J.P. Devlin, J. Phys. Chem. **76**, 1826 (1972).

53. B.S. Rama Rao, Proc. Ind. Acad. Sci. **A10**, 167 (1939); P.A. Moses, Proc. Ind. Acad. Sci. **A10**, 71 (1939); M.J. Chédin, J. de Phys. et le Radium, vol. V, ser. VII, 445 (1939); R. Ananthakrishnan, Proc. Ind. Acad. Sci. **A5**, 447 (1937).

54.(a) C_{2v} symmetry: G.W. Chantry, A. Horsfield, J.R. Morton, and D.H. Whiffen, Mol. Phys. **5**, 589 (1962). (b) D_{3h} symmetry: D.E. Wood and G.P. Lozos, J. Chem. Phys. **64**, 546 (1976); T.W. Martin, L.L. Swift, and J.H. Venable, Jr., J. Chem. Phys. **52**, 2138 (1970); R. Livingston and H. Zeldes, J. Chem. Phys. **41**, 4011 (1964). (c) A. Reuveni and Z. Luz, J. Mag. Res. **23**, 271 (1976): unable to determine.

55. J.T. Snodgrass, C.M. Roehl, P.A.M. van Koppen, W.E. Palke, and M.T. Bowers, J. Chem. Phys. **92**, 5935 (1990), and references within.

56. G. Herzberg, *Molecular Spectra and Molecular Structure III: Electronic Spectra and Electronic Structure of Polyatomic Molecules* (Van Nostrand Reinhold, New York, 1966), p. 152.

57. This 360 cm^{-1} frequency is based on our spectra and dispersed fluorescence results of Nelson et al.[8] and Kim et al. (B. Kim, P. Hunter, H.S. Johnston, J. Chem. Phys., submitted 1991). Ishiwata et al.[7] measured 380 cm^{-1} in their dispersed fluorescence spectra, but this small difference in frequency does not affect the essential details of our analysis.

58. R. B. Metz (Chemistry Dept., University of California, Berkeley), from the Franck-Condon factor program of Dr. G.B. Ellison; T.E. Sharp and H.M. Rosenstock, J. Chem. Phys. **41**, 3453 (1964); E. Hutchisson, Phys. Rev. **36**, 410 (1930).

59. R.B. Metz (Chemistry Dept., University of California, Berkeley); J.C.

Light, I.P. Hamilton and J.V. Lill, J. Chem. Phys. **82**, 1400 (1985).

60. K.M. Ervin, J. Ho, and W.C. Lineberger, J. Phys. Chem. **92**, 5405 (1988).

61. E.B. Wilson, Jr., J.C. Decius, and P.C. Cross, *Molecular Vibrations* (Dover, New York, 1980), p. 309.

62. G. Herzberg, *Molecular Spectra and Molecular Structure II: Infrared and Raman Spectra of Polyatomic Molecules* (Van Nostrand Reinhold, New York, 1945), p. 179.

63. Although the NO_3^- $v_4'' = 0$ level and the neutral $v_4' = 3$ level, for example, both have components of a_1' symmetry, this $\Delta v = 3$ transition is not allowed. The neutral level has vibrational angular momentum $l = 1$ and has zero overlap with the $v_4'' = 0$, $l = 0$ level of the ion.

64. J.M. Hollas, *High Resolution Spectroscopy* (Butterworths, London, 1982), p. 388.

65. M.Z. Zgierski and M. Pawlikowski, J. Chem. Phys. **70**, 3444 (1979); J.H. van der Waals, A.M.D. Berghuis, and M.S. de Groot, Mol. Phys. **21**, 497 (1971); J.H. van der Waals, A.M.D. Berghuis, and M.S. de Groot, Mol. Phys. **13**, 301 (1967).

66. H. Köppel, L.S. Cederbaum, and W. Domcke, J. Chem. Phys. **89**, 2023 (1988).

67. Ref. 56, p. 67.

68. S. Califano, *Vibrational States* (Wiley, New York, 1976), p. 35.

69. H. Köppel, L.S. Cederbaum, W. Domcke, and W. von Niessen, Chem. Phys. **37**, 303 (1979).

70. D.N. Mitchell, R.P. Wayne, P.J. Allen, R.P. Harrison, and R.J. Twin, J.C.S. Faraday II, **76**, 785 (1980).

5.2. An exact vibronic coupling calculation for NO_3: the $^2A_2'$ - $^2E'$ interaction

"It is a great merit of the Jahn-Teller effect that it disappears when not needed." -- J.H. Van Vleck

5.2.1. Introduction

Analysis of our photoelectron spectra of NO_3^- (section 5.1) showed anomalous features in the vibrational structure of the NO_3 ground state band: a large $v_4 = 1$ peak that is Franck-Condon forbidden, and variation of the height of that peak with laser polarization, implying that it is associated with a different electronic state. Franck-Condon simulations on several neutral potential energy surfaces, including a surface with three shallow minima, could not reproduce this band.

These effects were qualitatively explained by vibronic coupling between the $^2A_2'$ ground state and $^2E'$ second excited electronic state via the antisymmetric bending mode, ν_4 (e' symmetry). The $^2A_2'$ $v_4 = 1$ state mixes with the $^2E'$ $v_4 = 0$ and 2 states, borrowing intensity from the allowed transitions as well as some of their electronic character. Recent results from other experiments on the NO_3 $^2A_2'$ state[1,2,3] provide further support for the vibronic coupling model.

The next step in this analysis is a calculation of the perturbed energy levels and wavefunctions, to see if we can reproduce the $^2A_2'$ band in our photoelectron spectra. Calculations of this type were pioneered by Longuet-

Higgins and others,[4,5] extended to neutral photoelectron spectra by Cederbaum and Domcke,[6] and further developed by Köppel and others,[7] as discussed in section 5.1.4. We apply Köppel's methods to simulate our negative ion photoelectron spectra.

5.2.2. Method

The basic method of the vibronic coupling simulation is similar to that of the Franck-Condon simulations discussed earlier. The method is outlined here, and each step is described in detail below.

We wish to find the energy levels E and wavefunctions ψ that satisfy the Schrödinger equation, $H\psi = E\psi$. We

· define the Hamiltonian,

$$H(r;R) = T(r) + V(r) + T(R) + V(R) + V(r,R) \qquad (5.2.1)$$

to include the electronic kinetic energy T(r) and electronic potential energy V(r) as functions of the electronic coordinates r, nuclear kinetic energy T(R) and nuclear potential energy V(R) as functions of the nuclear coordinates R, and nuclear-electronic coupling terms V(r,R);

· choose a set of basis functions $\{\Phi\} = \{\phi_1, \phi_2, \phi_3 \ldots \phi_N\}$ to represent the unperturbed states, such that the wavefunction ψ can be expressed as a linear combination of the ϕ_i,

$$\psi_i = c_{1,i}\phi_1 + c_{2,i}\phi_2 + \ldots + c_{N,i}\phi_N \qquad (5.2.2)$$

· use the set of coupled equations $H\psi_i = E\psi_i$, multiplied on the left by ψ_i, to construct the matrix form of the Hamiltonian, with each matrix element $H_{ij} = \langle\phi_i|H|\phi_j\rangle$ representing the interaction between the ith and jth unperturbed states;

· determine the matrix elements, and

· diagonalize the Hamiltonian matrix **H** to obtain its eigenvectors and eigenvalues. The eigenvectors contain the coefficients of the N basis functions $\{c_{1,i}, c_{2,i}...c_{N,i}\}$, which define the eigenfunctions of the Hamiltonian. The eigenvalues give the energies of these states.

The principles of these calculations are explained in detail by Köppel et al.;[7] also relevant is the work of Haller et al.[8,9] on the BF_3^+ molecule, which is isoelectronic with NO_3.

In this work we examine the second-order linear (pseudo-Jahn-Teller) interaction between the $^2A_2'$ and $^2E'$ electronic states, which are coupled by the degenerate ν_4 vibrational mode (e' symmetry). Since we also observe a progression in the symmetric stretch, ν_1 (a_1'), we incorporate this into the calculation. We neglect first-order linear (Jahn-Teller) coupling within the $^2E'$ state via the ν_3 and ν_4 modes (both e'), and second-order linear coupling between the $^2E'$ state and the $^2E''$ first excited electronic state via ν_2 (a_2''), which would make the calculation significantly more difficult and are not required to produce good agreement between the simulation and the experimental spectra.

The unperturbed Hamiltonian

In the absence of vibronic coupling, the Hamiltonian for nuclear motion in the ν_1 mode (assuming a harmonic oscillator) is

$$\Omega_1 = -\frac{1}{2}\omega_1^{(A,E)}\frac{\partial^2}{\partial q_1^2} + \frac{1}{2}\omega_1^{(A,E)} q_1^2 \qquad (5.2.3)$$

and, in the ν_4 mode,

$$\Omega_4 = -\frac{1}{2}\omega_4^{(A,E)}\left(\frac{\partial^2}{\partial q_{4a}^2} + \frac{\partial^2}{\partial q_{4b}^2}\right) + \frac{1}{2}\omega_4^{(A,E)}\left(q_{4a}^2 + q_{4b}^2\right) \qquad (5.2.4)$$

with $\omega_i^{(A,E)}$ the unperturbed harmonic oscillator frequency. As discussed below, each unperturbed frequency ω_i is assumed to be the same in all neutral electronic states and in the negative ion. The q_i are dimensionless normal coordinates[10]

$$q_i = \sqrt{\frac{2\pi c \nu_i}{\hbar}}\, Q_i \qquad (5.2.5)$$

The unperturbed vibrational wavefunctions are designated $|n_1,n_4\rangle$, where n_1 and n_4 are the vibrational quantum numbers in the ν_1 and ν_4 modes. l_4 ($= n_4, n_4 - 2 \ldots - |n_4 - 2|, - |n_4|$) is the quantum number for vibrational angular momentum in the degenerate mode, and the alternative quantum numbers n_+, n_- for the degenerate components of the ν_4 vibration are defined as

$$n_+ = \frac{n_4 + l_4}{2}, \qquad n_- = \frac{n_4 - l_4}{2} \tag{5.2.6}$$

with $n_+ + n_- = n_4$.

The unperturbed Hamiltonian for electronic motion, in matrix form, is

$$H_{el}^{(0)} = \begin{bmatrix} \varepsilon_A & 0 & 0 \\ 0 & \varepsilon_E & 0 \\ 0 & 0 & \varepsilon_E \end{bmatrix} \tag{5.2.7}$$

which acts on the electronic states {A, E_+, E_-}, where $|A\rangle$ represents the $^2A_2'$ state and $|E_+\rangle$, $|E_-\rangle$ the degenerate components of the $^2E'$ state. ε_i is the vertical energy of electronic state i, and the zero of energy is defined as that for the unperturbed ground vibrational state of the $^2A_2'$ ground electronic state.

The overall unperturbed Hamiltonian, $H^{(0)}$ is thus

$$H^{(0)} = \Omega_1 \cdot \mathbf{I}_3 + \Omega_4 \cdot \mathbf{I}_3 + \begin{bmatrix} \varepsilon_A & 0 & 0 \\ 0 & \varepsilon_E & 0 \\ 0 & 0 & \varepsilon_E \end{bmatrix} \tag{5.2.8}$$

where $\mathbf{I}_3$ is the 3 x 3 unit matrix in the space of the A and E electronic states. The unperturbed wavefunctions can be denoted $|i; n_1, n_4\rangle = |i\rangle\ |n_1, n_4\rangle$, where $|i\rangle$ is the electronic wavefunction and $|n_1, n_4\rangle$ the vibrational wavefunction.

The perturbed Hamiltonian

The interaction between nuclear and electronic motion that couples the $^2A_2'$ and $^2E'$ states appears in V(r,R) in Eq. (5.2.1) as a term proportional to the nuclear displacement. In this calculation, the perturbation is due to the displacement in ν_4 only. As we discussed in Chapter 2, this treatment assumes that the coupling is weak enough that addition of a perturbing term is a good approximation to the coupling of electronic and nuclear coordinates. (This is not true, for example, for some very highly perturbed vibrational levels of NO_2 and similar molecules.)

In matrix form, the perturbation can be expressed as

$$H = \begin{bmatrix} 0 & \lambda_4 q_- & \lambda_4 q_+ \\ \lambda_4 q_+ & 0 & 0 \\ \lambda_4 q_- & 0 & 0 \end{bmatrix} \qquad (5.2.9)$$

where λ_4 is the coupling constant between the A and E states via ν_4, and $q_{+,-}$ are complex coordinates[11]

$$q_+ = \frac{1}{\sqrt{2}}\left(q_{4a} + iq_{4b}\right), \qquad q_- = \frac{1}{\sqrt{2}}\left(q_{4a} - iq_{4b}\right) \qquad (5.2.10)$$

where q_{4a} and q_{4b} are the degenerate components of the dimensionless normal coordinate q_4. We also add diagonal terms in q_1 to account for the displacement in the totally symmetric mode, ν_1, between the ion and neutral. The constant κ_1^i is a 'coupling constant' between the totally symmetric stretching motion (ν_1) and the electronic motion in the ith state, which we will

$$H = \begin{bmatrix} \kappa_1^A q_1 & 0 & 0 \\ 0 & \kappa_1^E q_1 & 0 \\ 0 & 0 & \kappa_1^E q_1 \end{bmatrix} \tag{5.2.11}$$

discuss in more detail below. We have assumed $\kappa_3 = \kappa_4 = 0$; these are the intrastate coupling constants for ν_3 and ν_4, which are responsible for the first-order Jahn-Teller effect in the ^{2}E' state.

The full Hamiltonian is thus

$$H^{PJT} = \Omega_1 \cdot \mathbb{I}_3 + \Omega_4 \cdot \mathbb{I}_3 + \begin{bmatrix} \varepsilon_A + \kappa_1^A q_1 & \lambda_4 q_- & \lambda_4 q_+ \\ \lambda_4 q_+ & \varepsilon_E + \kappa_1^E q_1 & 0 \\ \lambda_4 q_- & 0 & \varepsilon_E + \kappa_1^E q_1 \end{bmatrix} \tag{5.2.12}$$

Since we neglect first-order Jahn-Teller coupling, the projection of the total angular momentum on the z axis, $\mathbf{J}_z$, is conserved, with quantum number M_J.[a] The electronic orbital angular momentum for each unperturbed electronic state is characterized by its projection on the z axis, the quantum number Λ ($\Lambda = 0, \pm 1$ for the A, E_+ and E_- states respectively), but the perturbation couples vibronic levels in the A and E states and so Λ is no longer a 'good' quantum number. The vibrational angular momentum quantum number l_4 characterizes the unperturbed degenerate harmonic oscillator vibrational states, but the perturbation also mixes states with different l. Only

---

[a] We have used M_J here rather than the j or J used in many vibronic coupling papers, since this is the more conventional spectroscopic notation.

the total angular momentum is conserved, and $M_J = l_4 - \Lambda$ [14] is still a good quantum number.

Choice of basis set

The basis functions for the vibronic coupling problem are the solutions of the unperturbed vibronic Hamiltonian, $H^{(0)}$. This basis set gives a simple form of the Hamiltonian matrix, with few off-diagonal elements and a sparse, banded structure which is easier to diagonalize. For this problem, the best choice is a basis set of functions $\{\Phi\}$ which are products of complex diabatic electronic wavefunctions $|\phi\rangle$ and harmonic oscillator vibrational wavefunctions $|\chi\rangle$,[7]

$$|\Phi\rangle = |\phi_{elec}\rangle\ |\chi_{vib}\rangle \qquad (5.2.13)$$

The vibrational basis functions are limited to those modes which are active in the photoelectron spectrum: ν_1 and ν_4. We assume that the unperturbed vibrational frequencies are the same in the ion and in both electronic states of the neutral, which is a reasonable assumption because the changes in molecular orbital occupancy are in non-bonding molecular orbitals. This greatly simplifies the calculation of ion-neutral wavefunction overlap, because the coefficient of a particular basis function $|n_1,n_4\rangle$ will also describe the overlap of the neutral wavefunction with the anion state $|n_1,n_4\rangle$.

The electronic basis functions are limited to the states that interact directly: in this case, the $^2A_2'$ state and the doubly degenerate $^2E'$ state. The

non-adiabatic coupling terms are minimized by using a diabatic electronic basis set, so the Hamiltonian remains approximately diagonal in nuclear kinetic energy.[7,12,13] Use of complex electronic and vibrational basis functions further simplifies the Hamiltonian.[5,14,15,16,17,18]

The number of unperturbed vibrational basis functions used must be large enough that the perturbed states can be represented accurately by linear combinations of the basis functions. For zero perturbation the neutral vibronic functions are represented exactly by the basis functions, so very few functions are needed. For a strong perturbation the eigenstates are very different from the basis functions, and many harmonic oscillator basis functions are required to represent the perturbed eigenstate. Since this is a variational calculation, the energies obtained will be too high if the basis set is not large enough. We determined the required basis set size by increasing the number of basis functions until the energies of the most highly excited states observed in the $^2A_2'$ band converged.

Construction of the Hamiltonian matrix

Since the only states coupled by this perturbation are those with the same M_J value, the basis set can be separated into non-interacting manifolds of states with the same M_J value. For example, the $M_J = 0$ basis functions include:

A vibrational states with $l_4 = M_J + \Lambda = 0$,

$\mathbf{E}_+$ states with $l_4 = M_J + \Lambda = 1,$

and $\mathbf{E}_-$ states with $l_4 = M_J + \Lambda = -1.$

The Hamiltonian matrix thus decouples into sub-matrices, reducing the dimensions of the diagonalization problem. The problem is further simplified because the $\pm M_J$ matrices give identical eigenvalues and eigenvectors, so only one of the two need be diagonalized.

The matrix elements $H_{ij} = \langle \phi_i | H | \phi_j \rangle$ have been determined analytically by several authors (each, unfortunately, using different notation);[4,7,19] we use the formulae of Köppel et al..[7]

The matrix elements that are diagonal in Λ are:[7]

$$\begin{aligned} H_{ii} &= \langle i; n_1', n_4' | H | i; n_1, n_4 \rangle \\ &= (E_i + n_1\omega_1 + n_4\omega_4)\,\delta_{n_1',n_1}\delta_{n_+',n_+}\delta_{n_-',n_-} \\ &\quad + \kappa_1^i \left\{ \sqrt{\frac{n_1+1}{2}}\,\delta_{n_1',n_1+1} + \sqrt{\frac{n_1}{2}}\,\delta_{n_1',n_1-1} \right\} \delta_{n_+',n_+}\delta_{n_-',n_-} \end{aligned} \qquad (5.2.14)$$

where i indicates the electronic state (A, E_+ or E_-) and the E_i are the electronic state energies. κ_1 was introduced earlier, as a 'coupling constant': in terms more familiar to photoelectron spectroscopists, it defines the normal coordinate shift of the neutral potential energy curve relative to that of the ion, κ_1/ω_1. The relative peak intensities in the ν_1 progression follow a Poisson distribution which corresponds to the spectrum of these shifted harmonic oscillators,

$$I_{n0} = \exp(-a_1)\cdot \frac{a_1^{n_1}}{n_1!} \tag{5.2.15}$$

where $a_1=\frac{1}{2}(\kappa_1/\omega_1)^2$ is the Poisson parameter and I_{n0} is the intensity of the $1_0^{n1}4_0^0$ peak.[b]

The matrix elements off-diagonal in Λ are:[7]

$$\begin{aligned} H_{ij} &= \langle i;n_1',n_4' \,|\, H \,|\, j;n_1,n_4 \rangle \\ &= \lambda_4^{(i,j)} \left\{ \sqrt{\frac{n_+ +1}{2}}\, \delta_{n'_+,n_+} + \sqrt{\frac{n_+}{2}}\, \delta_{n'_+,n_+ +1} \right\} \delta_{n'_1,n_1} \delta_{n'_-,n_-} \\ &+ \lambda_4^{(i,j)} \left\{ \sqrt{\frac{n_- +1}{2}}\, \delta_{n'_-,n_- +1} + \sqrt{\frac{n_-}{2}}\, \delta_{n'_-,n_- -1} \right\} \delta_{n'_1,n_1}\, \delta_{n'_+,n_+} \end{aligned} \tag{5.2.16}$$

where $\lambda_4^{(i,j)}$ is the interstate coupling constant for the ith and jth electronic states. The λ that we use here is a factor of $\sqrt{2}$ less than that of section 5.1 because we used the definitions for real basis functions there, but use the definitions for complex functions for our calculations here.[13,20] Complex representations are used in most recent published calculations.[c]

We could simplify the Hamiltonian further by separating ν_1 and ν_4, since we assume $\kappa_1^A = \kappa_1^E$,[21] but it is convenient to solve both simultaneously and generate the combination bands.

---

[b] Each large number designates a vibrational mode, the subscript is the quantum number of the ion vibrational level, and the superscript is the neutral quantum number for the transition.

[c] Note that the two BF_3^+ papers (Ref. 8 and 9) use different conventions.

Peak positions and intensities: diagonalization

The next step in the calculation is diagonalization of the Hamiltonian sub-matrix $\mathbf{H}_{MJ}$ for each $M_J \geq 0$. The diagonalization routine is a standard algorithm from the Numerical Algorithms Group (NAG) library; since the maximum dimensions of the submatrices wre 250x250, no special techniques were required.

Diagonalization of each N_{MJ} x N_{MJ} submatrix yields N_{MJ} eigenvalues and N_{MJ} eigenvectors. The eigenvalues are the vibronic line positions. Each eigenvector has N_{MJ} elements, which are the expansion coefficients of the N_{MJ} basis functions in that submatrix:

$$\psi_i^{M_J} = c_{1,i}^{M_J}\phi_1^{M_J} + c_{2,i}^{M_J}\phi_2^{M_J} + \ldots + c_{N,i}^{M_J}\phi_N^{M_J} \qquad (5.2.17)$$

We checked our calculations by reproducing the eigenvalues and eigenvectors calculated for the $C_6H_6^+$ (E + B) x e problem by van der Waals et al..[19]

Most calculations of this type neglect hot bands, so only the overlap with the anion ground state $|n_1^-=0,n_4^-=0\rangle$ is required. In that case, the only neutral states which will contribute to the spectrum will be those with non-zero coefficients of the basis functions $|\mathbf{A};\ 0,0\rangle$, $|\mathbf{E}_+;\ 0,0\rangle$, and $|\mathbf{E}_-;\ 0,0\rangle$. Since these three basis functions appear in the M_J = 0, +1 and -1 sub-matrices respectively, the M_J = 0 and +1 sub-matrices must be diagonalized, and the peak intensity for the transition between the anion ground state $|n_1^- = 0,\ n_4^- = 0\rangle$ and neutral vibronic state $\langle i|$ will be

$$I\,(\,i \leftarrow 0,0) \propto \sum_{M_J=0}^{1} \left\{ \left(\sum_{j=1}^{N_M} c_{j,i}^{M_J}\, \tau_j\, \delta_{n_1^j,0}\, \delta_{n_4^j,0} \right)^2 \left(2-\delta_{0,M_J} \right) \right\} \qquad (5.2.18)$$

where the jth basis function in the ith eigenvector has quantum numbers n_1^j, n_4^j and expansion coefficient $c_{j,i}^{MJ}$. τ_j is the electronic transition dipole moment for the electronic state corresponding to the jth basis function, and the τ_j are assumed to be independent of the nuclear displacement. The factor of $(2-\delta_{0,MJ})$ accounts for contributions from the $\pm M_J$ submatrices for $M_J \neq 0$.

To calculate the intensities of transitions from the anion excited vibrational states $|n_1^-, n_4^-\rangle$, we must include a sum over all degenerate sub-levels $|n_1^-, n_4^-, l_4^-\rangle$:

$$I\left(i \leftarrow n_1^-, n_4^-, l_4^-\right) \propto \sum_{M_J=0}^{n_4^-+1} \left\{ P\left(n_4^-\right) \left[\sum_{l_4^- = -n_4^-}^{n_4^-} \left(\sum_{j=1}^{N_M} c_{j,i}^{M_J} \tau_j \delta_{n_1^j,n_1^-} \delta_{n_4^j,n_4^-} \right)^2 \delta_{l_4^j,l_4^-} \right] \left(2-\delta_{0,M_J}\right) \right\} \qquad (5.2.19)$$

Although we are now summing over the degenerate anion levels, the factor of $(2-\delta_{0,MJ})$ is not redundant; we sum over $M_J \geq 0$ only, and all the basis functions in the $M_J>0$ sub-matrices have $l_4 \geq 0$. The anion levels with $l_4^- < 0$ will thus have zero overlap with the neutral levels of the $M_J>0$ sub-matrices; we include the sum over all l_4^- because the $l_4^- = -1$ levels will overlap with the $|E_-; n_1, n_4; l_4 = -1\rangle$ levels in the $M_J = 0$ submatrix.

$P(n_4^-) = \exp(-\beta\omega_4 n_4^-)$ is the population of the anion sub-level (n_4^-, l_4^-) relative to $P(n_4^- = 0)$, with $\beta = hc/kT$. No degeneracy factor need be included

in P because we calculate transitions between sub-levels. (We do not calculate hot bands in the ν_1 mode because they are not significant in our spectra.) Here, we must diagonalize all the sub-matrices with $M_J \leq n_4^-$, for a transition from the anion level n_4^- to a vibronic level which is nominally associated with the A electronic state. (For levels associated with the E states, we must diagonalize all sub-matrices with $M_J \leq n_4^- + 1$.) The M_J value also provides some information about vibronic symmetry, since eigenstates of the M_J=3n (n=0,1,2...) matrices are of **a** symmetry.

Simulation of the photoelectron spectrum

We now have six parameters with which to fit our experimental peak positions and intensities: ω_1, κ_1, ω_4, λ_4, τ_A/τ_E and temperature. Most calculations of this type use *ab initio* estimates of the unperturbed vibrational frequencies and coupling constants, but the controversy over theoretical calculations of the ground-state surface of NO_3 (section 5.1) has left us without a universally accepted potential energy surface. Instead, we estimated parameters from experimental results and our previous calculations on adiabatic surfaces.

The A-E electronic state splitting was fixed at 1.87 eV, from absorption spectra.[22] We assumed ω_1 = 1057 cm^{-1} (0.130 eV) to match our experimental measurement for the NO_3 $^2A_2'$ band. We calculated κ_1 = 0.165 eV from Eq. (5.2.15) to give the correct ratio of peak intensities in the ν_1 progression. For

the ion and neutral unperturbed frequency ω_4 we assumed the ion vibrational frequency of 720 cm^{-1} (0.107 eV) measured in matrix experiments (see section 5.1). Our first guess for λ_4 = 0.205 eV came from the calculations of section 5.1 (weighted by $1/\sqrt{2}$, as discussed earlier), and we adjusted λ_4 to get the correct position for the peak at 0.693 eV (363 cm^{-1}) in the experimental spectrum (Fig. 5.10). The ratio of electronic transition dipole moments τ_E/τ_A and the temperature were then adjusted to give optimal peak intensities in the simulated spectrum.

In all simulations, the calculated intensities were convoluted with Gaussian peaks of fwhm 18 meV. Although our instrumental resolution is normally a function of electron kinetic energy and would vary across this band, these spectra were taken under conditions of appreciable space charge and the peak width is constant at about 18 meV across the progression.

5.2.3. Results and Discussion

The best fit simulated spectrum is shown in Figure 5.10, superimposed on the experimental spectrum (266 nm, $\theta = 0°$). This simulation was obtained with ω_1 = 0.130 eV, κ_1 = 0.165 eV, ω_4 = 0.107 eV, λ_4 = 0.265 eV, τ_A/τ_E = 4.4 and T = 430 K. We used 15 basis functions in the ν_4 mode and 10 in ν_1, giving Hamiltonian sub-matrices with dimensions 250x250.

Figure 5.11 shows the stick spectrum that underlies the convoluted simulation of Fig. 5.10. Each of these peaks can be assigned to a vibrational

Figure 5.10: Simulated photoelectron spectrum of NO_3^- (266 nm, $\theta = 0^\circ$),
from the vibronic coupling calculation for the $^2A_2' - ^2E'$ interaction.
$\omega_1 = 0.130$ eV, $\kappa_1 = 0.165$ eV, $\omega_4 = 0.107$ eV, $\lambda_4 = 0.265$ eV, T = 430 K, $\tau_E/\tau_A = 4.4$.

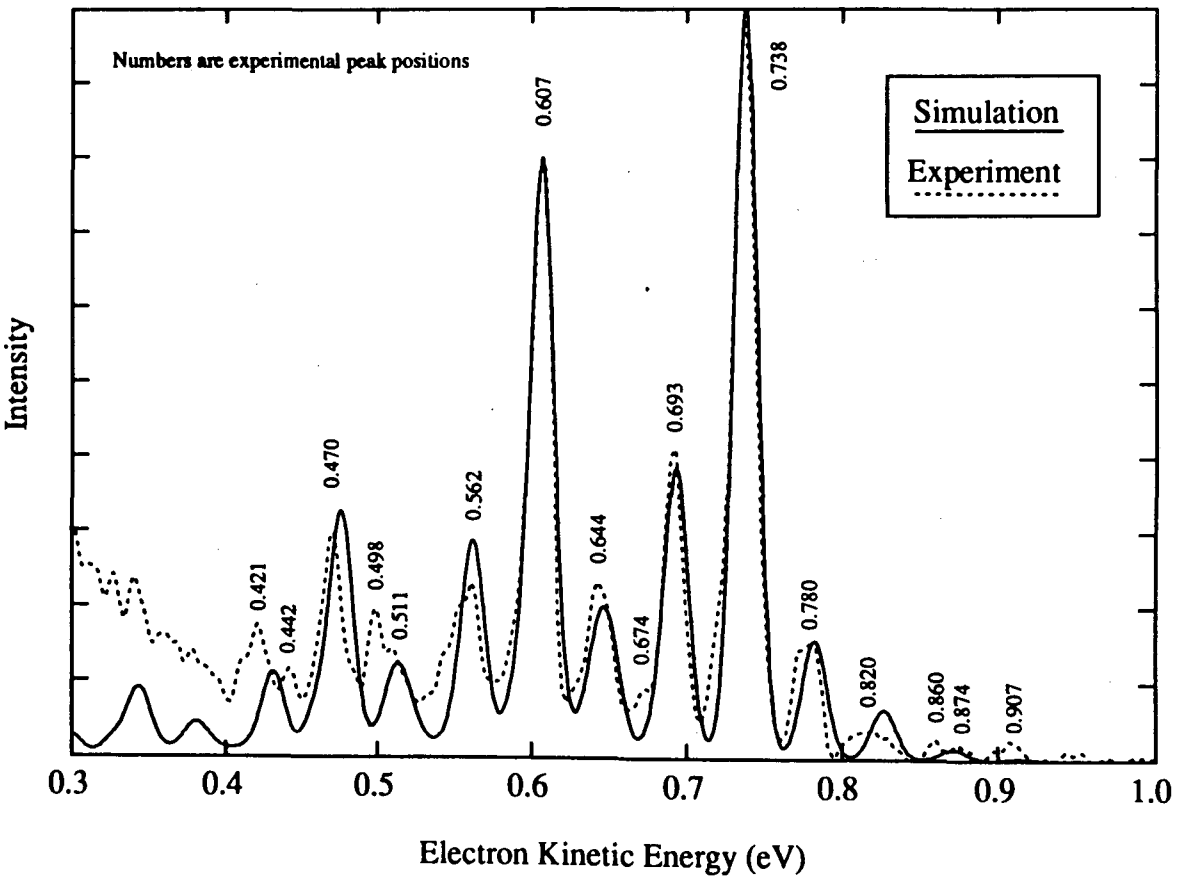

Figure 5.11: Simulated stick spectrum of the $^2A_2'$ band in the NO_3 photoelectron spectrum, from the vibronic coupling calculation.

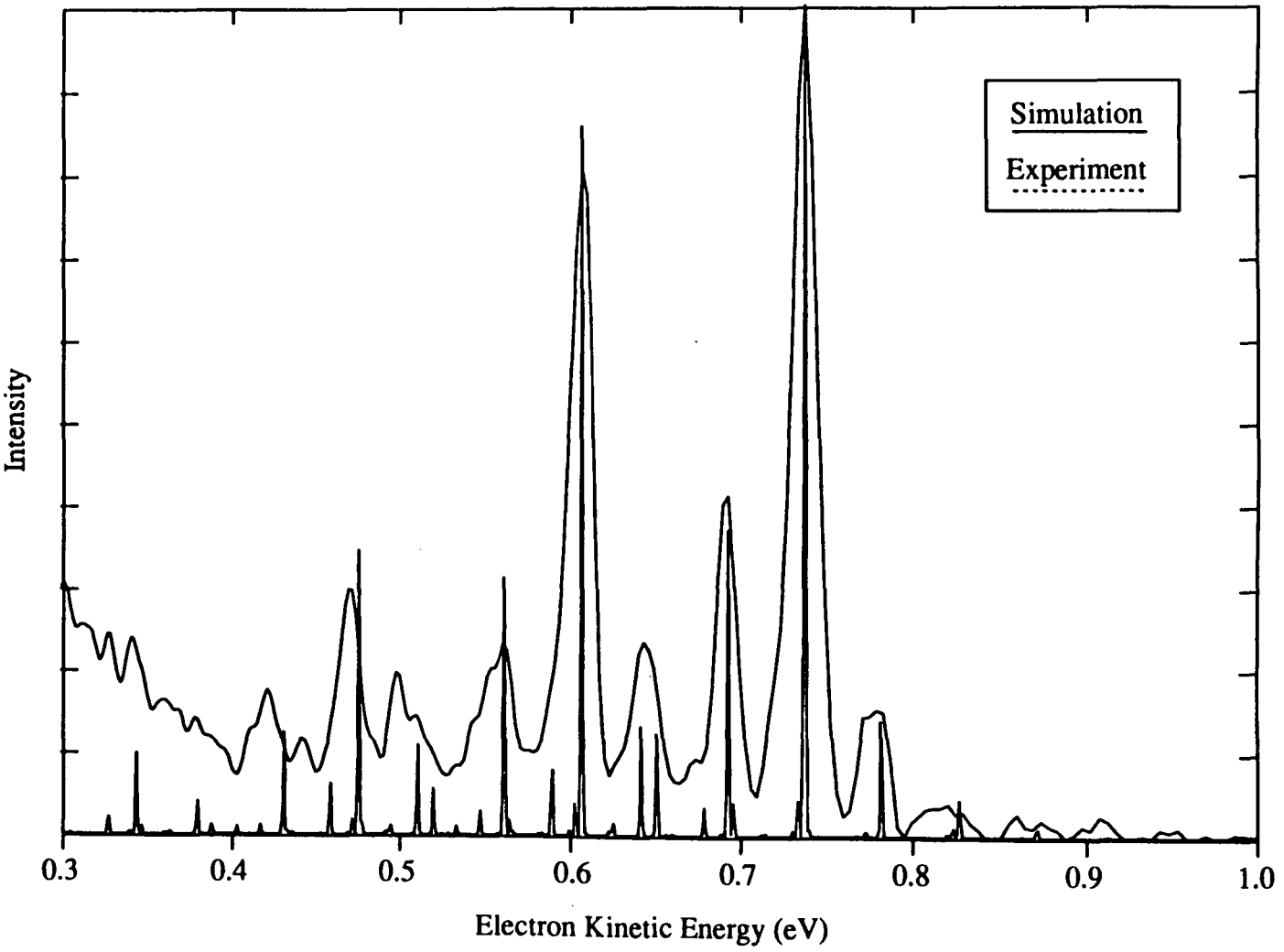

level within the electronic ground state; although Λ and l_4 are not strictly conserved, the coupling is weak enough that we can still assign peaks to vibronic states based on their 'Born-Oppenheimer parentage',[14] the unperturbed basis functions from which they resulted. Figure 5.12 shows the stick spectrum with assignments, and the simulated peak positions are compared to the experimental positions in Table 5.3.

We also obtained a photoelectron spectrum of NO_3^- at 266 nm at laser polarization angle $\theta = 90°$, which is shown in Figure 5.13. The $1_0^1 4_0^0$ and $1_0^0 4_0^1$ peaks are both relatively more intense than in the 0° spectrum. This intensity variation in the $v_4 = 1$ peak is explained by its mixing with the $v_4 = 0$ and 2 levels in the $^2E'$ state, and borrowing their electronic character. However, we cannot explain the variation in the $1_0^1 4_0^0$ peak intensity, which is just at the limit of the estimated uncertainty in peak height for each spectrum. At 213 nm, by contrast, there is no noticeable variation of the $1_0^1 4_0^0$ peak intensity with polarization. We decided to base our simulation on the θ=0° spectrum instead, because the ν_1 progression there could be reproduced better by a Poisson distribution.

The agreement between the simulation shown in Fig. 5.10 and our experimental spectrum at θ= 0° is very good. The $v_4 = 0$, 1, and 2 simulated and experimental peak positions and intensities match very well, although the agreement with peak positions at higher vibrational energy (low electron kinetic energy) is less satisfactory. This might be due to neglect of

Table 5.3: Experimental and calculated peak positions for the NO_3^- photoelectron spectrum at 266 nm, $\theta = 0°$. A complete list of simulated peak positions and assignments is given in Appendix 1.

Experimental position eV	cm^{-1}	Nominal assignment	Calculated position
0.820	-661	$1_0^0 4_1^0$	-720
0.780	-339	$1_0^0 4_1^1$	-357
0.738	0	$1_0^0 4_0^0$	0
		$1_0^1 4_1^0$	337
0.693	363	$1_0^0 4_0^1$	363
		$1_0^1 4_1^1$	700
0.644	758	$1_0^0 4_0^2$	775
0.607	1057	$1_0^1 4_0^0$	1057
		$1_0^0 4_0^3$	1195
0.562	1420	$1_0^1 4_0^1$	1420
0.511	1831	$1_0^2 4_1^1$	1757
0.498	1936	$1_0^1 4_0^2$	1832
0.470	2162	$1_0^2 4_0^0$	2114

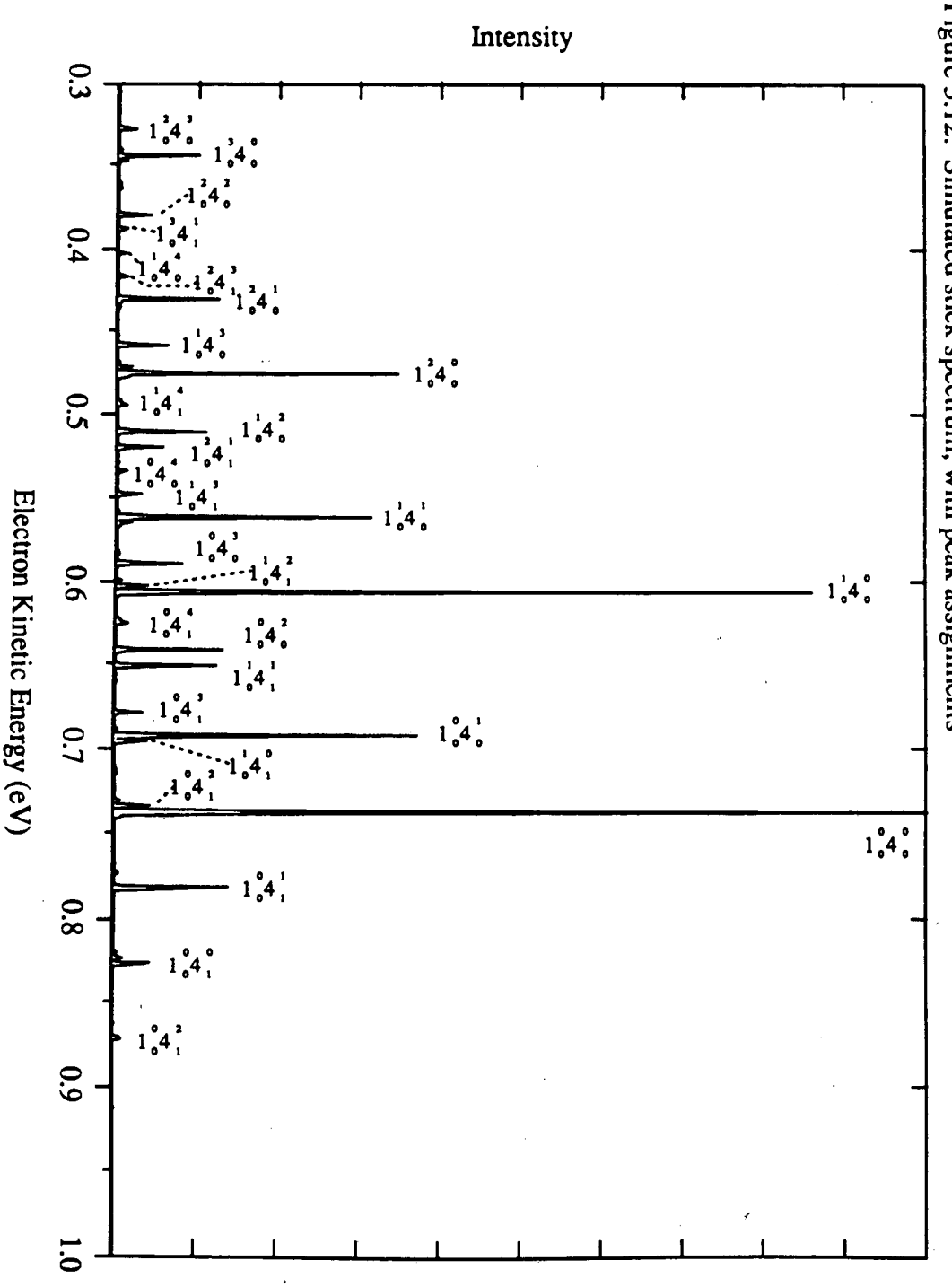

Figure 5.12: Simulated stick spectrum, with peak assignments

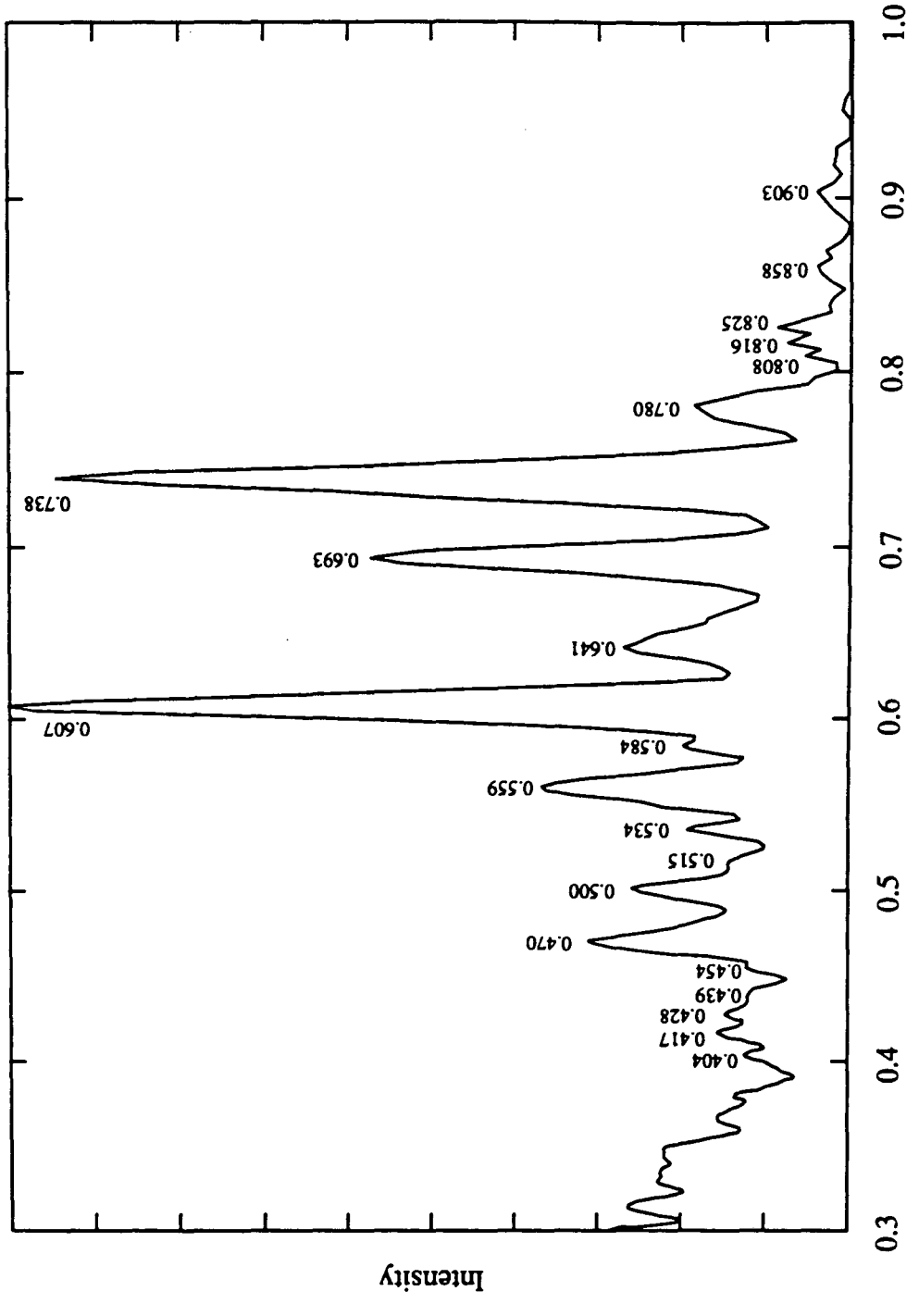

Figure 5.13: Photoelectron spectrum of NO_3^- at 266 nm, $\theta = 90^\circ$

anharmonicity in our oscillator potential. The simulated hot band positions and intensities are reproduced well. The experimental spectrum at 90° does not provide much additional information, although a few small peaks are more obvious at this angle.

This is the best simulation of our experimental results yet, and shows that a calculation which includes vibronic coupling effects can reproduce the anomalous structure of the ground-state band. A very important consequence of this calculation is that it provides quantitative validation for the vibronic coupling model, the **only** model for the NO_3 ground state that is consistent with all experimental results to date. Since the work described in section 5.1, new experimental studies of NO_3 have shown that vibronic coupling also explains the anomalous effects observed in high-resolution absorption spectra.[3] We briefly discuss those here, as well as new theoretical[23,24,25] work that is relevant to our analysis.

Comparison to high resolution experimental results

The high resolution infrared absorption spectra of Kawaguchi and coworkers[1,2,3] provide information complementary to ours. They observe progressions in the ν_2 and ν_3 modes which we do not see, but transitions to totally symmetric levels (including $v_1 = 1$) are forbidden in their spectra and the ν_4 frequency of 363 cm^{-1} is too low for them to observe the fundamental. Rotational analysis of the vibrational bands in these spectra requires vibronic

coupling to explain the unexpected behaviour of several fine-structure constants. Of particular interest to us is their conclusion (from the nature of the spin-orbit coupling constants) that the $^2A_2'$ and $^2E'$ states are coupled by both the ν_3 and ν_4 vibrations; we do not see any progression in ν_3, which implies that coupling in that mode is much weaker than that via ν_4.

Kawaguchi and coworkers have also recently observed several new vibrational bands in the NO_3 spectrum.[2] Although we do not calculate the ν_2 and ν_3 transitions, we can compare our simulation to their observed peak positions for the ν_1 and ν_4 combinations. For the $1_0^0 4_0^5$, $1_0^1 4_0^3$, and $1_0^2 4_0^1$ peaks, which they assign as 2024, 2155 and 2585 cm^{-1}, our simulated positions are 2097, 2252 and 2477 cm^{-1} respectively. The disagreement may be due to neglect of anharmonicity, and to propagation of our uncertainty in peak positions and fitting parameters due to our instrumental resolution.

One other interesting observation in the high-resolution spectra is the strong band observed by both Kawaguchi[2] and Friedl (in FTIR spectra[26]) at 1927 cm^{-1}, which has not yet been assigned. We do not find a transition at this energy in either the experimental or simulated spectrum, which implies that the 1927 cm^{-1} transition is not due to any combination of ν_1 and ν_4 alone, including hot bands.

The overall success of the vibronic coupling calculation in simulating the photoelectron spectrum suggests that this type of calculation for the NO_3 absorption spectra might facilitate interpretation of the high-resolution results.

Köppel and coworkers have performed such calculations for NO_2 and other molecules.[7]

Comparison with theoretical predictions

High level *ab initio* calculations on NO_3 continue to show symmetry breaking and C_{2v} minima at some levels, D_{3h} minima at others. Stanton, Gauss and Bartlett's CCSD results[24] give a triple-minimum potential energy surface for the NO_3 ground state. The D_{3h} point is a local maximum on this surface, and there are three equivalent C_{2v} minima with one long and two short N-O bonds. Conversion between these configurations proceeds via C_{2v} transition states which have two long N-O bonds, one short. Rapid conversion between the minima (pseudorotation[27]) gives an averaged D_{3h} geometry.

Can we reproduce our experimental spectra in simulations on this surface? We do not have an analytical fit to Stanton's surface, but the potential described by

$$V = \frac{1}{2} k r^2 - a|r| - \frac{1}{2} b r^2 \cos 3\theta \qquad (5.2.20)$$

has a similar form, with the D_{3h} maximum above the C_{2v} transition states between the minima. (This is the adiabatic potential for the lower sheet of a Jahn-Teller perturbed degenerate electronic state.[5]) The simulations discussed

in section 5.1 used a different form of triple-minimum potential,[d]

$$V = \frac{1}{2}kr^2 + a|r|(1 + \cos 3\theta) \qquad (5.2.21)$$

where the D_{3h} point is instead the transition state between the three C_{2v} minima and lies **below** the C_{2v} saddle points between the minima.

We carried out simulations on triple-minimum surfaces of the form of Eq. (5.2.20), assuming minima at -911 cm^{-1} and transition states at -719 cm^{-1} with respect to the D_{3h} maximum, to match the *ab initio* results. Energy levels and Franck-Condon intensities for the ν_4 mode were calculated using a two-dimensional DVR code,[28] as in the simulations described earlier in this chapter: in our initial calculation we tried simply to reproduce the ν_4 progression, and did not include hot bands or the ν_1 progression.

The calculations on the triple-minimum surface have only one adjustable parameter: k, the unperturbed oscillator frequency, which was adjusted to fit the peaks at 0.738, 0.693 and 0.644 eV (0, 363, 758 cm^{-1}). The best fit simulated spectrum is shown in Figure 5.14. This was obtained with k = 0.681 eV/Å^2, a = 0.368 eV/Å, and b = 0.040 eV/Å^2, assuming the origin to be at 0.738 eV. The agreement with peak positions is adequate (calculated positions are 0.738, 0.694, 0.668 and 0.635 eV / 0, 359, 562, and 829 cm^{-1}, for v_4 = 0, 2, 3, 4). The intensities, however, disagree completely. If we assume that the origin occurs at higher electron kinetic energy, we cannot match the peak positions

[d] This is the corrected form of the equation given in our first NO_3 paper.

Figure 5.14: Experimental and simulated spectra of NO_3^- (266 nm,θ= 0°) assuming a triple-minimum surface for NO_3 (ν_4 mode only). (Details in text.)

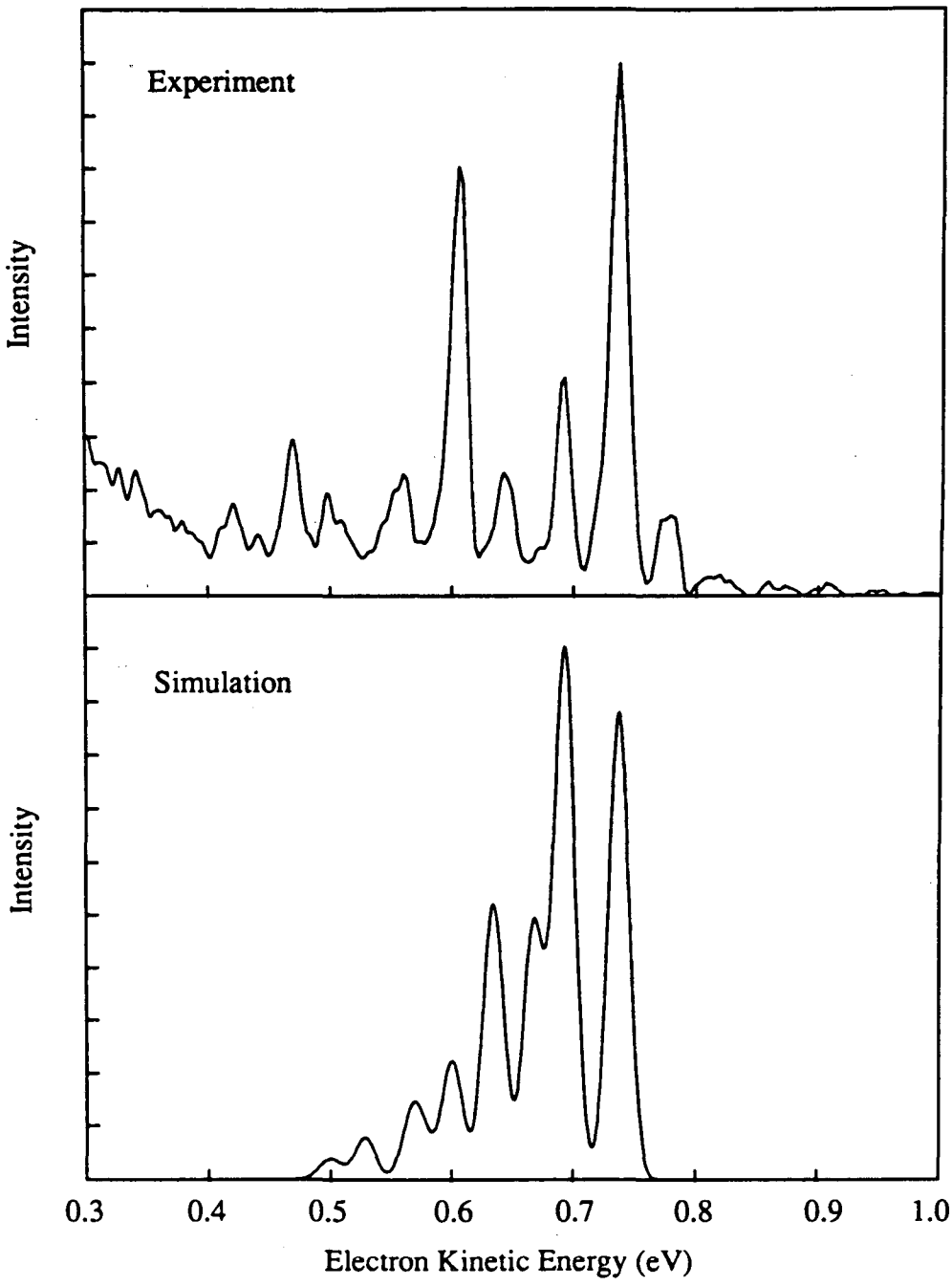

or intensities. Adding the ν_1 progression or hot bands would not solve this problem. This calculation predicts a low-lying e' state within about 100 cm^{-1} of the ground state, but no evidence of such a state has been observed in the high-resolution spectra.

The discrepancies between these simulations and the experimental spectra, combined with the results from section 5.1, suggest that a Franck-Condon analysis ignoring vibronic coupling is unlikely to reproduce our experimental results, regardless of the form of the ground-state potential. The ground-state equilibrium geometry of NO_3 is extremely sensitive to excitation of the ν_4 vibration, and including vibronic coupling is essential to any calculation.

5.2.4. The $^2E''$ band

Our calculations on the NO_3 ground state suggest that a vibronic coupling calculation should be valuable for analyzing the structure of the $^2E''$ band in the 213 nm photoelectron spectra ($\theta = 0°$, Figure 5.15, and $\theta = 90°$, Figure 5.16). The complexity and length of the $^2E''$ band suggest that the vibronic coupling involving this state is much stronger than that in the $^2A_2'$ state, and our ground-state calculations portend a difficult calculation for the $^2E''$ state vibronic coupling problem.

There are two Jahn-Teller active e' modes in the $^2E''$ state, ν_3 and ν_4, and the $^2E''$ and $^2E'$ states are coupled by the ν_2 vibration (a_2''). Although we could

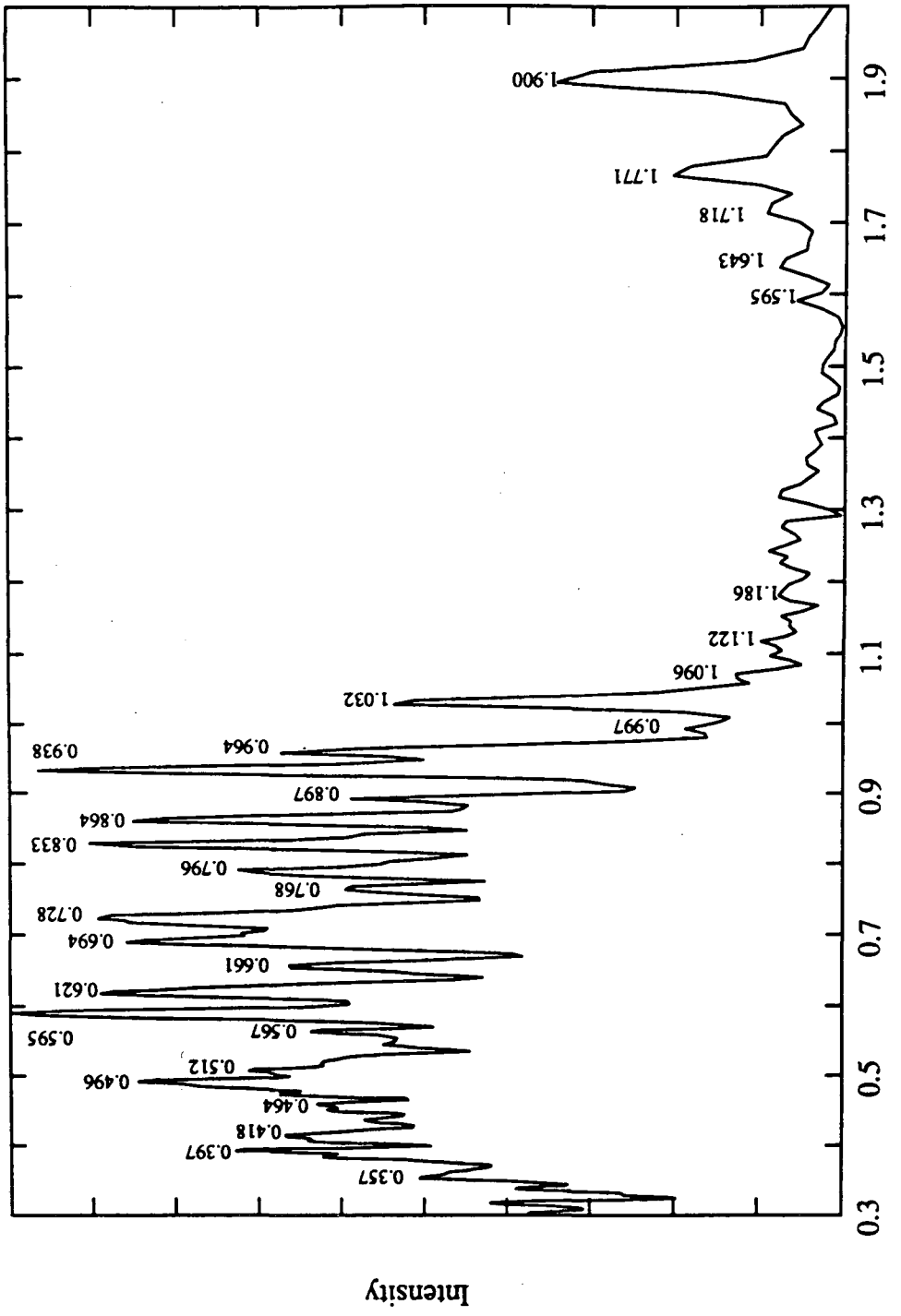

Figure 5.15: Photoelectron spectrum of NO_3^- at 213 nm, $\theta = 0.^\circ$

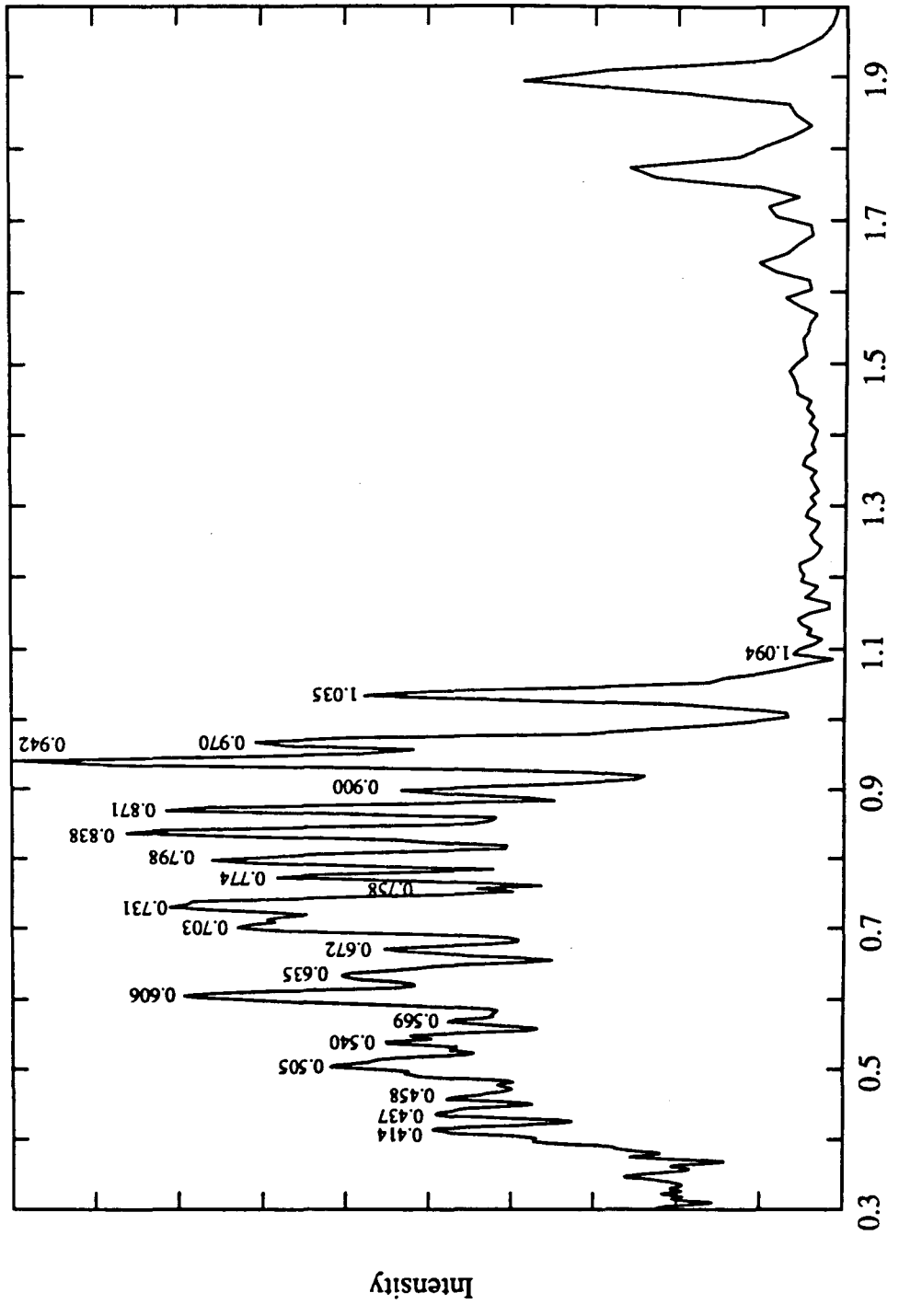

Figure 5.16: Photoelectron spectrum of $NO_3^{\cdot}$ at 213 nm, $\theta = 90^{\circ}$.

easily solve the problem for one Jahn-Teller active mode, the complexity of the band structure suggests that we would have to simultaneously consider at least the two Jahn-Teller active degenerate modes.[29] Even if convergence could be attained with a maximum occupation number of only 10 in each mode, the resulting Hamiltonian matrix would have dimensions of $N=10x10x10x10x2=2 \times 10^4$. The first-order Jahn-Teller perturbation (E x e) couples states with different K, so the Hamiltonian is no longer separable into submatrices by K and the entire 20,000x20,000 matrix must be diagonalized. In addition, since the energy range of the $^2E''$ band is much greater than that for the $^2A_2'$ band, we anticipate that much larger occupation numbers would be required than for the calculation described earlier. Problems of this magnitude require use of the Lanczos algorithm and other techniques suited to very large, sparse, banded matrices, as described by Köppel and coworkers. *Ab initio* calculations are also required, to provide coupling constants and vibrational frequencies for the $^2E''$ state, and we hope that the current theoretical interest in this problem will result in calculations of these parameters for the $^2E''$ state.

Kaldor's recent calculation[25] predicts that the $^2E''$ state will split into two Jahn-Teller components, $^2B_1$ at 0.890 eV above the ground state and $^2A_2$ at 1.032 eV (0.998 eV and 0.856 eV eKE in the 213 nm spectrum). If this were to occur, then the transition from the ground state ($^2B_2$ in C_{2v} symmetry) to the $^2A_2$ state would be electric dipole-allowed. No transition in this range has been observed in infrared or other optical spectra, although the transition might be

very weak because it is only vibronically allowed. The $^2E''$ band in our spectra is very long and does not look like two distinct vibrational progressions, although the peaks below about 0.7 eV are slightly more intense at $\theta=0°$ than at 90°, suggesting that two distinct electronic states might be present. A definitive analysis of this band will require a full calculation.

5.2.5. The $^2E'$ band

The $^2E'$ band is at 1.87 eV above the ground state, too high to be observed at either 266 or 213 nm. Although we do not observe the $^2E'$ band in our spectra, we can simulate the spectrum and compare the ν_1/ν_4 structure to any that might have been observed in absorption spectra.

We could obtain a photoelectron spectrum using an ArF excimer laser (193 nm, 6.43 eV), which would put the $^2E'$ band origin at about 0.62 eV. Figure 5.17 shows the simulated spectrum at 193 nm, obtained from the simulation for 266 nm by shifting the spectrum to higher energy. Note that the $^2E''$ band is not included in this calculation, and that the simulation considers only ν_1 and ν_4; if coupling via ν_2 and ν_3 were strong, the experimental spectrum would look very different.

The simulated $^2E'$ band dwarfs the $^2A_2'$ band in the simulated spectrum, due to the high τ_E/τ_A ratio. The magnitude of this ratio is extremely important in determining the borrowed peak intensity in the $^2A_2'$ state, and an experimental measurement would be very valuable as further validation of our

Figure 5.17: Simulated photoelectron spectrum of $NO_3^{\cdot}$ at 193 nm.

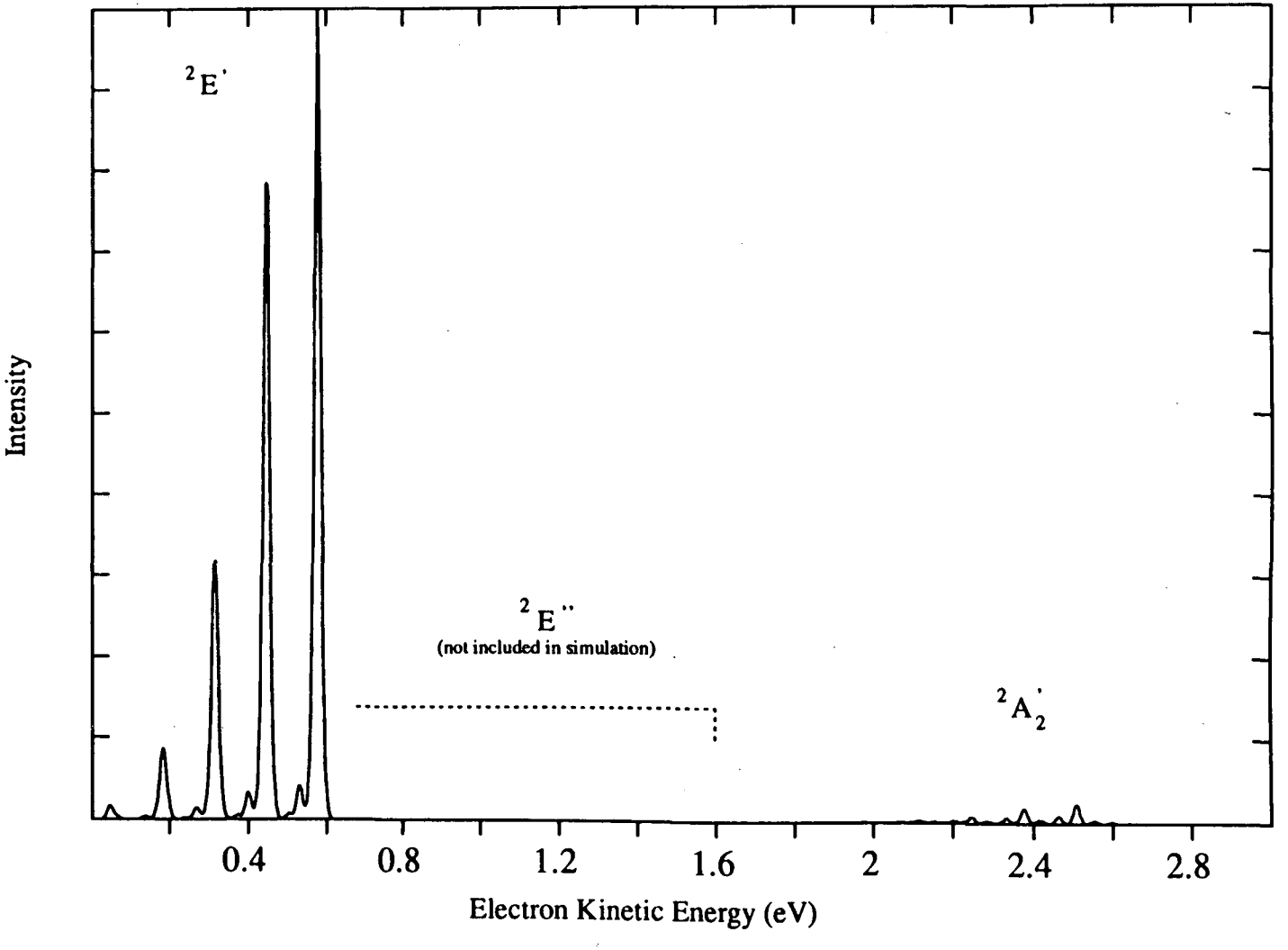

Figure 5.18: Simulated photoelectron spectrum of NO_3 at 193 nm. ($^2E'$ band only)

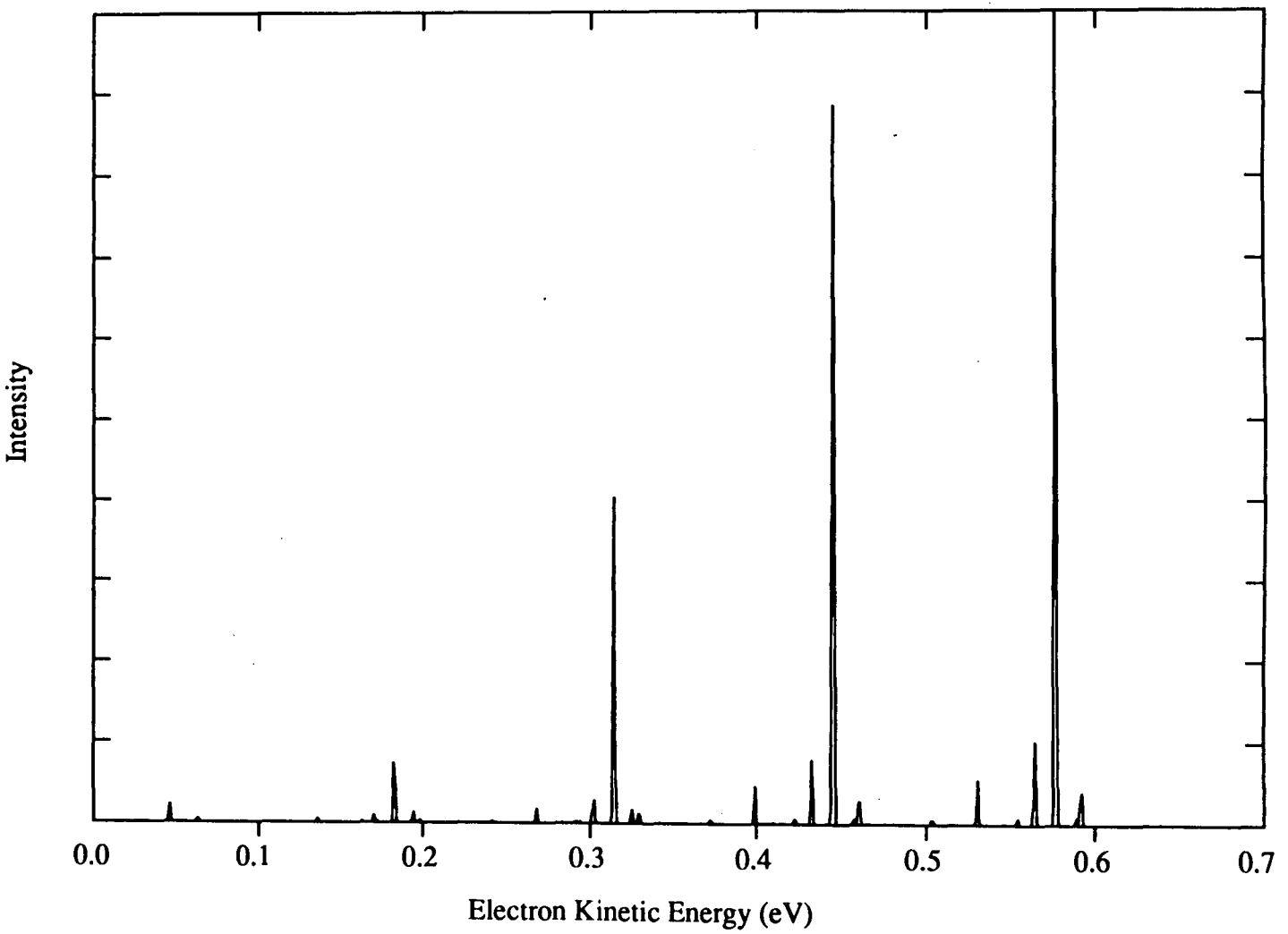

model.

Figure 5.18 shows the stick spectrum for the $^2E'$ band alone. The progression in ν_1 dominates the simulated photoelectron spectrum, with the ν_4 progression contributing only very small peaks. Spectra of the NO_3 $^2E'$ state obtained using other techniques[30,31,32] show the ν_1 progression dominating the spectrum ($\nu_1 \simeq 960$ cm^{-1}), with no evidence that the ν_4 progression is strongly excited; instead, the additional vibrational structure has been assigned to progressions in ν_2 and ν_3. The vibrational structure is much less complex than that observed in the $^2E''$ band in our spectra, implying that vibronic coupling is much stronger in the $^2E''$ state.

5.2.6. Conclusions

We have shown that a vibronic coupling calculation can reproduce the peak positions and intensities of the NO_3 $^2A_2'$ ground-state band in the photoelectron spectrum of NO_3^- at 266 nm. This is the first application of this method to a negative ion photoelectron spectrum, and includes calculation of hot band positions and intensities.

The $^2E''$ band cannot be further analyzed without a vibronic coupling calculation, which would be aided by the *ab initio* computation of vibrational frequencies and coupling constants.

Acknowledgements

This research was supported by the Air Force Office of Scientific Research under grant no. AFOSR-91-0084. A.W. thanks Ricky Metz for helpful discussions and for his DVR code. We thank Uzi Kaldor for a preprint of his results, and Randy Friedl for communicating his results to us prior to publication.

References for section 5.2:

1. K. Kawaguchi, E. Hirota, T. Ishiwata and I. Tanaka, J. Chem. Phys. **93**, 951 (1990).

2. K. Kawaguchi, T. Ishiwata, I. Tanaka and E. Hirota, Chem. Phys. Lett. **180**, 436 (1991).

3. E. Hirota, K. Kawaguchi, T. Ishiwata and I. Tanaka, J. Chem. Phys. **95**, 771 (1991).

4. H.C. Longuet-Higgins, U. Öpik, M.H.L. Pryce and R.A. Sack, Proc. Roy. Soc. London **A244**, 1 (1958).

5. H.C. Longuet-Higgins, Adv. Spectrosc. **2**, 249 (1961).

6. L.S. Cederbaum and W. Domcke, Adv. Chem. Phys. **36**, 205 (1977).

7. H. Köppel, W. Domcke, and L.S. Cederbaum, Adv. Chem. Phys. **57**, 59 (1984).

8. E. Haller, H. Köppel, L.S. Cederbaum, G. Bieri and W. von Niessen, Chem. Phys. Lett. **85**, 12 (1982).

9. E. Haller, H. Köppel, L.S. Cederbaum, W. von Niessen and G. Bieri, J. Chem. Phys. **78**, 1359 (1983).

10. S. Califano, *Vibrational States* (Wiley, New York, 1976), p. 35.

11. I.B. Bersuker and V.Z. Polinger, *Vibronic Interactions in Molecules and Crystals* (Springer-Verlag, New York, 1989), p. 33.

12. An elementary discussion may be found in T. Carrington, Acc. Chem. Res. **7**, 20 (1974).

13. W. Domcke, H. Köppel and L.S. Cederbaum, Mol. Phys. **43**, 851 (1981).

14. M.Z. Zgierski and M. Pawlikowski, J. Chem. Phys. **70**, 3444 (1979).

15. M.S. Child and H.C. Longuet-Higgins, Phil. Trans. Roy. Soc. London **254**, 259 (1961).

16. T.C. Thompson, D.G. Truhlar and C.A. Mead, J. Chem. Phys. **82**, 2392 (1985).

17. H. Köppel, L.S. Cederbaum, W. Domcke and W. von Niessen, Chem. Phys. **37**, 303 (1979).

18. R. Englman, *The Jahn-Teller Effect in Molecules and Crystals*, (Wiley-Interscience, London, 1972), p. 234.

19. J.H. van der Waals, A.M.D. Berghuis and M.S. de Groot, Mol. Phys. **21**, 497 (1971).

20. H. Köppel, L.S. Cederbaum, W. Domcke and S.S. Shaik, Angew. Chem. Int. Ed. Engl. **22**, 210 (1983).

21. Ref. 7, p. 78.

22. R.A. Graham and H.S. Johnston, J. Phys. Chem. **82**, 254 (1978).

23. V.R. Morris, S.C. Bhatia and J.H. Hall, Jr., J. Phys. Chem. **94**, 7414 (1990).

24. J.F. Stanton, J. Gauss and R.J. Bartlett, J. Chem. Phys. **94**, 4084 (1991).

25. U. Kaldor, Chem. Phys. Lett. **185**, 131 (1991).

26. R.R. Friedl, private communication (1991).

27. H.L. Strauss, Ann. Rev. Phys. Chem. **34**, 301 (1983).

28. R.B. Metz (Chemistry Dept., University of California, Berkeley); J.C. Light, I.P. Hamilton and J.V. Lill, J. Chem. Phys. **82**, 1400 (1985).

29. E. Haller, L.S. Cederbaum and W. Domcke, Mol. Phys. **41**, 1291 (1980).

30. R.A. Graham and H.S. Johnston, J. Phys. Chem. **82**, 254 (1978).

31. D.N. Mitchell, R.P. Wayne, P.J. Allen, R.P. Harrison and R.J. Twin, J.C.S. Faraday **II**, **76**, 785 (1980).

32. H.H. Nelson, L. Pasternack and J.R. McDonald, J. Phys. Chem. **87**, 1286 (1983).

6. Transition state spectroscopy

In this chapter, we discuss our work on neutral systems very different to the bound NO_2 and NO_3 molecules: the unstable and metastable transition state complexes of neutral bimolecular reactions.

6.1. Introduction

Transition state spectroscopy is motivated by a central problem in reaction dynamics -- that of describing a chemical reaction in microscopic detail. Describing a complex reaction is a great challenge because of the many details involved -- which reactant molecule orientations favour reaction, the structure of the intermediate complex, the vibrational and rotational state distribution of the product molecules, the rate of reaction, and more -- all of which are described by the multidimensional potential energy surface for the reaction.[1] A primary goal of research in reaction dynamics is the development of these potential energy surfaces: of critical importance is the region of each potential surface where reactants are transformed into products, through a series of configurations that we shall loosely call the transition state.[2]

To determine potential energy surfaces we rely on a combination of experimental and theoretical work, since neither one alone is sufficient. Only the simplest reactions - $H + H_2$, or at best $F + H_2$ - can be modelled accurately by *ab initio* calculations. Experimental information about the potential energy surface is usually limited to information specific to the asymptotic regions

(reactants and products), or measurements of overall quantities like rate constants. Model potential energy surfaces can be constructed, incorporating experimental information about reactants and products, reaction activation energy[a] and other parameters. Calculations on these surfaces predict product state distributions, reaction rates and cross sections which can be compared to experimental results, if available, and the model surface is successively refined to obtain the best possible agreement with experiment.

This approach, although useful, restricts the accuracy of the calculated surface. The reaction outcome depends on nuclear and electronic motion in the transition state region, yet the details of the potential energy surface in this region are often inferred from measurements of the reactant or product state distributions.

Direct examination of transition state species is a great challenge to the experimentalist. Conventional spectroscopic techniques generally cannot be used to study transition state species: the conversion process only takes about a picosecond, and the transient neutrals cannot be formed in high enough concentrations. Several experiments have been devised to circumvent these

---

[a] The activation energy, E_a, is an empirical quantity. It can be related to the classical barrier height E^* along the minimum energy path on the potential energy surface by several methods: one of the simplest gives $E_a = E^* -$ zpe(reactants) - zpe(transition state) (H.F. Schaefer, J. Phys. Chem. **89**, 5336 (1985)).

problems. Among them are the time-resolved experiments of Zewail and coworkers,[3] who study the evolution of an excited neutral complex into fragment molecules on the femtosecond time scale. Our technique represents a different class of experiment, designed to determine the electronic and vibrational energy levels and nuclear configuration for the transition state complex.

Many unstable neutral transition state species are free radicals which form stable negative ions. We can exploit this property by using negative ion photoelectron spectroscopy to determine the vibrational and electronic energy levels of the neutral transition state species. A schematic diagram of the photodetachment process is shown at right. Although the experimental technique is the same as that discussed in earlier chapters for bound neutrals, here the neutral molecule is **unstable** with respect to dissociation. We require instead that the **ion** be stable, and that the geometry of the negative ion be similar to that at the transition state region of the neutral potential energy surface, to ensure good Franck-

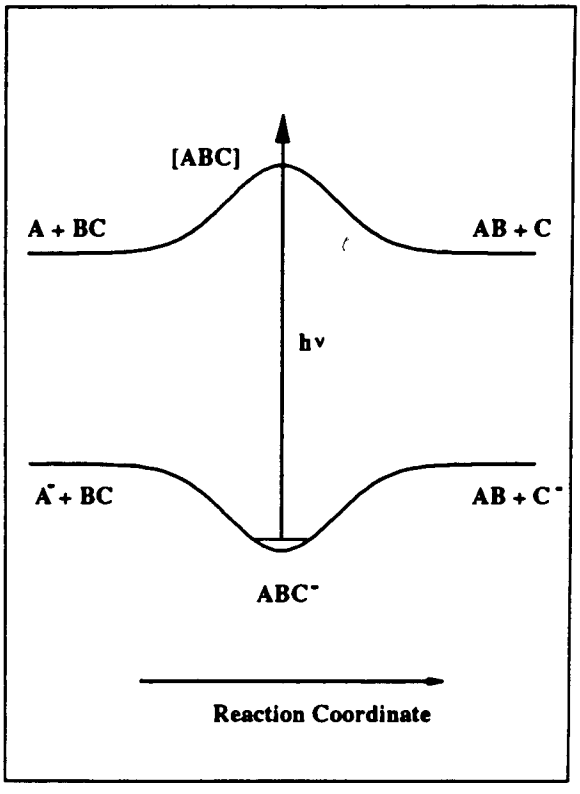

Condon overlap of the ion and neutral transition-state wavefunctions. Our experiment thus has the advantage of being sensitive to only one part of the potential energy surface, the Franck-Condon region.

A significant advantage of our technique over crossed molecular beams and other scattering experiments results from the neutral rotational state distribution. We use a free jet expansion in the ion source, so we produce a relatively narrow ion rotational state distribution and thus also a narrow neutral state distribution. In scattering experiments, however, sharp structure may be broadened out by the averaged contributions from reactants in many angular momentum states, and the features of interest may not be recognizable.

How does our information about the neutral energy levels relate to our goal of developing the potential energy surface? Although our experimental results cannot be directly inverted to give information about the potential energy surface, calculations on model surfaces give simulated spectra that can be compared with the experimental results. These simulations are generally very sensitive to the details of the transition state region of the potential energy surface, and indicate which aspects of the model surface require alterations.

We obtain the most information about the potential energy surface if the neutral species is relatively long-lived, although structure can still be observed in the photoelectron spectrum even when this is not true. If the transition

state species is unstable with respect to motion in any coordinate, then any features observed in the photoelectron spectrum are relatively broad (e.g. the photoelectron spectra of $CH_3OH \cdot F^-$ [4]). If the complex is stable with respect to motion perpendicular to the reaction coordinate, the peaks are narrower and more distinct. In the best case, that the complex is quasi-bound along the reaction coordinate, it may be relatively long-lived and the structure in the photoelectron spectrum relatively sharp.

These latter long-lived neutral species differ from van der Waals molecules and other bound states, which exist as a consequence of local minima in the potential energy surface. Rather, we are most interested in long-lived quasi-bound states which exist at the saddle point for many reactions. These states are responsible for the reactive scattering resonances[5] often predicted in quantal scattering calculations but experimentally observed in only a very few reactions.

The F + H_2/DH/D_2 reactions were the first for which experimental evidence of resonances was obtained, via crossed molecular beams experiments.[6] We studied these reactions by photoelectron spectroscopy of FH_2^- and its isotopic analogues, and our results are discussed at length in Chapter 7.

Other reactions predicted to show reactive scattering resonances include the heavy + light-heavy combinations X + HY, (X,Y = I, Br, Cl, F), and we include our work on I + HI here as one of the most interesting examples.

Early interest in these reactions was provoked by possible applications to chemical lasers, plus more general questions about the role of vibrational energy in these reactions,[7] and experimental work included determinations of product vibrational and rotational state distributions and rate constant measurements, particularly for the asymmetric reactions ($X \neq Y$).[8] The extreme mass combination, particularly for I + HI, has also made these reactions an important test of new scattering calculations.

Theoretical work on the X + HY reactions was motivated by early predictions of several interesting dynamic effects. First, translational energy appears to be conserved in these reactions, and so the thermoneutral X + HX(v) $\rightarrow$ XH(v') + X reactions are vibrationally adiabatic (v=v').[9] Second, calculations predict oscillations in reaction probability as a function of energy, and superimposed sharp resonance structure. Quantum mechanically, the oscillations are caused by resonance interference between wavefunctions for vibrationally adiabatic states of opposite parity. The classical analogue is that the light atom hops back and forth between the heavy atoms.[9]

The same extreme mass combination that makes I + HI the best example of these dynamical phenomena makes it impossible to obtain an accurate *ab initio* potential energy surface for this reaction, and necessitates making several approximations in scattering calculations on model potential energy surfaces.

The reaction is assumed to be collinear,[a] which simplifies scattering calculations because it allows the neglect of angular momentum effects. Hyperspherical coordinates (a form of mass-weighted polar coordinates)[10] are used, since for I + HI the skew angle between axes in mass-weighted skewed coordinates[11,12] is very small (7.2°),[13] complicating the problem. With inclusion of the DIVAH (diagonal vibrationally adiabatic hyperspherical) approximation,[14] the coordinates used for the 2D scattering calculation become very close to the normal coordinates for IHI. One designates heavy atom separation, the symmetric stretching motion, and the other the light atom position, the antisymmetric stretch. As a consequence of this adiabatic separation of slow and fast motions, a third dynamic phenomenon appears in scattering calculations on I + HI: calculations on I + HI predicted that bound states of the IHI transition state complex existed, even on purely repulsive potential energy surfaces.

These 'vibrationally bound' states were found first in collinear calculations[15] and exist even in three-dimensional calculations,[16] although

---

[a] A description of a triatomic reaction, A + BC, requires three coordinates and thus a four-dimensional potential energy surface. Representations of potential energy surfaces are often simplified by fixing the bond angle, so that the surface can be plotted in two dimensions as an energy contour diagram. Collinear surfaces assume a 180° bond angle.

the number of bound states decreases. These states exist because adiabatic separability is imposed on the nuclear degrees of freedom. Motion along the reaction coordinate corresponds to the symmetric stretch; motion perpendicular to that is the antisymmetric stretch. In the reactant and product valleys, the walls are relatively steep and the antisymmetric stretching frequency high. As the reaction proceeds towards the strong interaction region the potential energy along the minimum energy path increases, but the walls come less steep and the antisymmetric stretching frequency drops. At the top of the barrier, the potential is very broad and flat-bottomed. The condition for the existence of vibrationally bound states is that the decrease in zero point energy between the asymptotic region and the saddle point must exceed the barrier height. The system is then trapped in an effective minimum in the vibrationally adiabatic potential curve for the symmetric stretching states, and the halogen atoms are held together by rapid oscillation of the hydrogen atom between them.

The heavy + light-heavy reactions thus appeared to be ideal candidates for our transition state technique. Although the saddle point region would not normally support stationary vibrational states, we might observe sharp structure corresponding to resonance energies or to vibrationally bound states, as we discussed earlier. Several other conditions were also fulfilled. Stable XHX^- and XHY^- negative ions had been observed,[17] and the XHX^- ions were believed to be linear, symmetric ions with geometries similar to those at the

transition state regions of the neutral collinear model potential energy surfaces. The reactions were believed to be electronically adiabatic,[8,18] each occurring on a single potential energy surface, and we did not expect contributions from excited electronic states to complicate the spectra.

Our first experiments studied the Cl + HCl reaction,[19] and we went on to study all the X + HY reactions, symmetric and asymmetric.[20] The IHI^- spectra are particularly interesting because the structure is exceptionally sharp. Section 6.2 contains a short paper on the I + HI reaction that was written soon after we began our experiments, and section 6.3 briefly summarizes recent progress on I + HI.

References for section 6.1

1. G.M. Fernandez, J.A. Sordo and T.L. Sordo, "Analysis of Potential Energy Surfaces", J. Chem. Ed. **65**, 665 (1988), provide an elementary explanation of potential energy surfaces in general and the importance of the transition state.

2. J.C. Polanyi, Angew. Chem. Int. Ed. Engl. **26**, 939 (1987).

3. M. Gruebele and A.H. Zewail, *Physics Today*, May 1990, p.24. P.R. Brooks, Chem. Rev. **88**, 407 (1988).

4. S.E. Bradforth, D.W. Arnold, R.B. Metz, A. Weaver and D.M. Neumark, J. Phys. Chem. **95**, 8066 (1991).

5. R.J. Friedman and D.G. Truhlar, Chem. Phys. Lett. **183**, 539 (1991), provide a relatively short but very good elementary discussion of resonances in reactive scattering.

6. D.M. Neumark, A.M. Wodtke, G.N. Robinson, C.C. Hayden and Y.T. Lee, J. Chem. Phys. **82**, 3045 (1985). D.M. Neumark, A.M. Wodtke, G.N. Robinson, C.C. Hayden, K. Shobatake, R.K. Sparks, T.P. Schafer and Y.T. Lee, J. Chem. Phys. **82**, 3067 (1985).

7. J.C. Polanyi, Accts. Chem. Res. **5**, 161 (1972).

8. R.G. Macdonald and C.B. Moore, J. Chem. Phys. **73**, 1681 (1980).

9. C. Hiller, J. Manz, W.H. Miller and J. Römelt, J. Chem. Phys. **78**, 3850 (1983).

10. J.M. Launay and M. LeDourneuf, J. Phys. B: At. Mol. Phys. **15**, L455

(1982).

11. V.K. Babamov and R.A. Marcus, J. Chem. Phys. **74**, 1790 (1981).

12. B.C. Garrett, D.G. Truhlar, A.F. Wagner and T.H. Dunning, Jr., J. Chem. Phys. **78**, 4400 (1983).

13. J. Manz, R. Meyer, E. Pollak, J. Romelt and H.H.R. Schor, Chem. Phys. **83**, 333 (1984).

14. J. Römelt, Chem. Phys. **79**, 197 (1983).

15. J. Manz, R. Meyer, E. Pollak and J. Römelt, Chem. Phys. Lett. **93**, 184 (1982).

16. D.C. Clary and J.N.L. Connor, Chem. Phys. Lett. **94**, 81 (1983).

17. G. Caldwell and P. Kebarle, Can. J. Chem. **63**, 1399 (1985); C.M. Ellison, B.S. Ault, J. Phys. Chem. **83**, 832 (1979); K. Kawaguchi, E. Hirota, J. Chem. Phys. **87**, 6838 (1987); J. Chem. Phys. **84**, 2953 (1986). K. Kawaguchi, J. Chem. Phys. **88**, 4186 (1988).

18. N.C. Firth and R. Grice, J. Chem. Soc., Faraday Trans. II **87**, 1023 (1987).

19. R.B. Metz, T. Kitsopoulos, A. Weaver and D.M. Neumark, J. Chem. Phys. **88**, 1463 (1987).

20. (a) Cl + HCl and Br + HBr: R.B. Metz, A. Weaver, S.E. Bradforth, T.N. Kitsopoulos and D.M. Neumark, J. Phys. Chem. **94**, 1377 (1990). (b)F/Cl/Br + HI: S.E. Bradforth, A. Weaver, D.W. Arnold, R.B. Metz and D.M. Neumark, J. Chem. Phys. **92**, 7205 (1990). (c) Br + HI, F + HI, F + HBr: R.B. Metz, S.E.

Bradforth and D.M. Neumark, Adv. Chem. Phys., in press (1991).

6.2. Spectroscopy of the I + HI transition state region by photodetachment of IHI^-

A. Weaver, R.B. Metz,[a] S.E. Bradforth[b] and D.M. Neumark

Department of Chemistry, University of California, Berkeley, CA 94720

Abstract

The transition state region of the I + HI reaction has been studied by photoelectron spectroscopy of IHI^- and IDI^-. A well-resolved progression in the asymmetric stretch of the neutral IHI (IDI) complex is observed in each spectrum. These peaks apparently correspond to states of the complex that are unstable with respect to dissociation into I + HI (DI). The experimental peak positions, widths, and intensities are compared to simulated spectra generated from a collinear model potential energy surface. The results provide strong experimental evidence for quasi-bound states in heavy + light-heavy reactions.

Published in J. Phys. Chem. **92**, 5558 (1988).

[a] NSF Predoctoral Fellow

[b] Fulbright Scholar

6.2.1. Introduction

The construction of potential energy surfaces to describe chemical reactions is a primary goal of experimental and theoretical research in reaction dynamics. A critical element of this effort is an accurate description of the transition-state region: the area of the potential energy surface where chemical bond cleavage and formation occur. The importance of developing a direct probe of this region has motivated several versions of 'transition state spectroscopy'.[1] We have devised a new approach to this problem, in which the transition state region of a neutral bimolecular reaction is examined by photodetaching a stable negative ion similar in structure to the neutral transition-state complex. Photodetachment accesses the neutral potential energy surface under well-defined conditions, with the nuclei in the same configuration as in the ion. Any structure in the photoelectron spectrum of the ion then yields information about the transition-state region of the neutral surface.

We present here a study of the I + HI hydrogen-exchange reaction via photoelectron spectroscopy of IHI^- and IDI^-. This is an attractive system for our experiment. Matrix isolation studies[2] of IHI^-, in conjunction with recent high-resolution spectra[3] of the analogous ions FHF^- and $ClHCl^-$, imply that IHI^- is linear and centrosymmetric. If the minimum-energy path for the I + HI reaction is collinear, as has been assumed in most calculations,[4,5,6,7,8,9,10,11,12] the vertical photodetachment process should

access the transition-state region of the neutral potential energy surface. Most significantly, calculations on model I + HI surfaces predict that bound and long-lived vibrational states of the IHI complex exist.[4-10,13] The spectrum of these states is sensitive to the details of the surface near the transition state. Our experiment was motivated by the possibility that these states would appear as sharp structure in the photoelectron spectrum of IHI^-.

In work we reported recently,[14] the photoelectron spectrum of $ClHCl^-$ revealed a series of broad peaks which were assigned to a progression in the asymmetric stretch of the neutral ClHCl complex. The resolution of our instrument has been substantially improved since then. The IHI^- and IDI^- spectra reported here show well-resolved peaks of different widths, some only slightly wider than the instrumental resolution of 8 meV. We can interpret the positions and widths of these peaks using the same formalism that predicts quasi-bound states of the IHI complex.

6.2.2. Experimental section

A pulsed time-of-flight negative ion photoelectron spectrometer[15] is used in these experiments and will be described in detail in a future article.[16] Briefly, a 5% mixture of hydrogen iodide in argon at 2 atm pressure is expanded through a pulsed molecular beam valve and then crossed by a 1 keV electron beam just outside the valve orifice.[17] The resulting negative ions should cool internally in the free jet expansion. The ions are extracted form

the beam by a pulsed electric field and injected into a Wiley-McLaren time-of-flight mass spectrometer.[18] The ion beam crosses the pulsed photodetachment laser beam (Nd:YAG fourth harmonic, 266 nm) at the spatial focus of the mass spectrometer, 140 cm from the extraction region. A small fraction (0.01%) of the photodetached electrons is collected at the end of a 100-cm field-free flight tube orthogonal to the laser and ion beams. Electron kinetic energies are determined by time-of-flight analysis using a transient digitizer with 5 ns resolution. The measured spectrometer resolution is 8 meV at 0.65 eV electron kinetic energy and is proportional to $E^{3/2}$ at higher electron kinetic energy. The transmission of this system drops sharply at electron energies below 0.3 eV. The electron energy scale for each spectrum shown here was calibrated with Cl^-, Br^-, and I^- spectra taken on the same day. The ion density was sufficiently low that no space charge effects (peak broadening and shifting) were observed.

6.2.3. Results and Discussion

The photoelectron spectra of IHI^- and IDI^- each show three well-resolved peaks of widely varying widths (Figure 6.1) superimposed on an unstructured background. The highest energy peaks (labelled A) in these spectra coincide, and deuteration results in a large frequency shift of the two peaks at lower electron kinetic energy. Thus, peak A is the $0 \leftarrow 0$ transition of a progression in a vibrational mode in the neutral complex which primarily

Figure 6.1. Experimental and simulated photoelectron spectra of IHI^- and IDI^-. Experimental peak positions (peak widths, fwhm, in parentheses): IHI^-: 0.734 eV (0.074 eV), 0.560 (0.023), 0.369 (0.050). IDI^-: 0.734 (0.051), 0.608 (0.042), 0.486 (0.013). Peak A is the band origin in both spectra (see text). Average uncertainty in peak positions is ±5 meV. The relative energy of the I + HI(v=0) asymptotic channel is indicated by an arrow. Simulated spectra were derived from calculated Franck-Condon factors: broken vertical lines indicate continuum states. The simulated spectra have been shifted by -0.13 eV relative to I + HI(v=0) so that the $v_3' = 0$ transitions line up with the A peaks in the experimental spectra.

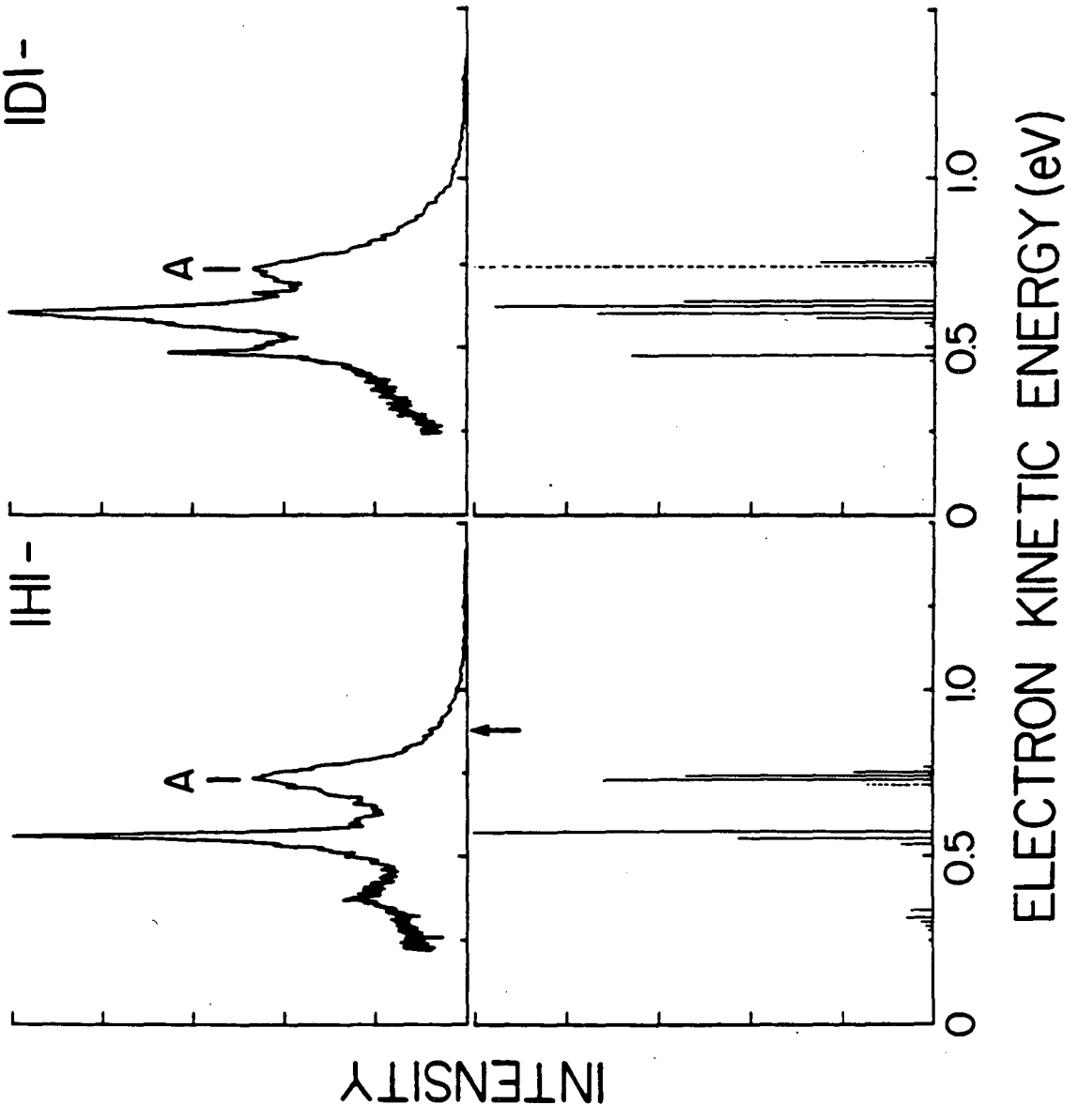
IDI-
IHI-
A
A
INTENSITY
0
0.5
1.0
0
0.5
1.0
ELECTRON KINETIC ENERGY (eV)

involves hydrogen atom motion, and the two slower peaks in each spectrum result from transitions to excited levels of this mode. We assign this progression to the asymmetric stretch (v_3) mode of the IHI complex rather than the bending mode. This assignment is supported by the analysis described below.

Since the v_3=0 state of the anion is totally symmetric, only transitions to even v_3' levels of the neutral are allowed. The three peaks in each spectrum therefore represent transitions to the v_3' = 0, 2 and 4 asymmetric stretch levels. (These are designated 0g, 1g and 2g, respectively, by Romelt.[5]) the measured spacing between the 0←0 and 2←0 transitions is 1360 ± 120 cm^{-1} and 1020 ± 120 cm^{-1} in the IHI^- and IDI^- spectra, respectively. This frequency is much smaller than the HI stretch (2309 cm^{-1}),[19] indicating that the hydrogen atom is interacting strongly with both iodine atoms as expected in the transition state region.

The energy of the I + HI (v = 0) asymptotic channel is indicated by the arrow in Figure 6.1. This energy is derived from the laser photon energy (4.66 eV), the electron affinity of iodine (3.0591 eV),[20] and the enthalpy of dissociation of IHI^- into I^- + HI(v=0) (0.74 ± 0.13 eV).[21] Based on these energies, all the observed peaks correspond to states of the IHI complex that lie above I + HI(v=0) and are therefore unstable with respect to dissociation. The small amount of signal to the right of the arrow may be from vibrationally excited ions.

Several theoretical papers have predicted the existence of bound states of IHI.[4,6,8,10,13,22] In order for the highest energy peak in each spectrum to be a transition to a bound state, the IHI^- dissociation energy would have to be at least 0.87 eV, which lies at the limit of the experimental error for the measured value. Thus, while our spectra suggest that bound states of IHI do not exist, this conclusion is not definitive.

In order to understand more fully the appearance of the spectra, particularly the striking variation in the peak widths, we consider asymmetric *and* symmetric stretch motion near the transition state on a collinear potential energy surface for the I + HI reaction. Figure 6.2 shows a model surface that has been used extensively in dynamical calculations for this reaction. This is a semiempirical, purely repulsive LEPS (London-Eyring-Polanyi-Sato) surface[23] with a barrier of 0.05 eV along the minimum energy path. The shaded area in Figure 6.2 shows the region of the surface accessible via photodetachment; it indicates where IHI^- in the vibrational ground state spends 95% of its time, assuming an inter-iodine distance R_{II} of 3.88 Å (see below).

Vibrational motion of the IHI complex in this region has been analyzed previously.[4-8,12] The modified hyperspherical coordinates ρ and z[24] in Figure 6.2 are convenient for this purpose. Here, $\rho=(m_{I,HI}/m_{HI})^{1/2} R_{II} = 7.981 R_{II}$ is the mass-weighted inter-iodine distance, and $z = 0.5(r_{IH} - r_{HI})$ corresponds to the position of the hydrogen atom between the iodine atoms. The symmetric

Figure 6.2. LEPS surface for the I + HI reaction, plotted in modified hyperspherical coordinates. Contours are at -2.6, -2.8, -3.0 and -3.16 eV with respect to three-atom dissociation. The saddle point is marked by a cross at R_{II} = 3.59 Å.

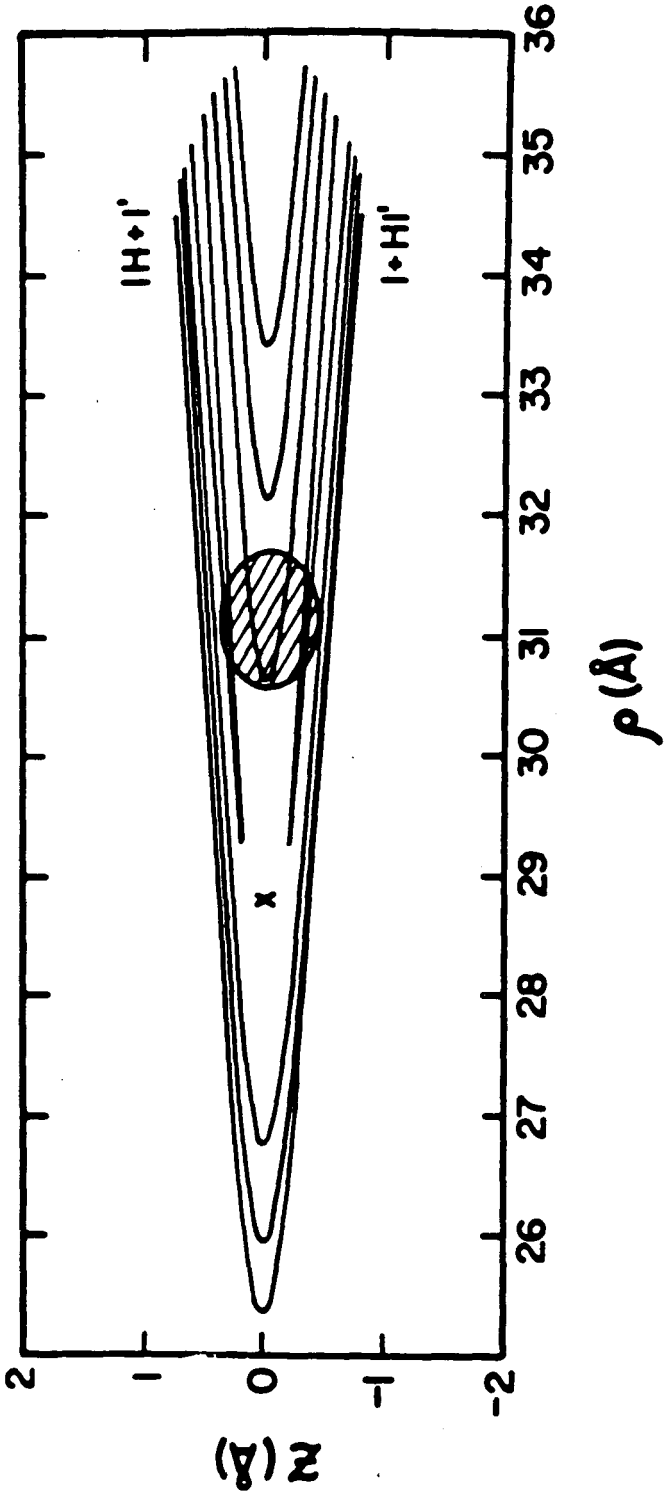
|H+I'
I+H|'
x
2
1
0
-1
-2
Z (Å)
26
27
28
29
30
31
32
33
34
35
36
ρ (Å)

stretch (v_1) vibration, in which only the iodine atoms move, occurs along the $z = 0$ line. In the asymmetric stretch the iodine atoms are nearly stationary while the hydrogen atom vibrates between them. This vibration occurs along a vertical line at constant ρ. The asymmetric stretch frequency is substantially higher than the symmetric stretch frequency because it involves light rather than heavy atom motion. This is the basis for the adiabatic separation of the symmetric and asymmetric stretch motions,[25] analogous to the Born-Oppenheimer separation of nuclear and electronic degrees of freedom. One solves for the asymmetric stretch levels at each ρ, obtaining a series of 'vibrationally adiabatic' curves (Figure 6.3) which are effective potentials for the *symmetric stretch* vibration. At large ρ, the $v_3' = 0, 2, 4$ curves correlate to the I + HI (DI) (v = 0, 1, 2) asymptotic energy levels (indicated by arrows in Figure 6.3).

Although the LEPS surface has no potential energy wells, each of these effective potentials has a minimum in the transition-state region.[4-6] These minima are sufficiently deep to support symmetric stretch states of the complex. Symmetric stretch states supported by the $v_3' = 0$ curve are bound since they lie below I + HI (DI) (v=0); these are 'vibrationally bound' states of IHI (IDI).[8] The symmetric stretch states supported by higher v_3' curves lie above I + HI (DI) (v=0) and are therefore quasi-bound. They lead to the sharp (0.1 meV wide) resonances that appear in reactive scattering calculations on this potential energy surface.[9]

Figure 6.3. Adiabatic curves for the v_3' = 0, 2 and 4 states of IHI and IDI and potential energy curve for the IHI^- and IDI^- symmetric stretch. The upper horizontal scale is the inter-iodine distance; the lower scale is the hyperspherical radius ($\rho \approx 7.981\ R_{II}$ for IHI, $5.679\ R_{II}$ for IDI). The vertical energy scale is referenced to three-atom dissociation. Arrows indicate relative energies of the I + HI (DI) (v = 0, 1, 2) asymptotic channels. The potential curve for IHI^- (IDI^-) is a harmonic oscillator centred at R_{II} = 3.88 Å and is plotted on the same scale as the adiabatic curves.

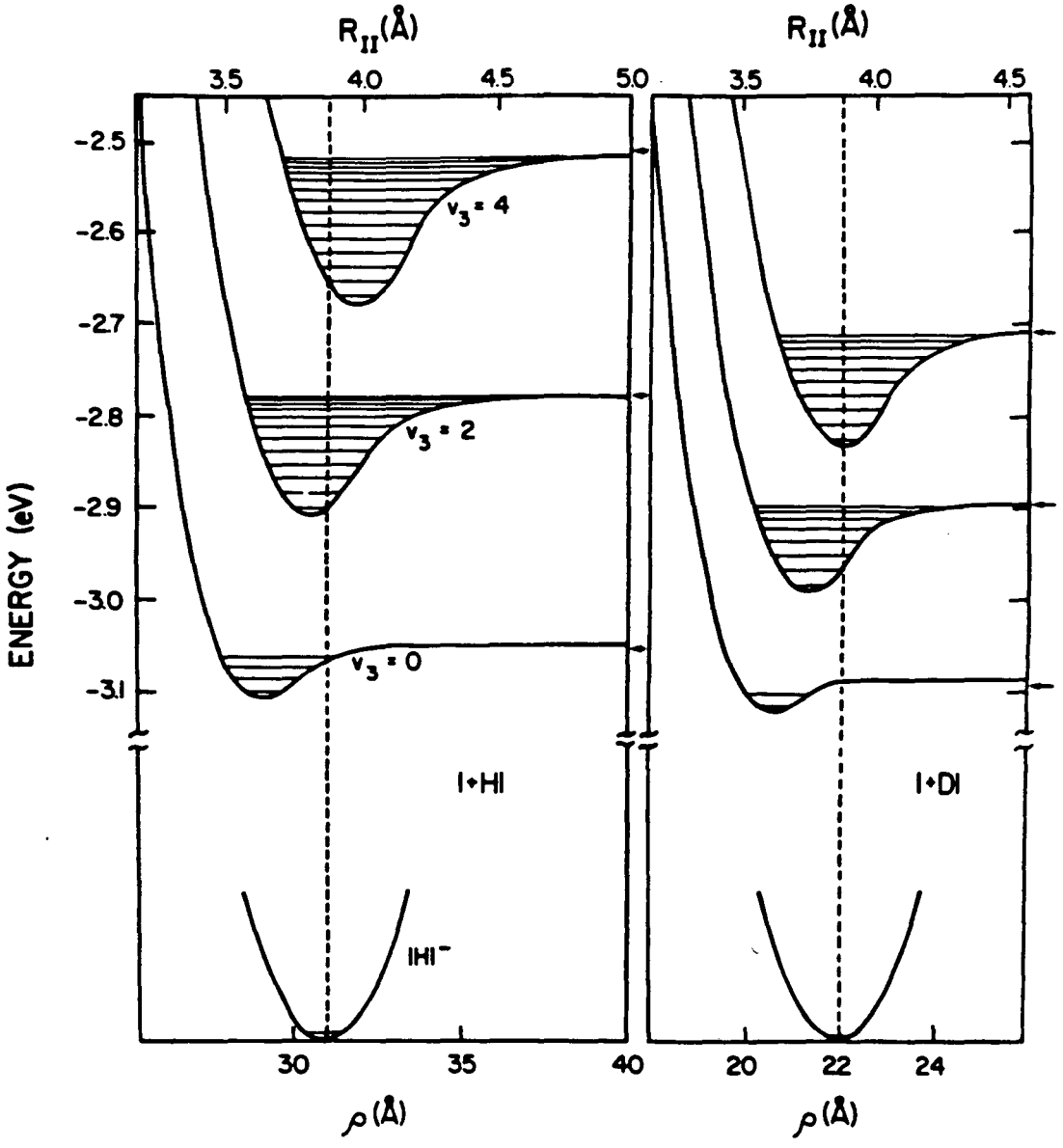
R_II(Å)
3.5
4.0
4.5
5.0
R_II(Å)
3.5
4.0
4.5
ENERGY (eV)
-2.5
-2.6
-2.7
-2.8
-2.9
-3.0
-3.1
v3 = 4
v3 = 2
v3 = 0
I+HI
I+DI
IHI⁻
30
35
40
20
22
24
ρ(Å)
ρ(Å)

We can interpret our results by considering the Franck-Condon overlap between the ion and the bound, quasi-bound and continuum states supported by the adiabatic curves of the neutral complex. The peak intensities in the photoelectron spectra are proportional to

$$\left| \int d\rho \left\{ \int dz\ \phi^{o}_{v3'}(z;\rho)\ \psi^{-}_{v3}(z) \right\} \chi^{o}_{v1',v3'}(\rho)\ \psi^{-}_{v1}(\rho) \right|^{2} \qquad (6.1)$$

In our approximate treatment, only transitions from the $v_1 = 0$ and $v_3 = 0$ states of the ion are considered; $\psi_{v1}^{-}(\rho)$ and $\psi_{v3}^{-}(\rho)$ are harmonic oscillator functions for these states. The frequencies used in constructing these wave functions are taken from matrix isolation spectroscopy.[2] For IHI^{-}, $\nu_1 = 121$ cm^{-1} and $\nu_3 = 682$ cm^{-1}. For IDI^{-}, $\nu_1 = 124$ cm^{-1} and $\nu_3 = 470$ cm^{-1}. The anion is assumed to be linear and centrosymmetric with the inter-iodine distance R_{II} = 3.88 Å. This distance has not been experimentally determined, and our choice is discussed below. The neutral asymmetric stretch wavefunctions $\phi_{v3'}^{o}(z;\rho)$ are the eigenfunctions of the double-minimum potential that results from cutting the LEPS surface at constant ρ. The $\chi_{v1',v3'}^{o}(\rho)$ are the bound symmetric stretch wavefunctions supported by the v_3' adiabatic curve.

Intensities for transitions to continuum states supported by each adiabatic curve were also calculated.[26] For each isotope, the continuum contribution is significant only for the $v_3' = 0$ state, and since the energy range of this contribution is less than the experimental resolution, it is represented

by a single (broken) line in each simulated spectrum.

The results of our Franck-Condon simulations are shown under the experimental spectra (Figure 6.1). The closely spaced symmetric stretch progressions in the simulated spectra are not resolved in the experimental spectra. This is not surprising, since the spacing between these transitions is near our resolution limit. Under these conditions, we interpret the width of each peak in the experimental spectra as a measure of how many symmetric stretch states in each adiabatic well have good Franck-Condon overlap with the ion. The 4←0 peak in the IDI^- spectrum is the narrowest (13 meV), suggesting that only one symmetric stretch state with $v_3' = 4$ has good overlap with the ion. The minimum in the IDI $v_3' = 4$ adiabatic curve occurs at R_{II} = 3.88 Å. If we take this as our value for the inter-iodine distance in the anion, the IDI^- detachment to $v_3' = 4$ will populate primarily the $v_1' = 0$ state (Figure 6.3). Transitions to the other v_3' levels will each populate several symmetric stretch and continuum states, resulting in broader peaks.

The simulated spectra generated by using this inter-iodine distance are qualitatively similar to the experimental spectra for both IHI^- and IDI^- (Figure 6.1). The extent of this agreement is encouraging since R_{II}, the only free parameter in our analysis, was chosen solely on the basis of the narrow 4←0 peak in the IDI^- spectrum. The simulations support the assignment of the peaks as a progression in the ν_3 mode of the complex and indicate that our analysis based on adiabatic curves for the collinear reaction is a reasonable

first approximation for interpreting our spectra.

The LEPS surface is only approximate, and a more accurate potential energy surface can be developed based on the discrepancies between the experimental and simulated spectra. For example, the $v_3' = 0$ peaks in both experimental spectra are broader and less intense than predicted by the simulations and, as noted earlier, lie above the dissociation asymptotes. These observations suggest that the $v_3' = 0$ adiabatic curves are purely repulsive for both IHI and IDI. Including the bending potential in our analysis should reduce the number of bound neutral states,[6,10,13,22], but in order to generate purely repulsive $v_3' = 0$ curves it might be necessary to use a surface with a higher barrier. An experimental determination of R_{II} would help considerably in the construction of an accurate potential energy surface from our data.

Finally, the narrow peak in the IHI^- spectrum provides the most compelling evidence yet for the existence of quasi-bound states in a heavy = light-heavy reaction. The peak width yields a lower bound of 0.1 ps for the lifetime of this state. This value is considerably shorter than that predicted by collinear calculations,[5] but the resolution of our instrument precludes a more precise determination. Planned experiments at higher resolution will provide a more definitive probe of the properties of these states.

Acknowledgements

Support from the Air Force Office of Scientific Research under Contract No.

AFOSR-87-0341 is gratefully acknowledged. D.M.N. thanks the Dreyfus Foundation for a Distinguished New Faculty Grant and the donors of the Petroleum Research Fund, administered by the American Chemical Society, for support. We thank Dr. R.J. LeRoy and Dr. G.B. Ellison for copies of their Franck-Condon factor computer programs.

References for section 6.2.

1. P.R. Brooks, Chem. Rev. **88**, 407 (1988). B.A. Collings, J.C. Polanyi, M.A. Smith, A. Stolow and A.W. Tarr, Phys. Rev. Lett. **59**, 2551 (1987). M. Dantus, M.J. Rosker, A.H. Zewail, J. Chem. Phys. **87**, 2395 (1987). A. Benz, H. Morgner, Mol. Phys. **57**, 319 (1986).

2. C.M. Ellison, B.S. Ault, J. Phys. Chem. **83**, 832 (1979).

3. K. Kawaguchi, E. Hirota, J. Chem. Phys. **87**, 6838 (1987); J. Chem. Phys. **84**, 2953 (1986). K. Kawaguchi, J. Chem. Phys. **88**, 4186 (1988).

4. J. Manz, R. Meyer, E. Pollak, J. Romelt, Chem. Phys. Lett. **93**, 184 (1982). J. Manz, R. Meyer, H.H.R. Schor, J. Chem. Phys. **80**, 1562 (1984).

5. J. Romelt, Chem. Phys. **79**, 197 (1983). The DIVAH correction has not been applied since it is negligible for these systems.

6. J. Manz, R. Meyer, E. Pollak, J. Romelt, H.H.R. Schor, Chem. Phys. **83**, 333 (1984).

7. J. Manz, J. Romelt, Chem. Phys. Lett. **81**, 179 (1981).

8. E. Pollak, J. Chem. Phys. **78**, 1228 (1983).

9. J.A. Kaye, A. Kuppermann, Chem. Phys. Lett. **77**, 573 (1981).

10. D.C. Clary, J.N.L. Connor, J. Phys. Chem. **88**, 2758 (1984).

11. I. Last, Chem. Phys. **69**, 193 (1982).

12. R.T. Skodje, M.J. Davis, J. Chem. Phys. **88**, 2429 (1988).

13. D.C. Clary, J.N.L. Connor, Chem. Phys. Lett. **94**, 81 (1983).

14. R.B. Metz, T. Kitsopoulos, A. Weaver, D.M. Neumark, J. Chem. Phys. **88**, 1463 (1988).

15. L.A. Posey, M.J. DeLuca, M.A. Johnson, Chem. Phys. Lett. **131**, 170 (1986). O. Cheshnovsky, S.H. Yang, C.L. Pettiette, M.J. Craycraft, R.E. Smalley, Chem. Phys. Lett. **138**, 119 (1987).

16. R.B. Metz, A. Weaver, S.E. Bradforth, T.N. Kitsopoulos, D.M. Neumark, J. Phys. Chem. **94**, 1377 (1990).

17. M.A. Johnson, M.L. Alexander, W.C. Lineberger, Chem. Phys. Lett. **112**, 285 (1984).

18. W.C. Wiley, I.H. McLaren, Rev. Sci. Instrum. **26**, 1150 (1955).

19. K.P. Huber, G. Herzberg, *Molecular Spectra and Molecular Structure. IV. Constants of Diatomic Molecules*. Van Nostrand (New York, 1979).

20. H. Hotop, W.C. Lineberger, J. Phys. Chem. Ref. Data **14**, 731 (1985).

21. G. Caldwell, P. Kebarle. Can. J. Chem. **63**, 1399 (1985).

22. E. Pollak, Chem. Phys. Lett. **94**, 85 (1983).

23. S. Sato, Bull. Chem. Soc. Jpn. **28**, 450 (1955).

24. G. Hauke, J. Manz, J. Romelt, J. Chem. Phys. **73**, 5040 (1980). A. Kuppermann, J.A. Kaye, J.P. Dwyer, Chem. Phys. Lett. **74**, 257 (1980).

25. V.K. Babamov, R.A. Marcus, J. Chem. Phys. **74**, 1790 (1981).

26. Intensities were calculated by using a modified version of the program by R.J. LeRoy: 'Bound→Continuum Intensities', University of Waterloo Chemical Physics Research Report CP-329, 1988.

6.3. I + HI: Postscript

The three years since publication of the I + HI paper have seen considerable progress in understanding this reaction. High resolution photodetachment spectroscopy has provided more experimental information, and new techniques for calculating neutral scattering wavefunctions have produced simulated photoelectron spectra which provide a test of the model potential energy surface. A brief summary of new results is given here.

High resolution zero kinetic energy (ZEKE) photodetachment spectra[1] reveal several narrow peaks for each single broader peak that we observed in the IHI^- spectrum. The structure of the $v_3' = 2$ and 4 peaks corresponds to transitions to symmetric stretch states which appear as resonances in quantal scattering calculations. The structure of the $v_3' = 0$ peak is dominated by transitions to direct scattering states, and corresponds to detachment to different HI rotational levels.

Simulations based on three-dimensional calculations[2,3,4] largely reproduce the high resolution structure, although discrepancies in peak positions, peak widths (compared to the high resolution spectrum) and predicted rotational state distributions (for $v_3' = 0$) indicate deficiencies in the LEPS surface and suggest that the barrier may be too low. Because this is a thermoneutral reaction, the barrier is the only significant feature on the potential energy surface and an accurate estimate of its height is particularly important. Unfortunately, experimental measurements are unlikely.

The deficiencies in the neutral surface might be identified more accurately if the ion parameters were better known, since changing the anion potential or bond length strongly affects the simulated photoelectron spectrum. It is possible that high-resolution infrared diode laser spectroscopy will yield vibrational frequencies and an accurate equilibrium geometry for IHI^-. A more precise measurement of the IHI^- binding energy is also desirable but unlikely.

Finally, the role of electronically excited states of the IHI complex is of interest. Spectra of IHI^- at 213 nm reveal additional structure at low electron kinetic energy due to transitions to an electronically excited state, and this is discussed in detail in Metz et al..[5]

References for section 6.3

1. I.M. Waller, T. Kitsopoulos and D.M. Neumark, J. Phys. Chem. **94**, 2240 (1990).

2. G.C. Schatz, J. Phys. Chem. **94**, 6157 (1990).

3. J.M. Bowman and B. Gazdy, J. Phys. Chem. **93**, 5129 (1989).

4. R.B. Metz, Ph.D. thesis, University of California, Berkeley, CA, 1991.

5. R.B. Metz, S.E. Bradforth and D.M. Neumark, Adv. Chem. Phys., in press 1991.

7. $F + H_2$: the prototype exoergic reaction[a]

7.1. Introduction

The propensity rules developed by Polanyi[1] classified reactions by mass, and we have already discussed I + HI as an example of the heavy + light-heavy reactions. $F + H_2$ is a classic example of both a highly exoergic and a heavy + light-light reaction, and the extensive experimental information available has contributed to its also becoming a standard for development and testing of new theoretical reactive scattering methods.

The earliest experiments on $F + H_2$ showed that it was a fast, highly exoergic reaction with a low activation energy (ΔH = 31.6 kcal/mol, E_a = 1.7 kcal/mol).[2] Infrared chemiluminescence[3,4] and chemical laser[5,6] experiments showed that most of the energy released ended up as product vibration, so much so that the product vibrational state distribution was dominated by $HF(v'=2)$. This interesting effect piqued the interest of theorists, and reactive scattering theory started to focus on $F + H_2$.

Reactive scattering theory and modern experimental techniques in reaction dynamics developed in parallel during the 1970's and 1980's, and Yuan Lee, John Polanyi and Dudley Herschbach were awarded the 1986 Nobel Prize in chemistry for their research in reaction dynamics.[7] The techniques

---

[a] This section is based on a forthcoming paper by A. Weaver and D.M. Neumark, 'Negative ion photodetachment as a probe of bimolecular transition states: the $F + H_2$ reaction', Faraday Discuss. Chem. Soc. (1991).

used in early experiments on F + H_2 and F + D_2 represented some of the most advanced experiments in reactive scattering, including the first product-state resolved angular distribution determined for any reaction.[8] The high resolution reactive scattering experiments on F + H_2 and its isotopic analogues by Neumark et al.[9] represented the culmination of almost twenty years' effort.

These crossed beams experiments on the F + H_2 reactions provided new evidence for several general predictions and reproduced some results of other experiments more accurately: the HF/DF product vibrational state population was inverted and the reactions were electronically adiabatic. The most revolutionary observation, however, was the forward-backward scattering of the HF/DF product in particular vibrational states -- the first experimental evidence of reactive scattering resonances.

Quantum mechanical calculations on the F + H_2 reactions had already predicted that resonances would exist, in a series of developments starting with the H + H_2 reaction that significantly advanced the art of reactive scattering theory beyond the standard of the late 1960's. The earliest calculations on F + H_2 used classical trajectory techniques on semi-empirical LEPS surfaces. The best of these surfaces was Muckerman's surface #5 (popularly known as M5),[10] which was adjusted so that classical trajectory results using transition state theory reproduced all the known experimental information at the time: the thermal rate constant, product vibrational and rotational state distribution and the F + D_2 product angular distribution.

Collinear[11] and three-dimensional[12] quantum mechanical scattering results on M5 produced long-lived resonance states of the FH_2 complex that intrigued both theorists and experimentalists, but comparison of the calculations to experimental results showed the limitations of the M5 surface, particularly its exit-channel adiabatic barriers where none should exist. (Despite these limitations, M5 is still used in some calculations where a relatively simple parameterization of the F + H_2 surface is required.)

Computational advances made it possible to obtain *ab initio* F + H_2 potential energy surfaces,[13] but these results raised several interesting questions. The *ab initio* barrier height was substantially higher than that of the LEPS-type surfaces, and although the activation energy derived from it was similar to an early measurement of 1.71 kcal/mol,[14] new measurements of E_a = 0.860 kcal/mol[15] and 1.18 kcal/mol[16] indicated that the barrier should be even lower. The *ab initio* results also suggested that the minimum energy path was not collinear.[17]

The semi-empirical surfaces developed after M5 are much more sophisticated and incorporate *ab initio* data, particularly in the saddle point region where direct experimental information has not been available. The T5a surface[18] was the best of several surfaces developed by Truhlar and coworkers that were based on the LEPS form of M5, but added localized potentials to fit experimental and *ab initio* results[18,19,20,21,22,23] and corrected several of M5's deficiencies. The T5a exit valley and saddle-point bending potential were

fitted to the *ab initio* result, and the barrier height was adjusted so that variational transition state theory calculations reproduced the thermal rate constant.

This more accurate potential energy surface for F + H_2 has served as a springboard for further developments in reactive scattering methodology. The T5a results include several calculations of the reaction probabilities restricted to total angular momentum J = 0, for the F + H_2,[24,25,26,27,28] F + D_2,[28,29] and F + HD[30] reactions. The first accurate total[31] and differential[32] reactive cross sections were calculated for the H + H_2 reaction, and these methods have also been applied to calculate total reaction cross sections for F + H_2,[33,34,35] and differential cross sections[36] for this reaction.

However, it became apparent relatively early that T5a also had deficiencies. Including higher orders of electron correlation in the *ab initio* calculation of the bending potential reduced the barrier height and flattened the bending potential at the saddle point. Worse, comparison to experimental results shows significant discrepancies. First, the predicted product vibrational distributions do not agree with experimental results. Both the J = 0 and total cross section quantal calculations on several surfaces predict HF(v=3) to be the dominant vibrational product of the F + H_2 reaction, over a wide energy range. The experimental results show that HF(v=2) dominates. The J = 0 calculations on the F + D_2 and F + HD reactions on T5a[29,30] predict DF(v=4) to be the dominant DF channel, in contrast to the experimental

finding that DF(v=3) dominates.[9,37] Second, the calculated product angular distributions do not agree with experimental results. The differential cross section calculations[36] at a collision energy of 0.12 eV predict the HF(v=3) product to peak at Θ_{cm} = 0° (forward scattering), which agrees with the crossed beam experiments.[9] While both the calculated and experimental angular distributions for HF(v=2) peak at Θ_{cm} = 180° (backward scattering), the calculated distribution shows significantly more forward scattering than the experimental distribution.

The 5SEC and 5SEC-W surfaces[38] were intended to correct several of the T5a deficiencies. Inclusion of higher-order correlation effects modified the entrance channel and saddle point region, so that the barrier is lower, earlier, and the bending potential is flatter at the saddle point. The entrance valley was modified to incorporate dispersion interactions and adjusted to agree with new experimental data[39] on van der Waals interactions. The exit valley for both surfaces is essentially the same as that of T5a, which was considered to be the best available. However, the 5SEC results[40] may produce the same incorrect product vibrational state distribution as T5a, although the calculated populations differ somewhat. Since the product valleys are very similar, this implies that other areas of the potential energy surface are important in determining the product state distribution. The question that arises now is this: how can these very complicated surfaces be modified to bring their predictions into closer agreement with experiment?

Some interesting additional information is provided by classical trajectory calculations. Polanyi's early classical trajectory calculations on LEPS surfaces showed that the product vibrational state distribution was most sensitive to the potential gradient in the reactant valley leading up to the saddle point.[1,41] The slope leading down into the product valley was less important, and the distribution was generally much more sensitive to details of the surface in the entrance valley and saddle point/interaction regions. This was explained in terms of the time that a given trajectory spent in a particular region; once past the saddle point, there was no mechanism for converting between translational and vibrational energy, and so the exit valley was much less important. These results suggest that 5SEC should be further modified in the entrance channel and saddle-point regions, but how relevant are these LEPS surface classical trajectory calculations to calculations on these new, high-level surfaces, when quantal effects like resonances are believed to be important? And, how can we evaluate the potential energy surface experimentally?

Experiments that yield information about a specific region of the potential energy surface become very appealing here, and the idea of transition state spectroscopy is most attractive because it suggests possible evaluation of this very important region of the potential energy surface, rather than the asymptotic regions. Faubel and coworkers can examine the entrance channel $F \cdot\cdot D_2$ interactions through scattering experiments at low collision energies,[42]

for example, but one might be able to produce several potential energy surfaces that fit asymptotic information like this. Judson and Rabitz[43] have discussed the possibility that one might generate entire families of surfaces to fit particular experimental data using classical trajectory calculations, without obtaining the true potential energy surface. Interesting questions of this type are raised by the work of Takayanagi and coworkers,[44,45] who found that they could reproduce some of the experimental results in classical trajectory calculations as a consequence of the topology of a modified LEPS surface, without invoking quantal effects at all.

An experiment which examines the transition state region itself removes much of the ambiguity inherent in fitting this region using only asymptotic measurements, and we have studied the F + H_2 transition state region via negative ion photoelectron spectroscopy of FH_2^-. Our results for the heavy + light-heavy reactions (see earlier sections of this chapter) showed that the photoelectron spectrum of the anion XHY^- could provide information about the transition state region of the X + HY reaction, provided that the anion geometry was similar to that at the neutral transition state.[46,47] The FH_2^-/F + H_2 system is, in principle, amenable to this technique. *Ab initio* calculations of the anion geometry[48] indicate that it is similar to the saddle point geometry on T5a and other model surfaces, so photodetachment experiments should provide information about this very important region of the F + H_2 surface.

We have obtained photoelectron spectra of the negative ions FH_2^-, FD_2^-, and FDH^-. As we shall see, comparing the experimental photoelectron spectra to calculations on the T5a surface should provide a test of this surface near the saddle point. Although many of these calculations consider only total angular momentum J = 0, the comparison should be valid because our anion rotational temperature is relatively low and the neutral rotational states should be limited to small values of J.[62] Relevant theoretical work includes various scattering calculations, plus Zhang and Miller's simulations of the FH_2^- and FD_2^- photoelectron spectra (using Nichols' *ab initio* results for the anion,[48] and the T5a surface for the neutral reaction).[27,28]

Our first experiments[49] on FH_2^- yielded a photoelectron spectrum that was considerably broader and less structured than the simulated spectrum. At the time, we speculated that some of the difference might have resulted from overlapping transitions to several $F + H_2$ electronic states, which were not included in the simulation. Here, we present spectra in which the contribution from low-lying excited electronic states appears to have been largely eliminated. The resulting spectra of FH_2^- and its isotopic variants show resolved structure which allows a detailed comparison between experiment and theory.

7.2. Experimental

Experiments were performed on the negative ion time-of-flight

photoelectron spectrometer described in Chapter 3. The negative ions FH_2^-, FD_2^-, and FDH^- were produced from a 15% NF_3/85% H_2 (D_2, DH) mixture, at a pulsed valve backing pressure of 60 psig. The ion formation process is assumed to be

$$\begin{aligned} NF_3 + e^- &\rightarrow F^- + NF_2 \quad \textit{dissociative attachment} \\ F^- + H_2 &\rightarrow F^-\cdot H_2 \quad \textit{cluster formation} \end{aligned} \tag{7.1}$$

Most of the spectra presented here were taken at photodetachment wavelengths of 266 nm (Nd:YAG fourth harmonic, 4.66 eV). Spectra of FH_2^- were also obtained at 213 nm. Spectra of each anion were obtained at both vertical ($\theta = 0°$) and horizontal ($\theta = 90°$) polarization of the laser beam with respect to the direction of electron detection.

Average data acquisition times were about seven hours per spectrum at 0°, twelve hours at 90°. These relatively long signal-averaging times were necessitated by the low signal-to-noise level in our spectra. Recent modifications to our instrument have increased the signal-to-noise level in FH_2^- spectra by a factor of three to four, and new spectra may show additional structure that was not evident in the spectra shown here.[50]

7.3. Results and analysis

The photoelectron spectra of FH_2^-, FD_2^-, and FDH^- at 266 nm are shown in Figures 7.1-7.3. Each spectrum shows fairly broad features at electron kinetic energies below 1.2 eV, plus sharp peaks at 1.26 and 1.21 eV

Figure 7.1. Photoelectron spectra of FH_2^- at 266 nm, at laser polarization angles θ = 0 and 90°. Positions of the labelled peaks (A-D) are given in Table 7.1. Arrows indicate asymptotic energies of product channels, as follows: (a) F + H_2(v=0), (b) H + HF(v=3), (c) H + HF(v=4), (d) F + H_2(v=1). The peaks at 1.26 and 1.21 eV result from two-photon transitions to F($^2P_{3/2}$), F($^2P_{1/2}$), as discussed in the text.

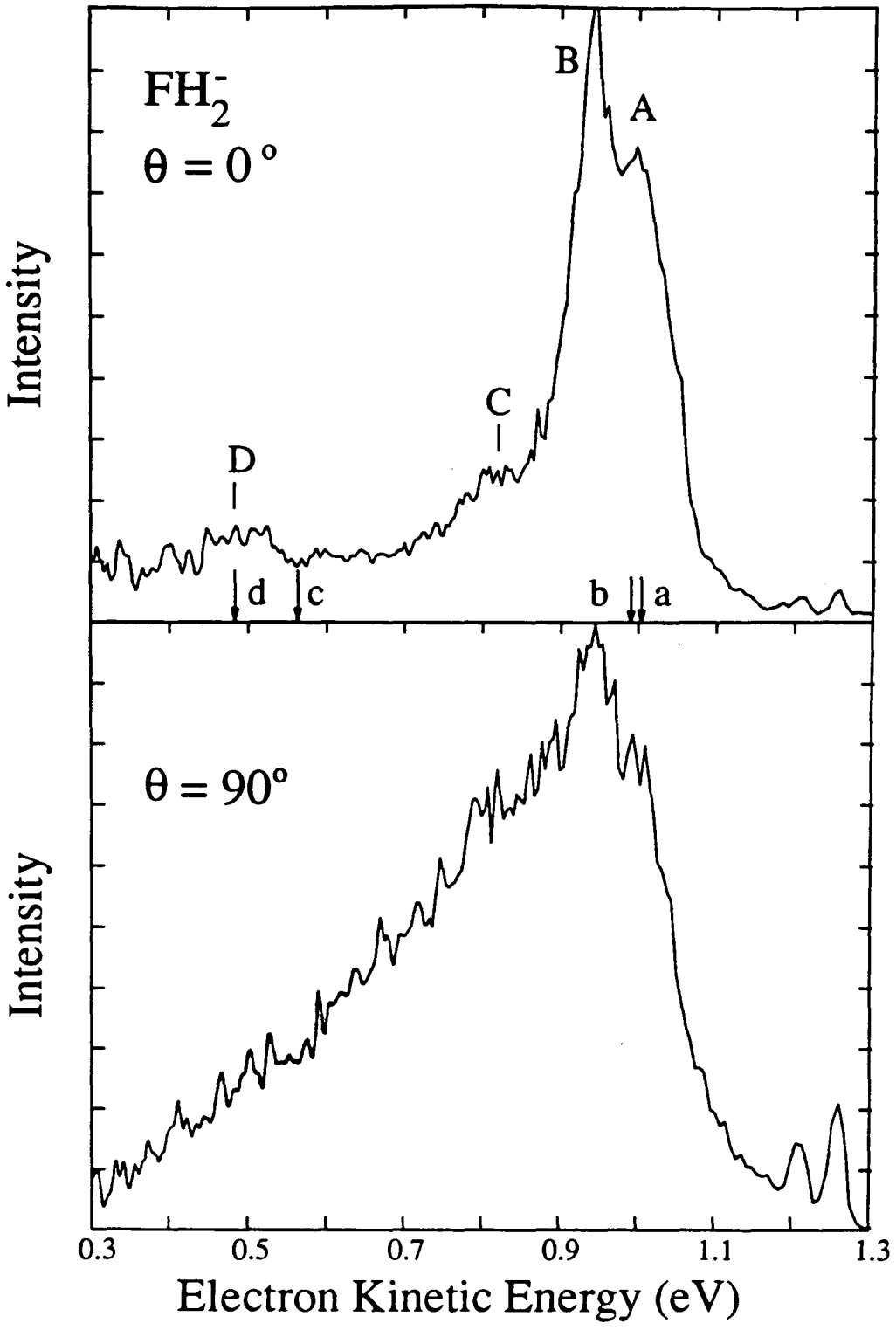
FH_2^-
θ = 0°
B
A
C
D
d
c
b
a
Intensity
θ = 90°
Intensity
0.3
0.5
0.7
0.9
1.1
1.3
Electron Kinetic Energy (eV)

Figure 7.2. Photoelectron spectra of FD_2^- at 266 nm, at laser polarization angles θ = 0 and 90°. Positions of the labelled peaks (B-D) are given in Table 7.1. Arrows indicate asymptotic energies of product channels, as follows: (a) D + DF(v=4), (b) F + D_2(v=0), (c) D + DF(v=5), (d) F + D_2(v=1).

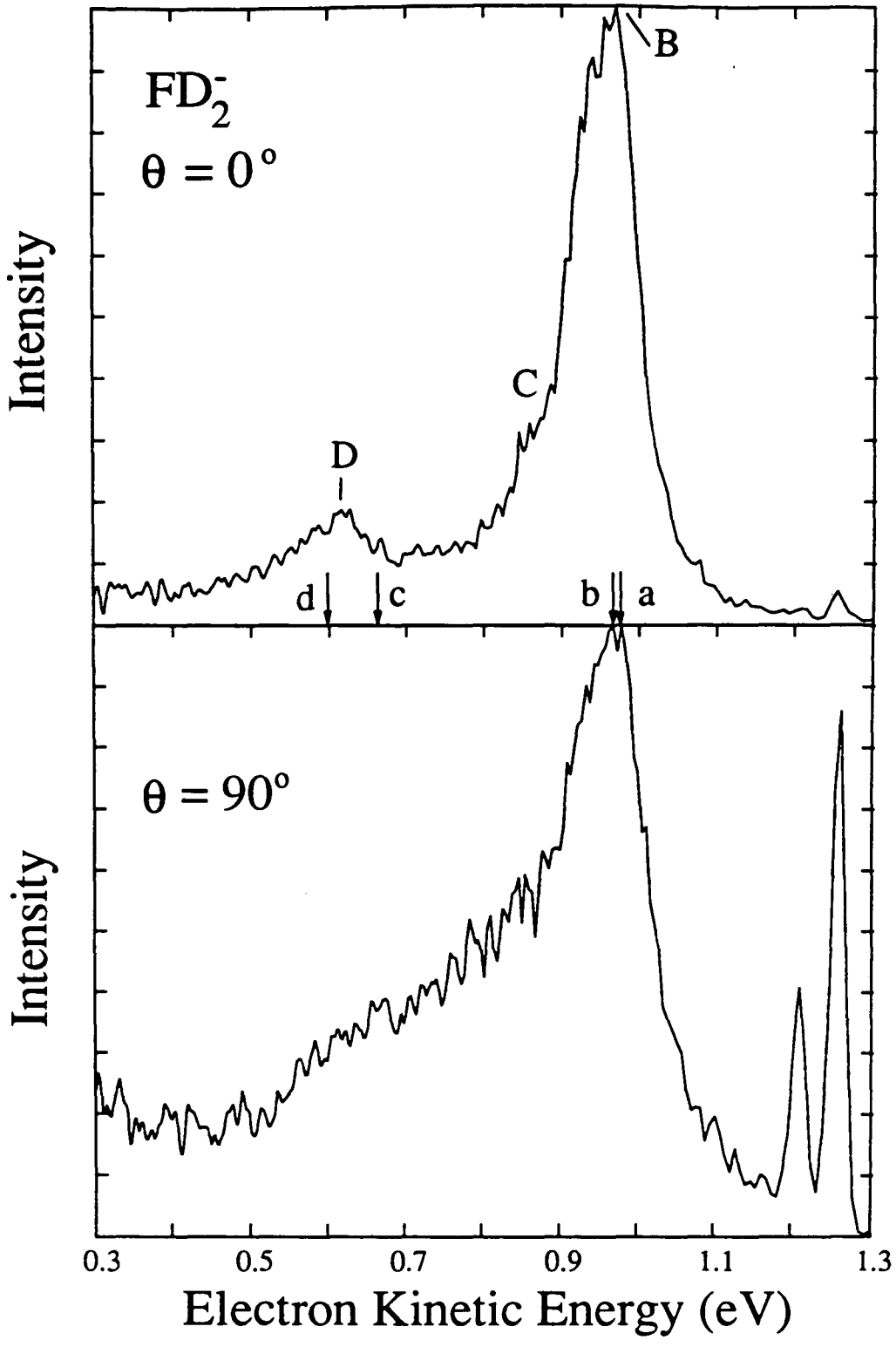
FD2-
θ = 0°
B
C
D
d
c
b
a
Intensity
θ = 90°
Intensity
0.3
0.5
0.7
0.9
1.1
1.3
Electron Kinetic Energy (eV)

Figure 7.3. Photoelectron spectra of FDH^- at 266 nm, at laser polarization angles θ = 0 and 90°. Positions of the labelled peaks (B-D) are given in Table 7.1. Arrows indicate asymptotic energies of product channels, as follows: (a) F + DH(v=0), (b) FH(v=3) + D, (c) FD(v=5) + H, (d) F + DH(v=1), (e) FD(v=6) + H.

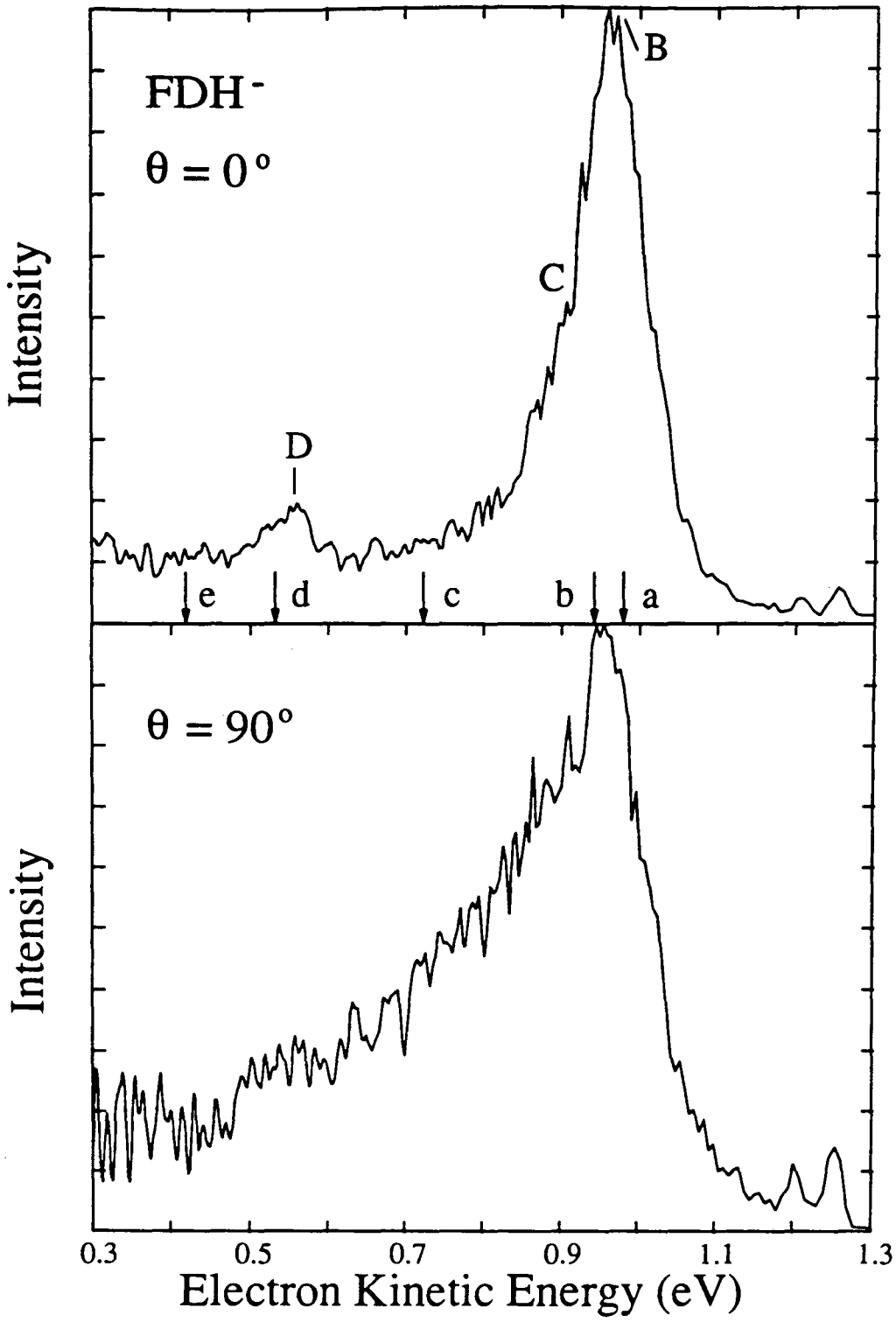
FDH⁻
θ = 0°
B
C
D
e
d
c
b
a
Intensity
θ = 90°
Intensity
0.3
0.5
0.7
0.9
1.1
1.3
Electron Kinetic Energy (eV)

electron kinetic energy.

The overall appearance of these spectra changes drastically with rotation of laser polarization. At θ=90° the photoelectron signal intensity decreases slowly between 0.9 eV and 0.3 eV, and no significant structure is observed below about 0.9 eV. At θ=0°, by contrast, the signal intensity decreases rapidly below 0.9 eV and one or more broad, small peaks are observed in the spectrum of each anion. The relative intensity of the sharp peaks above 1.2 eV is considerably higher at θ=90°.

These two sharp peaks are at identical energies to the two peaks seen in the F^- photoelectron spectrum at 266 nm. We believe that they arise from a two-photon process: the first photon dissociates the FH_2^- anion to $H_2 + F^-$, and the second photon detaches the electron from F^-. The two peaks correspond to transitions to the fluorine spin-orbit states, the $F(^2P_{3/2})$ ground state and the $F(^2P_{1/2})$ excited state 0.050 eV above.[51] The change in relative intensity with polarization rotation is due to the change in photoelectron angular distribution.[52] We have observed peaks due to similar two-photon processes in spectra of other molecules.

We are more interested in the broad features below 1.2 eV, since they represent transitions to the neutral FH_2 complex. At θ=0°, four resolved peaks of varying widths are evident in the FH_2^- spectrum and two in the FD_2^- and FDH^- spectra. The electron kinetic energy of each peak is listed in Table 7.1. The peaks at 0.997 and 0.942 eV (A and B) in the FH_2^- spectrum at θ=0° also

Table 7.1. Peak positions, $\theta = 0°$ spectra.

Ion	Peak Position (eV)†			
	A	B	C	D
FH_2^-	0.997	0.942	0.82	0.48
FD_2^-		0.960*	-	0.617
FHD^-		0.965*	-	0.559

† Uncertainties in peak positions are 0.010 eV for peaks A and B, 0.015 eV for peaks C and D.

* The B peak position quoted here is that of the rightmost small peak on the larger peak.

appear in the θ=90° spectrum.

Isotopic substitution affects the peak positions in the θ=0° spectra significantly. Peak A in the FH_2^- spectrum seems to have disappeared in the FD_2^- and FDH^- spectra. Peak D, at 0.48 eV in the FH_2^- spectrum, shifts to progressively higher electron kinetic energies in the FDH^- and FD_2^- spectra. Peak C, at 0.82 eV in the FH_2^- spectrum, also appears to shift to higher electron energy in the other two spectra and becomes an unresolved shoulder on the side of peak B.

The electron kinetic energy of each peak in the FH_2^- spectrum is related to the internal energy $E^{(0)}$ of the FH_2 complex by

$$eKE = h\nu - D_0 - EA(F) - E^{(0)} + E^{(-)}. \qquad (7.2)$$

Here hν is the photodetachment photon energy (4.66 eV), D_0 is the dissociation energy of the anion ground state to $F^- + H_2(v=0)$, and EA(F) is the electron affinity of the fluorine atom (3.401 eV)[53]. $E^{(0)}$ is the internal energy of the FH_2 complex relative to $F + H_2(v=0)$; in a scattering experiment with ground-state reactants, this would be the collision energy. $E^{(-)}$ is the internal energy of the anion, which we assume to be zero because the anions are expected to be vibrationally and rotationally cold. Finally, we require D_0 for FH_2^-. We assume D_0 to be 0.260 eV, from a comparison of our FH_2^- spectrum at θ=0° with the simulation of Zhang and Miller[27] (see section 7.4.3). The relation between eKE and $E^{(0)}$ for the FH_2^- spectrum is then

$$eKE(eV) = 0.999 - E^{(0)}(eV). \tag{7.3}$$

Figure 7.4 presents a schematic diagram of these energy levels for the F + H_2 system.

To determine similar equations for the FD_2^- and FDH^- spectra, we require values of D_0 for each. We estimated $D_0(FH_2^-)$ above, and can calculate D_e:

$$D_e = D_0(FH_2^-) + zpe(FH_2^-) - zpe(H_2) \tag{7.4}$$

The vibrational zero-point energies of FH_2^- and H_2 are calculated from Nichols' MCSCF vibrational frequencies.[48] FH_2^- is predicted to have a linear equilibrium geometry, with harmonic vibrational frequencies ω_1 = 292 cm^{-1} (H_2··F^- stretch), ω_2 = 773 cm^{-1} (degenerate bend), and ω_3 = 4143 cm^{-1} (H-H stretch). At the same level of theory, the H_2 harmonic frequency is 4224 cm^{-1}. Using these frequencies, we calculate D_e=0.369 eV for FH_2^-, FD_2^- and FDH^-.

Second, we apply zero-point corrections for the other isotopes, calculated by scaling the FH_2^- vibrational frequencies. ω_2 is estimated from the MCSCF frequency and CCSD(T) bond lengths,[48] using the equations for a linear XYZ molecule.[54] The H_2··F^- stretch, ω_1, is treated as a diatomic vibration and

Figure 7.4: Energy level diagram for the FH_2^- photodetachment experiment

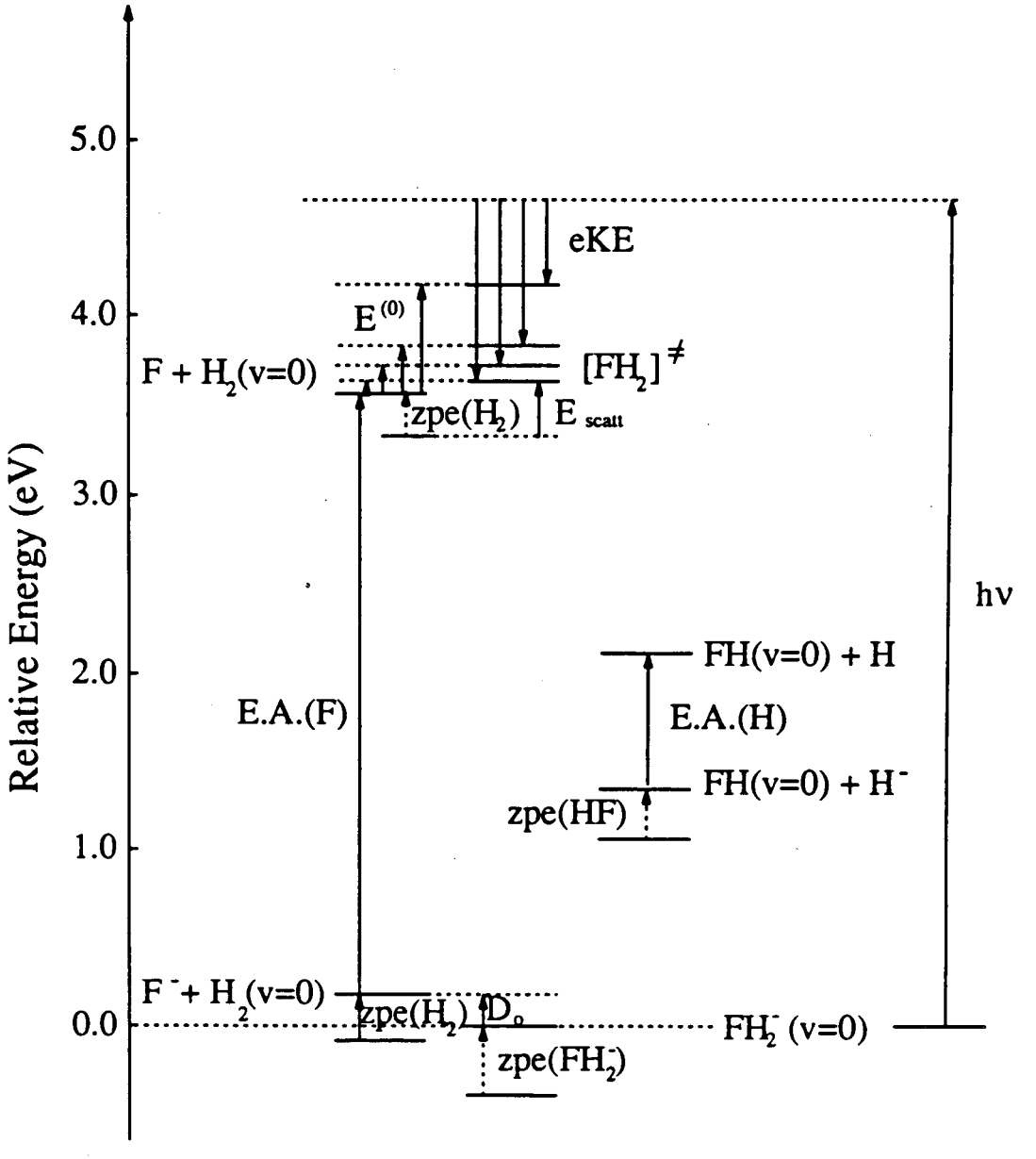

Solid arrows indicate experimentally measured quantities.

Dotted arrows indicate quantities estimated from ab initio calculations.

scaled accordingly.[b] The H-H stretch, ω_3, is also treated as a diatomic vibration and scaled. We obtain $D_0 = 0.291$ eV for FD_2^-. If we treat linear FHD^- and FDH^- as distinct species, a reasonable assumption since ω_2 is relatively high, we obtain $D_0 = 0.270$ eV for FHD^- and $D_0 = 0.280$ eV for FDH^-. Thus,

$$\begin{aligned} eKE\ (eV) &= 0.968 - E^{(0)}\ (eV) && (FD_2^-) \\ eKE &= 0.989 - E^{(0)} && (FHD^-) \\ eKE &= 0.979 - E^{(0)} && (FDH^-) \end{aligned} \tag{7.5}$$

The differences in D_0 between FDH^- and FHD^- result from the lower bend frequency in FDH^- (by 0.010 eV). Since D_0 for FDH^- is higher, it is more strongly bound and should be the favoured form of the anion in our cold ion beam.

By combining Eqs. 7.3 and 7.5 with the reaction exoergicities for $F + H_2$ ($\Delta E = 1.391$ eV), $F + D_2$ (1.382 eV), $F + HD \rightarrow HF + D$ (1.355 eV), and $F + DH \rightarrow FD + H$ (1.424 eV),[55] we can determine the electron kinetic energies which correspond to photodetaching the anion ground state and forming various asymptotic states $F + H_2(v)$, $H + HF(v)$, etc. For example, to calculate the

---

[b] In scaling the frequencies, we use the usual equations for frequency and reduced mass:

$$\omega = \frac{1}{2\pi}\sqrt{\frac{k}{\mu}}\ ;\quad \mu = \frac{m_1 m_2}{m_1 + m_2}$$

energy for the H + HF(v = 3) state:

$$\begin{aligned} eke &= 0.999 - E^{(0)} \\ &= 0.999 - [v\,\omega_{HF} - \omega_e x_{e(HF)}(v^2+v)] \end{aligned}$$

Using previously measured vibrational frequencies and anharmonicities,[c] we obtain eke = 0.985 eV for the H + HF(v = 3) asymptote. The asymptotic state energies are indicated by arrows in Figures 7.1-7.3, and identified in the figure captions. Any feature in the photoelectron spectrum at *higher* electron kinetic energy than a given asymptotic state corresponds to a state of the neutral complex with energy *below* that of the asymptotic state, and vice versa.

7.4. Discussion

This discussion of our results includes three general topics. First, we discuss the changes in overall shape of the photoelectron spectra with laser polarization, and show that the θ=0° spectra include only transitions to the neutral electronic ground states. This ground-state structure is then analyzed, using information from scattering calculations and experiments. Finally, we compare the FH_2^- and FD_2^- spectra with simulated spectra calculated on the T5a surface by Zhang and Miller,[27,28] evaluate T5a and discuss other model potential energy surfaces for these reactions.

---

[c] H_2: ω = 4400 cm^{-1}, $\omega_e x_e$ = 121 cm^{-1}; D_2: ω = 3118 cm^{-1}, $\omega_e x_e$ = 64 cm^{-1}; HD: ω = 3812 cm^{-1}, $\omega_e x_e$ = 91 cm^{-1}; HF: ω = 4138 cm^{-1}, $\omega_e x_e$ = 90 cm^{-1}; DF: ω = 2998 cm^{-1}, $\omega_e x_e$ = 46 cm^{-1}. (Ref. 55)

7.4.1. Laser polarization dependence

Photodetachment transitions from the anion to several neutral electronic states can contribute additional structure to the photoelectron spectra. For example, the photoelectron spectra[56] of $BrHBr^-$, IHI^-, FHI^-, $ClHI^-$, and $FHBr^-$ show well-separated bands due to transitions to different electronic states of the neutral complex. In spectra where these electronic bands overlap, interpretation is considerably more difficult. *Ab initio* calculations by Yamashita and Morokuma[57] suggest that this may occur in the $ClHCl^-$ spectrum.[58]

The FH_2^- spectra are likely to include contributions from several, possibly overlapping, electronic bands. The interaction of $F(^2P_{3/2,1/2})$ with $H_2(^1\Sigma_g^+)$ yields three potential energy surfaces:[59] $1^2A'$, $^2A''$, and $2^2A'$ assuming C_s symmetry, or $^2\Sigma^+_{1/2}$ and $^2\Pi_{1/2,3/2}$ assuming collinear ($C_{\infty v}$) geometry. In the F + H_2 asymptotic region, the $1^2A'$ and $^2A''$ surfaces become degenerate and correlate to $F(^2P_{3/2}) + H_2(^1\Sigma_g^+)$, while the $2^2A'$ surface correlates to $F(^2P_{1/2}) + H_2(^1\Sigma_g^+)$. The $^2\Sigma_{1/2}^+$ surface (the lowest-lying of the three) correlates to ground state $HF(^1\Sigma^+) + H(^2S_{1/2})$ products. The other two surfaces are expected to be non-reactive since they correlate to electronically excited products, $HF(^3\Pi_{0+,0-,1,2}) + H(^2S_{1/2})$.[60]

All three neutral potential energy surfaces are accessible via photodetachment of FH_2^-, which has molecular orbital occupancy

$1\sigma^2 2\sigma^2 3\sigma^2 1\pi^4 4\sigma^2$ (assuming linear geometry; an alternative notation is $...(2p\pi)^4(2p\sigma)^2$). The transition to the $^2\Sigma_{1/2}^+$ ground state surface requires removal of a 4σ electron, and transitions to the excited states ($^2\Pi$) require removal of a 1π electron. Nichols et al.[48] have calculated that the vertical detachment energies to these neutral $^2\Sigma^+$ and $^2\Pi$ states differ by only 0.25 eV.

As we have seen in other photoelectron spectra and discussed in section 3.3.6, the photoelectron angular distribution can provide important information about the contributions from transitions to different electronic states. If a band in a photoelectron spectrum is due to a single electronic transition, its overall intensity might vary with laser polarization but its shape should not change significantly.

Since the band shapes in the FH_2^-, FD_2^-, and FDH^- spectra depend strongly on laser polarization, we infer that these spectra include contributions from several electronic transitions characterized by different values of the anisotropy parameter $\beta(E)$. We can explain the laser polarization effects by attributing the major peaks (A-D) in the $\theta=0°$ spectra to transitions to the ground state neutral surface; the $\theta=90°$ spectra include transitions to both ground and excited states, and the excited state transitions are responsible for the additional electron signal between 0.9 and 0.3 eV, which obscures peaks C and D observed in the $\theta=0°$ spectra.

The value of β is strongly dependent on the anion molecular orbital from which the electron is removed. One might expect to be able to characterize the

complete photoelectron spectrum using only two values of β,[61] since the transition to the ground state $F + H_2$ surface involves removal of a σ electron and transitions to the excited states occur by removal of a π electron. The contribution of excited state transitions to the $\theta=0°$ spectrum will be zero if $\beta = -1$ for these bands. Conversely, the absolute intensity of peak B (and peak A in the FH_2^- spectrum) is greater in the $\theta=0°$ spectra than in the $\theta=90°$ spectra, which implies $\beta > 0$ for the ground state transition.

The assignment of all the structure in the $\theta=0°$ spectra to ground state transitions is supported by variations in the peak positions with isotopic substitution, as expected for vibrational transitions within a single electronic band. This assignment is further validated by comparison of the experimental and simulated spectra in section 7.4.3. The ability to eliminate excited state transitions by varying the laser polarization is an important result, since it means that we can use the $\theta=0°$ spectra to study the ground state surface for the $F + H_2$ reaction.

7.4.2. Interpretation of the photoelectron spectra

We next consider the origin of the peaks in the $\theta=0°$ photoelectron spectra. Each peak results from particularly good overlap of the anion wavefunction with a set of neutral scattering wavefunctions, which can happen in two ways. A scattering resonance is often characterized by a set of scattering wavefunctions which occur over a relatively narrow energy range

and are localized in the transition state region. If these resonance wavefunctions have good spatial overlap with the anion wavefunction, then a peak is observed in the photoelectron spectrum with width inversely proportional to the resonance lifetime.[d] Reactive scattering calculations show that resonances usually occur right at or just below the energetic threshold for an asymptotic channel.

Peaks in the photoelectron spectrum can also occur at energies where there are scattering wavefunctions with nearly zero momentum along the dissociation coordinate in the Franck-Condon region, which can happen near adiabatic barriers on the neutral potential energy surface. These transitions to direct scattering states can occur at energies well above the nearest asymptotic channel, and are usually considerably broader than transitions to resonance scattering states. The direct scattering states may adiabatically correlate to either reactant or product asymptotic states. Schatz[62] has discussed both types of transitions in more detail.[63] [e]

We can use information from reactive scattering calculations to

---

[d] $\Delta E\ \Delta t \approx 10^{-15}$ (ΔE in eV, Δt in s).

[e] Friedman and Truhlar (Ref. 63) have recently shown that the 'direct scattering' states are also associated with poles of the S-matrix and can be classified as resonance states. We use the labels 'resonance' or 'direct' scattering state here simply to differentiate between longer-lived states which give sharp peaks and short-lived states which give broader peaks.

determine which peaks in our spectra correspond to transitions to resonance scattering states. As mentioned earlier, the comparison to J = 0 calculations should be valid.

Calculations on the F + H_2 reaction using the T5a surface[24,25,27,28,33] show a small peak in the J = 0 reaction probability for production of HF(v=2), at collision energy $E^{(0)}$ = 0.018 eV. This peak is attributed to a 'closed-channel' resonance because (i) it occurs just below the H + HF(v=3) threshold at $E^{(0)}$ = 0.020 eV and (ii) the behavior of the S-matrix in the vicinity of the peak is characteristic of a resonance.[24,25] The value of $E^{(0)}$ = 0.018 eV for the scattering resonance corresponds to eKE = 0.981 eV in the FH_2^- photoelectron spectrum (see Eq. 7.3). This is very close to peak A at 0.997 eV in the experimental spectrum, strongly suggesting that peak A results from a transition to a resonance scattering state.

Peak B at eKE = 0.942 eV in the FH_2^- spectrum corresponds to a collision energy of 0.057 eV, which is well above the H + HF(v=3) threshold. In scattering calculations, the reaction probability for HF(v=3) production at this collision energy is substantial and varies slowly as a function of energy. Peak B in the FH_2^- spectrum is therefore most likely a transition to a direct scattering state.

Unlike the FH_2^- spectrum, the FD_2^- and FDH^- spectra exhibit a single broad peak near 0.96 eV. In the calculation of the J = 0 reaction probability for the F + D_2 reaction,[29] no resonance is observed near the reaction threshold.

There is no closed DF channel just above the reaction threshold, in contrast to the F + H_2 reaction, because production of DF(v=4) is slightly exoergic. From the scattering calculation, we would expect only a single peak near 1 eV in the photoelectron spectrum due to a transition to a direct scattering state, and this is consistent with peak B in the FD_2^- spectrum.

For the F + HD reaction, DF(v=4) production is slightly exoergic while HF(v=3) production is endoergic by 0.056 eV. The F + HD reactive scattering calculation[30] thus shows no resonance in the DF channel, but shows a strong resonance at $E^{(0)}$ = 0.024 eV in the HF channel. The similarity between the FD_2^- and FDH^- photoelectron spectra implies that this resonance does not contribute to the FDH^- spectrum. FDH^- should dominate over FHD^- in our cold ion beam, as discussed in section 7.3, and photodetachment of FDH^- should lead primarily to FD + H and F + DH production (since the anion equilibrium geometry is predicted to be linear). The apparent absence of transitions to resonance scattering states of FH + D from the photoelectron spectrum may thus be due to the absence of significant FH + D production via photodetachment. Even if there were some FHD^- present, the FH(v = 3) + D scattering resonance would appear at eKE = 0.965 eV, and its contribution to the spectrum might be obscured by peak B.

We next consider peak D in the three spectra. Figures 7.1-7.3 show that this peak corresponds to a transition to levels of the neutral complex that lie at or slightly below the reactant asymptotic channel F + H_2(v=1), F + D_2(v=1),

or F + DH(v=1). (This channel is labelled (d) in all three figures.) This suggests that these peaks correspond to transitions to resonance scattering states in which the scattering wavefunctions are localized on the reactant side of the potential energy surface, which is consistent with Pack's scattering calculation[24] that predicts a resonance at the F + H_2(v=1) threshold.

In summary, the appearance of the main peaks in the FH_2^-, FD_2^-, and FDH^- photoelectron spectra can be explained with reference to scattering calculations on the F + H_2, F + D_2, and F + HD reactions on the T5a surface. We next compare our results to simulated spectra in an attempt to evaluate the transition-state region of T5a.

7.4.3. Comparison of experimental and simulated spectra

The accuracy of model potential energy surfaces for the F + H_2 reaction can be examined by comparing our FH_2^- spectrum to simulations. Zhang and Miller[27,28] simulated the FH_2^- and FD_2^- spectra using the T5a surface[18] for the neutral reaction and assuming *ab initio* values for the geometry and vibrational frequencies of the anion.[f] The simulated spectrum was obtained

---

[f] Both simulations used *ab initio* values from an earlier version of the Ref. 48 calculations: r_{FH} = 1.74 Å, r_{HH} = 0.796 Å, ω_1 = 302 cm^{-1}, ω_2 = 693 cm^{-1}, ω_3 = 3816 cm^{-1} for FH_2^-. Note that the bond distances quoted in Ref. 28 are Jacobi coordinates: R is the distance from the F atom to the centre of mass of H_2, and r is the H-H bond length (both in bohr).

by calculating the Franck-Condon overlap between the anion ground vibrational wavefunction and the three-dimensional scattering wavefunctions supported by the T5a surface. Again, although these simulations assume J = 0 for both anion and neutral, comparison to our experiment is reasonable because we expect the anions to be rotationally cold.

Although the anion is only weakly bound (the binding energy, D_0, is 0.26 eV) and its calculated equilibrium geometry (r_{HF} = 1.690 Å, r_{HH} = 0.770 Å)[48] resembles the reactants more than the products, the reaction has an early barrier. The Franck-Condon region of good spatial overlap between anion and neutral wavefunctions is centred on the reactant side of the T5a saddle point and includes the saddle point (r_{HF} = 1.572 Å, r_{HH} = 0.762 Å),[18] so we expect to be able to use our experimental information to evaluate the saddle-point region of the T5a surface.

In Figure 7.5, the simulated spectra are superimposed on the experimental FH_2^- and FD_2^- spectra at θ=0°. These figures were drawn so that the position of the most intense peak in each simulated spectrum matched the position of the experimental peak B. In order for these peaks to align, the relationship between electron kinetic energy and scattering energy E_{scatt} must be eKE = 1.272 - E_{scatt} in the FH_2^- spectrum, and eKE = 1.2 - E_{scatt} in the FD_2^-

Figure 7.5. Experimental ($\theta = 0°$) and simulated photoelectron spectra of FH_2^- and FD_2^- at 266 nm. The dotted lines are the simulated photoelectron spectra of Zhang and Miller.[28] These plots assume eKE = 1.272 - E_{scatt} for FH_2^-, eKE = 1.2 - E_{scatt} for FD_2^- (see text).

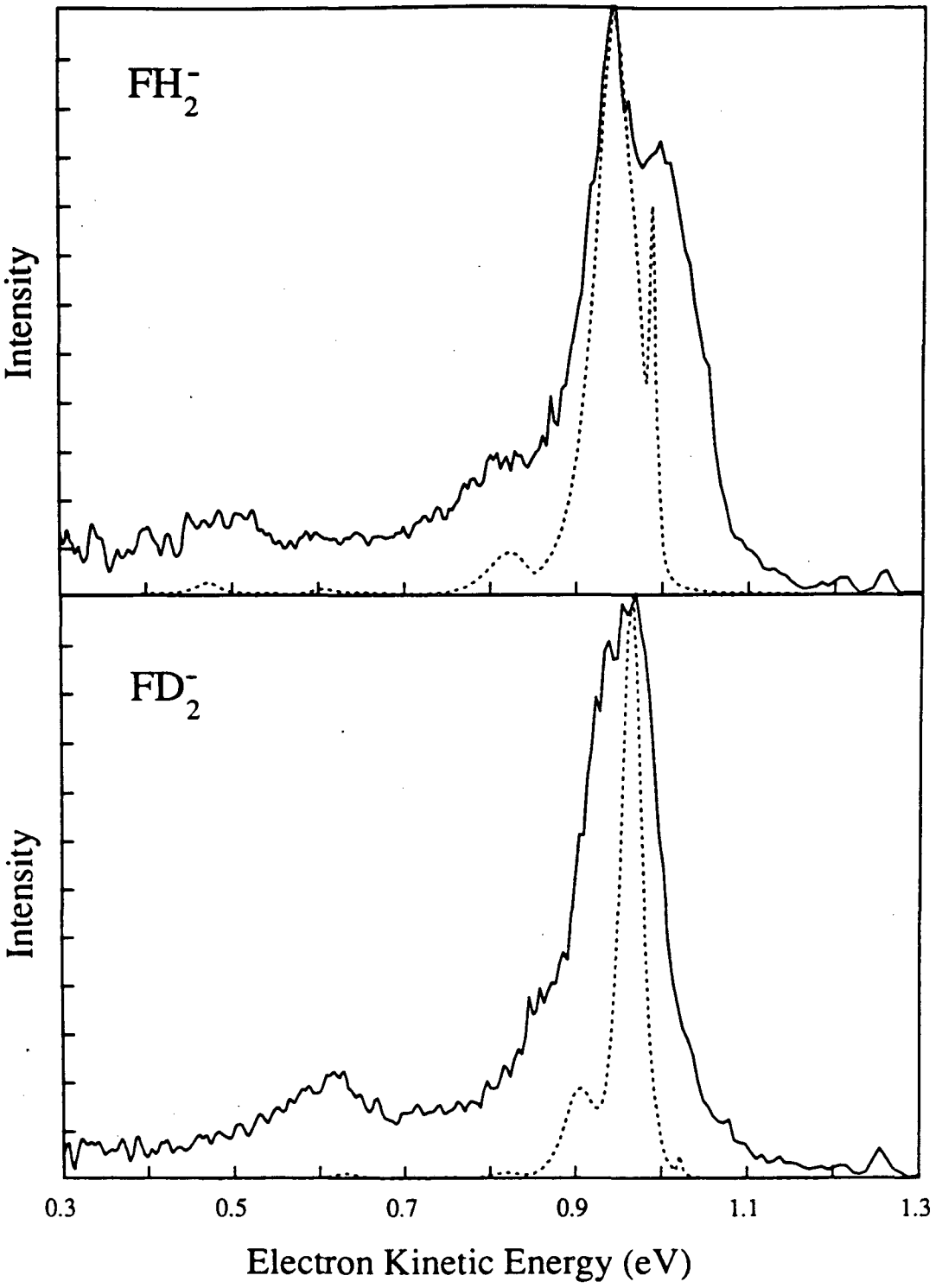
FH2-
Intensity
FD2-
Intensity
0.3
0.5
0.7
0.9
1.1
1.3
Electron Kinetic Energy (eV)

spectrum.[g] E_{scatt} is defined with respect to F + H_2 at the bottom of the H_2 well, and differs from the collision energy $E^{(0)}$ in equation 7.3 by the zero-point energy of H_2 (which we calculate from the MCSCF *ab initio* frequency[48]); the analog to Eq. 7.3 is eke = 1.010 - $E^{(0)}$, giving a value of D_0 = 0.249 eV for FH_2^-. The value of 0.260 eV for D_0 given in section 7.3 was calculated before these new simulations appeared, by comparing our results to an earlier simulation.[27] The difference is negligible, given the limited experimental resolution, and both estimates lie well within the uncertainty of the *ab initio* value (0.20 ± 0.10 eV).[48]

The structure in the simulated spectra is very similar to that in the experimental spectra, and corroborates the assignment made by comparison with scattering calculations. The FH_2^- simulated spectrum includes a narrow peak that coincides with the experimental sharp A peak, and appears as a resonance in the HF(v=2) reaction probability. Most of the intensity in the simulated spectrum results from large Franck-Condon factors between the anion ground state and direct scattering states. The structure of the FD_2^- spectrum is similar to that of the FH_2^- spectrum, but the sharp resonance is absent because the corresponding resonance energy is below the F + D_2 threshold, as discussed earlier. Again, good overlap with direct scattering states provides most of the peak intensity in the spectrum.

---

[g] The equation ε = 1.14 - E that appeared in Ref. 28 was incorrect (J.Z.H. Zhang, private communication 1991).

There are several differences between the experimental and simulated spectra. The splitting between peaks A and B is 0.055 eV in the experimental FH_2^- spectrum and only 0.045 eV in the simulation. The simulated C and D peak positions for FD_2^- show similar discrepancies with experiment, and the FD_2^- simulated B peak is much narrower than experiment. Some of these discrepancies could be due to the uncertainty in the anion geometry, as noted earlier; the anion bond lengths (r_{HF} = 1.74 Å, r_{HH} = 0.796 Å) used for this simulation were based on an early *ab initio* estimate. Using a more recent estimate (r_{HF} = 1.69 Å, r_{HH} = 0.770 Å)[48] would place the Franck-Condon region even closer to the collinear saddle point on the T5a surface (r_{HF} = 1.572 Å, r_{HH} = 0.762 Å).[18] Overlap with the H + HF direct scattering states would improve and the contribution of peaks associated with F + H_2 direct scattering states would decrease (as shown in Zhang and Miller's simulations[27]). Among other effects, the intensity of the A peak in the FH_2^- spectrum would increase relative to the B and C peaks.

The experimental spectrum has much more intensity above about 1 eV than does the simulation, particularly for FH_2^-. An earlier simulation[27] considered only energies accessible from F + H_2 reactants, and cut off at eKE > 0.999 eV (where $E^{(0)} = 0$). Photodetachment of FH_2^- can also access HF + H neutral scattering states which lie below F + $H_2(v=0)$, so the comparison above 1 eV was not valid. The simulation shown here[28] includes contributions from these product channel states, but they do not have good Franck-Condon

overlap with the anion wavefunction and hence contribute little more to the simulated spectrum. The simulated intensity at electron kinetic energies above 1 eV would increase if the ion geometry were closer to that at the saddle point (as discussed in the last paragraph), and might be increased by including transitions from excited vibrational states of the anion ('hot bands'); the anion is predicted to have a low-frequency vibration at 292 cm^{-1}, and the population of the anion v_1=1 level would be almost 6% of the total population at a moderate beam temperature of 150 K.

Figure 7.6 shows the 213 nm spectrum of FH_2^- at θ = 0°.[64] It is essentially identical to the 266 nm spectrum. Although the degraded resolution at 213 nm (5.83 eV) is expected to broaden any narrow features, the overall peak shape is remarkably similar. Differences between simulated and experimental peak positions are more obvious than in the 266 nm spectrum, although we hesitate to make definitive conclusions from the low-signal region at low electron kinetic energy (around peak D).

The overall agreement between the experimental and simulated spectra is remarkable, considering that D_0 was the only parameter adjusted in drawing Figures 7.5 and 7.6 and given the uncertainty in the anion geometry and the deficiencies of the T5a surface. It appears that the important features in our θ=0° photoelectron spectra can be explained with reference to calculations on the T5a surface. Since our photoelectron spectra are sensitive only to the region of the surface that has good overlap with the anion wavefunction, which

Figure 7.6. Experimental and simulated photoelectron spectra of FH_2^- at 213 nm

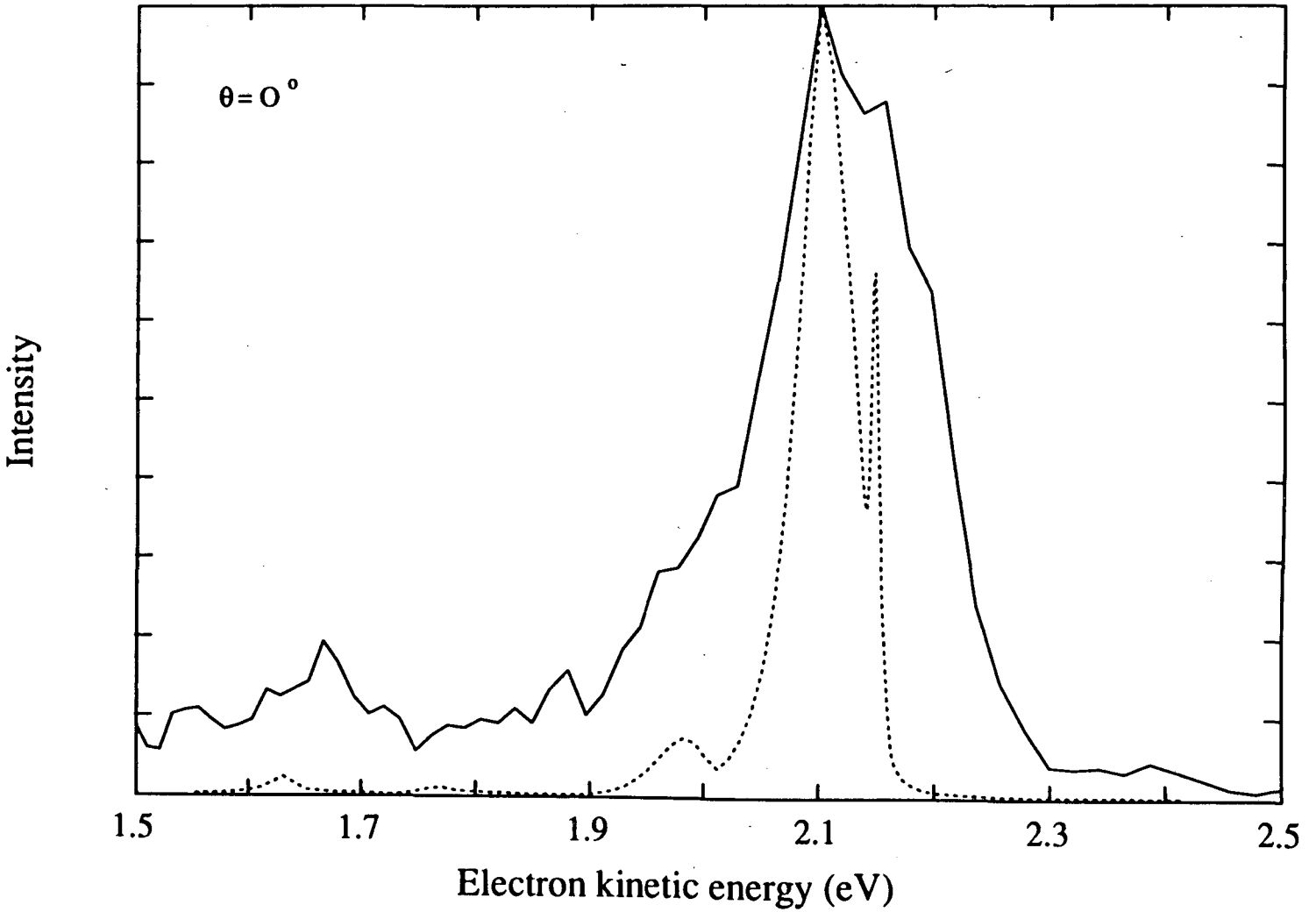

(as discussed above) includes the saddle point region, our results suggest that the T5a surface is sufficiently accurate in the saddle point region to reproduce our results.

Several details of the calculated product state distribution on T5a disagree with experimental results. Scattering calculations predict incorrect product vibrational branching ratios, as discussed in the Introduction. In addition, the calculated product angular distributions do not agree with experiment. The calculated F + H_2 differential cross section[36] shows the HF(v=3) product to peak at Θ_{cm} = 0°, in agreement with experiment. However, the calculated HF(v=2) product angular distribution also exhibits significant forward scattering (at Θ_{cm} = 0°) although none was seen in the crossed beams experiment.[9] Both the scattering calculations and the simulation of Zhang and Miller predict the existence of an F + H_2 resonance at $E^{(0)}$ = 0.018 eV, which is corroborated by the FH_2^- photoelectron spectrum. Calculations indicate that this resonance decays to H + HF(v=2) - for a J = 0 reactive collision, the HF(v=3) channel is closed - but the forward-scattered HF(v=3) product observed in the crossed beam experiments was interpreted as evidence for resonance decay to HF(v=3) only. The calculations and experiments can be reconciled by noting that $E^{(0)}$ for the J = 0 resonance lies below the collision energies used in the crossed beam experiments (0.03-0.15 eV), so the experiments could only access rotationally excited resonance states (J > 0) in collisions. These rotationally excited resonances should have enough energy

to decay to H + HF(v=3); only 0.002 eV more energy is required. Assuming that forward-scattered product is correlated with resonances in this reaction, it thus appears that the resonance decay products are not quite correctly predicted on the T5a surface. In the next section, we consider possible modifications to the T5a surface and their implications.

7.4.4. New potential energy surfaces for F + H_2

The development of new potential energy surfaces for F + H_2 is an extremely active area of research - in the last year we have seen two new surfaces[38,65] - and keeping up with new developments is a challenge. Although we could not discuss all new results here, the 5SEC surface is particularly relevant because of Hahn and Taylor's recent classical trajectory calculations and their discussion of our photoelectron spectra.

Simulations on T5a agree with our experimental results, suggesting that T5a is adequate in the saddle point region. Yet high-level *ab initio* calculations indicate that this region of T5a is not accurate - the barrier should be lower and the bending potential flatter. These two findings are not really contradictory, since the required modifications to T5a are relatively subtle, and there may be several surfaces which fit limited amounts of experimental data. We cannot know whether a given surface is the true surface, only whether or not it produces results that fit our data. Consider the IHI^- spectrum, for example.[66] The model surface used in virtually all calculations is a LEPS

surface with an estimated barrier height, because no experimental information is available. Compared to the highly fitted new surfaces for F + H_2 this is a very crude approximation, yet with few adjustable parameters we can obtain good agreement between the basic features of the simulated and experimental spectra. It is the finer details of the simulation that will respond to more subtle changes in the potential (as Metz showed for $BrHBr^-$ [46]): details like the B peak width in the FD_2^- spectrum, the energies of the C and D peaks in both spectra, and the behaviour with isotopic substitution.

Given these constraints, then, how would we expect quantum simulations on 5SEC to differ from those on T5a? The most obvious change is the saddle point position, which is earlier on 5SEC. The collinear saddle point lies at r_{FH}=1.677 Å, r_{HH}=0.762 Å,[38] which is almost identical to the *ab initio* prediction for the FH_2^- anion geometry[48] but lies further toward the reactant valley. As shown by Zhang and Miller in their simulations on T5a,[27] moving the anion geometry to the product side of the saddle point gives more intensity in the H + HF scattering states and increases the intensity of peak A relative to B.

Although quantum effects are known to be important in the F + H_2 reaction, classical trajectory calculations provide complementary information about the reaction dynamics and the nature of the scattering states. Hahn and Taylor[67] performed simulations on 5SEC in an attempt to find classical

analogues for the resonances.[h] They obtain periodic orbits at the same energies as those of the peaks in our spectra. The trajectories of peaks A and C are 'exchange periodic orbits' trapped in the strong interaction region. The B and D trajectories are 'in-channel periodic orbits', associated with adiabatic barriers in the entrance valley. This distinction between longer and shorter-lived states is the same as that between 'resonance' and 'direct' scattering states that we mentioned earlier.

The physical picture provided by the classical trajectories can be compared to our assignment. The A trajectory is trapped in the early part of the H + HF product valley (as is the C trajectory) - we assigned peak A to a transition to a resonance scattering state associated with HF(v = 2). In addition, Taylor predicts that the A periodic orbits for F + D_2 and F + DH will spend very little time in the area corresponding to the anion Franck-Condon region, explaining the disappearance of peak A in the FD_2^- and FDH^- spectra. The B and D trajectories are in-channel periodic orbits localized in the entrance channel, and we attributed the B peak to a transition to a direct scattering state. Although we assigned the D peak to a transition to a resonance scattering state, the peak is relatively broad, suggesting that the resonance is relatively short-lived. It is clearly helpful to be able to incorporate the results of quantal and classical scattering calculations into

---

[h] They used the same anion geometry as Zhang and Miller (Ref. 27), rather than the more recent estimate of Nichols et al. (Ref. 48).

analysis of our experimental results.

Acknowledgements

Support from the Air Force Office of Scientific Research under Grant No. AFOSR-91-0084 is gratefully acknowledged. Further support came from a grant-in-aid from the National Academy of Sciences through Sigma Xi, the Scientific Research Society. We thank Jack Simons for sending us the results of his FH_2^- calculation prior to publication. We thank Bill Miller and John Zhang for several interesting discussions. A.W. thanks Howard Taylor for a helpful discussion.

References:

1. J.C. Polanyi, Accts. Chem. Res. **5**, 161 (1972).

2. P.D. Mercer and H.O. Pritchard, J. Phys. Chem. **63**, 1468 (1959).

3. J. C. Polanyi and D. C. Tardy, J. Chem. Phys. **51**, 5717 (1969); J. C. Polanyi and K. B. Woodall, *ibid.* **57**, 1574 (1972).

4. N. Jonathan, C. M. Melliar-Smith, and D. H. Slater, Mol. Phys. **20**, 93 (1971).

5. J. H. Parker and G. C. Pimentel, J. Chem. Phys. **51**, 91 (1969); R. D. Coombe and G. C. Pimentel, *ibid.* **59**, 251 (1973).

6. M. J. Berry, J. Chem. Phys. **59**, 6229 (1973).

7. Their three Nobel prize lectures provide a relevant and interesting introduction to the topics discussed in this chapter, and Yuan Lee's lecture includes a summary of his group's $F + H_2$ work. Y.T. Lee, Angew. Chem. Int. Ed. Engl. **26**, 939 (1987). J.C. Polanyi, *ibid.* **26**, 952 (1987). D.R. Herschbach, *ibid.* **26**, 1221 (1987).

8. T. P. Schafer, P. E. Siska, J. M. Parson, F. P. Tully, Y. C. Wong, and Y. T. Lee, J. Chem. Phys. **53**, 3385 (1970).

9. D. M. Neumark, A. M. Wodtke, G. N. Robinson, C. C. Hayden, and Y. T. Lee, J. Chem. Phys. **82**, 3045 (1985); D. M. Neumark, A. M. Wodtke, G. N. Robinson, C. C. Hayden, K. Shobatake, R. K. Sparks, T. P. Schafer, and Y. T. Lee, *ibid.* **82**, 3067 (1985).

10. J. T. Muckerman, in Theoretical Chemistry-Advances and Perspectives,

ed. H. Eyring and D. Henderson (Academic, New York, 1981), vol. 6A, pp. 1-77

11. G. C. Schatz, J. M. Bowman, and A. Kuppermann, J. Chem. Phys. **63**, 674 (1975); S. L. Latham, J. F. McNutt, R. E. Wyatt, and M. J. Redmon, J. Chem. Phys. **69**, 3746 (1978); J. N. L. Connor, W. Jakubetz, and J. Manz, Mol. Phys. **35**, 1301 (1978); J. M. Launay and M. Le Dourneuf, J. Phys. B **15**, L455 (1982).

12. M. J. Redmon and R. E. Wyatt, Chem. Phys. Lett. **63**, 209 (1979)

13. C. F. Bender, P. K. Pearson, S. V. O'Neill, and H. F. Schaefer III, J. Chem. Phys. **56**, 4626 (1972); C. F. Bender, S. V. O'Neill, P. K. Pearson, and H. F. Schaefer III, Science, **176**, 1412 (1972).

14. P.D. Mercer and H.O. Pritchard, J. Phys. Chem. **63**, 1468 (1959). Another measurement of E_a = 1.6 kcal/mol (K. Homann, W.C. Soloman, J. Warnatz, H.G. Wagner and C. Zetzsch, Ber. Bunsenges. Phys. Chem. **74**, 585 (1970)) was believed to be less accurate.

15. E. Wurzberg and P.L. Houston, J. Chem. Phys. **72**, 4811 (1980).

16. R.F. Heidner, J.F. Bott, C.E. Gardner and J.E. Melzer, J. Chem. Phys. **72**, 4815 (1980).

17. D. W. Schwenke, R. Steckler, F. B. Brown, and D. G. Truhlar, J. CHem. Phys. **84**, 5706 (1986).

18. R. Steckler, D. G. Truhlar, and B. C. Garrett, J. Chem. Phys. **82**, 5499 (1985).

19. F. B. Brown, R. Steckler, D. W. Schwenke, D. G. Truhlar, and B. C.

Garrett, J. Chem. Phys. **82**, 188 (1985); D. W. Schwenke, R. Steckler, F. B. Brown, and D. G. Truhlar, *ibid.* **86**, 2443 (1987).

20. H. F. Schaefer, J. Phys. Chem. **89**, 5336 (1985); M. J. Frisch, B. Liu, J. S. Binkley, H. F. Schaefer, and W. H. Miller, Chem. Phys. Lett. **114**, 1 (1985); G. E. Scuseria and H. F. Schaefer, J. Chem. Phys. **88**, 7024 (1988).

21. C. W. Bauschlicher Jr., S. P. Walch, S. R. Langhoff, P. R. Taylor, and R. L. Jaffe, J. Chem. Phys. **88**, 1743 (1988).

22. R. J. Bartlett, J. Phys. Chem. **93**, 1697 (1989).

23. C.W. Bauschlicher Jr. and S.R. Langhoff, Adv. Chem. Phys. **77**, 103 (1990).

24. J. D. Kress, Z. Bacic, G. A. Parker, and R. T. Pack, Chem. Phys. Lett. **157**, 484 (1989); Z. Bacic, J. D. Kress, G. A. Parker, and R. T. Pack, J. Chem. Phys. **92**, 2344 (1990)

25. C.-H. Yu, D. J. Kouri, M. Zhao, D. G. Truhlar and D.W. Schwenke, Chem. Phys. Lett. **157**, 491 (1989); C.-H. Yu, D. J. Kouri, M. Zhao, D. G. Truhlar, and D. W. Schwenke, Int. J. Quantum Chem. Symp. **23**, 45 (1989).

26. D. E. Manolopoulos, M. D'Mello, and R. E. Wyatt, J. Chem. Phys. **93**, 403 (1990).

27. J. Z. H. Zhang and W. H. Miller, J. Chem. Phys. **92**, 1811 (1990).

28. J.Z.H. Zhang, W.H. Miller, A. Weaver and D.M. Neumark, Chem. Phys. Lett. **182**, 283 (1991).

29. M. D'Mello, D. E. Manolopoulos, and R. E. Wyatt, Chem. Phys. Lett.

168, 113 (1990).

30. D. E. Manolopoulos, M. D'Mello, R. E. Wyatt, and R. B. Walker, Chem. Phys. Lett. **169**, 482 (1990).

31. J. Z. H. Zhang and W. H. Miller, Chem. Phys. Lett. **153**, 465 (1988); D. E. Manolopoulos and R. E. Wyatt, Chem. Phys. Lett. **159**, 123 (1989).

32. J. Z. H. Zhang and W. H. Miller, J. Chem. Phys. **91**, 1528 (1989); M. Zhao, D. G. Truhlar, D. W. Schwenke, and D. J. Kouri, J. Phys. Chem. **94**, 7074 (1990).

33. J. M. Launay and M. LeDourneuf. Chem. Phys. Lett. **169**, 473 (1990).

34. D. Neuhauser, R. S. Judson, R. L. Jaffe, M. Baer, and D. J. Kouri, Chem. Phys. Lett. **176**, 546 (1991).

35. J.Z.H. Zhang, Chem. Phys. Lett. **181**, 63 (1991).

36. J. M. Launay, Theor. Chim. Acta **79**, 183 (1991).

37. M. Faubel, S. Schlemmer, F. Sondermann and J.P. Toennies, J. Chem. Phys. **94**, 4676 (1991).

38. G.C. Lynch, R. Steckler, D.W. Schwenke, A.J.C. Varandas, D.G. Truhlar and B.C. Garrett, J. Chem. Phys. **94**, 7136 (1991).

39. V. Aquilanti, R. Candori, D. Cappelletti, E. Luzzatti, and F. Pirani, Chem. Phys. **145**, 293 (1990). Faubel and coworkers (Ref. 37) also plan investigations of the entrance channel potential.

40. G.C. Lynch, P. Halvick, M. Zhao, D.G. Truhlar, C-h Yu, D.J. Kouri, and D.W. Schwenke, J. Chem. Phys. **94**, 7150 (1991).

41. J.C. Polanyi and J.L. Schreiber, Discuss. Faraday Soc. **62**, 267 (1977).

42. S. Schlemmer, private communication 1991.

43. R.S. Judson and H. Rabitz, J. Chem. Phys. **90**, 2283 (1989).

44. T. Takayanagi and S. Sato, Chem. Phys. Lett. **144**, 191 (1988).

45. T. Takayanagi, S. Tsunashima and S. Sato, J. Chem. Phys. **93**, 2487 (1990).

46. R. B. Metz, A. Weaver, S. E. Bradforth, T. N. Kitsopoulos, and D. M. Neumark, J. Phys. Chem. **94**, 1377 (1990).

47. S. E. Bradforth, A. Weaver, D. W. Arnold, R. B. Metz, and D. M. Neumark, J. Chem. Phys. **92**, 7205 (1990).

48. J. A. Nichols, R. A. Kendall, S. J. Cole, and J. Simons, J. Phys. Chem. **95**, 1074 (1991).

49. A. Weaver, R. B. Metz, S. E. Bradforth, and D. M. Neumark, J. Chem. Phys. **83**, 5352 (1990).

50. S.E. Bradforth and D.W. Arnold, 1991.

51. C.E. Moore, *Atomic Energy Levels*, Vol. I, p. 60. (National Bureau of Standards, Washington 1949).

52. J. Cooper and R.N. Zare, J. Chem. Phys. **48**, 942 (1968).

53. C. Blondel, P. Cacciani, C. Delsart, and R. Trainham, Phys. Rev. A, **40**, 3698 (1989).

54. G. Herzberg, *Molecular Spectra and Molecular Structure II. Infrared and Raman Spectra of Polyatomic Molecules* (Van Nostrand, New York, 1945), p. 173.

55. K. P. Huber and G. Herzberg, *Molecular Spectra and Molecular Structure IV. Constants of Diatomic Molecules* (Van Nostrand, New York, 1979).

56. R. B. Metz, S. E. Bradforth, and D. M. Neumark, Adv. Chem. Phys. (in press 1991).

57. K. Yamashita and K. Morokuma, J. Chem. Phys. **93**, 3716 (1990).

58. R.B. Metz, T. Kitsopoulos, A. Weaver, D.M. Neumark, J. Chem. Phys. **88**, 1463 (1988).

59. D. G. Truhlar, J. Chem. Phys. **56**, 3189 (1972); J. T. Muckerman and M. D. Newton, *ibid.* **56**, 3191 (1972); N. C. Blais and D. G. Truhlar, *ibid.* **58**, 1090 (1973); J. C. Tully, *ibid.* **60**, 3042 (1974); R.L. Jaffe, K. Morokuma and T.F. George, *ibid.* **63**, 3417 (1975); F. Rebentrost and W. A. Lester, Jr., *ibid.* **63**, 3737 (1975); A. Komornicki, K. Morokuma, and T. F. George, *ibid.* **67**, 5012 (1977); M.B. Faist and J.T. Muckerman, *ibid.* **71**, 233 (1979); B. Lepetit, J.M. Launay and M. LeDourneuf, Chem. Phys. **106**, 111 (1986).

60. A general reference: I.W.M. Smith, *Kinetics and Dynamics of Elementary Gas Reactions* (Butterworth, London, 1980) pp. 54-57.

61. J.H.D. Eland, *Photoelectron spectroscopy* (Butterworth: Southampton, 1984), p. 85.

62. G. C. Schatz, J. Chem. Phys. **90**, 1237 (1989); J. Phys. Chem. **94**, 6157 (1990).

63. R.J. Friedman and D.G. Truhlar, Chem. Phys. Lett. **183**, 539 (1991).

64. S.E. Bradforth, unpublished results 1991.

65. J.S. Wright, R.J. Williams and R.E. Wyatt, Chem. Phys. Lett. **184**, 159 (1991).

66. A. Weaver, R.B. Metz, S.E. Bradforth and D.M. Neumark, J. Phys. Chem. **92**, 5558 (1988).

67. O. Hahn and H.S. Taylor, J. Chem. Phys., submitted 1991.

Appendix 1. Simulated peak positions and intensities, NO_3^- photoelectron spectrum at 266 nm.

The M_J value designates the sub-matrix which contains the neutral vibronic state, at energy E°. The anion vibrational energy is E^-. The ΔE are calculated with respect to the energy of the lowest eigenstate of the M_J sub-matrix (nominally the $|A;0,0\rangle$ state). The electron kinetic energy is $eKE = h\nu - E.A.(NO_3) - E^\circ + E^-$, where the laser energy $h\nu$ and electron affinity are given below.

Although n_4 is not strictly conserved, the peaks with appreciable intensity are tentatively assigned according to their parent states.

M_J	E°(eV)	E^-(eV)	ΔE(eV)	ΔE(cm-1)	Height	eKE(eV)	Asst.
0	-0.150	0.000	0.000	0.0	1.000	0.738	$1_0^0 4_0^0$
0	-0.150	0.089	-0.089	-720.0	0.053	0.827	$1_0^0 4_1^0$
0	-0.054	0.000	0.096	774.9	0.121	0.642	$1_0^0 4_0^2$
0	-0.054	0.089	0.007	54.9	0.007	0.731	$1_0^0 4_1^2$
0	-0.054	0.179	-0.082	-665.1	0.005	0.820	$1_0^0 4_2^2$
0	-0.019	0.000	0.131	1057.0	0.793	0.607	$1_0^1 4_0^0$
0	-0.019	0.089	0.042	337.0	0.042	0.696	$1_0^1 4_1^0$
0	0.054	0.000	0.204	1644.0	0.011	0.534	$1_0^0 4_0^4$
0	0.054	0.089	0.115	924.0	0.007	0.623	$1_0^0 4_1^4$
0	0.054	0.179	0.025	204.0	0.002	0.713	$1_0^0 4_2^4$
0	0.077	0.000	0.227	1831.9	0.096	0.511	$1_0^1 4_0^2$
0	0.077	0.089	0.138	1111.9	0.006	0.600	$1_0^1 4_1^2$
0	0.077	0.179	0.049	391.9	0.004	0.689	$1_0^1 4_2^2$
0	0.112	0.000	0.262	2114.4	0.314	0.476	$1_0^2 4_0^0$
0	0.112	0.089	0.173	1394.4	0.017	0.565	$1_0^2 4_1^0$
0	0.168	0.089	0.229	1850.6	0.002	0.509	$1_0^0 4_1^6$
0	0.185	0.000	0.335	2701.0	0.008	0.403	$1_0^1 4_0^4$
0	0.185	0.089	0.246	1981.0	0.005	0.492	$1_0^1 4_1^4$
0	0.185	0.179	0.156	1261.0	0.002	0.582	$1_0^1 4_2^4$
0	0.208	0.000	0.358	2889.3	0.038	0.380	$1_0^2 4_0^2$
0	0.208	0.089	0.269	2169.3	0.002	0.469	$1_0^2 4_1^2$
0	0.208	0.179	0.180	1449.3	0.002	0.558	$1_0^2 4_2^2$
0	0.244	0.000	0.394	3177.1	0.083	0.344	$1_0^3 4_0^0$
0	0.244	0.089	0.305	2457.1	0.004	0.433	$1_0^3 4_1^0$
0	0.299	0.089	0.361	2907.6	0.001	0.377	$1_0^1 4_1^6$
0	0.316	0.000	0.466	3758.4	0.003	0.272	$1_0^2 4_0^4$
0	0.316	0.089	0.377	3038.4	0.002	0.361	$1_0^2 4_1^4$
0	0.340	0.000	0.490	3952.1	0.010	0.248	$1_0^3 4_0^2$
0	0.380	0.000	0.530	4276.9	0.016	0.208	$1_0^4 4_0^0$
0	0.476	0.000	0.626	5051.8	0.002	0.112	$1_0^4 4_0^2$
0	0.531	0.000	0.681	5495.2	0.002	0.057	
1	-0.105	0.000	0.045	362.8	0.351	0.693	$1_0^0 4_0^1$

M_J	E°(eV)	E¬(eV)	ΔE(eV)	ΔE(cm-1)	Height	eKE(eV)	Asst.
1	-0.105	0.089	-0.044	-357.2	0.163	0.782	$1_0{}^0 4_1{}^1$
1	-0.105	0.179	-0.134	-1077.2	0.014	0.872	$1_0{}^0 4_2{}^1$
1	-0.002	0.000	0.148	1195.4	0.080	0.590	$1_0{}^0 4_0{}^3$
1	-0.002	0.089	0.059	475.4	0.033	0.679	$1_0{}^0 4_1{}^3$
1	-0.002	0.179	-0.030	-244.6	0.001	0.768	$1_0{}^0 4_2{}^3$
1	0.026	0.000	0.176	1419.9	0.278	0.562	$1_0{}^1 4_0{}^1$
1	0.026	0.089	0.087	699.9	0.129	0.651	$1_0{}^1 4_1{}^1$
1	0.026	0.179	-0.002	-20.1	0.011	0.740	$1_0{}^1 4_2{}^1$
1	0.110	0.000	0.260	2097.2	0.011	0.478	$1_0{}^0 4_0{}^5$
1	0.110	0.089	0.171	1377.2	0.004	0.567	$1_0{}^0 4_1{}^5$
1	0.110	0.179	0.081	657.2	0.002	0.657	$1_0{}^0 4_2{}^5$
1	0.129	0.000	0.279	2252.4	0.063	0.459	$1_0{}^1 4_0{}^3$
1	0.129	0.089	0.190	1532.4	0.026	0.548	$1_0{}^1 4_1{}^3$
1	0.157	0.000	0.307	2477.2	0.110	0.431	$1_0{}^2 4_0{}^1$
1	0.157	0.089	0.218	1757.2	0.051	0.520	$1_0{}^2 4_1{}^1$
1	0.157	0.179	0.129	1037.2	0.004	0.609	$1_0{}^2 4_2{}^1$
1	0.228	0.000	0.378	3049.2	0.001	0.360	$1_0{}^0 4_0{}^7$
1	0.241	0.000	0.391	3154.2	0.009	0.347	$1_0{}^1 4_0{}^5$
1	0.241	0.089	0.302	2434.2	0.003	0.436	$1_0{}^1 4_1{}^5$
1	0.241	0.179	0.213	1714.2	0.001	0.525	$1_0{}^1 4_2{}^5$
1	0.260	0.000	0.410	3309.8	0.025	0.328	$1_0{}^2 4_0{}^3$
1	0.260	0.089	0.321	2589.8	0.010	0.417	$1_0{}^2 4_1{}^3$
1	0.289	0.000	0.439	3540.0	0.029	0.299	$1_0{}^3 4_0{}^1$
1	0.289	0.089	0.350	2820.0	0.014	0.388	$1_0{}^3 4_1{}^1$
1	0.289	0.179	0.260	2100.0	0.001	0.478	$1_0{}^3 4_2{}^1$
1	0.372	0.000	0.522	4211.6	0.003	0.216	
1	0.372	0.089	0.433	3491.6	0.001	0.305	
1	0.392	0.000	0.542	4372.5	0.007	0.196	
1	0.392	0.089	0.453	3652.5	0.003	0.285	
1	0.425	0.000	0.575	4639.7	0.006	0.163	
1	0.425	0.089	0.486	3919.7	0.003	0.252	
1	0.528	0.000	0.678	5472.3	0.001	0.060	
2	-0.057	0.089	0.004	29.2	0.056	0.734	$1_0{}^0 4_1{}^2$
2	-0.057	0.179	-0.086	-690.8	0.014	0.824	$1_0{}^0 4_2{}^2$
2	-0.057	0.268	-0.175	-1410.8	0.002	0.913	$1_0{}^0 4_3{}^2$
2	0.051	0.089	0.112	905.8	0.017	0.626	$1_0{}^0 4_1{}^4$
2	0.051	0.179	0.023	185.8	0.004	0.715	$1_0{}^0 4_2{}^4$
2	0.074	0.089	0.135	1086.2	0.044	0.603	$1_0{}^1 4_1{}^2$
2	0.074	0.179	0.045	366.2	0.011	0.693	$1_0{}^1 4_2{}^2$
2	0.074	0.268	-0.044	-353.8	0.001	0.782	$1_0{}^1 4_3{}^2$
2	0.167	0.089	0.228	1836.4	0.003	0.510	
2	0.182	0.089	0.243	1962.8	0.013	0.495	$1_0{}^1 4_1{}^4$
2	0.182	0.179	0.154	1242.8	0.003	0.584	$1_0{}^1 4_2{}^4$

M_J	E°(eV)	E⁻(eV)	ΔE(eV)	ΔE(cm-1)	Height	eKE(eV)	Asst.
2	0.205	0.089	0.266	2143.6	0.018	0.472	$1_0^2 4_1^2$
2	0.205	0.179	0.177	1423.6	0.004	0.561	$1_0^2 4_2^2$
2	0.298	0.089	0.359	2893.4	0.002	0.379	
2	0.313	0.089	0.374	3020.2	0.005	0.364	
2	0.313	0.179	0.285	2300.2	0.001	0.453	
2	0.337	0.089	0.398	3206.3	0.005	0.340	
2	0.337	0.179	0.308	2486.3	0.001	0.430	
2	0.445	0.089	0.506	4082.9	0.001	0.232	
3	-0.007	0.179	-0.035	-285.9	0.007	0.773	$1_0^0 4_1^3$
3	-0.007	0.268	-0.125	-1005.9	0.001	0.863	$1_0^0 4_2^3$
3	0.106	0.179	0.078	625.9	0.002	0.660	
3	0.124	0.179	0.096	771.2	0.005	0.642	
3	0.237	0.179	0.209	1682.9	0.002	0.529	
3	0.255	0.179	0.227	1828.5	0.002	0.511	

Parameters used in simulation:

$\omega_1^A = \omega_1^E = \omega_1^- = 1057.0$ cm-1, 0.131 eV.

$\omega_4^A = \omega_4^E = \omega_4^- = 720.0$ cm-1, 0.089 eV.

$\kappa_1 = 0.165$ eV in $^2A_2'$ and $^2E'$ states

$\lambda_4 = 0.265$ eV.

Electronic state energies $\varepsilon_A = 0.00$ eV, $\varepsilon_E = 1.87$ eV.

Adiabatic electron affinity 3.922 eV (a difference of -0.015 eV from our estimated electron affinity, due to the space charge effects in our 266 nm spectra).

Laser energy 4.660 eV.

Ratio of electronic transition dipole moments $\tau_E/\tau_A = 4.400$.

$\omega_4^- = 720.0$ cm^{-1}, T = 430 K (for hot band calculation).

Construct Hamiltonian assuming n4max of 14, n1max of 9; order 240

LAWRENCE BERKELEY LABORATORY
UNIVERSITY OF CALIFORNIA
TECHNICAL INFORMATION DEPARTMENT
BERKELEY, CALIFORNIA 94720